5-2021

Investigation of Bio-Inspired Pin Geometries for Enhanced Heat Transfer Applications

Anish Prasad

INVESTIGATION OF BIO-INSPIRED PIN GEOMETRIES FOR HEAT TRANSFER APPLICATIONS

By

Anish Prasad

A Dissertation Submitted to the Faculty of Embry-Riddle Aeronautical University

In Partial Fulfillment of the Requirements for the Degree of

Doctor of Philosophy in Aerospace Engineering

May 2021

Embry-Riddle Aeronautical University

Daytona Beach, Florida

INVESTIGATION OF BIO-INSPIRED PIN GEOMETRIES FOR ENHANCED HEAT TRANSFER APPLICATIONS

By

Anish Prasad

This Dissertation was prepared under the direction of the candidate's Dissertation Committee Chair, Dr. Mark Ricklick, Department of Aerospace Engineering, and has been approved by the members of the Dissertation Committee. It was submitted to the Office of the Senior Vice President for Academic Affairs and Provost, and was accepted in the partial fulfillment of the requirements for the Degree of Philosophy in Aerospace Engineering.

DISSERTATION COMMITTEE

Mark Ricklick — Digitally signed by Mark Ricklick Date: 2021.04.28 14:54:04 -04'00'

Chairman, Dr. Mark Ricklick

J. Gordon Leishman — Digitally signed by J. Gordon Leishman Date: 2021.04.29 18:32:37 -04'00'

Member, Dr. J. Gordon Leishman

William Engblom — Digitally signed by William Engblom Date: 2021.04.28 16:34:12 -04'00'

Member, Dr. William Engblom

Sandra Boetcher — Digitally signed by Sandra Boetcher Date: 2021.04.28 17:54:32 -04'00'

Member, Dr. Sandra Boetcher

Marwan Al-Haik — Digitally signed by Marwan Al-Haik DN: cn=Marwan Al-Haik, o=Embry-Riddle Aeronautical University, ou=Aerospace Engineering, email=alhaikm@erau.edu, c=US Date: 2021.04.29 21:06:14 -04'00'

Graduate Program Coordinator,
Dr. Marwan Al-Haik

04/29/2021

Date

Maj Dean Mirmirani — Digitally signed by Maj Dean Mirmirani Date: 2021.04.30 08:54:47 -04'00'

Dean of the College of Engineering,
Dr. Maj Mirmirani

04/30/2021

Date

Lon Moeller — Digitally signed by Lon Moeller Date: 2021.04.30 09:52:32 -04'00'

Senior Vice President for Academic Affairs and Provost,
Dr. Lon Moeller

04/30/2021

Date

ACKNOWLEDGEMENTS

First, I would like to express my gratitude to my family and friends, especially my Mom and Dad for their prayers and support. To my advisor Dr. Mark Ricklick, I express my appreciation for all the support and guidance you gave me over the years and finally I would like to thank my committee members for their support.

ABSTRACT

Array of circular cylindrical pins or tubes are one of the most widely used type of convection cooling systems, profoundly used in the internal cooling of gas turbine blades. They promote heat transfer due to flow acceleration, secondary flows and wake shedding, at the expense of large pressure loss and unsteadiness in the flow. The need to reduce pressure loss and maintain the heat transfer rates are a much needed requirement for a variety of industries to improve the cooling efficiency. One such prominent line of research is conducted on optimizing the design of the circular cylindrical pins to increase their cooling performance. Bio-mimicked harbor seal whisker have been studied from an aerodynamic standpoint, due to their ability to reduce drag and flow unsteadiness. While applying this mimicked geometry in thermal management research, it was found that they lead to reduction in cooling system pumping power requirements, with the potential to maintain heat transfer performance. The seal whisker geometry consists of streamwise and spanwise undulations which reduce the size of the wake and coherent structures shed from the body; a result of an added component of streamwise vorticity along the pin surface. In addition, the vortex shedding frequency becomes less pronounced, leading to significantly reduced lateral loading on the modified cylinder. These whisker geometries are studied for their aero behavior but not from a thermal performance stand point. Hence the main objective of this study is to understand and utilize different flow physics of these whisker geometries in a wall bounded configuration. Computational studies have shown that the modified wake and vortex shedding structures resulting from the geometry tend to reduce the total pressure loss throughout the system without significantly degrading the cooling levels and experimental results agree with these findings. In

comparison to a conventional elliptical pin the bio pins have an increase in thermal performance at constant pressure drop by 9% and by 45% in comparison to a conventional cylindrical pin. These findings are important to the gas turbine community and heat exchangers as reduced penalties associated with cooling flows directly translate to improved thermodynamic and propulsive efficiencies.

TABLE OF CONTENTS

ACKNOWLEDGEMENTS iii

ABSTRACT iv

LIST OF FIGURES ix

LIST OF TABLES xxii

NOMENCLATURE xxiii

1. Introduction 1
    1.1. Motivation 2
    1.2. Turbine Blade Cooling 2
        1.2.1. Pin Fin Channel 4
    1.3. Biomimicry 6

2. Literature Review 10
    2.1. Conventional Pins 10
    2.2. Non – conventional Pins 15
    2.3. Biomimicry 21
    2.4. Hypothesis 28

3. Methodology 30
    3.1. Pin Design 30
        3.1.1. Initial Pin Design 30
        3.1.2. Final Pin Design 31
    3.2. Computational Setup 34
        3.2.1. Mesh Independent Study 36
    3.3. Experimental Setup 38
        3.3.1. Heat Leakage Test 43
        3.3.2. Temperature Sensitive Paint (TSP) 45
    3.4. Hotwire Anemometry 48
        3.4.1. Calibration of Hotwire 52
        3.4.2. Validation of Hotwire and Calibration Setup 53
    3.5. Pressure Transducers 55
    3.6. Data Reduction 56
        3.6.1. Endwall Nusselt Number 56
        3.6.2. Pin Surface Average Nusselt Number (ESM) 58
        3.6.3. Pressure Data 59
        3.6.4. Reynolds Number 60
        3.6.5. Friction Factor 62
        3.6.6. Turbulence Intensity 63
        3.6.7. Uncertainty Analysis 63
4. Results 65

4.1. Computational Study – Initial Pin Design 65
4.1.1. Endwall Nusselt Number 65
4.1.2. Pin Circumferential Data 68
4.1.3. Pin Surface Average Nusselt Number 76
4.1.4. Pressure Drop Along the Channel 79
4.1.5. Reynolds Number Effects 80
4.1.6. Turbulent Kinetic Energy 86
4.1.7. Spectral Analysis 97
4.2. Computational Study – Initial Pin Design 102
4.2.1. Endwall Nusselt Number 102
4.2.2. Pin Surface Average Nusselt Number 104
4.2.3. Pressure Drop 106
4.2.4. Thermal Performance 109
4.2.5. Turbulent Kinetic Energy Along the Channel 114
4.2.6. Pin Circumferential Data 115
4.2.7. Turbulent Kinetic Energy 120
4.2.8. Contour Plots 124
4.2.9. Spectral Analysis 130
4.2.10. Array Sensitivity 137
4.2.11. Infinite Pin 143
4.2.12. Reynolds Number Effect 146
4.2.13. Engineered Pin Designs Based on Bio Pin Geometries 148
4.2.14. Laminar Case Study 154
4.3. Experimental Results – Initial Pin Design 157
4.3.1. Test Setup Validation 157
4.3.2. Endwall Nusselt Number 162
4.3.3. Pressure Drop Along the Channel 165
4.3.4. Reynolds Number Effects 167
4.3.5. Spectral Analysis 170
4.4. Experimental Results – Final Pin Design 173
4.4.1. Endwall Nusselt Number 173
4.4.2. Pressure Drop Along the Channel 178
4.4.3. Pin Surface Nusselt Number 182
4.4.4. Reynolds Number Effects 183
4.4.5. Spectral Analysis 187
4.4.6. Turbulence Intensity 189

5. Conclusions 191

REFERENCES 198

PUBLICATIONS 203

APPENDIX 204
A.1. Reynolds Number for a Harbor seal whisker 204
A.2. 3D Printed Harbor Seal Whisker Geometries 204

A.3. Time Step 205
A.4. Plots 206

LIST OF FIGURES

Figure		Page
1.1	Brayton cycle	1
1.2	Turbine inlet temperatures over the years.....	3
1.3	Blade cooling techniques	3
1.4	Flow feature in a pin fin channel	4
1.5	Endwall Nusselt number contour (CFD) – Cylindrical pin fin array.....	5
1.6	Turbine vane cross section.....	6
1.7	Biological vs. engineered hawkmoth (manduca sexta) wing.....	7
1.8	Left – Humpback whales' flipper, middle – Humpback whales' flipper airfoil model and Right – Humpback whales' flipper turbine blade model.....	8
1.9	Left – Maple seed in time as it falls to the ground and Right – PowerCone.....	9
2.1	Inline and staggered pin fin array	11
2.2	Different streamwise and spanwise spacing for H/d=1	12
2.3	Array averaged Nusselt number.....	12
2.4	Regionally – averaged Nu and flow separation angle	13
2.5	Time averaged Nusselt number normalized with Nusselt number average (Nu/Nuave) for Re = 30,000, Top: URANS; middle: hybrid LES/URANS; bottom: experiment.	14
2.6	Geometry of stepped circular pin fin	15
2.7	Comparison of thermal performance for stepped pin fins	16

Figure Page

2.8 Streamlines: A – Cylindrical pin fin, B – stepped pin fin and C – optimized stepped pin fin 16

2.9 Microchannel model with different pins shapes 17

2.10 Nusselt number and pressure drop for different pin geometry 17

2.11 Flow visualization (left) and thermal performance (right) of porous pins 18

2.12 Pin model: Circular pin, Standard elliptical pin (SEF) and pin based on NACA 0024 (N fin) 18

2.13 Pin fin heat sink model with impingement cooling 19

2.14 Circular cylinders with periodic array of fins 20

2.15 Instantaneous streamwise contours at different locations along the pin axis 20

2.16 Frossling number (left) and friction factor (right) comparison 21

2.17 Sensing abilities of harbor seal whisker 22

2.18 Vortex induced vibrations 22

2.19 Seal whisker's shape 22

2.20 Structure of Harbor seal and California sea lion vibrissae 23

2.21 Frequency and velocity for flow induced vibration 24

2.22 Wake flow behind different cross section bodies 25

2.23 a) whisker-like geometry with no undulations on major axis, b) whisker-like geometry with no undulations on minor axis, c) whisker-like geometry with no offset angle, d) whisker-like geometry with constant offset angle (17.6°), and e) real whisker geometry 26

Figure Page

2.24 Piezoelectric sensor with circular cylinder (left) and whisker-like (right) structure mounted at the center of the membrane 27

2.25 Harbor seal whisker inspired turbine blade geometries 27

3.1 Seal whisker structure 30

3.2 Adapted whisker geometries 31

3.3 Replica of the harbor seal whisker geometry 33

3.4 Pin geometries in groups 1, 2 and 3 34

3.5 Computational model 35

3.6 Mesh independent study 37

3.7 Mesh – G2TV 38

3.8 Schematic of experimental setup 39

3.9 Initial pin design – test section setup 39

3.10 Final pin design – test section setup 40

3.11 Inconel heater strips 41

3.12 Test section – internally heated pins 42

3.13 TSP excitation, CMOS camera and LED light 42

3.14 Schematic of test section 43

3.15 Schematic of heat leakage test 44

3.16 Heat leakage test setup 44

3.17 Heat leakage test 44

Figure Page

3.18 Jablonski diagram 45

3.19 Reference image and data image 46

3.20 Calibration of TSP 47

3.21 Single component hotwire probe 48

3.22 Schematic of hotwire calibration device 49

3.23 Hotwire Calibration device 50

3.24 Nozzle design 51

3.25 Nozzle velocity contour 51

3.26 Nozzle velocity vector 52

3.27 Hotwire validation 53

3.28 Schematic of hotwire setup 54

3.29 Hotwire setup 55

3.30 Schematic of Kulite pressure transducer 56

3.31 Layout of the test section with boundary conditions 58

4.1 Spanwise average Nusselt number for Re = 2,700 66

4.2 Endwall Nusselt number contour for Re = 2,700 66

4.3 Spanwise average Nusselt number for Re = 5,200 67

4.4 Spanwise average Nusselt number for Re = 15,500 68

4.5 Circumferential pattern 68

Figure Page

4.6 Row 1 pin circumferential Cp data for Re = 2,700 69

4.7 Row 1 pin circumferential Frossling number data for Re = 2,700 69

4.8 Row 5 pin circumferential C_p data for Re = 2,700..... 70

4.9 Row 5 pin circumferential Frossling number data for Re = 2,700 70

4.10 Row 1 pin circumferential Cp data for Re = 5,200 72

4.11 Row 1 pin circumferential Frossling number data for Re = 5,200 72

4.12 Row 5 pin circumferential Cp data for Re = 5,200 73

4.13 Row 5 pin circumferential Frossling number data for Re = 5,200 73

4.14 Row 1 pin circumferential Cp data for Re = 15,500 74

4.15 Row 1 pin circumferential Frossling number data for Re = 15,500 75

4.16 Row 1 pin circumferential Cp data for Re = 15,500 75

4.17 Row 5 pin circumferential Frossling number data for Re = 15,500 76

4.18 Pin surface average Frossling number for Re = 2,700 77

4.19 Pin surface average Frossling number for Re = 5,200 77

4.20 Pin surface average Frossling number for Re = 15,500 78

4.21 Pressure drop along the channel for Re = 2,700 79

4.22 Pressure drop along the channel for Re = 5,200 79

4.23 Pressure drop along the channel for Re = 15,500 80

4.24 Channel average Nusselt number vs friction factor for Re = 2,700..... 81

Figure Page

4.25 Endwall average Nusselt number vs friction factor for Re = 2,700..... 81

4.26 Pin surface average Nusselt number vs friction factor for Re = 2,700 81

4.27 Channel average Nusselt number vs friction factor for Re = 5,200..... 83

4.28 Endwall average Nusselt number vs friction factor for Re = 5,200..... 83

4.29 Pin surface average Nusselt number vs friction factor for Re = 5,200 83

4.30 Channel average Nusselt number vs friction factor for Re = 15,500..... 85

4.31 Endwall average Nusselt number vs friction factor for Re = 15,500..... 85

4.32 Pin surface average Nusselt number vs friction factor for Re = 15,500 ... 85

4.33 TKE along the channel for Re = 2,700 86

4.34 TKE along the channel for Re = 5,200 86

4.35 TKE along the channel for Re = 15,500 87

4.36 TKE – axial direction for Re = 2,700..... 88

4.37 TKE – axial direction for Re = 5,200..... 89

4.38 TKE – axial direction for Re = 15,500..... 90

4.39 TKE – spanwise direction for Re = 5,200..... 91

4.40 TKE – spanwise direction for Re = 15,500..... 92

4.41 CP1 – TKE contour for Re = 15,500 93

4.42 BP2 – TKE contour for Re = 15,500 93

4.43 EP1 – TKE contour for Re = 15,500..... 94

Figure Page

4.44 BP1 – TKE contour for Re = 15,500 94

4.45 CP1 – Vorticity contour for Re = 15,500 95

4.46 BP2 – Vorticity contour for Re = 15,500 95

4.47 EP1 – Vorticity contour for Re = 15,500 96

4.48 BP1 – Vorticity contour for Re = 15,500 96

4.49 PSD: Row 1 for Re = 5,200 99

4.50 PSD: Row 3 for Re = 5,200 100

4.51 PSD: Row 5 for Re = 5,200 101

4.52 Spanwise average endwall Nusselt number for group 1 pins 102

4.53 Spanwise average endwall Nusselt number for group 2 and 3 pins..... 103

4.54 Group 1: Row average Nusselt number 104

4.55 Group 2 and 3: Row average Nusselt number 105

4.56 Group 1: Pressure drop along the channel 107

4.57 Group 2 and 3: Pressure drop along the channel 107

4.58 Endwall average Nusselt number for Group 1 pins 109

4.59 Pin surface average Nusselt number for Group 1 pins..... 110

4.60 Channel average Nusselt number for Group 1 pins 110

4.61 Endwall average Nusselt number for Group 2 and 3 pins 111

4.62 Pin surface average Nusselt number for Group 2 and 3 pins..... 112

Figure Page

4.63 Channel average Nusselt number for Group 2 and 3 pins 112

4.64 TKE – Group 1 114

4.65 TKE – Group 2 and 3 115

4.66 Row 1 pin circumferential wall shear stress 116

4.67 Row 1 pin circumferential coefficient of pressure 116

4.68 Row 1 pin circumferential Frossling number 117

4.69 Row 5 pin circumferential wall shear stress 119

4.70 Row 5 pin circumferential coefficient of pressure 119

4.71 Row 5 pin circumferential Frossling number 120

4.72 TKE behind row 1 121

4.73 TKE behind row 3 122

4.74 TKE behind row 5 122

4.75 TKE behind row 7 123

4.76 Spanwise TKE data behind row 7 124

4.77 Mean of endwall Nusselt number 125

4.78 TKE – G2C 126

4.79 TKE – G2E 126

4.80 TKE – G2TV 127

4.81 TKE – G2TRV 127

Figure Page

4.82 Vorticity – G2C 128

4.83 Vorticity – G2E 128

4.84 Vorticity – G2TV 129

4.85 Vorticity – G2TRV 129

4.86 FFT – Lift on pin G2TV 131

4.87 FFT – Drag on pin G2TV 131

4.88 FFT – G2TV 132

4.89 FFT – G2TRV 133

4.90 FFT – G2E 134

4.91 FFT – G2C 135

4.92 Endwall average Nusselt number – reduced array dimensions 137

4.93 Endwall Nusselt number contour – reduced array dimensions 138

4.94 Pin surface average Nusselt number – reduced array dimension 139

4.95 Pin surface average Nusselt number – reduced array dimension 140

4.96 Endwall thermal performance 140

4.97 Pin thermal performance 141

4.98 Channel average thermal performance 141

4.99 TKE along the channel for reduced array dimension 142

4.100 TKE contour for reduced array dimensions 143

Figure Page

4.101 Infinite pin – pin surface average Nusselt number 144

4.102 Infinite pin – Pressure drop along the channel..... 145

4.103 Infinite pin – Thermal performance 145

4.104 Nu vs f – Enwall average Nusselt number..... 146

4.105 Nu vs f – Pin surface average Nusselt number 147

4.106 Nu vs f – Channel average Nusselt number..... 147

4.107 NC1 and NC2 geometry..... 149

4.108 Spanwise average Nusselt number for pin NC1 and NC2 149

4.109 Pin surface average Nusselt number for pin NC1 and NC2 150

4.110 Pressure drop along the channel for pin NC1 and NC2..... 151

4.111 Endwall Nusselt number for pin NC1 and NC2 151

4.112 Pin average Nusselt number for pin NC1 and NC2..... 152

4.113 Channel average Nusselt number for pin NC1 and NC2..... 152

4.114 TKE along the channel in NC1 and NC2..... 153

4.115 TKE contour for NC1 and NC2 153

4.116 Pin surface average Nusselt number laminar case..... 155

4.117 Pressure drop across the channel for laminar case..... 156

4.118 Thermal performance of laminar case 157

4.119 Comparison of analytical solution with Ames for Re = 3,000..... 158

Figure Page

4.120 Comparison of analytical solution with Ames for Re = 10,000..... 159

4.121 Comparison of analytical solution with Ames for Re = 30,000..... 160

4.122 Comparison of average endwall and pin Nusselt numbers 161

4.123 Comparison of Channel average Nusselt number..... 161

4.124 Endwall Nusselt number contour for Reynolds number = 12,000..... 162

4.125 Spanwise average endwall Nusselt number for Reynolds number = 2,000..... 163

4.126 Spanwise average endwall Nusselt number for Reynolds number = 4,000..... 164

4.127 Spanwise average endwall Nusselt number for Reynolds number = 12,000..... 164

4.128 Pressure drop along the channel for Reynolds number = 2,000 165

4.129 Pressure drop along the channel for Reynolds number = 4,000 166

4.130 Pressure drop along the channel for Reynolds number = 12,000 166

4.131 Nusselt number over various Reynolds number 167

4.132 Thermal performance for Reynolds number = 2,000..... 168

4.133 Thermal performance for Reynolds number = 4,000..... 168

4.134 Thermal performance for Reynolds number = 12,000..... 168

4.135 FFT experiment – CP1 row 1..... 170

4.136 Experiment FFT – CP1 170

4.137 Experiment FFT – BP2 171

Figure		Page
4.138	Experiment FFT – BP1	172
4.139	Spanwise average Nusselt number for Smooth channel	174
4.140	Temperature contour (TSP)	175
4.141	Nusselt number contour for Re = 30,000	175
4.142	Spanwise average Nusselt number for Re = 15,000	176
4.143	Spanwise average Nusselt number for Re = 30,000	176
4.144	Spanwise average Nusselt number for Re = 60,000	177
4.145	Spanwise average Nusselt number for Re = 85,000	177
4.146	Pressure drop along the channel for G2E – Re = 15,000	178
4.147	Pressure drop along the channel for G2TV – Re = 15,000	179
4.148	Pressure drop along the channel for G2TRV – Re = 15,000	179
4.149	Pressure drop along the channel for G2E – Re = 30,000	179
4.150	Pressure drop along the channel for G2TV – Re = 30,000	180
4.151	Pressure drop along the channel for G2TRV – Re = 30,000	180
4.152	Pressure drop along the channel for Re = 15,000	181
4.153	Pressure drop along the channel for Re = 30,000	181
4.154	Pressure drop along the channel for Re = 60,000	181
4.155	Pressure drop along the channel for Re = 85,000	182
4.156	Pin row average Nusselt number for Re = 60,000	183

Figure		Page
4.157	Endwall Nusselt number over Reynolds number	184
4.158	Thermal performance comparison for Re = 15,000	185
4.159	Thermal performance comparison for Re = 30,000	185
4.160	Thermal performance at various Reynolds number	186
4.161	FFT – Smooth channel	188
4.162	FFT – Row 1	188
4.163	FFT – Row 5	189
4.164	Velocity magnitude and TI for pin G2TV behind row 1 and 5 pin	190
A.1	3D printed geometries – Initial Pin Design	205
A.2	3D printed geometries – Final Pin Design	205
A.3	Spanwise average endwall Nusselt number for group 1 pins	206
A.4	Spanwise average endwall Nusselt number for group 2 and 3 pins	207
A.5	Group 1: Row average Nusselt number	207
A.6	Group 2 and 3: Row average Nusselt number	208
A.7	Group 1: Pressure drop along the channel	208
A.8	Group 2 and 3: Pressure drop along the channel	209
A.9	TKE – Group 1	209
A.10	TKE – Group 2 and 3	210

LIST OF TABLES

Table		Page
3.1	Mesh independent study	36
3.2	Mesh independent study	37
4.1	Max flux comparison	173
5.1	Initial pin design – CFD – Thermal Performance	192
5.2	Initial pin design – Experiment – Endwall thermal performance	193
5.3	Final pin design – CFD – Thermal performance – Re = 30,000	194
5.4	Final pin design – CFD – Thermal performance – Re = 15,000	195
5.5	Final pin design – Experiment – Endwall thermal performance	196

NOMENCLATURE

A_c	Cross-sectional area	m^2
A_s	Surface area	m^2
a_∞	Speed of sound	m/s
B or b	Systematic uncertainty	
C_0 to C_4	Coefficients	
CFD	Computational Fluid Dynamics	
C_p	Specific heat capacity at constant pressure	J/Kg.K
CMC	Ceramic Matrix Composite	
CMOS	Complementary Metal Oxide Semiconductor	
D	Characteristic diameter	m
d/H	Pin diameter to height ratio	
e_1 to e_n	Measuring device errors	
E_a	Recorded voltage	V
E_{corr}	Corrected voltage	V
ESM	Extended Surface Methodology	
f	Friction factor	
GPM	Gallons per minute	
H	Height of the channel	m
H/D	Pin height to major diameter ratio	

h	Heat transfer coefficient	$W/m^2.K$
h/H	Pin height of the channel height ratio	
I	Current	A
I_s	Surface intensity	
I_{ref}	Reference intensity	
k	Thermal conductivity	W/m.K
k_0	Sutherland's constant for thermal conductivity	W/m.K
L	Length of the channel	m
LED	Light emitting diode	
n	Number of pixels in streamwise direction	
N	Sample size	
Nu	Nusselt number	
m	Fin parameter	
M	Period of the undulations	
M_∞	Mach number of jet out of the nozzle	
$\dot{\mathbf{m}}$	Mass flow	Kg/s
P	Pressure	Pa
P_0	Chamber pressure	Pa
P_c	Pressure correction	Psig
PVC	Polyvinyl chloride	

P_∞	Atmospheric pressure of the room	Pa
q”	Heat flux	W/m^2
$q”_{loss}$	Heat flux lost	W/m^2
$q”_{sup}$	Heat flux supplied	W/m^2
q(x)	Heat supplied per spanwise row of pixel	W/m
$\dot{q}$	Internal heat generation	W/m^3
R	Gas constant	J/Kg.K
RANS	Reynolds Averaged Navier Stokes	
Re	Reynolds number	
S	Random uncertainty	
S1/d	Spanwise pin spacing	
S2/d	Streamwise pin spacing	
SCFM	Standard cubic feet per minute	
SST	Shear Stress Transport	
S_k	Sutherland’s constant for temperature	K
T	Temperature	K
T_3	Turbine inlet temperature	K
T_4	Turbine exit temperature	K
T_0	Calibration temperature	K
T_0	Sutherland’s constant for temperature	K

t_{95}	Student t confidence interval	
T_a	Ambient temperature	K
T_b	Bulk temperature	K
TBC	Thermal Barrier Coating	
T_c	Temperature correction	°R
TI	Turbulence Intensity	
T_{ref}	Reference temperature	K
T_s	Surface temperature	K
TSP	Temperature Sensitive Paint	
T_w	Wall Temperature	K
T_w/T_c	Heating loads	
T_∞	Temperature of the jet	K
u_y	Calculated uncertainty	
U_y	Final uncertainty	
V	Voltage	V
V	Velocity	m/s
VARIAC	Variable AC voltage	
V_{mean}	Mean velocity	m/s
V_{rms}	Standard deviation of velocity	m/s
V_∞	Jet velocity	m/s

w	Width of strip	m
X	Streamwise spacing	m
Y	Spanwise spacing	m
α	Peak plane angle	°
β	Valley plane angle	°
γ	Ratio of specific heats	
ρ	Resistivity	Ω.m
ρ	Density	Kg/m^3
$\theta(x)$	$T(x) - T_b$	
μ	Dynamic viscosity	Pa.s
μ_0	Sutherland's constant for dynamic viscosity	Pa.s
σ_x	Standard deviation	

1. Introduction

Most energy-based systems in use employ some form of convection based thermal management. Gas turbine engines power most of the passenger aircrafts operating today. The efficiency of the gas turbine is directly related to the turbine inlet temperature, and the effectiveness of the hot section cooling systems. The gas turbine works on Brayton cycle, illustrated in the temperature and entropy diagram in Figure 1.1.

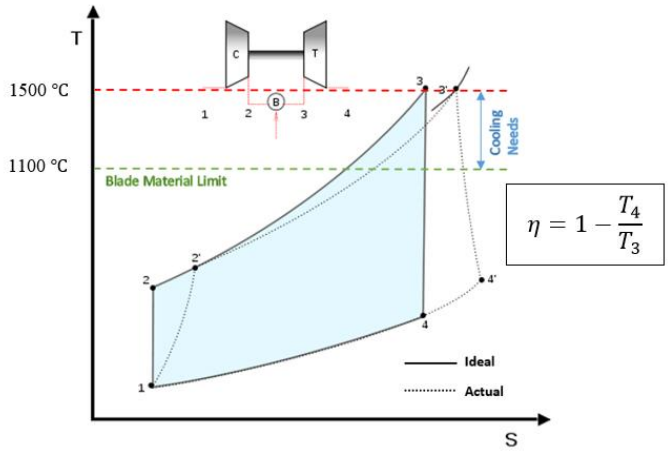

Figure 1.1 Brayton cycle

The efficiency of the Brayton cycle is governed by the equation shown in the Figure 1.1. In the ideal case, the Brayton cycle will not have any losses, but in the real world there are losses, which is illustrated by the actual Brayton cycle. Here T_3 represents the turbine inlet temperature, and as seen from the Brayton cycle, higher the temperature at the inlet of the turbine, better the efficiency of the Brayton cycle. Hence gas turbine manufacturers strive to achieve the highest turbine inlet temperatures within the safe operating limits of the blade material.

1.1. Motivation

Modern gas turbine designs have taken advantage of advanced cooling technologies to the extent that rotor experiences inlet temperatures several hundred Kelvin beyond the safe operating point of the exotic materials used within them (Sautner, Clouser, & Han, 1992), with limits continuing to be pushed. The importance of this is highlighted by the fact that a 56 Kelvin increase in hot gas temperature potentially yields an increase of up to 13% in power output or 4% in simple cycle efficiency (Boyce, 2006). The task of a cooling design is not only to keep the maximum temperature of the blade itself below a safe level, but also minimize spatial variations in temperature that can create thermal stress (Iacovides & Launder, 2006). Future advances, however, are becoming more difficult to achieve, as the rate of technology improvement has somewhat reached a plateau in the past 10 years (Bunker, 2006; Downs & Landis, 2009).

There is a need in improved cooling techniques, which takes advantage of advanced design, materials and their manufacturing methods. In most heat exchange applications, an array of constant cross section cylinders are widely employed; hence they have been heavily studied in the literature. This gives us the opportunity to come upon with novel ideas leading to innovative pin structures for the potential to have better performance.

1.2. Turbine Blade Cooling

The maximum attainable turbine inlet temperatures ultimately depend on the maximum combustion temperature of the fuels used for power generation today with some losses, which can reach temperatures close to 1700°C as seen in Figure 1.2. Cooling air around 650°C is extracted from the compressor and passes through the turbine blade. With the hot gases and cooling air, the temperature of the turbine blades

can be lowered to approximately 1000°C, which is permissible for reliable and safe operation of the engine (Gas turbine handbook, 2006).

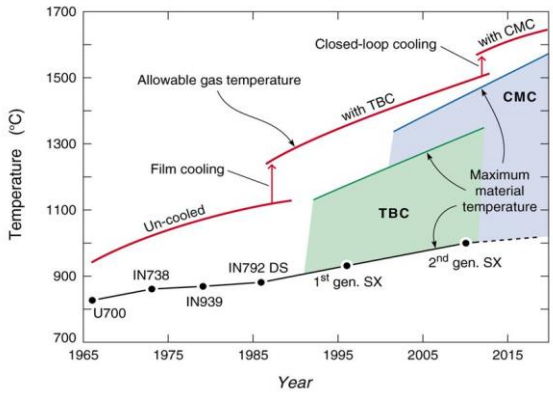

Figure 1.2 Turbine inlet temperatures over the years (Wadley Research Group)

Cooling of turbine blades started with simple convection cooling (internal cooling). Later various methods such as film cooling, Thermal Barrier Coating (TBC) allowed to increase the operating temperature of the blade. Figure 1.3 shows the different cooling techniques implemented in a conventional gas turbine blade.

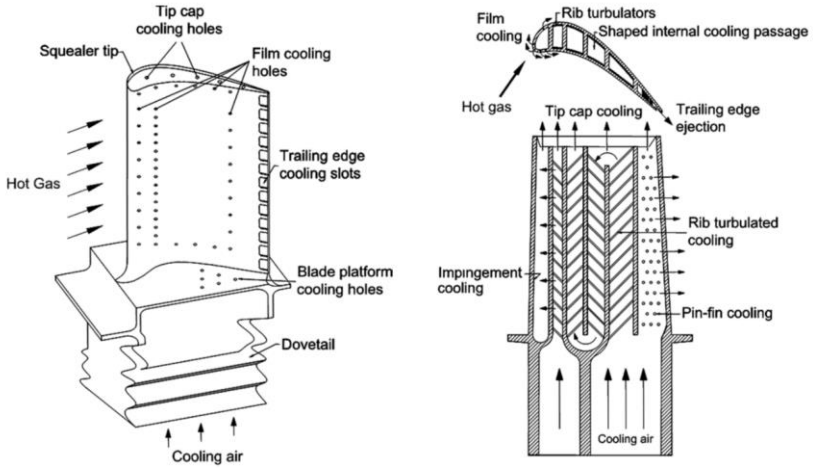

Figure 1.3 Blade cooling techniques (Han, 2004)

The cooling techniques for the turbine blade comprises of both internal and external cooling. The internal cooling technique comprises of different methods such as, jet impingement cooling, rib turbulated cooling, dimple cooling and pin fin cooling. External cooling technique utilizes film cooling holes. Apart from these convection type cooling methods, other advanced methods such as Thermal Barrier Coating (TBC), and Ceramic Matrix Composite (CMC) materials are used to further enhance the heat transfer.

1.2.1. Pin fin channel

A pin fin channel is made up of fins, usually cylindrical in shape, arranged in a staggered or non-staggered array. Figure 1.4 represent the flow feature in a typical pin fin channel geometry. The resulting shedding of vortex, as seen in Figure 1.4 caused by unsteady separation is a significant driver of heat transfer on the backside of the pin (Ames & Dvorak, 2006).

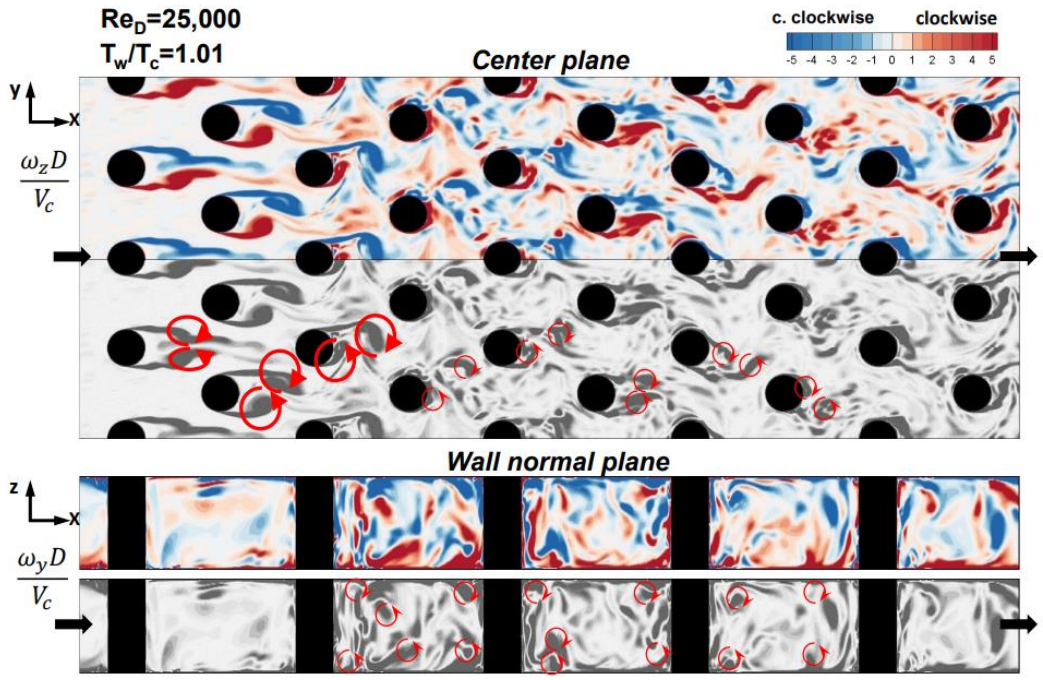

Figure 1.4 Flow feature in a pin fin channel (Shih, 2018)

An internal cooling channel with a pin fin array is characterized by regions of accelerated flows between the pins, stagnation flows, localized low and high pressure regions, flow separation zones and end wall boundary layer flow features that enhance the rates of convective heat transfer (Ames et al., 2006; Chyu et al., 1999; Metzger et al., 1982). The main contributors to the heat transfer are the stagnation at the leading edge and the horseshoe vortex created by the pin – endwall to flow interaction (Chyu, Hsing, Shih, & Natarajan, 1999). Figure 1.5 shows the flow feature of the flow interaction with the endwall due to the presence of the cylindrical pins.

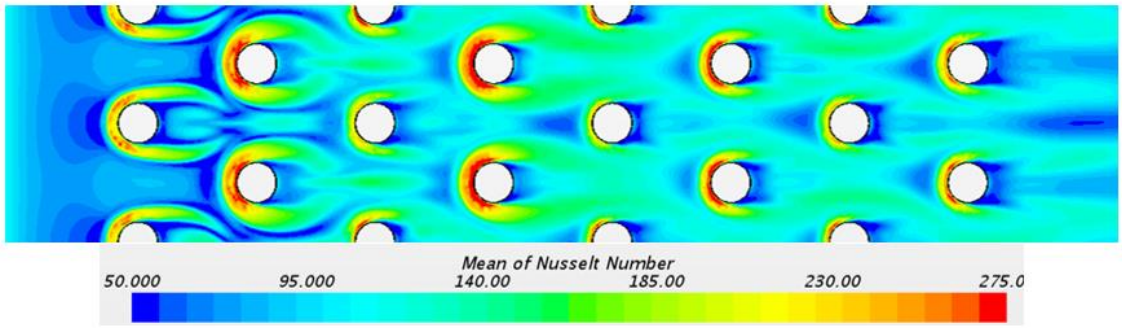

Figure 1.5 Endwall Nusselt number contour (CFD) – Cylindrical pin fin array

As seen in the contour, the horseshoe vortex just forms upstream of the base of the pin and the vortex warps around the pins (Gas turbine handbook, 2006). They create additional flow mixing and therefore enhance the heat transfer. The pin shape and size also have a profound impact on the heat transfer in the cooling passage of a pin fin channel. Also, the effect of coolant extraction must be considered, since pin fins are commonly coupled with trailing edge ejection in a turbine blade/vane as shown in Figure 1.6.

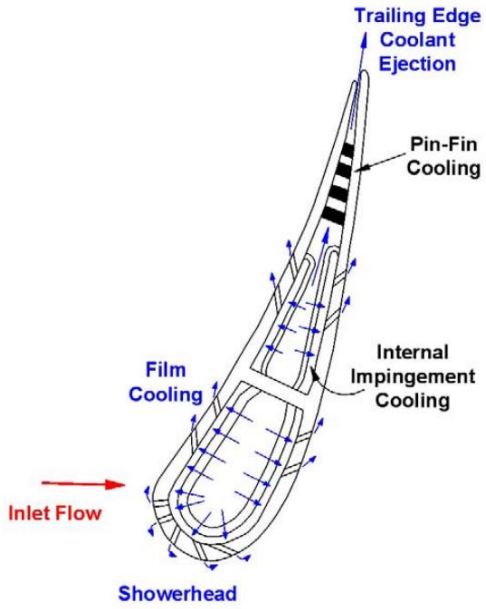

Figure 1.6 Turbine vane cross section (Gas turbine handbook, 2006)

1.3. Biomimicry

Biomimicry (from bios meaning life, and mimesis, meaning to imitate) is a discipline that imitates nature's designs to solve human design problems (Benyus, 1997). Biomimicry and bio-inspired devices have gained interest recently, due to the optimized designs presented in nature through evolution. Biomimicry has found applications in a variety of fields, including modeling bumblebees and other insects in flapping wing aerodynamics. The wing from the insect manduca sexta, as shown in Figure 1.7 is an inspiration for the application of flapping wing aerodynamics.

Figure 1.7 Biological vs. engineered hawkmoth (manduca sexta) wing (DeLuca, 2013)

Several objectives were achieved by studying the wing of this insect, such as the wing rotation angle and effective control methods (DeLuca, 2013). The insect Bumblebees also serves as an inspiration for application of flapping wing aerodynamics. Its wing generates a lift coefficient of 0.5894, the stall angle was observed at +16° angle of attack and the minimum coefficient of drag was observed to be -0.2389 at an angle of attack of -7° (Thompson et al., 2015). Settles et al. (2003) studied about gas sampling based on canine olfactory airflows, separate flow pathways are provided for the inspired and expired air by way of nozzle flexure, these were studied for the purpose of chemosensing (Settles, Douglas, & Dodson-Dreibelbis, 2003).

The fish scale was mimicked for microscale passages for enhanced heat transfer. It was observed that the thermos-hydraulic performance factor was increased by 43% compared to a smooth passage (Goh & Ooi, 2016). Different fractal geometries inspired by plant leaves with different surface wettability were studied to be used for heat exchanger surface treatment for condensation and frosting application (Huang, Hwang, & Radermacher, 2017).

Fish et al. (2011) and Miklosovic et al. (2004) investigated the application of tubercles on humpback whales' flipper, as seen in Figure 1.8. It was observed that the use of tubercles on the leading edge of an airfoil increased the lift by 6% and increased the stall angle by 40% with comparison to NACA 0020 airfoil, while maintaining the coefficient of drag (Fish et al., 2011; Miklosovic et al., 2004).

Tubercles on humpback whales' flipper are also studied to be used in wind turbine blades, as seen in Figure 1.8. WhalePower Corporation demonstrated that using tubercles based on humpback whales' flipper on wind turbine blades will overcome the poor

reliability when winds fall, noise – especially tip chatter caused by tip stalling, and poor performance in unsteady or turbulent air (Whalepower Corporation).

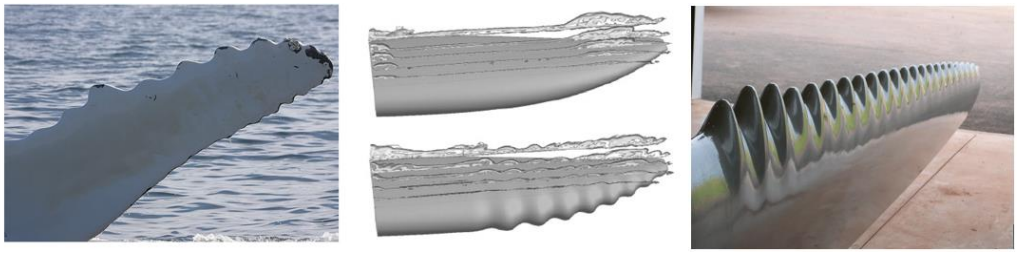

Figure 1.8 Left – Humpback whales' flipper (Asknature), middle – Humpback whales' flipper airfoil model (Fish et al., 2011) and Right – Humpback whales' flipper turbine blade model (Whalepower Corporation)

Biome-Renewables proposed retrofitting a wind turbine with a PowerCone, as seen in Figure 1.9 which channels incoming wind onto the blades to address root leakage. This results in obtaining more power. The PowerCone design is based on kingfisher's beak and the maple seed. The PowerCone has a 53% peak aerodynamic efficiency and 13% increase in annual energy production, while experiencing reduced loads and generating less noise (Biome-Renewables®).

Biomimicry still imposes a main challenge, of how to access the information needed to use biomimicry in an effective and successful way (Volstad & Boks, 2012). The research entitled to this dissertation, which imitates harbor seal's whisker shape to a pin geometry, also faces the same challenge, as the whiskers are naturally designed for their hydrodynamic benefits. However, in this research they are used for thermodynamic and aerodynamic purpose. Hence accessing the information needed to obtain a successful thermal performance benefit from this whisker shape pin geometry will be the challenge for this study.

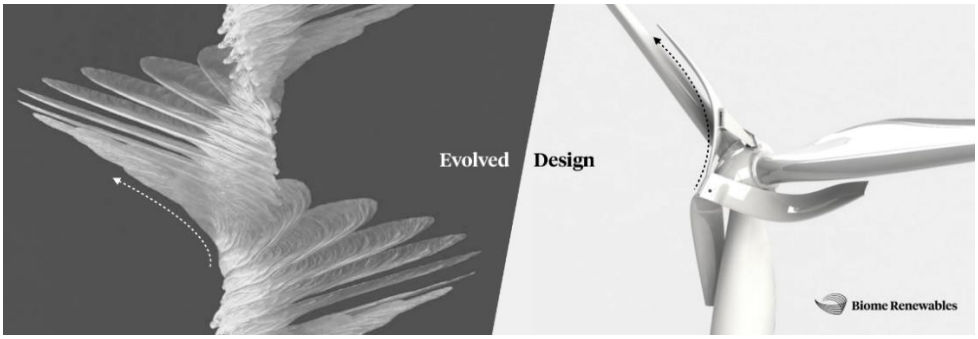

Figure 1.9 Left – Maple seed in time as it falls to the ground and Right – PowerCone (Biome-Renewables®)

2. Literature Review

Numerous studies have been carried out using different pin geometries, in this section these studies are categorized into two parts, conventional and non-conventional pins. Studies done using harbor seal whiskers will be discussed, which will lead to the hypothesis of this current study.

2.1. Conventional Pins

The circular cross section cylinders have been extensively used in thermal management applications due to better heat transfer characteristics, but at the cost of pumping power requirements; hence increasing heat transfer characteristics will subsequently increase the pumping power requirements.

The behavior of flow around the pin significantly affects the heat transfer and it has been detailed in literature that the presence of the pin breaks up the boundary layer creating a horseshoe vortex, as seen in Figure 1.5. The horseshoe vortex created by the presence of the pin produces high wall shear stress beneath it, resulting in high heat transfer from the wall, the resulting flow separation around the pin results in large pressure loss (Chyu, 1990). The pin fin channel has been heavily studied in the literature in an effort to describe the heat transfer, flow behavior, and improve prediction abilities.

VanFossen (1982) studied about staggered array of short pin fins, two different model geometries was used in three variations: copper pins, wooden pins, and inclined copper pins. It was concluded that the average heat transfer coefficient on the pin surface is about 35 percent larger than that on the endwall. At low Reynolds number, pins angled at 60º have 50% greater effective heat transfer than perpendicular pins (VanFossen, 1982).

Chyu et al. (1999) investigated about pin fin array configuration: inline and staggered,

as seen in Figure 2.1. Two features were implemented, one is the isothermal boundary conditions over the entire channel and second is attaining true row averaged data. This study concluded the heat transfer coefficient on the pin surface is higher than the endwall by approximately 10 to 20% (Chyu et al., 1999).

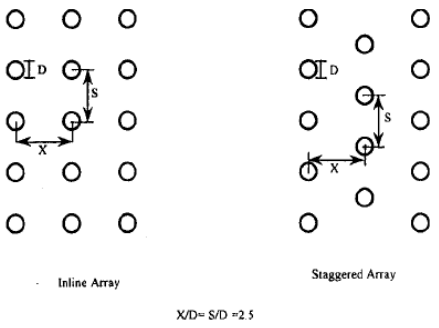

Figure 2.1 Inline and staggered pin fin array (Chyu et al., 1999)

Ames and Dvorak (2006) investigated flow features and aspects of turbulent transport in a pin fin array, in order to better understand the flow physics. He concluded that the flow has significant unsteadiness due to vortex shedding from the pins and the relative intensity of vortex shedding increases with Reynolds number. Vortex shedding from pins in row 2 is significantly stronger than shedding from pins in row 1, as seen in Figure 1.4 and the relative intensity of this shedding has been shown to correlate well with backside heat transfer rates (Ames & Dvorak, 2006).

In a pin fin array, the flow of fluid around the pin causes turbulent wakes, which increases as the flow moves downstream. These turbulent wakes result in high levels of total pressure loss in these regions. This overall pressure drop in the channel can be used to throttle the flow. As a result, relatively small driving pressures can be supplied to these fin arrays (Ciha, 2014).

Lawson et al. (2011) discussed about the augmentation in convective heat transfer due to different spacing in the pin fin arrays, as shown in Figure 2.2. Their study showed that the heat transfer in an array of pin fins increased with decreased spanwise (S1/d) and streamwise (S2/d) pin spacing with a stronger dependence on streamwise spacing than spanwise spacing (Lawson, Thrift, Thole, & Kohli, 2011). Figure 2.3 summarizes array averaged Nusselt number for different pin spacing.

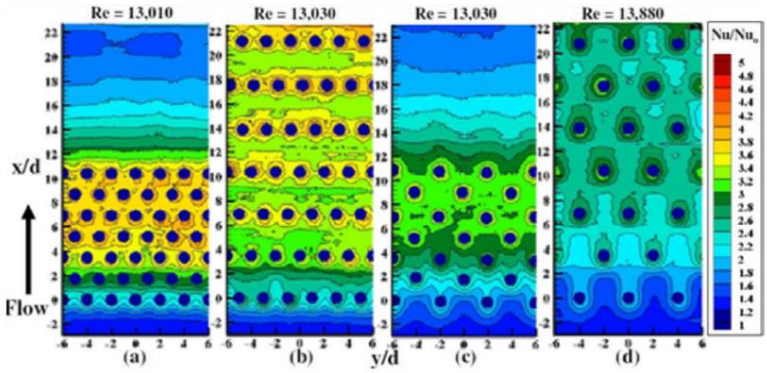

(a) S1/d = 2, S2/d = 1.73, (b) S1/d = 2, S2/d = 3.46, (c) S1/d = 4, S2/d = 1.73, and (d) S1/d = 4, S2/d = 3.46

Figure 2.2 Different streamwise and spanwise spacing for H/d=1 (Lawson et al., 2011)

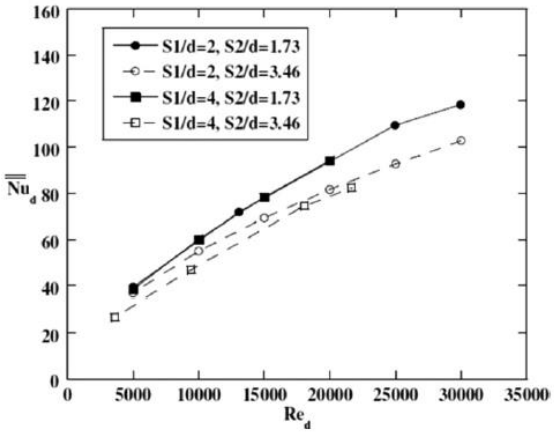

Figure 2.3 Array averaged Nusselt number (Lawson et al., 2011)

Lee et al. (2019) studied about the effect of heating loads (T_w/T_c) on the unsteady flows and heat transfer in an internal cooling passage with a staggered array of pin fins. Results from their study show that, as the heating load increases, the mean Nusselt number and the flow separation angle around the pin decreases (Lee, Shih, Bryden, & Dennis, 2018), as depicted in Figure 2.4.

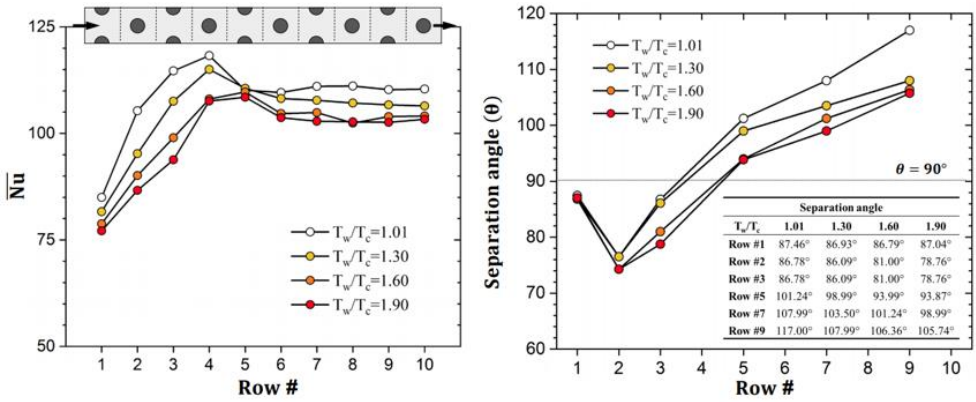

Figure 2.4 Regionally – averaged Nu and flow separation angle (Lee et al., 2019)

In terms of CFD, a thorough study was done by Fernandes et al. (2017) in comparing selected commercially available turbulence models. From the results of the study, it can be summarized that, in the case of pin-fin cooling channels, realizable k – ε turbulence model performed poorly in comparison to experimental data for different Reynolds numbers, the quadratic version of the k – ε turbulence model differed by 8% on average for higher Reynolds numbers and k – ω SST turbulence model had the overall better agreement to experimental data for different Reynolds numbers (Fernandes, Ricklick, Prasad, & Pai, 2017).

Paniagua et al. (2014) compared Large Eddy Simulations with different subgrid-scale models (WALE, QR, and VMS) for a matrix of wall bounded 8x8 cylindrical pins. His

team found that QR eddy viscosity model better predicted the pressure distribution around the pins, but the velocity field of the channel was in better agreement with the experimental results when WALE model was used. For averaged heat transfer results all the three subgrid scale models had the ability to predict fairly well for this kind of geometry (Paniagua, Lehmkuhl, Oliet, & Perez-Segarra, 2014).

Delibra et al. (2010) studied vortex structures and heat transfer in a pin fin channel using LES with RANS wall-treatment (hybrid model). This study also compared the hybrid LES model with URANS and experimental results. Figure 2.5 shows the time averaged endwall Nusselt number for URANS, hybrid and experiment.

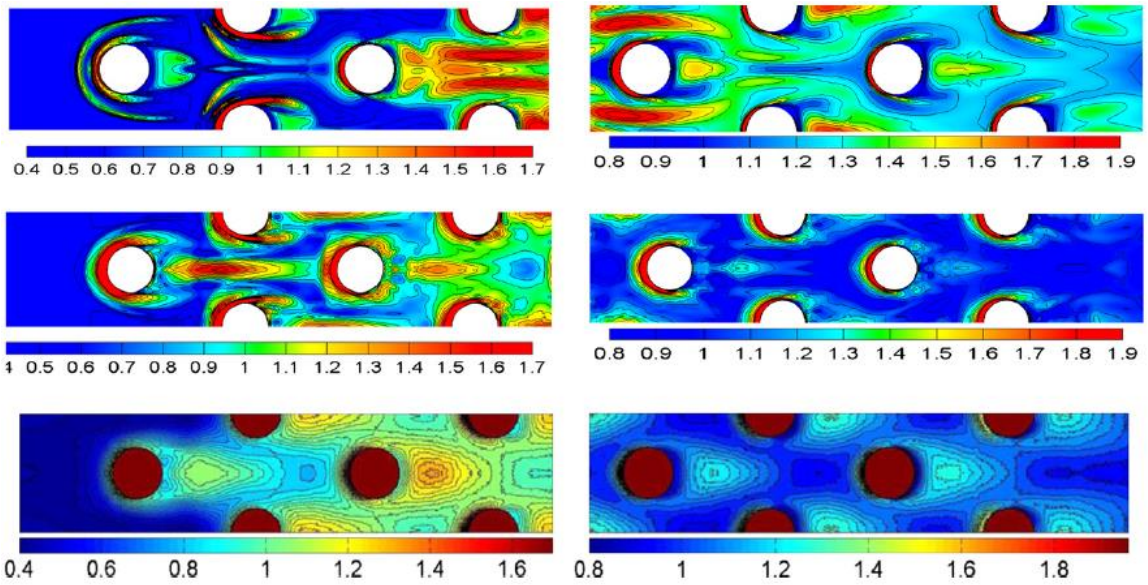

Figure 2.5 Time averaged Nusselt number normalized with Nusselt number average (Nu/Nu_{ave}) for Re = 30,000, Top: URANS; middle: hybrid LES/URANS; bottom: experiment. (Delibra et al., 2010)

It was summarized in this study that the hybrid approach showed visible improvements over URANS using the same computational grid. As the local convection

associated with large vortex systems is the dominant heat transfer mode away from the near-wall layers gives support to using a hybrid URANS/LES approach in treating convective heat transfer in complex configurations dominated by separated flows over bluff bodies (Delibra, Hanjalic, Borello, & Rispoli, 2010). In manufacturing aspect, the circular cylindrical pins are relatively easy to manufacture and hence, this configuration is often found in commercial applications.

2.2. Non – Conventional Pins

Several researchers have investigated benefits associated with non-conventional pins. Kim and Moon (2009) investigated stepped circular pin shapes, as shown in Figure 2.6, in an effort to enhance heat transfer and thermal performance.

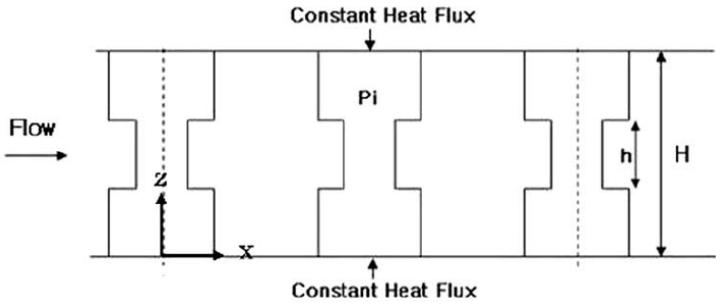

Figure 2.6 Geometry of stepped circular pin fin (Kim & Moon, 2009)

These stepped pins were optimized based on the ratio of height of smaller diameter part of the pin-fin to height of the channel (h/H) and ratio of smaller diameter of the pin-fin to height of the channel (d/H). They showed significant improvements were possible in terms of thermal performance at constant pumping power as compared to straight pin shapes, as summarized in Figure 2.7 (Kim & Moon, 2009).

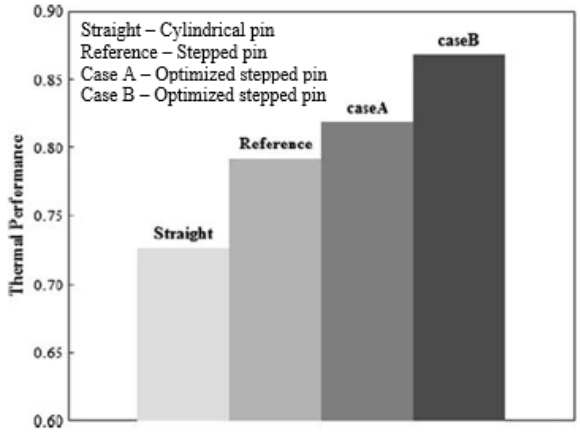

Figure 2.7 Comparison of thermal performance for stepped pin fins (Kim & Moon, 2009)

The enhancement of thermal performance in stepped pin fins is attributed to the fact that the vortices arises from the steps promotes heat transfer while the pressure loss is reduced by the smaller blockage ratio due to the steps (Kim & Moon, 2009). Figure 2.8 shows the streamlines of vortices in the axial plane.

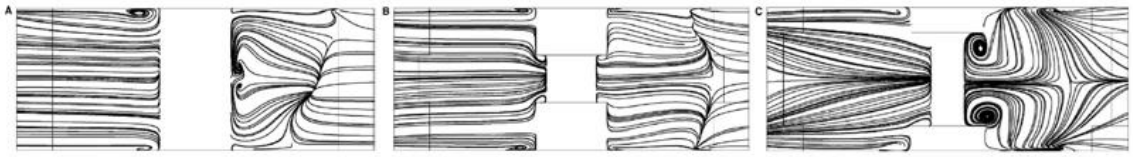

Figure 2.8 Streamlines: A – Cylindrical pin fin, B – stepped pin fin and C – optimized stepped pin fin (Kim & Moon, 2009)

Tullius et al. (2012) investigated the impact of normal and non-circular fin shapes, as shown in Figure 2.9, on heat transfer and pressure drop in a microchannel. Different fin shapes yield Nusselt number values within 37% of each other at high Reynolds number with improved performance observed with triangular pins and smallest pressure drop recorded in elliptical pins (Tullius et al., 2012).

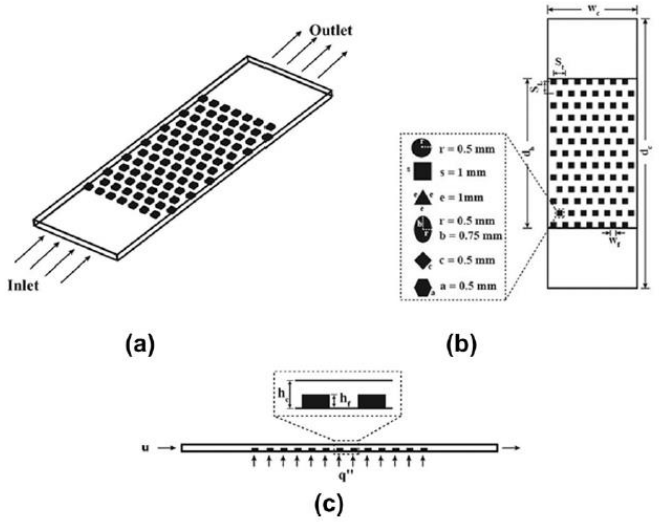

Figure 2.9 Microchannel model with different pins shapes (J. Tullius, T. Tullius, & Bayazitoglu, 2012)

Figure 2.10 summarizes the result for Nusselt number and pressure drop for different pin geometries. As mentioned previously, we can see in Figure 2.10, the triangular pin has the largest Nusselt number and the elliptical pin due to its aerodynamic shape has the lowest pressure drop at the expense of heat transfer performance.

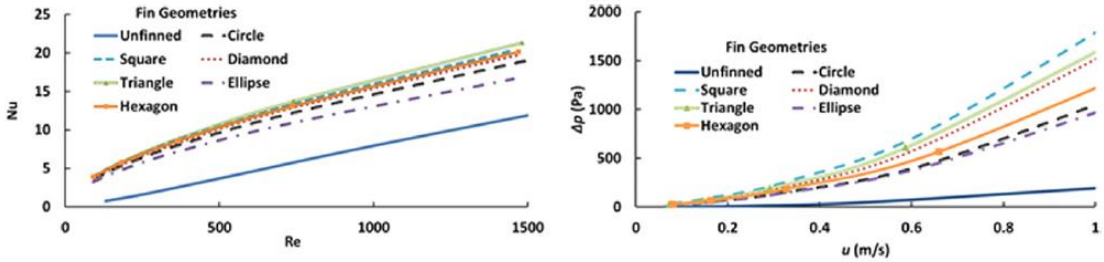

Figure 2.10 Nusselt number and pressure drop for different pin geometry (Tullius et al., 2012)

Pent et al. (2009) investigated the performance of a porous pin fin array, in an attempt to reduce the pressure drop across the system, as illustrated in Figure 2.11.

However, the flow separates from the porous pin surface relatively early which increases the size of the wake along with pressure penalties, as seen in Figure 2.11 (Pent, Kapat, & Ricklick, 2009).

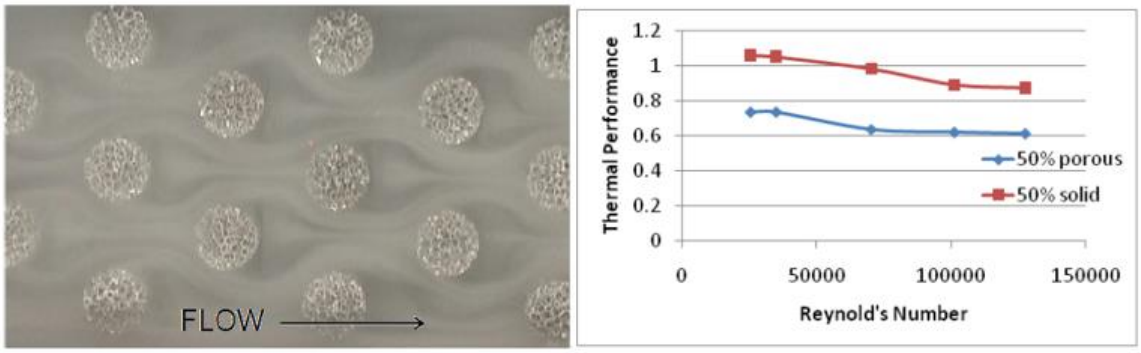

Figure 2.11 Flow visualization (left) and thermal performance (right) of porous pins (Pent et al., 2009)

Uzol and Camci (2005) conducted a study to compare end-wall heat transfer enhancements and total pressure loss between circular, elliptical and a pin based on NACA 0024 airfoil, as shown in Figure 2.12. From their study, the Nusselt number for the circular fin array was about 27% higher on average than the elliptical and NACA fin arrays. The Pressure loss levels for the circular fin are 46.5% and 59.5% higher on average than those of the elliptical and NACA fins, respectively (Uzol & Camci, 2005).

Figure 2.12 Pin model: Circular pin, Standard elliptical pin (SEF) and pin based on NACA 0024 (N fin) (Uzol & Camci, 2005)

Kondo et al. (2000) investigated an approach for the design and optimization of pin fin heat sink cooled by impingement, as shown in Figure 2.13. For a model of 60-by-60-mm, Kondo concluded the optimum fin geometry to be, pin diameter of 0.35 mm, minimum spacing between pins are 0.65 mm, number of pins to be 3481 pins, and pin height of 17 mm (Kondo, Matsuhima, & Komatsu, 2000).

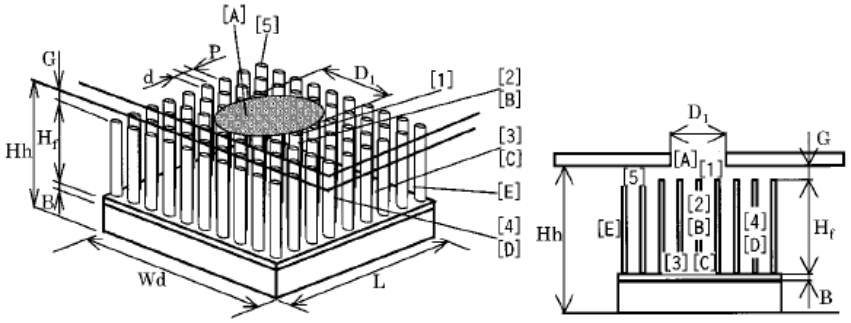

Figure 2.13 Pin fin heat sink model with impingement cooling (Kondo et al., 2000)

Benjan (2000) conducted the geometric optimization of T-shaped fins. He concluded that the constructal optimization, based on constructal law could lead to substantial increases in global conductance relative to current optimal designs that fill the same volume and use the same amount of fin material (Benjan, 2000).

Lee et al. (2004) conducted numerical simulations of flow past a circular cylinder with periodic array of fins, as seen in Figure 2.14. The presence of the periodic array of fins break down the flow structures which leads to a decrease in pressure drop, however due to vortex dislocation and cylinder end effects, as illustrated in Figure 2.15, the mean local heat transfer is reduced by 25%, even though the total area exposed to the flow for finned cylinder is three times that of the smooth cylinder (Lee, Ha, Balachandar, & Lee,

2004). Hence the Nusselt number, Strouhal number and mean pressure drag coefficients for the finned cylinder are smaller in comparison to smooth cylinder (Lee et al., 2004).

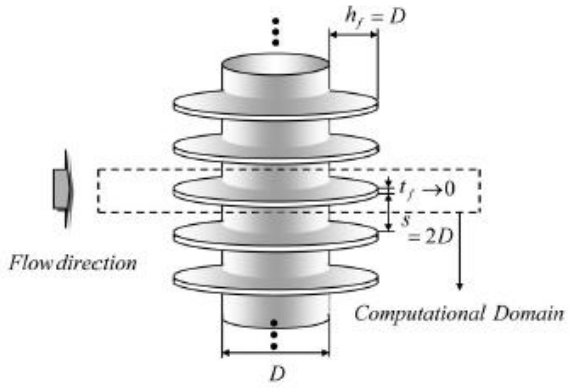

Figure 2.14 Circular cylinders with periodic array of fins (Lee et al., 2004)

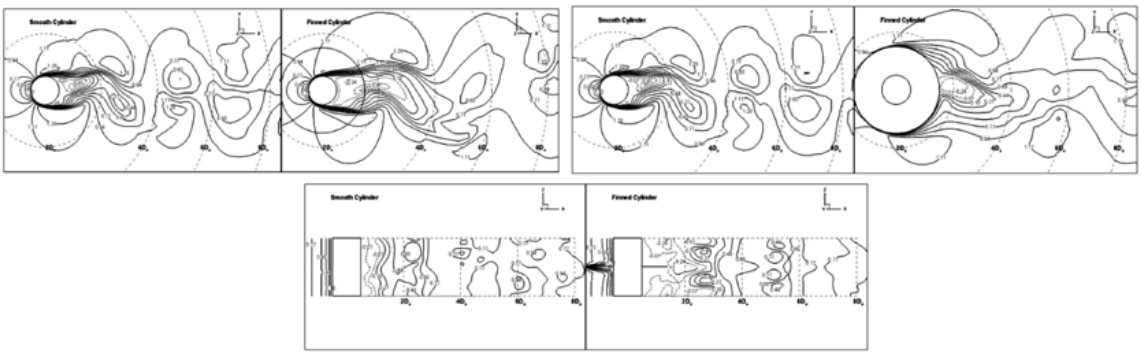

Figure 2.15 Instantaneous streamwise contours at different locations along the pin axis (Lee et al., 2004)

Kirsch et al. (2014) compared the pin surface heat transfer in arrays of oblong and cylindrical pins. The research concluded that, cylindrical pins generated elevated channel turbulence and therefore produced higher overall heat transfer when compared to the oblong pins. Oblong pins led to a lower pressure drop within the array compared to cylindrical pins. As shown in Figure 2.16, the results also indicated the importance of

spacing and Reynolds number effects on the pin surface heat transfer with oblong pins being severely affected by these parameters, given that they affected the boundary layer growth along the surface (Kirsch, Ostanek, & Thole, 2014).

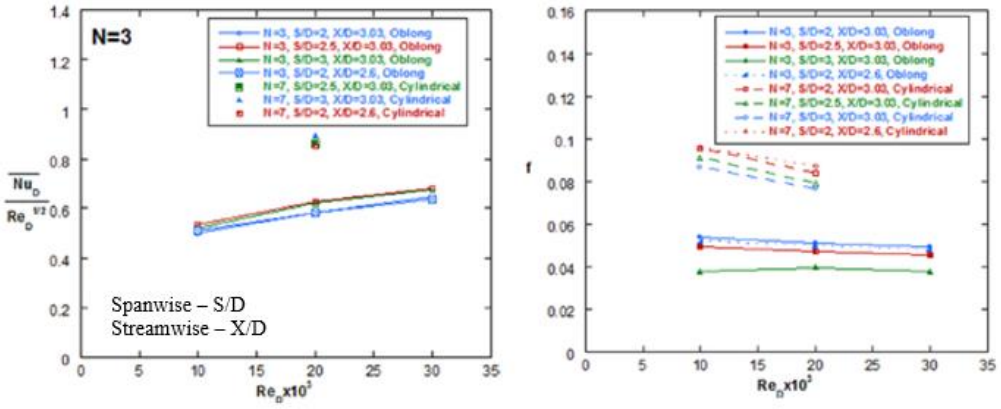

Figure 2.16 Frossling number (left) and friction factor (right) comparison (Kirsch et al., 2014)

2.3. Biomimicry

Biomimicry and bio-inspired devices have gained interest recently, due to the optimized designs presented in nature through evolution. This discipline imitates nature's designs to solve human design problems (Benyus, 1997). The main topic of this study is the natural design of harbor seal whisker.

Harbor seals are evolved to locate the footprints (wake) fish leave behind in water. The seals can sense these vortices left by the flick of a fish's fins using their whiskers, as illustrated in Figure 2.17 (Beam, 2016). This behavior of the seal's whisker sensing vortices is surprising because, it is well known that a cylindrical/elliptical object such as a whisker should naturally vibrate in flowing water, which hinders sensing other vibrations, as shown in Figure 2.18.

Figure 2.17 Sensing abilities of harbor seal whisker (Beam, 2016)

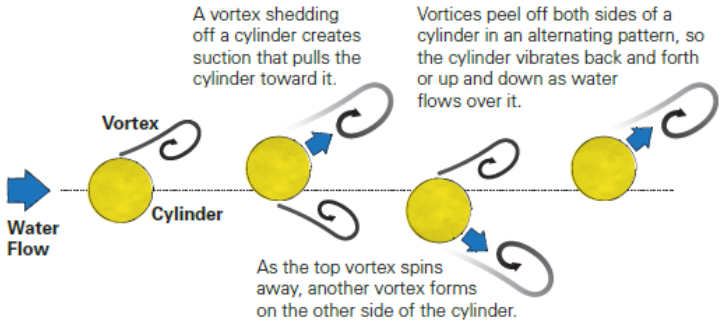

Figure 2.18 Vortex induced vibrations (Beam, 2016)

But upon close observation it was found that the seal's whiskers did not appear to vibrate, and it was theorized that this may be related to the seal whiskers' unusual shape. From the top they are elliptical, and from the side they are wavy, shown in Figure 2.19.

Figure 2.19 Seal whisker's shape (Beam, 2016; Hanke et al., 2010)

The harbor seal whisker has been studied heavily in the literature, in an effort to understand their acute sensing abilities (Beem & Triantafyllou, 2015 and Miersch et al., 2011). Beem & Triantafyllou (2015) studied about the detectability of a specific object (such as a cylinder) in the flow stream by using harbor seal whisker and found out that the presence of distinct wakes was detectable at 160 times the whisker's minor diameter downstream.

In addition, it was also indicated that the whisker geometry vibrates with large amplitude at the Strouhal frequency of the upstream cylinder and practically ceases to vibrate when the upstream cylinder is removed (Beem & Triantafyllou, 2015). In harbor seal whiskers, it was found that the undulated shape results in reduced vortex induced excitations and diminishes the strength of organized flow structures in the wake (Beem, Dahl, & Triantafyllou, 2011; Weymouth, & Triantafyllou, 2011).

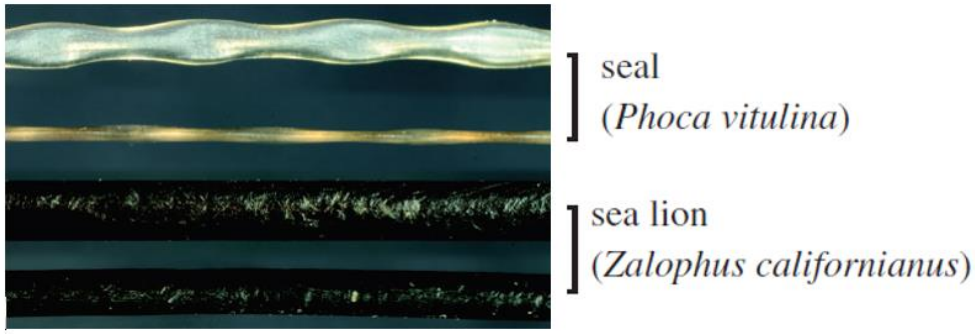

Figure 2.20 Structure of Harbor seal and California sea lion vibrissae (Hanke et al., 2010; Miersch et al., 2011)

Miersch et al. (2011) investigated about the detection of external hydrodynamic information by harbor seal and California sea lion whiskers, as shown in Figure 2.20. By this research, it was found that the sensory performance of both the whiskers were similar

but indicated that California sea lion whisker had a reduced temporal resolution in comparison to the harbor seal whisker. This deficit in temporal resolution will cause an impaired spatial perception of vortex patterns (Miersch et al., 2011).

Murphy et al. (2013) studied about the effect of angle of orientation on flow induced vibration of pinniped (seals) vibrissae (whiskers). Summarized in Figure 2.21, it was found that the angle of orientation, rather than species differences and thus surface structure of the vibrissa, had the greatest effect on the frequency and velocity of flow-induced vibrations. (Murphy, Eberhardt, Calhoun, D.A. Mann, & K.A. Mann, 2013).

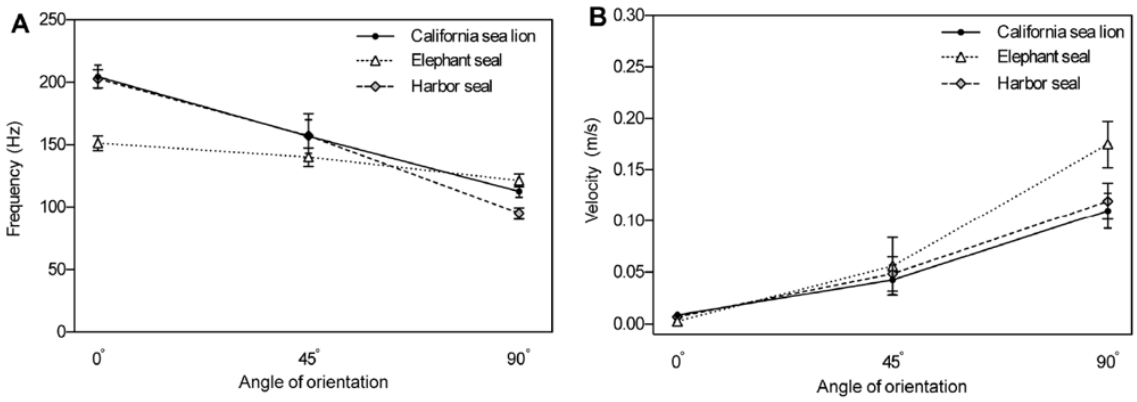

Figure 2.21 Frequency and velocity for flow induced vibration (Murphy et al., 2013)

Hanke et al. (2010) also studied the vortex induced vibration of harbor seal whiskers. He concluded that few or no vortex-induced vibrations occur on harbor seal vibrissae owing to the effective suppression of the periodic forces. The research indicated a reduction of the standard deviation of the lift and drag forces of approximately 90% on the harbor seal vibrissa as compared with those on a circular cylinder and their numerical results fell within ± 30% of the experimental values (Hanke et al., 2010). Figure 2.22

shows the harbor seal whisker geometry and the wake flow behind whisker in comparison to an ellipse and a cylinder.

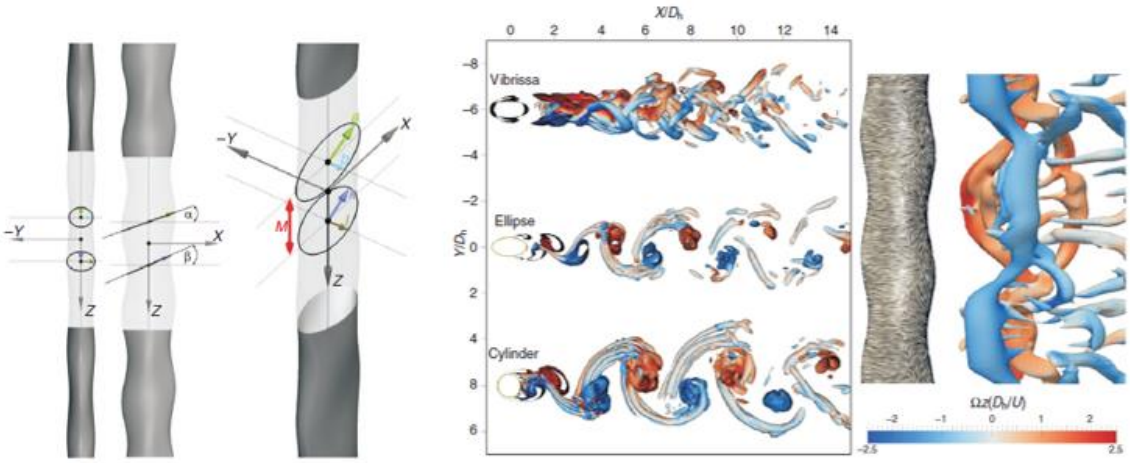

Figure 2.22 Wake flow behind different cross section bodies (Hanke et al., 2010)

From Figure 2.22, it can be seen that no large scale periodic vortex formations are seen in the wake of the vibrissa. The separation of Kármán vortices as seen in a cylindrical structure is replaced by complex 3D vortex structure behind the vibrissa. The separation of these complex vortex structures occur simultaneously across the axial direction, also the region of vortex formation is considerably shifted downstream compared to the cylindrical and elliptical structures wake. Hence the gap between the structure and the region with fluctuating flow, results in symmetric pressure imposition leading to reduction in large periodic forces on the vibrissa and thus reducing vortex induced vibrations (Hanke et al., 2010).

Hans et al. (2013) studied about the force reduction properties of harbor seal whisker-like geometries, as seen in Figure 2.23. They found that the undulations on both axes are

necessary for the lift force reduction. When the undulation on one of the axis is eliminated the lift coefficient increase by 8 times.

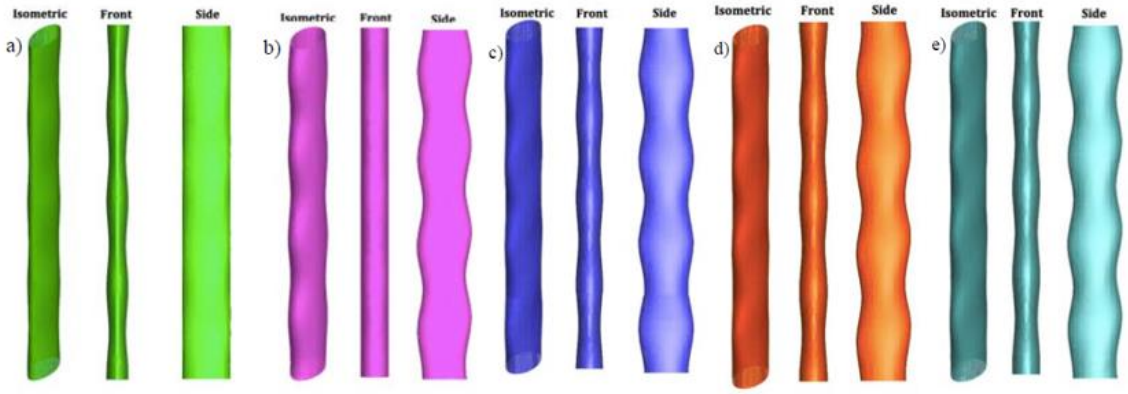

Figure 2.23 a) whisker-like geometry with no undulations on major axis, b) whisker-like geometry with no undulations on minor axis, c) whisker-like geometry with no offset angle, d) whisker-like geometry with constant offset angle (17.6°), and e) real whisker geometry (Hans et al., 2013)

The undulations on the minor axis reduces the drag coefficient by 26% (Hans, Miao, Weymouth, & Triantafyllou, 2013). Due to the reduced lifting forces and flow induced vibrations, the harbor seal whiskers are an ideal solution to micro-sensors (Hans et al., 2011; Liu et al., 2013; Beem & Triantafyllou, 2012).

Kottapali et al. (2015) studied about the application of harbor seal whiskers to flow sensors due to reduction in vortex induced vibrations, as seen in Figure 2.24. It was observed that the amplitude of vortex induced vibration frequency peak for the whisker-like structure is 50 times smaller than the circular cylinder (Kottapalli, Asadnia, Miao, & Triantafyllou, 2015).

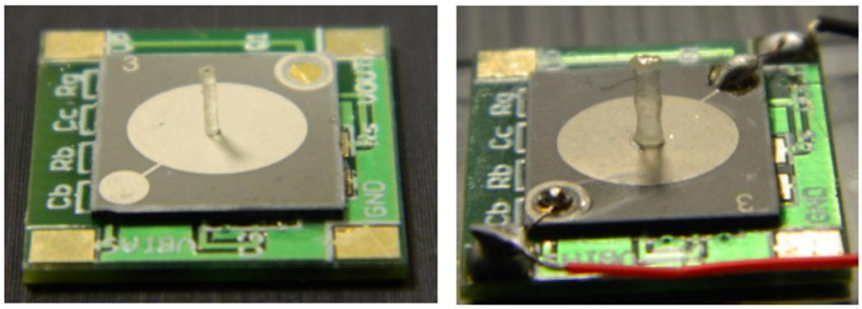

Figure 2.24 Piezoelectric sensor with circular cylinder (left) and whisker-like (right) structure mounted at the center of the membrane (Kottapalli et al., 2015)

Most recently, NASA researchers have investigated the benefits associated with larger scale structures, such as adaptations to turbine blades, as seen in Figure 2.25. From this study, reduced aerodynamic loading and total pressure loss has been observed, associated with the streamwise vortex – mainstream flow interactions. In general, the elimination of large-scale coherent structures and resulting reduced wake size have an all-around positive impact aerodynamically and indicated that it could lead to a reduction in drag by 50% (Shyam et al., 2015).

Figure 2.25 Harbor seal whisker inspired turbine blade geometries (Shyam et al., 2015)

With the advent of advanced manufacturing techniques, such as three-dimensional

printing of high-strength alloys (Bernstein et al., 2013), implementation of such bio-inspired devices are now a possibility.

2.4. Hypothesis

While the use of harbor seal whiskers has been studied for aerodynamic benefits, they have not been applied to thermal management configurations, such as the gas turbine blade trailing edge or heat exchangers.

This leads to the hypothesis; Use of bio-inspired harbor seal whisker shaped pins in a pin fin channel has the potential to improve heat transfer characteristics in comparison to conventional shaped pins. The overall objective of the study is to elucidate, quantify and optimize the thermal transport behavior of a bio-inspired cylinder array configuration as compared to a bank of circular and elliptical cylinders.

Achievement of this objective will directly contribute to the improved thermal design of many energy-based products, further improve the understanding of biologically developed geometries, and aid heat transfer engineers in the ever-challenging goal of decoupling heat transfer and pressure loss. It will extend the work in computational and experimental analysis of novel cooling geometries for propulsion and energy systems, and the engineering community's work in biomimicry for heat transfer.

To achieve this objective, several smaller objectives have been established. Each of these objectives are tied to a specific task and contribute to the overall success of this research.

- Characterize heat transfer and pressure drop sensitivity, over a range of Reynolds numbers for the bio-inspired harbor seal whisker geometry (bio pins) using CFD.
    - This will identify the important geometric feature and a reduction of the

design space from thermal standpoint.

- Experimental verification of heat transfer and pressure loss performance for selected geometries.
    - This will identify the shortcomings in the various simulation methodologies, providing a means for benchmarking the results.
- Comparison of major flow structures between traditional cylinders and bio pins, and their impact on thermal performance.
    - This will lead to better understanding of the aero thermal behavior of the bio-inspired configurations.

3. Methodology

This study utilizes both computational and experimental setup to test different pinfin geometries in a channel configuration. This section will discuss the pin designs, the computational and experimental setup, instrumentation used and data reduction.

3.1. Pin Designs

Harbor seal whiskers have two distinct elliptical shapes in their structure formed at certain angles, which gives their unique undulation (waviness), as shown in Figure 3.1. As discussed in the literature these undulations are the cause for their hydrodynamic properties.

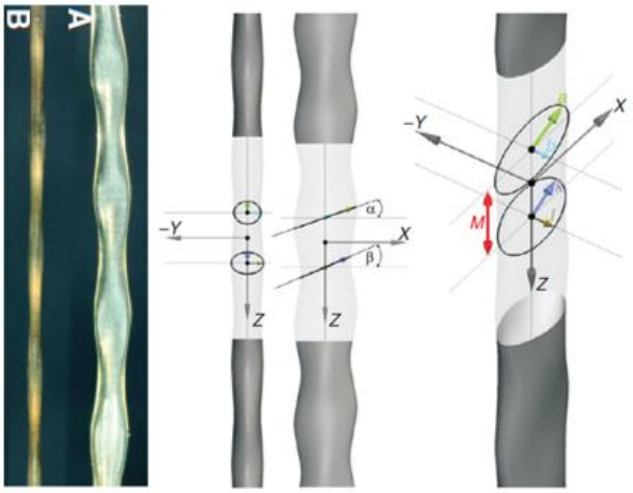

Figure 3.1 Seal whisker structure (Hanke et al., 2010)

3.1.1. Initial Pin Design

For initial study the pin geometries were scaled heavily from an already scaled up whisker's geometry. Scaling of the first geometry (BP1) was focused in the axial direction so as to maintain a large number of undulations, scaling 0.125X in the pin axis

direction, and 0.68X in the streamwise (X) direction, also a baseline cylinder with diameter 0.015 m was created to match the major diameter of BP1. The pin height to major diameter (H/D) of the pins are 2. Since the seal whisker is naturally elliptical in nature, and to account for this, two steps were taken. The first step was to scale the first geometry (BP1) in the spanwise direction in order to generate a bio-cylinder with a circular base (BP2). The second was to utilize a second baseline of elliptical cross section pin (EP1), matching BP1's base profile. The geometrical design of all 4 pins is shown in Figure 3.2. The major diameter of the base of all the 4 pins are identical. Due to computational and experimental expense, judicious choice of modifications was made to the natural whisker geometry for the initial study.

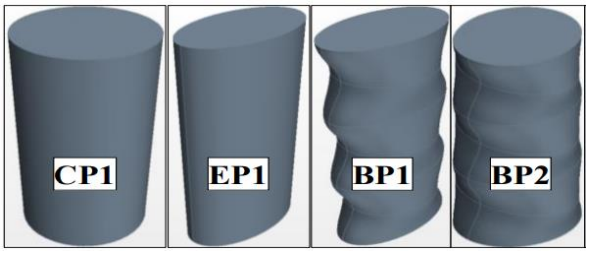

Figure 3.2 Adapted whisker geometries

3.1.2. Final Pin Design

To better understand the natural design of whiskers for heat transfer purpose, the final pin designs were made to preserve the natural shape of the undulations present in the whisker. A replica of the whisker geometry was created in CAD, but this geometry was scaled uniformly in all dimensions 12.6 times from the whisker's natural dimensions in order to better fit our computational and experimental setup. The replica is shown in Figure 3.3.

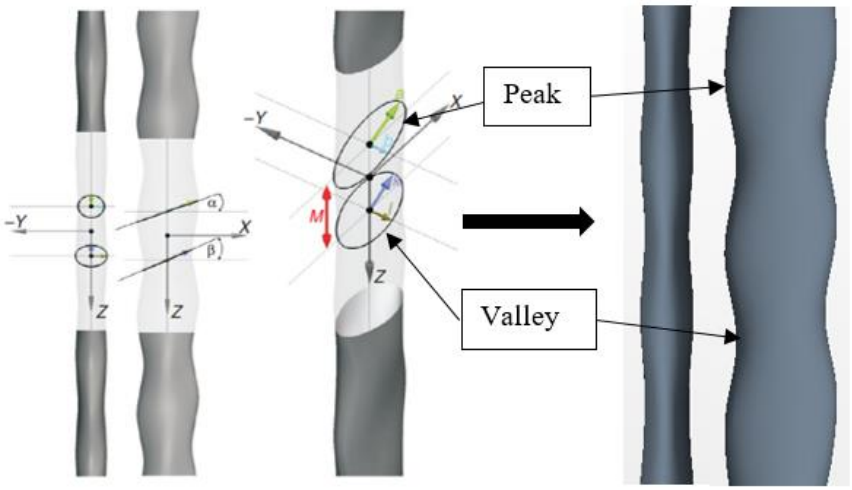

Figure 3.3 Replica of the harbor seal whisker geometry

The dimensions of the final pin design: period of the undulations (M) is 11.466 mm, peak major and minor radius are 7.497 mm and 3.024 mm, valley major and minor radius are 5.985 mm and 3.654 mm and the peak and valley plane angles (α and β) are 15.27° and 17.60°. The height of the pin is 30 mm.

Three groups of pins were created as part of the final pin design. Group 1, the pins are created based on the elliptical shape of the peak, group 2, the pins are created based on the elliptical shape of the valley and group 3 is an extension of group 2.

In group 1, the first geometry is made by cropping the bio pins to retain two peaks (G1TP). The second geometry is a 180° rotation of the first geometry (G1TPR). As seen in Figure 3.3, the peak and valley ellipse are at a particular angle. Hence the second geometry is made to see the effects of the angles of undulations facing the flow. The third geometry is a pure elliptical pin (G1E), who's major and minor diameter are the same as the peak ellipse in the bio pin. The fourth pin is a pure cylindrical pin (G1C) with the diameter equal to the minor diameter of the peak. The fifth pin (G1TPZ) is similar to first

and second geometry, the undulation angle are kept zero to see the effects. The sixth geometry (G1TRP) has a reduction in the period of the undulation from 11.466 mm to 7.67 mm, to include three peaks and two valleys. All these geometries are made to have approximately 13% endwall blockage (based on endwall dimensions) in the channel.

In group 2, the first geometry is made by cropping the bio pins to retain two valley (G2TV). The second geometry is a 180° rotation of the first geometry (G2TVR). The third geometry is a pure elliptical pin (G2E), who's major and minor diameter are the same as the valley ellipse in the bio pin. The fourth pin is a pure cylindrical pin (G2C) with the diameter equal to the minor diameter of the valley. The fifth pin (G2TVZ) is similar to first and second geometry, the undulation angle are kept zero to see the effects. The sixth geometry (G2TRV) has a reduction in the period of the undulation from 11.466 mm to 7.67 mm, to include three valleys and two peaks. All these geometries are made to have approximately 16% endwall blockage in the channel.

In group 3, the first geometry is G2TV the same one in group 2, this geometry is included for comparison. The second geometry (G2TVSP) is made from G2TV with the streamwise undulation removed. The third geometry (G2TVST) is made from G2TV with the spanwise undulation removed. Geometry 2 and 3 are made to study the effect of undulation on the streamwise and spanwise direction. Figure 3.4 shows the shape of the pin geometries in group 1, 2 and 3.

All bio pins including the initial pin design used in this study were 3D printed using Shapeways 3D printing service. The pins were 3D printed using Nylon 12 material. Some of the pins in the final pin design, especially the pins used in the center of the channel were 3D printed using Aluminum, so that they could be internally heated.

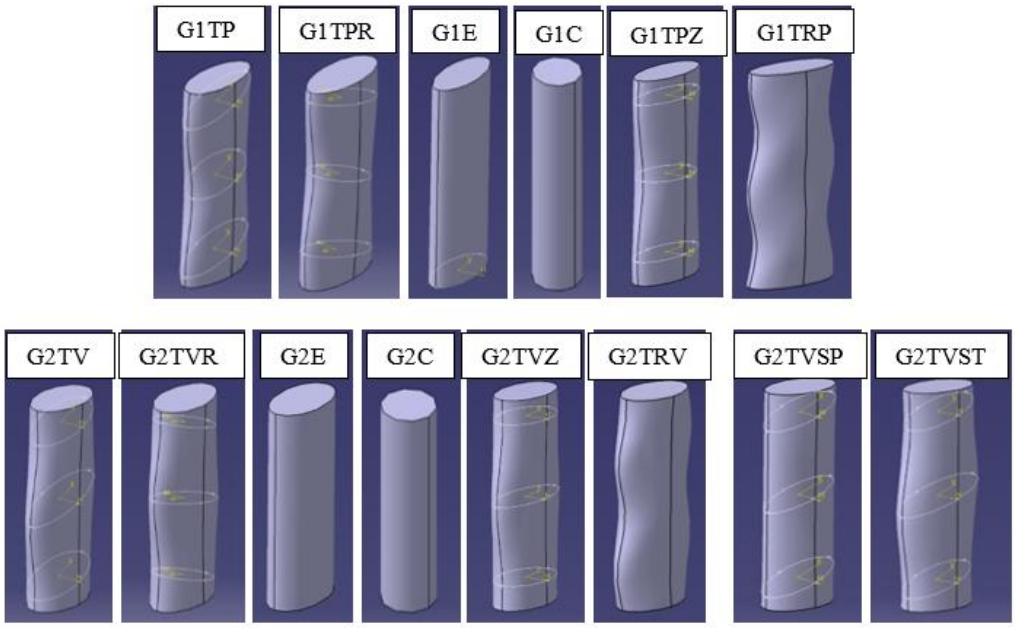

Figure 3.4 Pin geometries in groups 1, 2 and 3

3.2. Computational Setup

The numerical test utilizes an unsteady k-ω SST Reynolds Averaged Navier Stokes (RANS) modeling approach, using a commercial software, STAR CCM+. As discussed in the literature, previous efforts have shown that the shear stress transport (SST) k – ω turbulence model yields the most accurate predictions for pin fin channel thermal performance, as compared against experimental results (Fernandes et al., 2017).

For the initial pin design study a time step of 0.2 ms was used, with 5 inner iterations per time step and for the final pin design study a time step of 0.1 ms was used, with 5 inner iterations for each time step. The characteristic length scale (characteristic diameter) is taken to be the CP1 diameter (0.015 m) for the initial pin design study and the hydraulic diameter of the channel for the final pin design study. Since the channel is modelled to be infinity long in the spanwise direction (periodic boundary), the hydraulic

dimeter of the channel is calculated to be two times the height of the channel (2H).

The array was composed of 8 rows of pins arranged in a staggered manner with spanwise (Y) and streamwise (X) spacing of 45 mm each and channel height (H) of 30 mm. A smooth channel case without the pins was also modeled. The boundary conditions are shown in Figure 3.5.

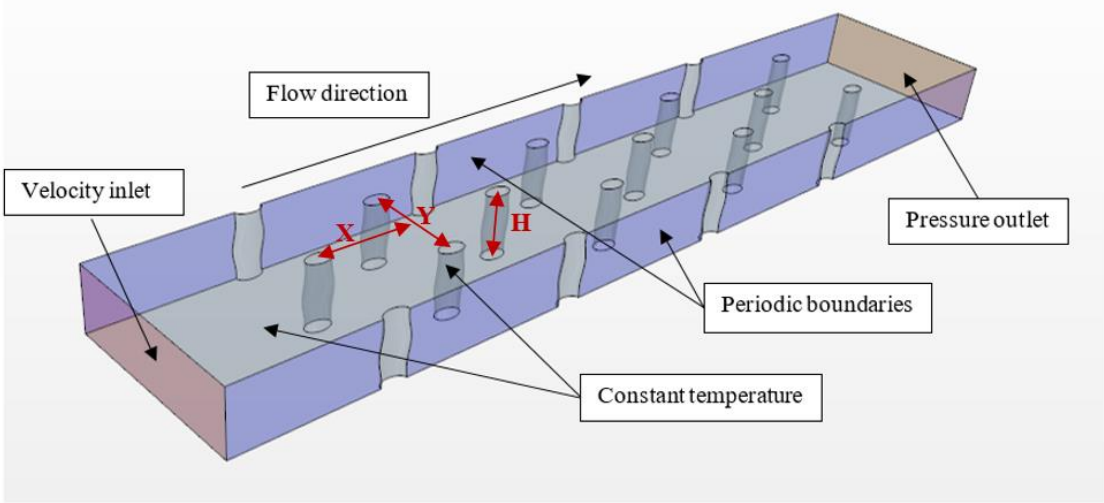

Figure 3.5 Computational model

As shown in Figure 3.5, the pins, the top and the bottom endwall were given a constant static temperature condition with a specified fluid velocity at the inlet and a pressure outlet condition at the exit of the channel. Sidewalls were set to periodic boundaries.

The Nusselt number calculated in the following results was based on CP1 diameter for the initial pin design study and the hydraulic diameter of the channel for the final pin design study. For the initial pin design study three Reynolds numbers 2700, 5200 and 15,000 was used. The Reynolds number is based on the inlet velocity of 2.85 m/s, 5.48

m/s and 16.15 m/s and CP1 diameter (0.15 m). For the final pin design study a Reynolds number of 15,000 and 30,000 was used. The Reynolds number is based on the inlet velocity of 3.925 m/s and 7.85 m/s and the hydraulic diameter (2H).

3.2.1. Mesh Independent Study

For the final pin design study, a mesh independence study was conducted to determine the optimum mesh condition for the simulation. The study was conducted for the case G2TV and for a Reynolds number of 30,000.

To maintain a wall Y+ of less than 1, the total number of prism layers used are 20 and the prism layer thickness is 1.5 mm with a growth rate of 1.3. These values were chosen from the initial study for the mesh. Different base sizes were tested to obtain a suitable mesh. A point was created in the domain to obtain data for comparison, as shown in Table 3.1 and Figure 3.6. The endwall average and pin average Nusselt number, and pressure drop across the channel are compared in Table 3.2. The percentage difference is obtained by comparing the data from each cell count to the data from the maximum cell count.

Table 3.1

Mesh independent study

Base size (mm)	# Cells	Wall Y+	Static Pressure (Pa)	% Difference	Temperature (K)	% Difference
0.5	18087899	< 1	28.227	–	301.256	–
0.55	14558846	< 1	28.249	0.08	301.385	0.04
0.6	12194267	< 1	28.136	0.33	301.259	0.001
0.65	10459643	< 1	27.742	1.72	301.258	0.001
0.7	9012607	< 1	27.649	1.89	301.28	0.01

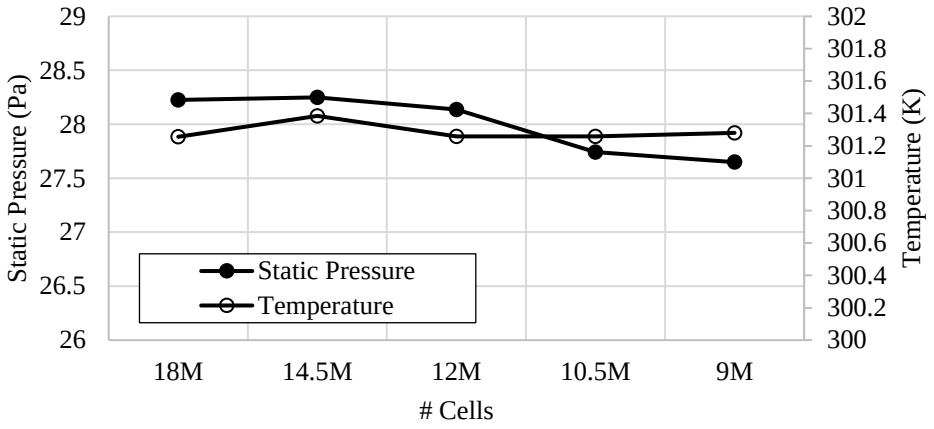

Figure 3.6 Mesh independent study

Table 3.2

Mesh independent study

Base size (mm)	Endwall – Nu	% Difference	Pin – Nu	% Difference	Pressure Drop (Pa)	% Difference
0.5	94.582	–	223.753	–	50.714	–
0.55	94.886	0.321	224.514	0.34	50.691	0.004
0.6	94.721	0.146	224.638	0.395	50.622	0.181
0.65	94.009	0.605	224.738	0.456	50.357	0.703
0.7	93.711	0.921	224.761	0.451	50.341	0.734

From the tables and figure, we can see that base size less than 0.6 mm has less than 1% percentage difference in all categories. Hence, to reduce the computational cost and time the base size 0.6 mm is chosen. Therefore, all the pin cases had approximately 12 million cells, based on base size of 0.6 mm from the mesh independence study. Figure 3.7 shows the cross section of the mesh.

Mesh independent study was not conducted for initial pin design study, as it was considered a preliminary investigation focused on trends. A Base size of 0.6 mm with a total number of 20 prism layers of thickness 1.5mm was used. All the pin cases had

approximately 10.5 million cells. Three Reynolds numbers 2,700, 5,200 and 15,500 was used in this preliminary computational study.

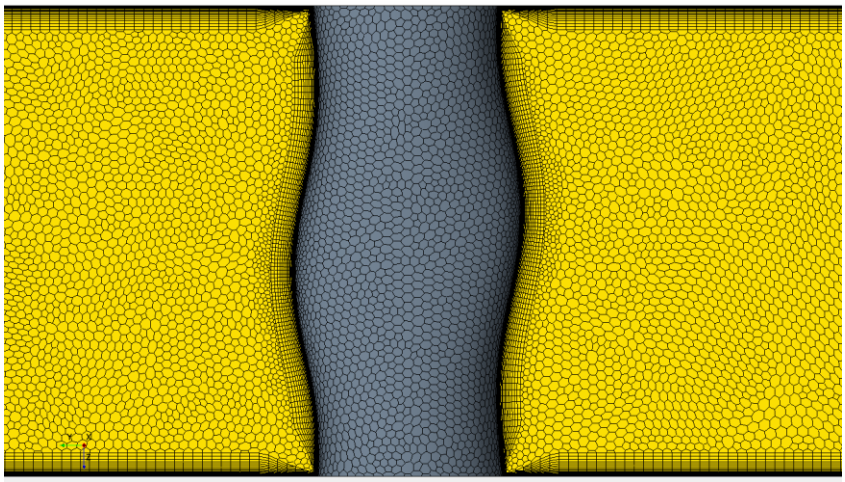

Figure 3.7 Mesh – G2TV

The Reynolds number is based on the inlet velocity of 2.85 m/s, 5.48 m/s and 16.15 m/s and CP1 diameter (0.015 m). The wall Y+ was maintained at less than 1 for 2,700 and 5,200 Reynolds number cases and less than 2 for 15,000 Reynolds number case.

3.3. Experimental Setup

A pin fin channel was created using 1 inch think acrylic plates for the experimental setup, a schematic of the setup is shown in Figure 3.8. The test section is connected to an inlet and an outset section, the outlet section is connected to a converging duct and connected to a centrifugal blower under suction using PVC pipes. A venturi flow meter is used in-line to measure the pressure drop using a digital manometer to calculate the mass flow rate, hence calculate velocity and Reynolds number. Pressure transducers are used to obtain pressure drop data in the test section and thermocouples are used to obtain inlet air temperature and the reference temperature on the endwall for post processing TSP.

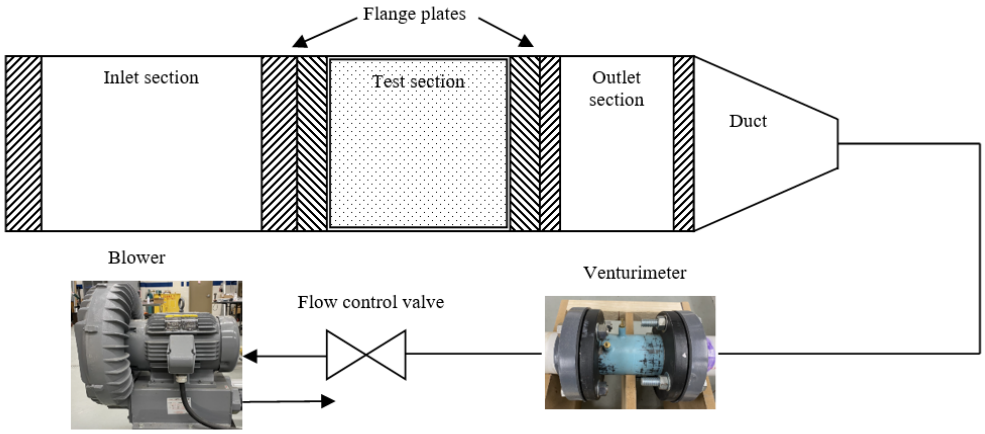

Figure 3.8 Schematic of experimental setup

The test section used for the initial pin setup was 15.75 inch long, for the final pin setup the test section was extended in the entrance and at the exit to have a total length of 20.67 inch. The extension was done to neglect any effect at the entrance of the test section due to the connection of the Inconel strips. Figure 3.9 and Figure 3.10 shows the setup and view of the test section.

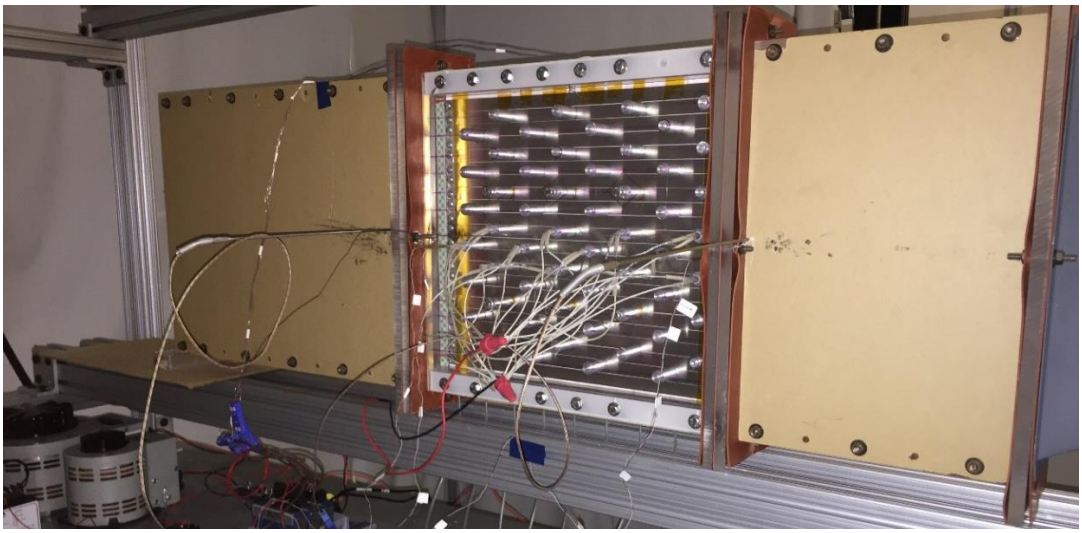

Figure 3.9 Initial pin design – test section setup

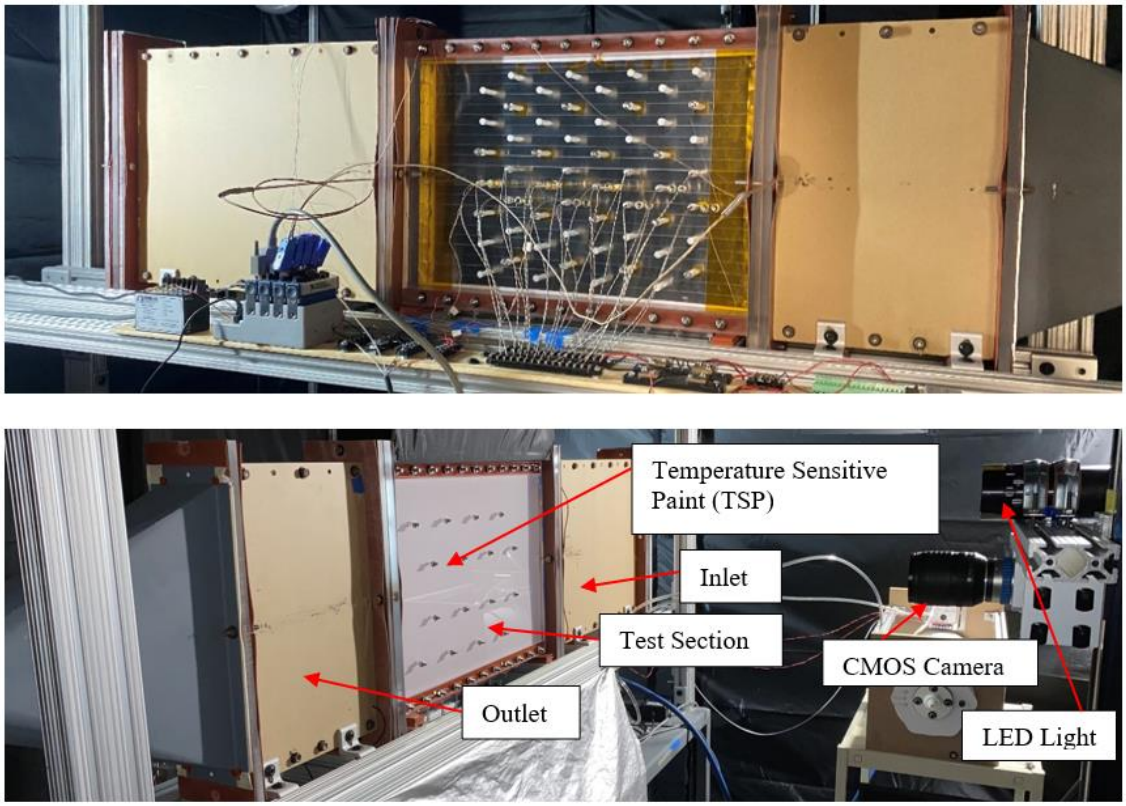

Figure 3.10 Final pin design – test section setup

The inlet section (approx. $9D_h$ in length) which is attached to the upstream of the test section allows the flow to be hydrodynamically fully develop before reaching the test section. The inlet does not have any external heat addition hence the flow does not thermally develop before entering the test section. Thermal development starts at the entrance of the test section.

The pin array in the test section was composed of 8 rows of pins, 7 pins in each row, arranged in a staggered manner with spanwise (Y) and streamwise (X) spacing of 45 mm each and channel height (H) of 30 mm. The end wall of the acrylic test section was painted with a uniform coat of Temperature Sensitive Paint TSP (from ISSI), above which the strips were placed using a double sided high-strength tape, as shown in Figure

3.14. The strips were connected in series, as shown in Figure 3.11. These were then connected to a VARIAC to form a series circuit. The pins were placed on top of the Inconel heater strips.

Some of the pins were internally heated using cartridge heaters specifically the central section of the setup to reduce lateral conduction, as shown in Figure 3.12. The data from the regions surrounding these pins are post-processed and presented in results. A scientific grade CMOS camera was used to capture the TSP, which was excited by LED light of certain wavelength as shown in Figure 3.13. A constant heat flux was supplied to the Inconel strips through Joule heating by varying the voltage.

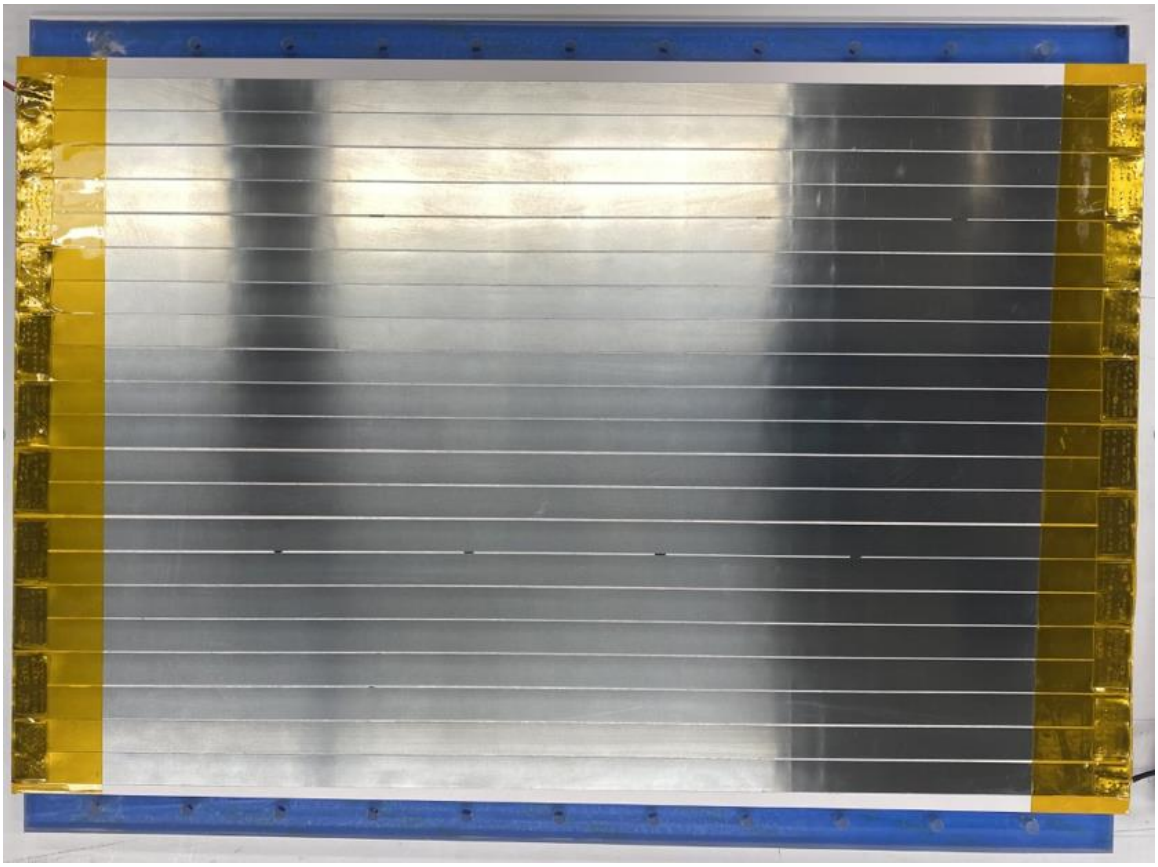

Figure 3.11 Inconel heater strips

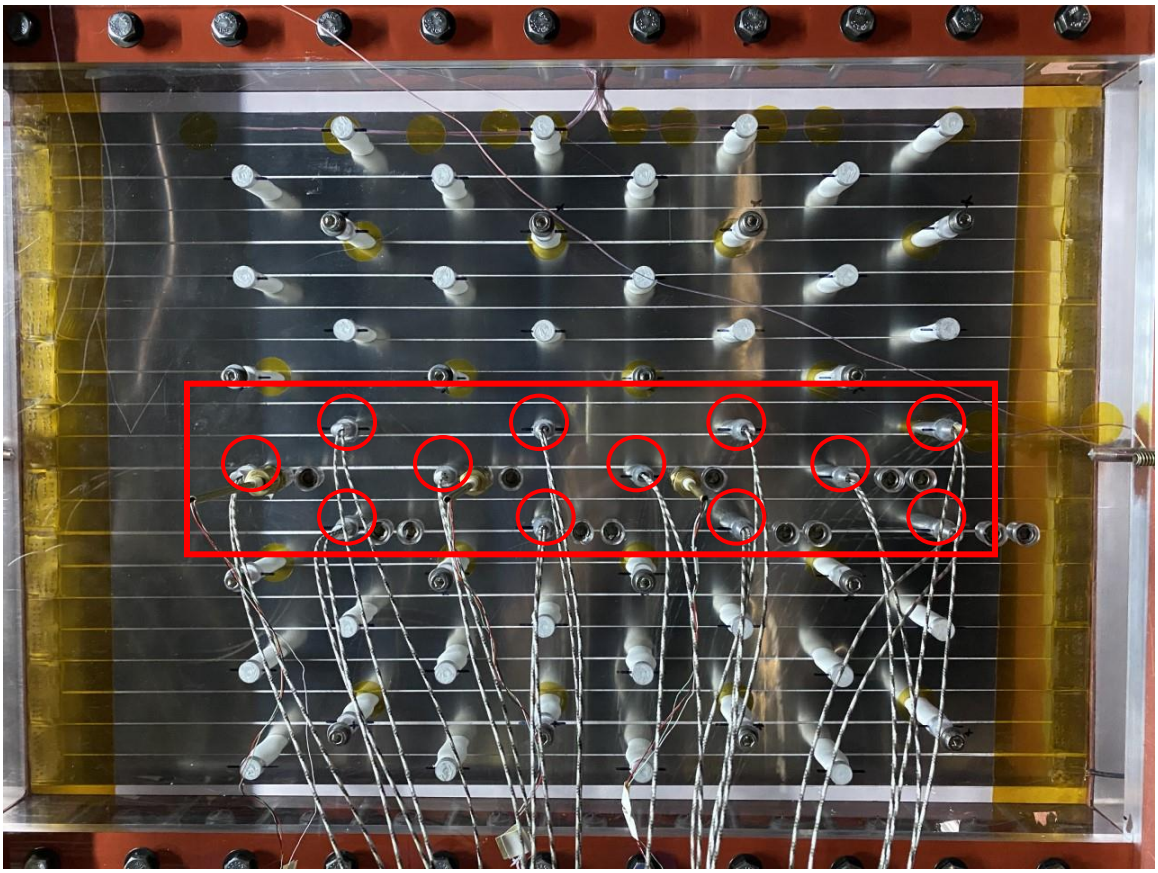

Figure 3.12 Test section – internally heated pins

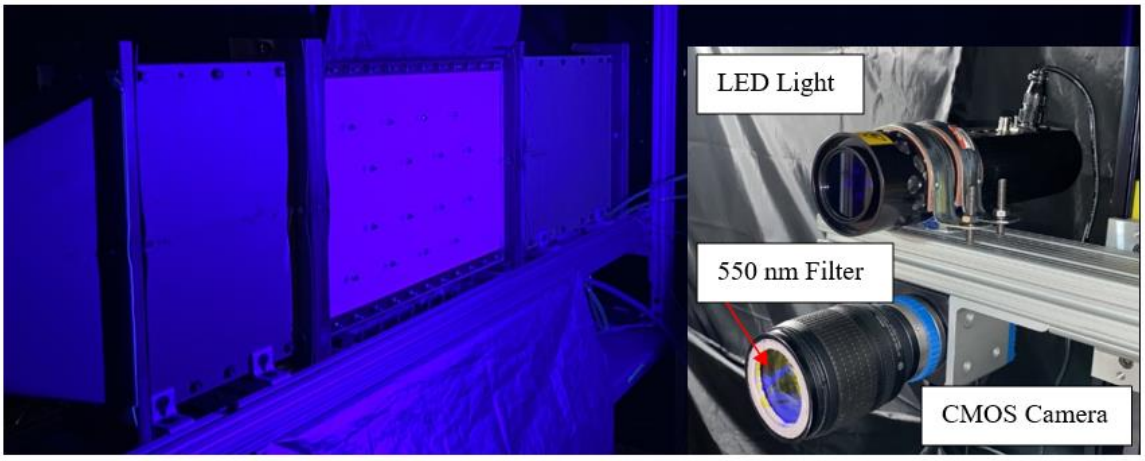

Figure 3.13 TSP excitation, CMOS camera and LED light

As seen from Figure 3.12 fasteners are used to secure a proper fit between the top and bottom plate, since acrylic plates warp due to constant heating, which leads to the pins not touching the bottom plate. Hence this problem is avoided by using fasteners. The schematic of the test section is shown in Figure 3.14.

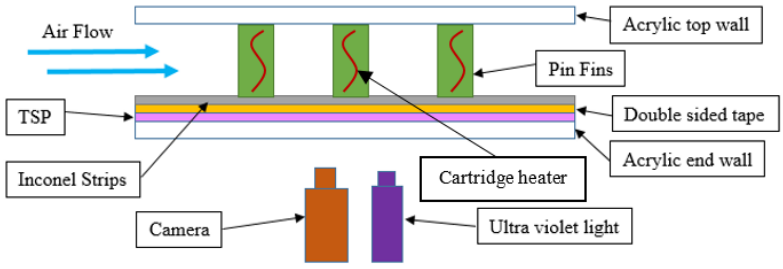

Figure 3.14 Schematic of test section

3.3.1. Heat Leakage Test

As mentioned earlier, a constant heat flux was supplied to the Inconel strips via Joule heating by varying the applied voltage. In order to account for the heat lost to the surrounding through the acrylic endwall (bottom wall), a heat leakage test was conducted. The test section was filled with insulating material to prevent natural convection and a heat flux was applied using the Inconel heater strips attached to the bottom wall. Figure 3.15 and Figure 3.16 shows the schematic and setup of heat leakage test. The applied heat flux under these conditions was assumed to pass through the 1 inch thick acrylic bottom wall into the room. The heat lost to surrounding was found and correlated as a function of the difference in temperature between the wall and room. Equation 1 and Figure 3.17.

$$q''_{loss} = 6.31442 * \Delta T \quad (1)$$

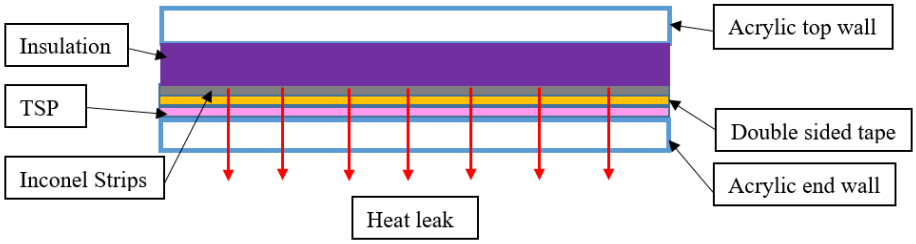

Figure 3.15 Schematic of heat leakage test

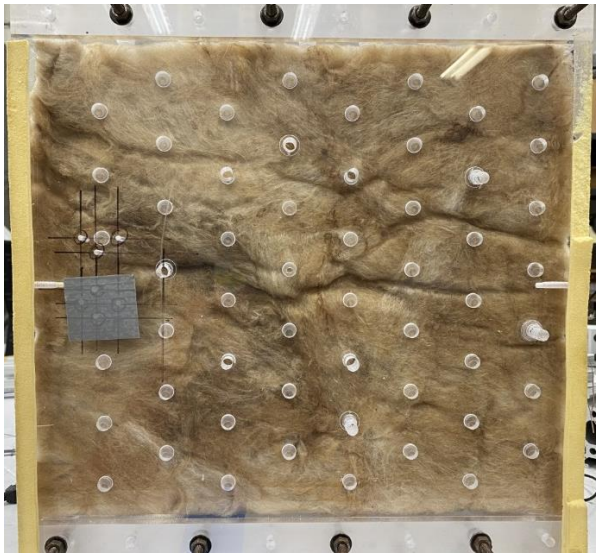

Figure 3.16 Heat leakage test setup

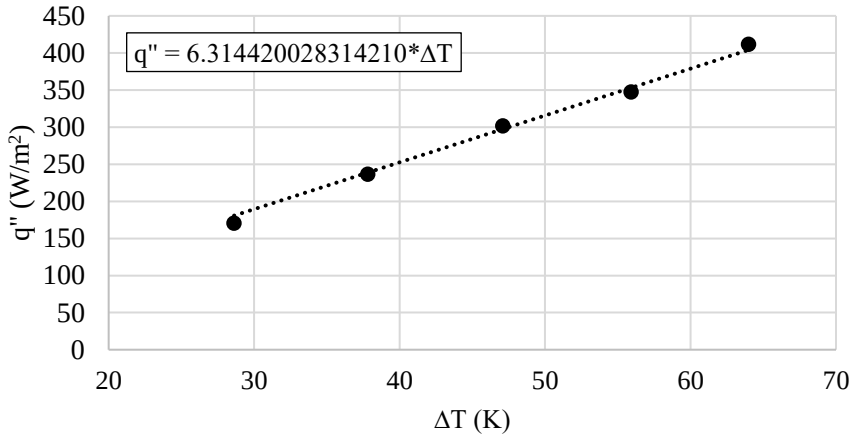

Figure 3.17 Heat leakage test

3.3.2. Temperature Sensitive Paint (TSP)

TSP provides a convenient way to obtain local temperature data. It is a luminescent paint with fluorescent molecules suspended within a binder. The TSP molecules are excited to a higher energy state when exposed to light of appropriate wavelength (excitation wavelength). The Jablonski diagram shown in Figure 3.18, describes the transition of the molecules.

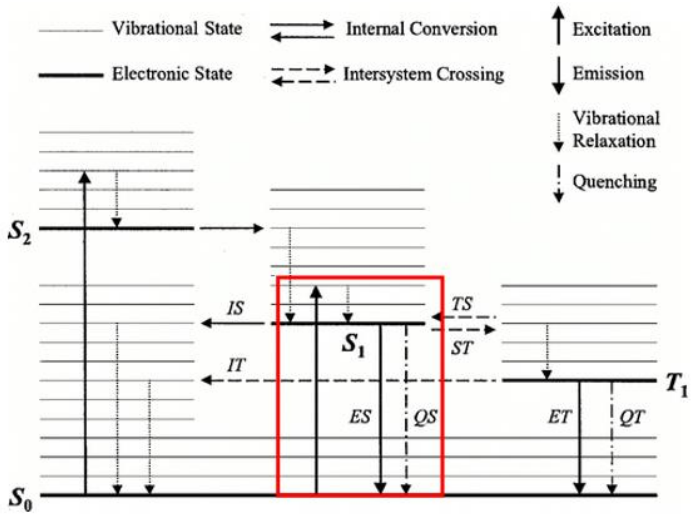

Figure 3.18 Jablonski diagram (Bell et al., 2001)

The excited molecules can return to ground state by emitting photons of particular wavelength (emission wavelength) through luminescence and without emitting photons by thermal quenching. In thermal quenching the molecules vibrate and collide with one another, lose energy, and returns to ground state. In a given instant the molecules return to the ground state by both luminescence and thermal quenching, but the number of molecules returned by each method differs statistically in regards to temperature applied. For this research UniCoat TSP (from the manufacturer ISSI) was used having excitation

wavelength of 380 – 520 nm and emission wavelength of 500 – 720 nm (Innovative Scientific Solutions, Inc.). A LED source (from the manufacturer ISSI) with a wavelength of 400 nm was used to excite the TSP molecules.

The intensity of the paint varies with the number of photons emitted. Increase in temperature will statistically increase the return of photons to ground state through thermal quenching, thereby decreasing the intensity of the paint (intensity is related to the measure of photons emitted from the TSP, which are then captured by the photodetector). A scientific grade camera (CMOS) is used to capture the intensity of the light emitted by the TSP, with a long pass filter (wavelength 550 nm) to distinguish between the excited and the emitted wavelength.

In Figure 3.19, the reference image is taken before the heated run with known intensity and reference temperature (measured and confirmed with multiple thermocouples across different locations). The data image is that of the heated run where the intensity of the paint is known but the surface temperature of the paint is unknown.

Figure 3.19 Reference image and data image

TSP is calibrated with a calibration curve of intensity ratio vs temperature difference. Using this calibration curve, the temperature of the data image can be found. The calibration uncertainty of TSP was found to be ± 0.93 °C for temperature ranges of 22 to 90 °C in previous studies (Liu, 2006). A detailed description of TSP and PSP technologies has been presented by Liu (2006) and Liu et al. (1995).

Temperature sensitive paint is calibrated in a controlled setup, both reference image and data image is taken with known temperature. The temperature is obtained using multiple thermocouples placed on top of the test coupon. The test coupon is heated to multiple temperature readings and measurements are made, when steady state is attained for each temperature reading. Equation 2 and Figure 3.20 shows the calibration result of the TSP.

$$\frac{T_S - T_{ref}}{100} = 2.52\left(\frac{I_S}{I_{ref}}\right)^4 - 8.30\left(\frac{I_S}{I_{ref}}\right)^3 + 10.18\left(\frac{I_S}{I_{ref}}\right)^2 - 6.24\left(\frac{I_S}{I_{ref}}\right) + 1.85 \quad (2)$$

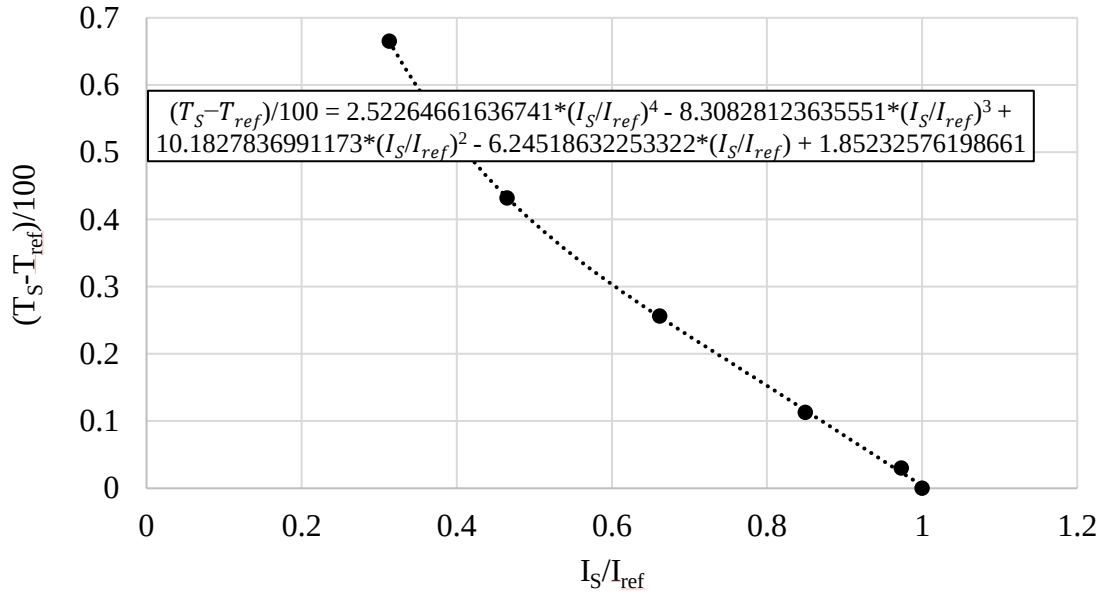

Figure 3.20 Calibration of TSP

3.4. Hotwire Anemometry

An anemometer is an analogue instrument designed for measurement of velocity in fluids and is especially suited for measurements of fast velocity fluctuations. It works on the basis of convective heat transfer from a heated sensor to the surrounding fluid, the heat transfer being primarily related to the fluid velocity. By using very fine wire sensors placed in the fluid and the electronics with the servo-loop amplifier, it is possible to measure velocity fluctuations of fine scale and of high frequencies. The advantages of hotwire anemometer over other flow measuring instruments is that the output is voltage, so no information is lost and has very high temporal resolution, which makes it ideal for temporal power spectra (Dantec Dynamics).

A single component hotwire probe, as shown in Figure 3.21 is used to measure velocity fluctuations to calculate turbulence intensity. The hotwire probe needs to be calibrated every time before obtaining a set of measurements. Hence a calibration device is built for the purpose of hotwire calibration.

Figure 3.21 Single component hotwire probe

A hotwire calibration device consists of a chamber with flow conditioning materials placed inside and a nozzle at the exit to create a steady jet. The flow conditioning material used are, stainless steel wool, baffle plate, stainless steel mesh, and honeycomb

mesh. The chamber is made of 6 inch diameter PVC pipe and PVC caps, the honeycomb mesh is made of stainless steel, 3 inch thick and 1/4 inch cell size. A schematic of the hotwire calibration device is shown in Figure 3.22.

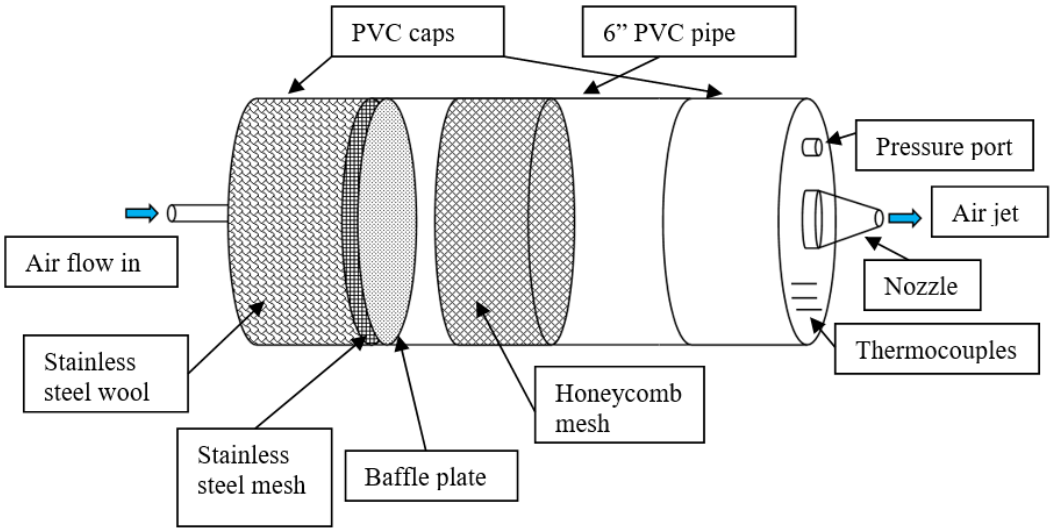

Figure 3.22 Schematic of hotwire calibration device

The stainless steel wool is used to spread the flow throughout the chamber, since the flow is coming through a smaller diameter tubing. The stainless steel mesh is used to hold the stainless steel wool in place. The baffle plate spreads out the flow evenly throughout the chamber. The Honeycomb mesh is used to straighten the flow. Hence the nozzle receives a straightened, uniformly distributed flow.

The chamber length should be in the range of 0.5 – 3 times the hydraulic diameter in order to have uniform air flow and avoid boundary layer growth, greater than 3 times the hydraulic diameter would increase the boundary layer thickness (Barlow, Rae & Pope, 1999). Hence, the chamber length for this setup was made to be approximately 2.5 times

the hydraulic diameter, the chamber length starts after the baffle plate and end at the nozzle entrance. Figure 3.23 shows the setup inside and outside the calibration device.

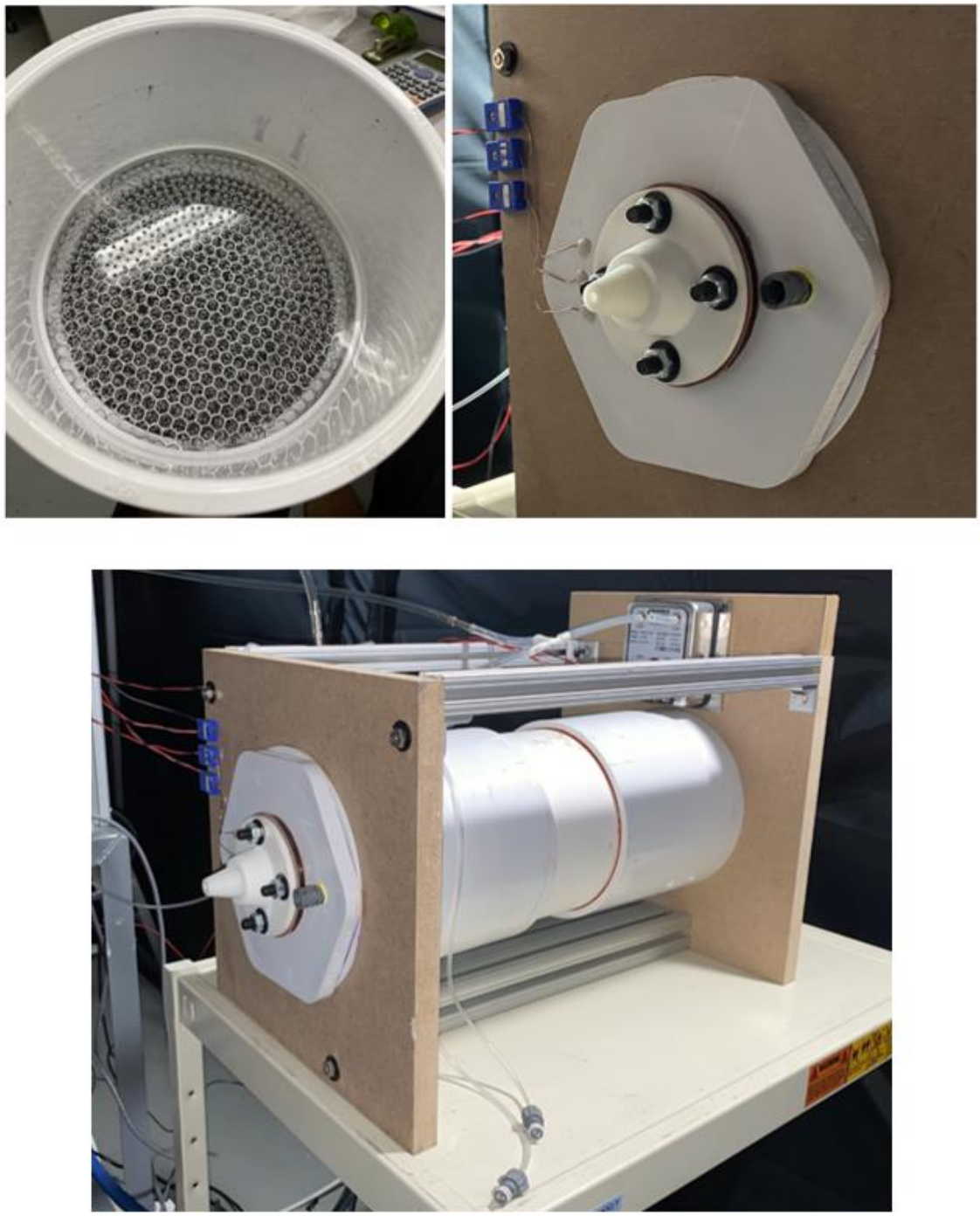

Figure 3.23 Hotwire Calibration device

The nozzle was designed in CATIA and 3D printed using Shapeways 3D printing services, Accura Xtreme 200 material was used for 3D printing. The nozzle is designed to have the flow enter and exit axially. The nozzle design was also validated computationally using STAR CCM+. Figure 3.24 shows the nozzle design and Figure 3.25 and Figure 3.26 shows the air flow through the nozzle.

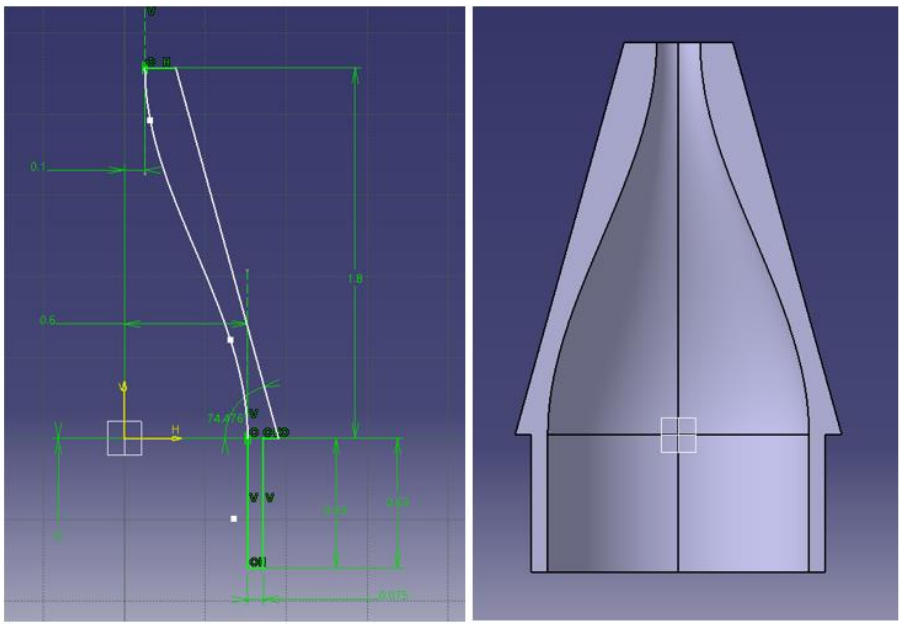

Figure 3.24 Nozzle design

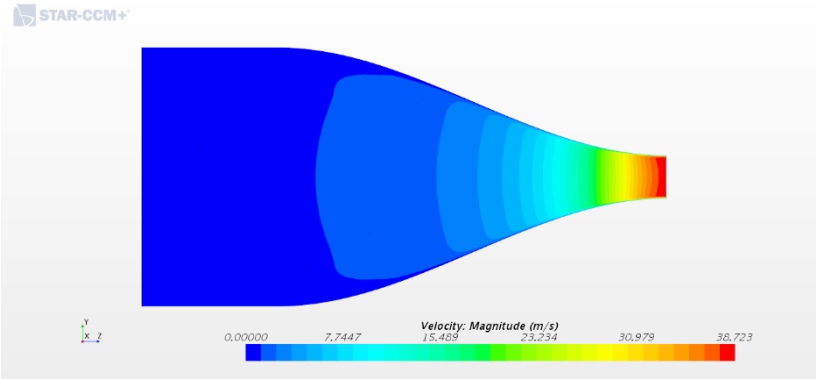

Figure 3.25 Nozzle velocity contour

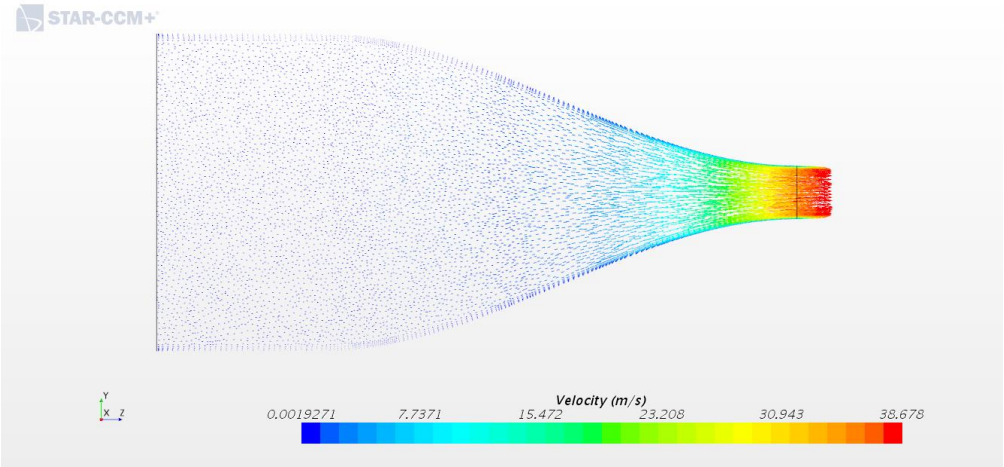

Figure 3.26 Nozzle velocity vector

3.4.1. Calibration of Hotwire

The velocity of the jet out of the nozzle is controlled by the chamber pressure. Flow regulators are used to control the chamber pressure of the calibration device. The hot wire is kept near the nozzle exit. For the flow out of the nozzle at each chamber pressure the voltage of the hotwire is recorded. The velocity of the flow out of the nozzle is calculated based on isentropic equation, as given by Equation 3.

$$\frac{P_0}{P_\infty} = \left(1 + \frac{\gamma - 1}{2} {M_\infty}^2\right)^{\frac{\gamma}{(\gamma-1)}} \tag{3}$$

Where P_0 is the chamber pressure, P_∞ is the atmospheric pressure of the room, γ is the ratio of specific heats (for air γ = 1.4) and M_∞ the Mach number of the jet out of the nozzle. From Mach number velocity of the jet is calculated based on Equation 4.

$$V_\infty = M_\infty \times a_\infty \tag{4}$$

$$a_\infty = \sqrt{\gamma R T_\infty} \tag{5}$$

Where a_∞ is the speed of sound given by Equation 5. R is the gas constant for air (287

J/KgK) and T_∞ is the temperature of the jet obtained from the thermocouples in the calibration device. A temperature correction is applied to the recorded hotwire voltage to obtain a corrected voltage, given by Equation 6.

$$E_{corr} = \sqrt{\frac{T_w - T_0}{T_w - T_a}} \times E_a \quad (6)$$

Where E_a is the recorded voltage, E_{corr} is the corrected voltage, T_w is the wire temperature (set by the device), T_a is the ambient temperature during calibration and T_0 is the calibration temperature (average of initial and final jet temperature). A 4th order polynomial curve fit is applied between the corrected voltage and the calculated velocity based on isentropic equation, the format of calibration equation is given by Equation 7.

$$V = C_0 + C_1 E_{corr} + C_2 {E_{corr}}^2 + C_3 {E_{corr}}^3 + C_4 {E_{corr}}^4 \quad (7)$$

3.4.2. Validation of Hotwire and Calibration Setup

The validation of hotwire is done by comparing the velocity measured by the hotwire using the calibration equation and the velocity measured using a pitot static tube. The same calibration device is used for this validation process as it will also be self-validated in this process.

Figure 3.27 compares the chamber pressure of the calibration setup to the velocity measured by the hotwire, pitot static tube and the isentropic equation. We can see from the graph that velocity measured by the hotwire and the pitot static tube are almost identical for a given chamber pressure. Hence, this validates the hotwire and the calibration setup. In the experimental setup the hotwire is placed behind row 1 and row 5 pins. The hotwire can be moved axially, spanwise and streamwise direction using a 3 – axis traverse. Figure 3.28 show the schematic of hotwire setup in the experiment.

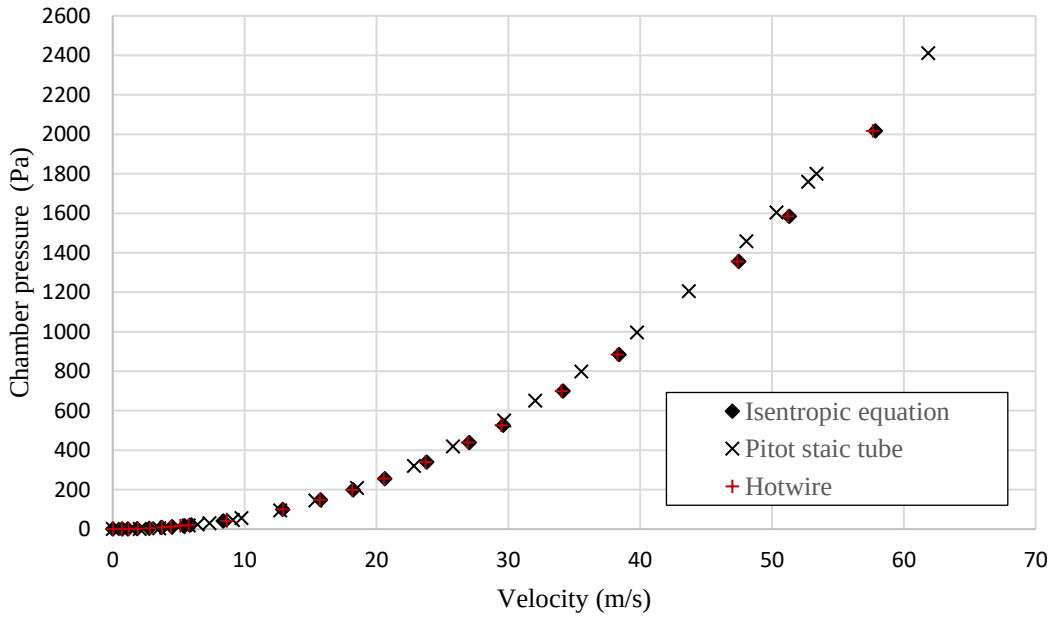

Figure 3.27 Hotwire validation

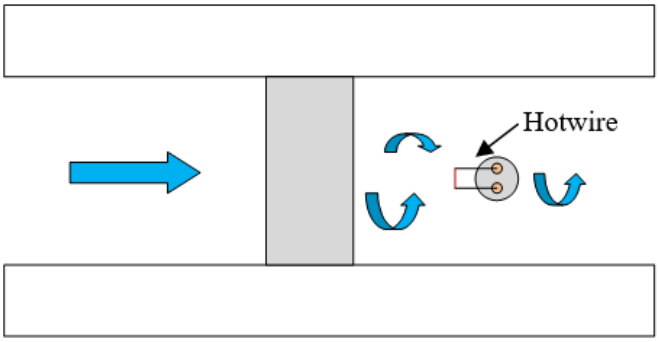

Figure 3.28 Schematic of hotwire setup

Figure 3.29 shows the hotwire setup in the experiment. The hotwire and acrylic plate is attached to a 3-axis traverse, vacuum grease is applied between two of the acrylic plates as seen in the figure, to seal the gaps as the top plate moves with the traverse. The bottom acrylic plate is screwed to the test section side wall.

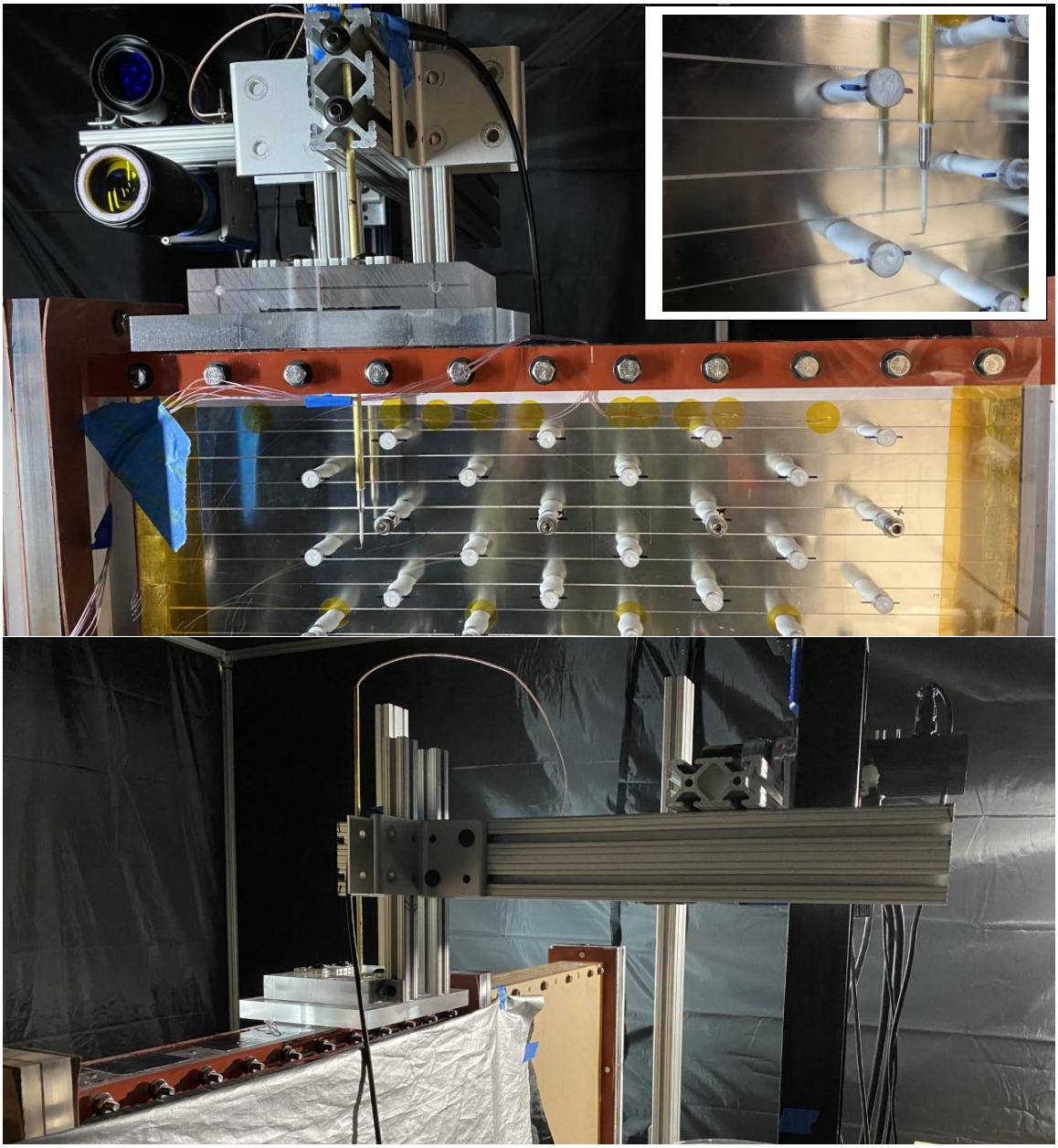

Figure 3.29 Hotwire setup

3.5. Pressure Transducers

Pressure ports are located at the side wall to measure the pressure drop across the channel. They are located, such that they are between two rows of pins. These ports are connected to an Omega differential pressure transducer (model PX409-2.5CGV).

Miniature pressure transducers are placed on the top wall behind row 1, row 3 and row 5 pins to measure the pressure fluctuations. They are used to analyze the unsteady wake shedding from the pins. Figure 3.30 shows the miniature pressure transducer from the manufacturer Kulite (model XCL-072-5D) and the schematic of the placement in the test section. The Kulite pressure transducer should be flush with the top wall.

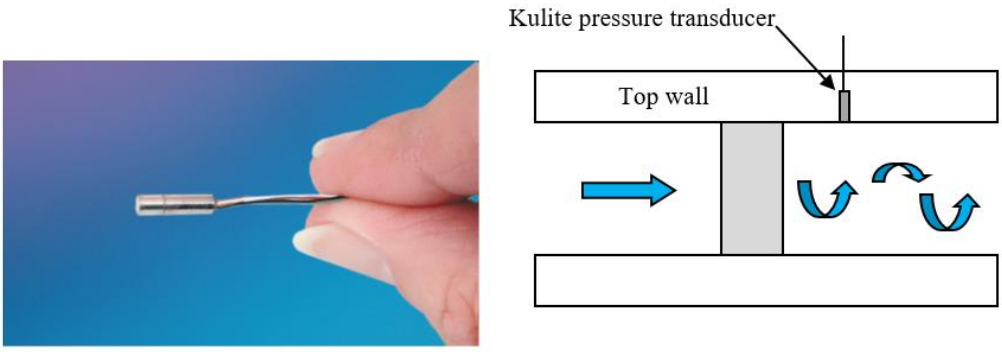

Figure 3.30 Schematic of Kulite pressure transducer

3.6. Data Reduction

3.6.1. Endwall Nusselt number

Nusselt number is given by,

$$Nu = \frac{h * D}{k} \tag{8}$$

Where h is the heat transfer coefficient, D is the characteristic diameter and k is the thermal conductivity of air calculated based on Sutherland's equation, as shown in Equation 9.

$$k = k_0 \left(\frac{T}{T_0}\right)^{3/2} \frac{T_0 + S_k}{T + S_k} \tag{9}$$

Where k_0, T_0 and S_k are Sutherland's constant. For air k_0 = 0.0241 W/m.K, T_0 = 273 K

and S_k = 194 K. T is the bulk temperature of the flow.

From Newton's law of cooling heat transfer coefficient (h) is given by,

$$h = \frac{q''_{sup} - q''_{loss}}{(T_s - T_b)} \tag{10}$$

Where T_s is the surface temperature, T_b is the bulk temperature of the flow, q''_{sup} is the heat flux supplied to the Inconel strip, and q''_{loss} is the heat flux lost due to heat leakage through the acrylic endwall. From Equation 1 the q''_{loss} is given by,

$$q''_{loss} = 6.31442 * (T_s - T_{ambient}) \tag{11}$$

$$q''_{sup} = \frac{I^2 \rho}{w^2 t} \tag{12}$$

Where ρ is the resistivity of the Inconel material, I is the current supplied, w is the width of the Inconel strips and t is the thickness of the strip. The surface temperature (T_s) of the Inconel strips is obtained by post processing the TSP data. The bulk temperature is calculated using an energy balance given by Equation 13.

$$T_b^{i(x)} = T_b^{i-1(x)} + \frac{q(x)}{\dot{m} C_p} \tag{13}$$

The left hand side of the equation is the bulk temperature of the current pixel in the x direction (streamwise) calculated using the bulk temperature of the previous pixel. $q(x)$ is the heat supplied per span wise row of pixel, $\dot{m}$ is the mass flow rate into the channel while C_p is the specific heat capacity of the air based on the mean bulk temperature.

$$q(x) = \frac{(q''_{sup} - q''_{loss}) * A_S}{n} \tag{14}$$

Where A_s is the total surface area of the strips and n is the total number of pixels in the streamwise direction.

3.6.2. Pin Surface Average Nusselt number (ESM)

The extended surface boundary conditions from the present experimental setup can be stated as follows; pin of finite length, known constant heat flux at the base, insulated tip, forced convection on the surface of the fin as well as uniform internal heat generation within the pin. We assume a 1D model for simplicity, allowed with the use of a low Biot number for the pin (Pai, Prasad & Ricklick, 2020). All distances are measured from the base of the pin. A simple schematic of the boundary conditions can be seen in Figure 3.31.

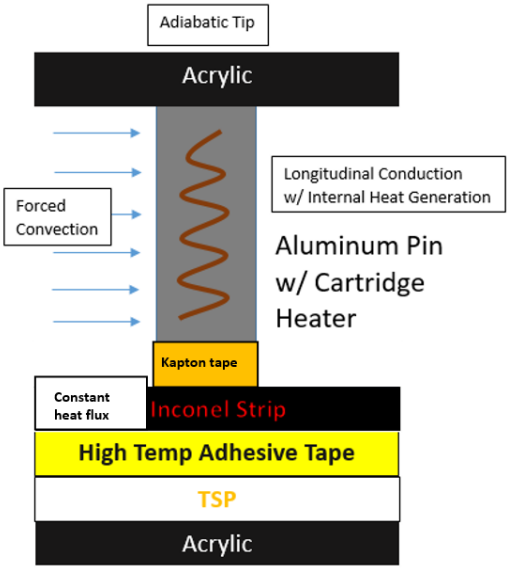

Figure 3.31 Layout of the test section with boundary conditions (Pai et al., 2020).

The governing equation for such a system is given by the 1D fin conduction equation with internal heat generation as seen in Equation 15 (Bejan & Kraus, 2003).

$$\frac{d^2\theta}{dx^2} - m^2\theta = -\frac{\dot{q}}{k} \tag{15}$$

Where $m = \sqrt{\frac{hP}{kA_c}}$ & $\theta(x) = T(x) - T_b$. The general solution is obtained by solving

the above equation using the method of annihilators.

$$\theta(x) = c_1 e^{mx} + c_2 e^{-mx} + c_3 \tag{16}$$

The boundary conditions can be expressed mathematically as,

$$at\ x = 0, \quad -k\frac{d\theta}{dx} = q"_b \qquad\qquad at\ x = L, \quad \frac{d\theta}{dx} = 0 \tag{17}$$

Using the above boundary conditions, the solution for such a system is given by (Pai et al., 2020),

$$\theta(x) = \frac{(q"_b * e^{mx-2mL} + q"_b * e^{-mx})}{km(1 - e^{-2mL})} + \frac{\dot{q}}{km^2} \tag{18}$$

This gives the temperature distribution along the length of the pin, in term of the excess temperature. For *x = 0*, that is at the base of the pin, the temperature is obtained experimentally along with the T_b that is the bulk temperature. The values of heat flux through the base and the internal heat generation through the pins are also known. Thus, Equation 18 reduces to a non-linear equation of unknown *m*. Thus, the surface average pin heat transfer coefficient contained within the fin parameter (*m*) is calculated by using an iterative approach (Pai et al., 2020). And finally the pin surface average Nusselt number is calculated by using Equation 8, in which *k* is the thermal conductivity of the pin material.

fsolve() function is used in MATLAB to solve this equation iteratively. The initial guess for the heat transfer coefficient (h) was the theoretical fin parameter based on the pin dimensions. The solution was not dependent on the initial guess (Pai et al., 2020). The *fsolve()* function uses a Trust-Region Dogleg method by default to obtain a solution.

3.6.3. Pressure Data

The pressure measured by the Omega pressure transducer (model PX409-2.5CGV) is

calculated by using Equation 19.

$$P = \frac{2.5 \times V}{5} \tag{19}$$

Where P is the gauge pressure measured in psi and V is the voltage recorded from the output of the pressure transducer.

The pressure fluctuation measured using Kulite pressure transducer (model XCL-072-5D) is calculated by using Equation 20.

$$P = \frac{5 \times V}{0.045} \tag{20}$$

Where P is the gauge pressure measured in psi and V is the voltage recorded from the output of the Kulite pressure transducer.

Two omega pressure transducers were used to measure the chamber pressure for the hotwire calibration device, one for the lower end (Omega pressure transducer model PX653-0.1D5V) and the other for medium to high end (Omega pressure transducer model PX409-2.5CGV). The pressure measured by the Omega pressure transducer (model PX653-0.1D5V) is calculated by using Equation 21.

$$P = (0.025 \times V) - 0.025 \tag{21}$$

Where P is the gauge pressure measured in inch of water and V is the voltage recorded from the output of the pressure transducer.

3.6.4. Reynolds Number

The Reynolds number is calculated using Equation 22.

$$Re = \frac{\dot{m}D}{A_c \mu} \tag{22}$$

Where $\dot{m}$ is the mass flow rate of the flow, D is the characteristic diameter (CP1 diameter for initial pin design and 2H for the final pin design), A_c is the cross sectional

area of the test section (either inlet or the effective cross sectional area with respect to the pins) and μ is the dynamic viscosity of the flow.

The mass flow rate is calculated by measuring the pressure drop across a venturi flow meter. Dynamic viscosity is calculated using the Sutherland's equation as shown in Equation 22.

$$\mu = \mu_0 \left(\frac{T}{T_0}\right)^{3/2} \frac{T_0 + S_\mu}{T + S_\mu} \tag{23}$$

Where μ_0, T_0 and S_μ are Sutherland's constant. For air μ_0 = 1.716*10^{-5} Pa.s, T_0 = 273 K and S_μ = 111 K. T is the temperature of the flow through the venturi flow meter. Equation 24 – 30 shows the steps used to calculate the mass flow rate from the pressure drop (ΔP) obtained from the venturi flow meter.

$$GPM = C_1 \times \Delta P^{C_2} \tag{24}$$

Equation 24 is a power curve fit obtained from the ΔP vs GPM data given by the venturi flow meter manufacturer Presco. This GPM data is calibrated for different ΔP by the manufacturer for a venturi flow meter specification of schedule 40, and with water at 60 °F.

$$T_c = \sqrt{\frac{T + 460}{520}} \tag{25}$$

Where T_c is the temperature correction to get the temperature in standard condition and T is the temperature of the flow through the venturi flow meter measured in °F.

$$P_c = \sqrt{\frac{14.73}{P + 14.73}} \tag{26}$$

Where P_c is the pressure correction to get the pressure in standard condition and P is the upstream gauge pressure of the venturimter measured in psi.

$$SCFM = \frac{GPM \times 3.8}{T_c \times P_c} \tag{27}$$

$$\rho = \frac{P}{R \times T} \tag{28}$$

Density in lb/ft^3 is multiplied to SCFM to get mass flow rate. The density is calculated based on standard atmospheric pressure and temperature condition and by using equation of state, Equation 28.

$$\dot{m} = SCFM \times 0.0765 \tag{29}$$

In Equation 29 the mass flow calculated is in lb/min. Equation 30 shows the mass flow rate calculated in Kg/s.

$$\dot{m} = \frac{\dot{m}(in\ lb/min) \times 0.453592}{60} \tag{30}$$

The velocity of the flow in the test section is calculated from mass flow rate equation as shown in equation 31.

$$V = \frac{\dot{m}}{\rho A_c} \tag{31}$$

Where ρ is the density of the flow, A_c is the cross sectional area of the test section (either inlet or the effective cross sectional area with respect to the pins). If the inlet cross sectional area is used then the velocity calculated will be inlet velocity to the test section (used in initial and final pin design) and if the effective cross sectional area with respect to the pins is used then the velocity calculated will be the velocity between the pins in the first row of the test section, which in turn would be the maximum velocity in the test section (used in validation experimental test setup).

3.6.5. Friction Factor

A pressure loss form of friction factor (*f*) known as Darcy–Weisbach equation is used.

$$f = \frac{2\Delta P D}{\rho V^2 L} \tag{32}$$

Where D is the characteristic diameter, L is the length of the channel, ρ is the density of the fluid, ΔP is the pressure drop across the channel and V is the inlet velocity of the channel.

3.6.6. Turbulence Intensity

Turbulence intensity (TI) is calculated using the velocity fluctuations measured by the hotwire anemometer, given by Equation 33.

$$TI = \frac{V_{rms}}{V_{mean}} \tag{33}$$

Where standard deviation of velocity (V_{rms}) is given by,

$$V_{rms} = \sqrt{\frac{1}{N-1}\sum_{1}^{N}(V_i - V_{mean})^2} \tag{34}$$

Where N is the sample size and mean of velocity measurements is given by,

$$V_{mean} = \frac{1}{N}\sum_{1}^{N} V_i \tag{35}$$

3.6.7. Uncertainty Analysis

The uncertainty in the experimental results are calculated by using root sum square method (Moffat, 1988; Prasad & Ricklick, 2017). If result y in the experiment is calculated using Equation 36, with variables m and x.

$$y = mx \tag{36}$$

Then the uncertainty in the result y is given by,

$$u_y = \sqrt{\left(\frac{\partial y}{\partial m} * b_m\right)^2 + \left(\frac{\partial y}{\partial x} * b_x\right)^2 + \left(\frac{\partial y}{\partial m} * S_m\right)^2 + \left(\frac{\partial y}{\partial x} * S_x\right)^2} \quad (37)$$

Where systematic uncertainty is represented by *b* and random uncertainty is represented by *S*. The calculated uncertainty u_y take into consideration the errors of each measurements by propagating the error throughout using root sum square method. The final uncertainty with the 95% level of confidence is given by,

$$U_y = t_{95} \times u_y \quad (38)$$

Where t_{95} is the t value chosen from the student t distribution table based on the level of confidence desired and the degree of freedom considered. The t_{95} value should only be affected by the random uncertainty but not the systematic uncertainty, hence the systematic uncertainty is divided by the t_{95} value, before taken into root sum square to calculate the total uncertainty (Prasad & Ricklick, 2017).

$$b_x = \frac{B_x}{t_{95}} \quad (39)$$

Systematic uncertainty is calculated from the bias error of the measurements made by a measuring instrument/device, the systematic uncertainty for a variable is given by,

$$B_x = \sqrt{{e_1}^2 + {e_2}^2 \ldots\ldots + {e_n}^2} \quad (40)$$

Where variables $e_1, e_2 \ldots\ldots e_n$ are the different types of errors in a measuring device for a single measurement. Systematic uncertainty is also known by bias uncertainty. Random uncertainty is calculated from the standard deviation given by Equation 41, it describes the precision and the repeatability of the measurement. It is also called as standard deviation of the mean.

$$S_x = \frac{\sigma_x}{\sqrt{N}} \quad (41)$$

4. Results

The results section will be split into four parts, the first two will discuss the computational results and the latter two will discuss the experimental results for both initial and final pin designs.

4.1. Computational Study – Initial Pin Design

As mentioned in pin design, the initial pin design consists of pins CP1, EP1, BP1 and BP2. CP1 is a circular pin, EP1 is an elliptical pin, BP1 is a bio pin of elliptical cross section and BP2 is a bio pin of circular cross section. These initial pin designs were part of preliminary computational study. Three Reynolds numbers 2,700, 5,200 and 15,500 was used in this preliminary computational study. The Reynolds number is based on the inlet velocity of 2.85 m/s, 5.48 m/s and 16.15 m/s, CP1 diameter (0.15 m) and the inlet cross sectional area of the test section.

4.1.1. Endwall Nusselt Number

Figure 4.1 – Figure 4.4 shows the result for spanwise average Nusselt number for all Reynolds number cases and also the endwall Nusselt number contour. The spanwise average Nusselt number is normalized with respect to square root of Reynolds number. $Nu/Re^{1/2}$ is called the Frossling number, which is used for heat transfer scaling.

From Figure 4.2, for the bio pin BP1 and BP2, we can see that the wake created behind the horseshoe vortex from row 2 onwards is broken as compared to pin CP1 and EP1. The wake as seen in the endwall contour is created form the core flow to endwall interaction. As seen from the literature the seal whiskers break down the wake due to the added vorticity component, this is seen in the endwall results of the Nusselt number contour.

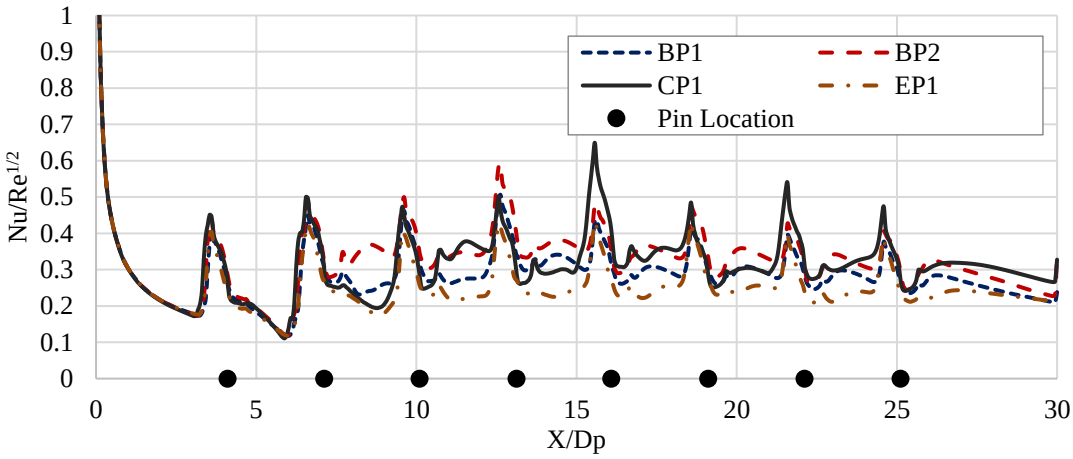

Figure 4.1 Spanwise average Nusselt number for Re = 2,700.

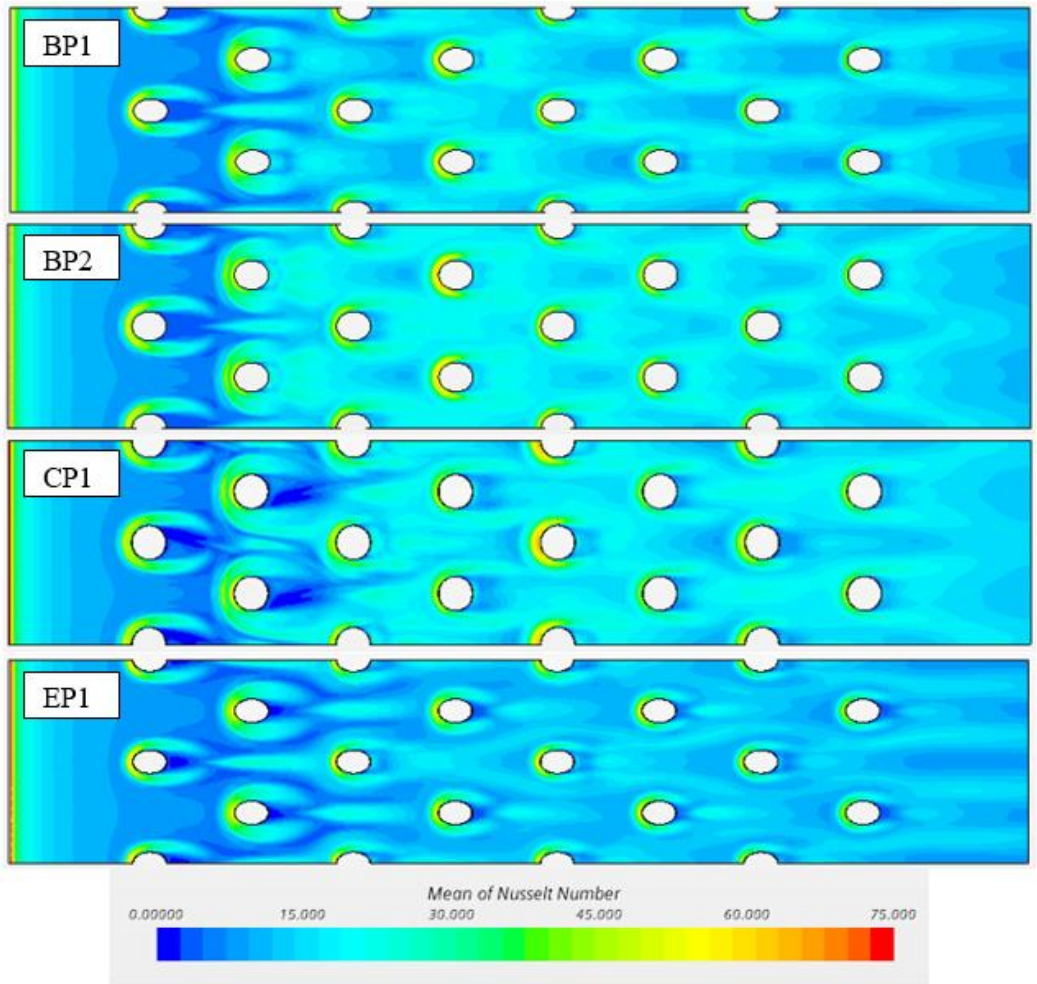

Figure 4.2 Endwall Nusselt number contour for Re = 2,700

The flow structure at the endwall near row 1 pins remains the same for all the pins shapes, this can also be seen from the spanwise average results from Figure 4.1. From Figure 4.1 we can also see that the wake region of BP2 has a higher Nusselt number enhancement in comparison to the other pins, since the complex wake structure behind the pin causes a higher Nusselt number augmentation at the endwall.

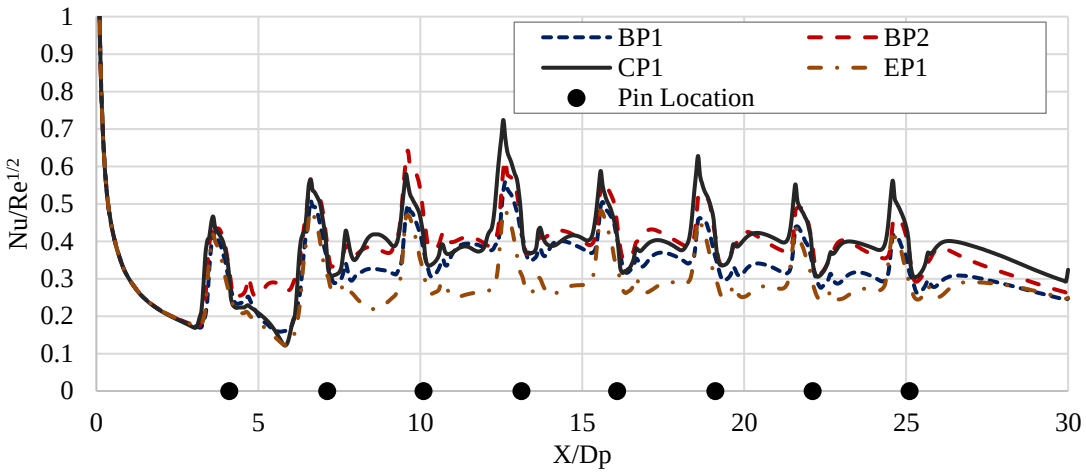

Figure 4.3 Spanwise average Nusselt number for Re = 5,200

From Figure 4.3 we can see the trend for the spanwise average endwall Nusselt number is the same as seen in Figure 4.1 for Re of 2,700 case. The only difference is the increase in the Nusselt number augmentation in the wake region due to the increase in momentum, which can also be seen in Figure 4.4 for Re of 15,500. In Figure 4.4 it can also be seen the Nusselt number at the stagnation region and behind the pins is higher and due to more momentum in the flow. The increase in Nusselt number augmentation in the wake region is due to the increase in the magnitude of turbulence wake structure as the momentum of the flow is increased.

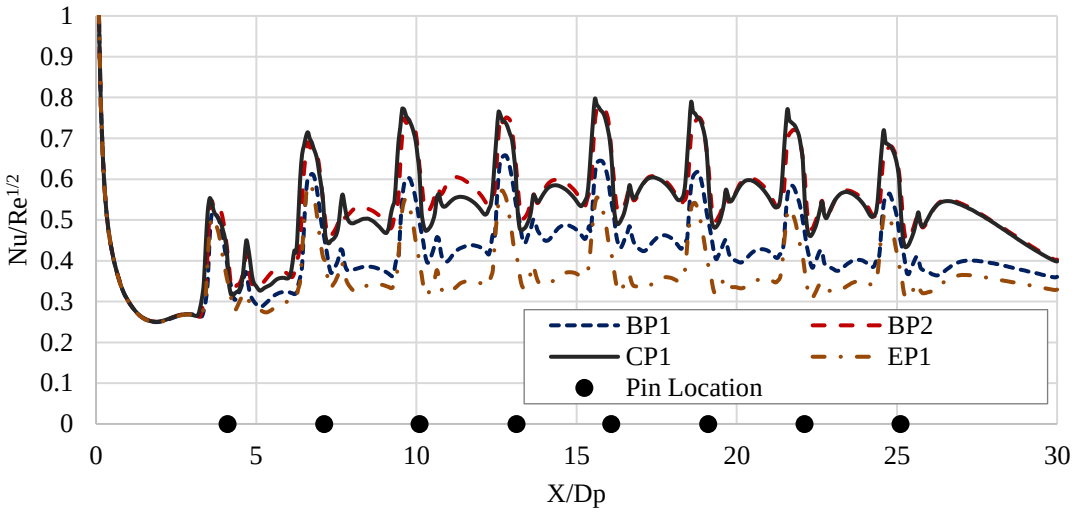

Figure 4.4 Spanwise average Nusselt number for Re = 15,500

4.1.2. Pin Circumferential Data

The undulations of the bio pins are defined by alternating peaks and valleys, the peak becomes a valley, and the valley becomes a peak around the side of the pin as seen in Figure 4.5. The circumferential distribution of peaks and valleys are compared individually with CP1 and EP1 for Nusselt number and coefficient of pressure (C_p), from Figure 4.6 to Figure 4.17.

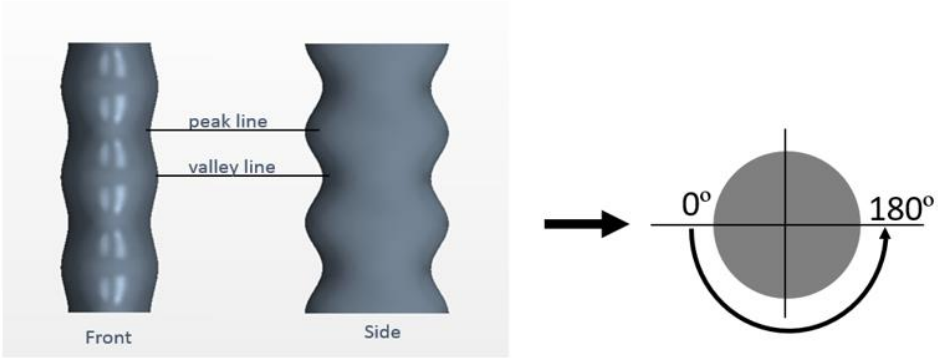

Figure 4.5 Circumferential pattern

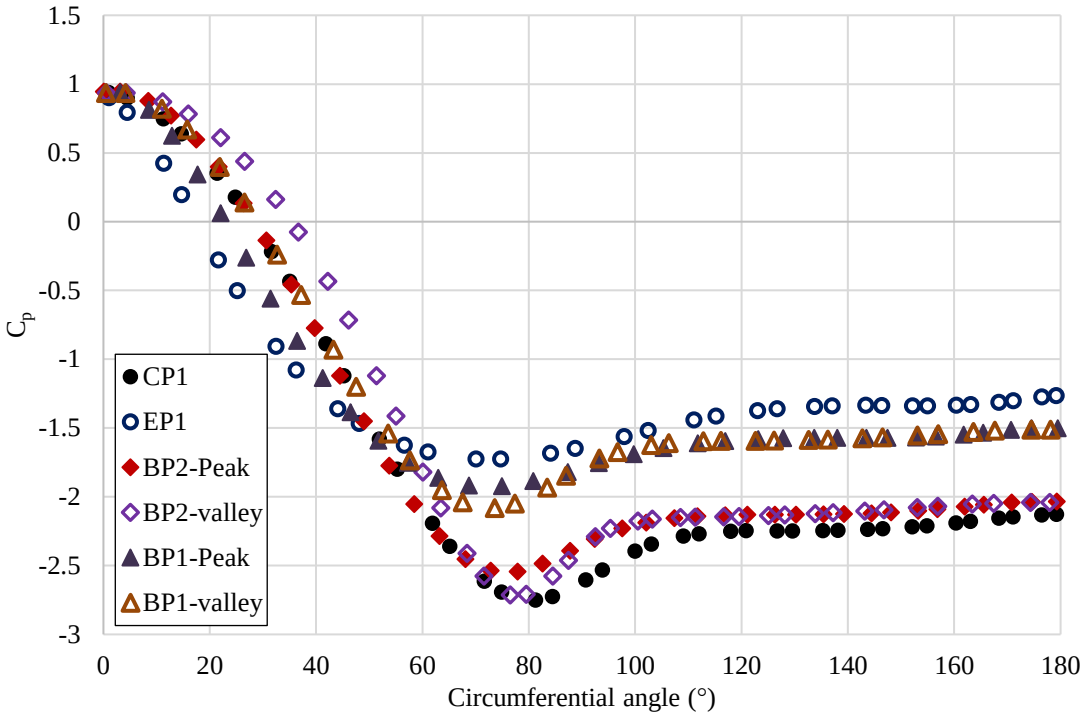

Figure 4.6 Row 1 pin circumferential C_p data for Re = 2,700

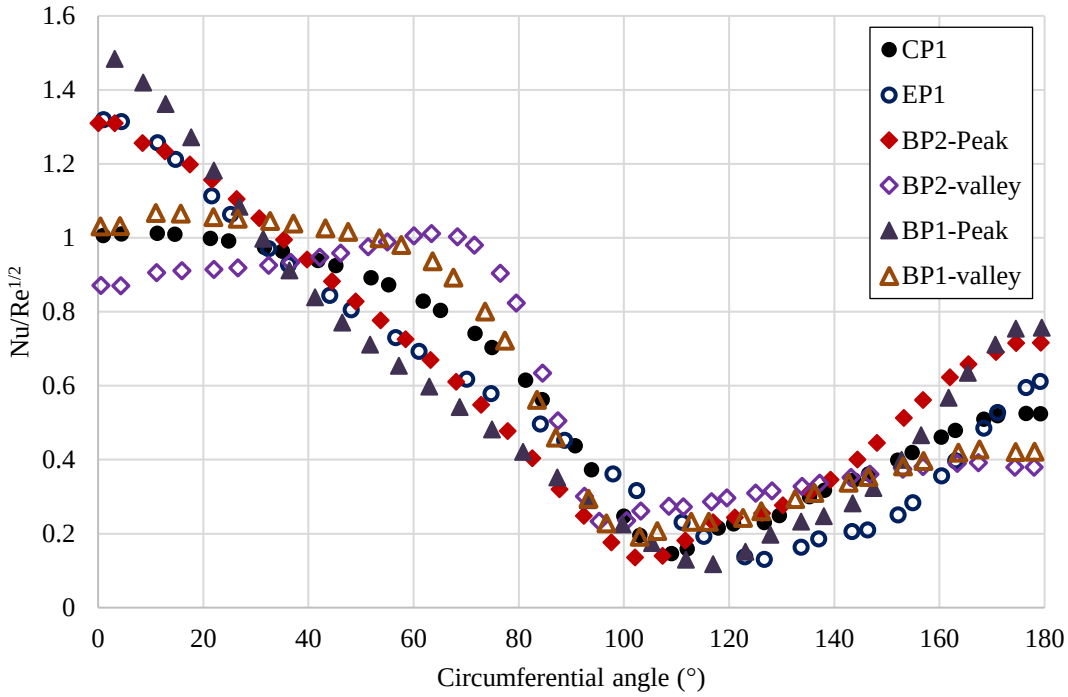

Figure 4.7 Row 1 pin circumferential Frossling number data for Re = 2,700

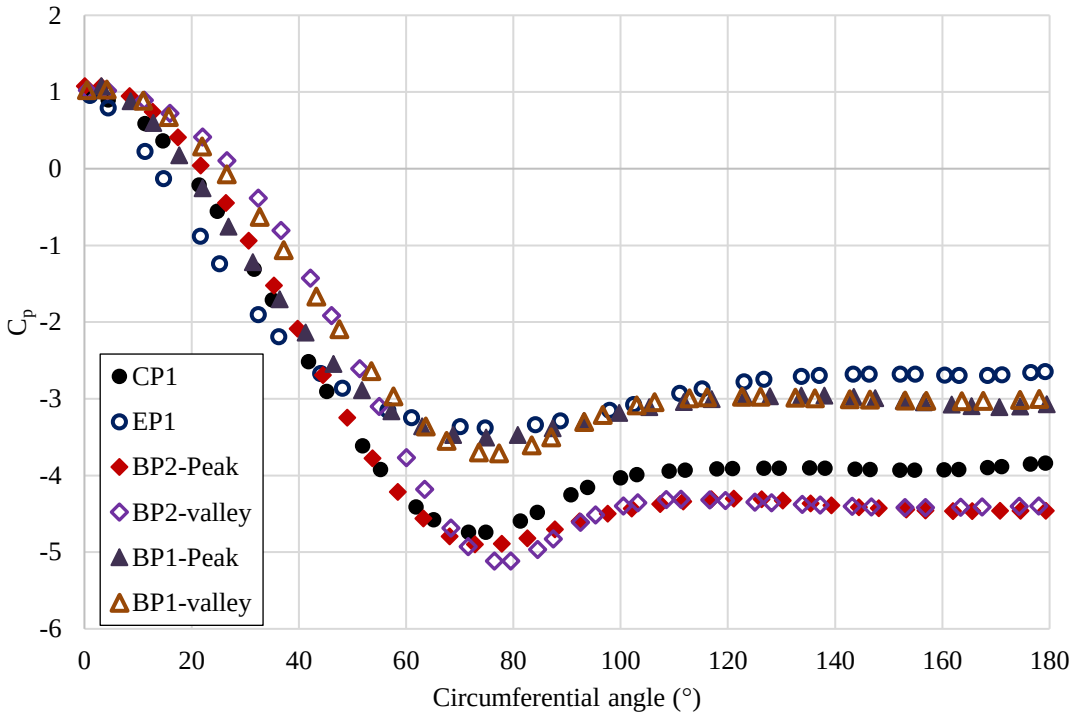

Figure 4.8 Row 5 pin circumferential C_p data for Re = 2,700

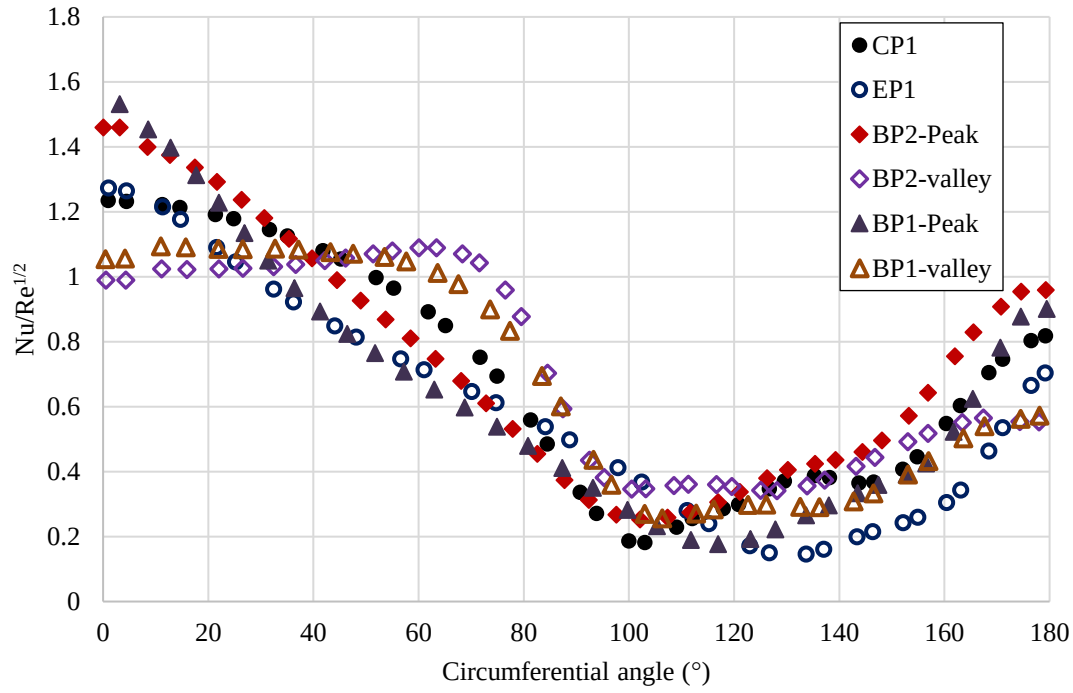

Figure 4.9 Row 5 pin circumferential Frossling number data for Re = 2,700

From Figure 4.6 and Figure 4.7 we can see that the elliptical shaped structures EP1 and BP1 (at the peak and the valley section), the flow separates around 125°, 115° and 105° while the cylindrical shaped structures CP1 and BP2 (at the peak and the valley section) the flow separates around 110°, 102° and 96°. The larger curvature in the cylindrical pin structures accelerate the flow faster in comparison to the slender elliptical pin structures, which causes the flow to separate faster and also leads to the increase in Nusselt number value in the flow acceleration region of the pin as seen in Figure 4.7.

In Figure 4.7 we can also see that the stagnation point Nusselt number is high for peak regions, as these regions have edges with smaller radius compared to the valley regions. The structures with these edges are EP1, BP1 – Peak and BP2 – Peak. At the back side of the pins, due to the turbulence and mixing created by flow separation there is an increase in Nusselt number. The pin structures with peak regions have a significant increase in Nusselt number around 180°, this is due to the creation of partial stagnation region at the trailing edge of the pins. Also as discussed before the valley becomes the peak around the side of the pin, this creates a secondary stagnation region which increases the Nusselt number as seen from BP2 – valley and BP1 – Valley in Figure 4.7.

Downstream of the domain, in row 5 pins, the results from Figure 4.8 and Figure 4.9 are mostly similar to the results in the row 1 pins as discussed above. The main difference being the flow separates faster in CP1 around 100° in row 5 instead of 110° in row 1 and the respective increase in the Nusselt number at the leading edge stagnation region and the trailing edge of the pin due to the increase in the mixing of flow downstream of the channel. The undulations in BP2 keeps the flow attached longer and has the same separation angle of that of row 1.

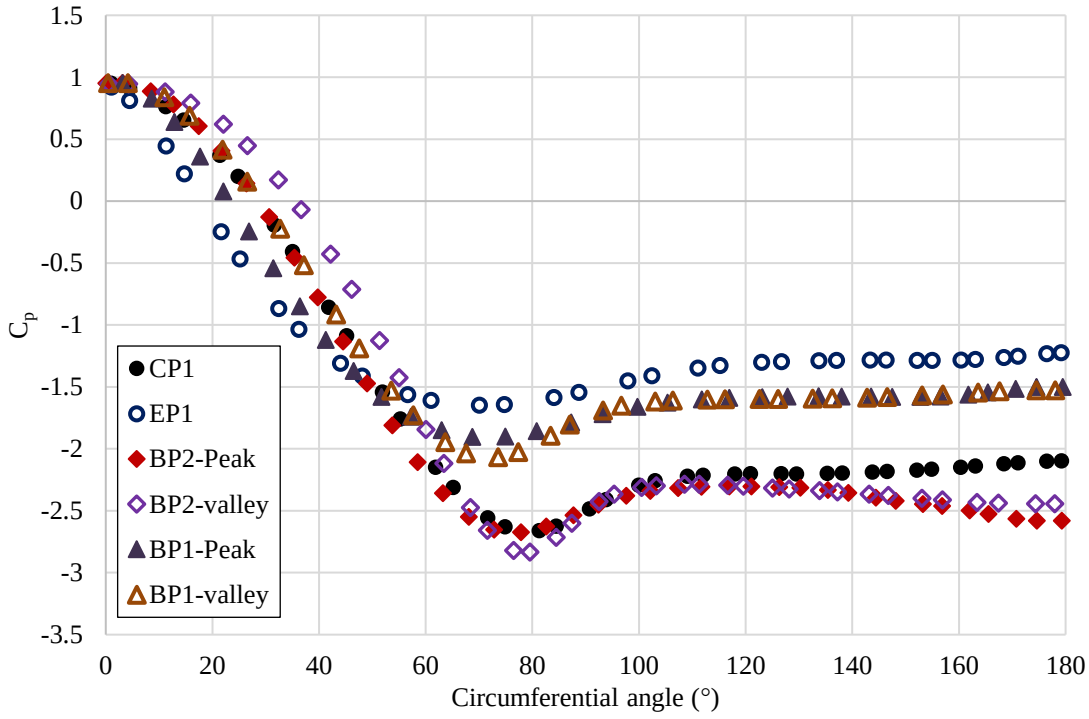

Figure 4.10 Row 1 pin circumferential C_p data for Re = 5,200

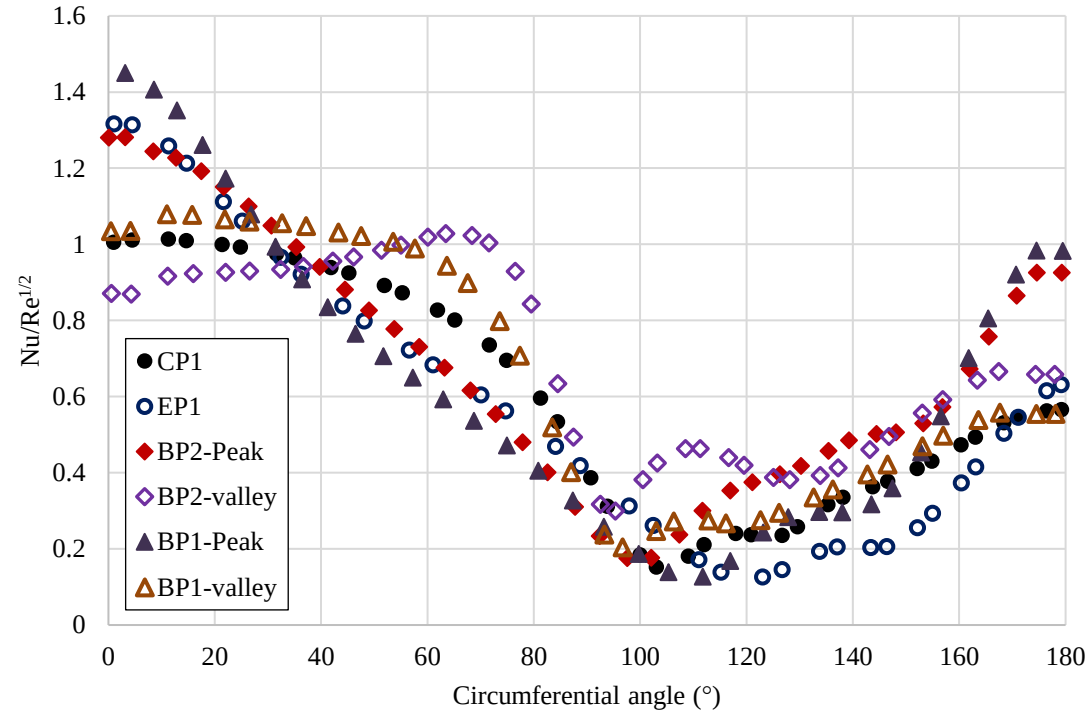

Figure 4.11 Row 1 pin circumferential Frossling number data for Re = 5,200

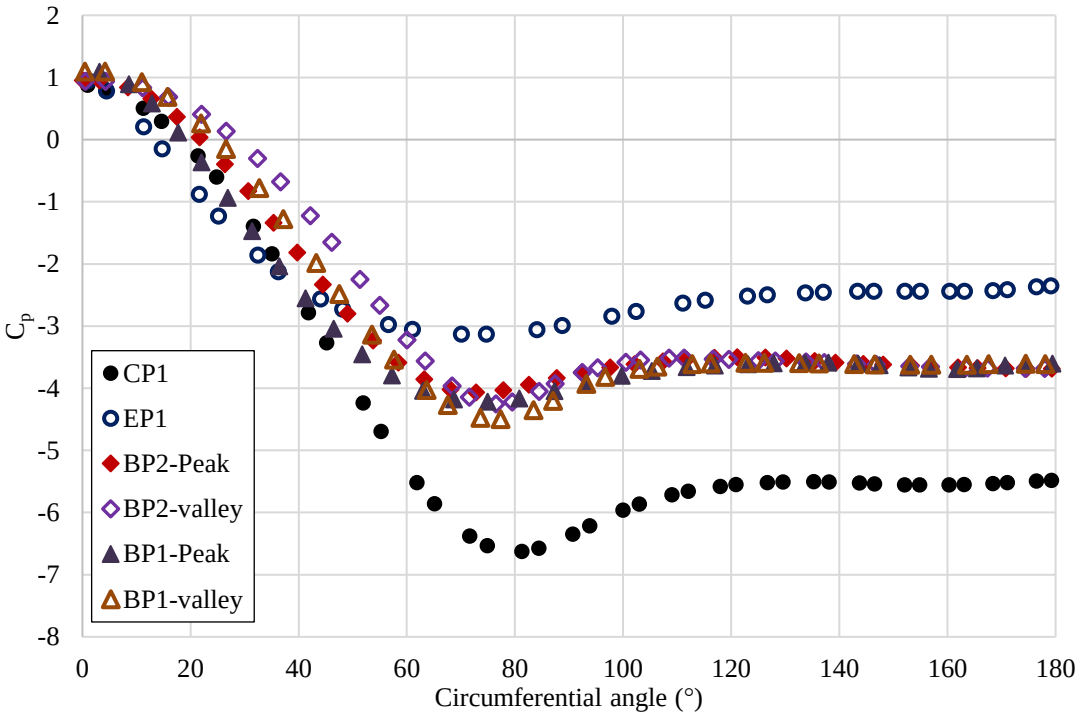

Figure 4.12 Row 5 pin circumferential C_p data for Re = 5,200

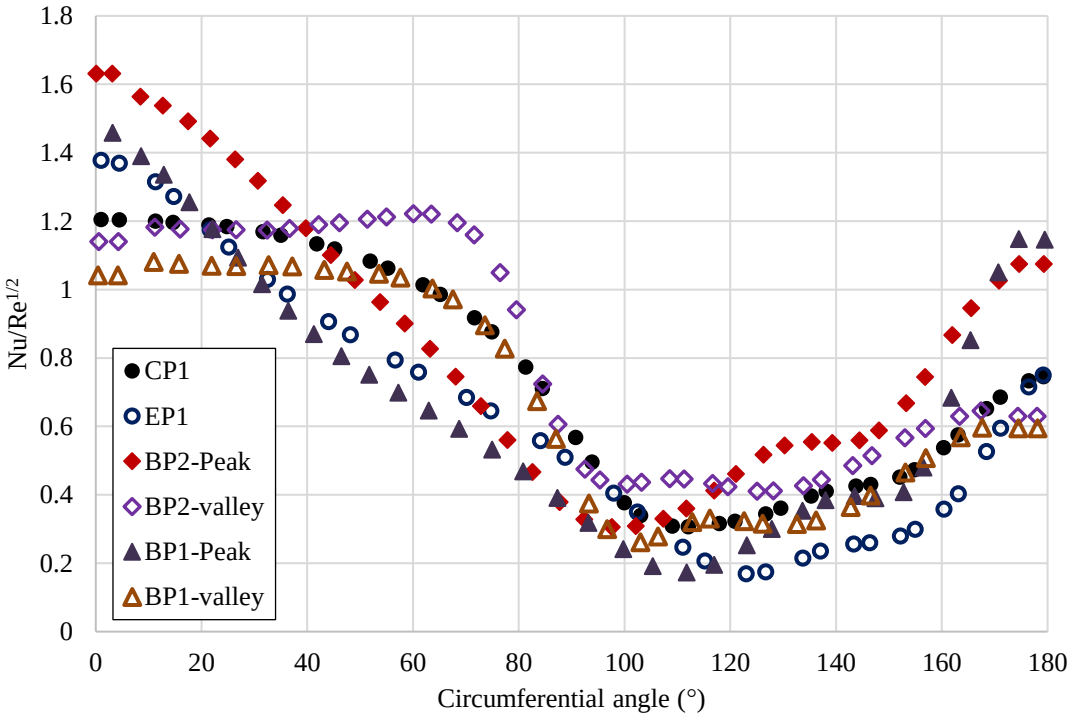

Figure 4.13 Row 5 pin circumferential Frossling number data for Re = 5,200

Figure 4.10 – Figure 4.11 represents row 1 pin circumferential data for Reynolds number of 5,200. These results are similar to the results discussed for Reynolds number of 2,700. The main notable difference is the decrease in C_p around 180° for pin BP2 (at the peak and valley section). This suggests a momentum increase in the turbulence wake created by the pins, which thereby increases the Nusselt number at the trailing edges of the pin, as seen in Figure 4.11.

Figure 4.12 and Figure 4.13 represents row 5 pin circumferential data for Reynolds number of 5,200. In comparison to the lower Reynolds number case, the flow around the pin CP1 and BP1 – valley section has a higher rate of acceleration, which increases the Nusselt number as seen in Figure 4.13. The stagnation region Nusselt number is higher for BP2 – Peak in comparison to the other pin structures.

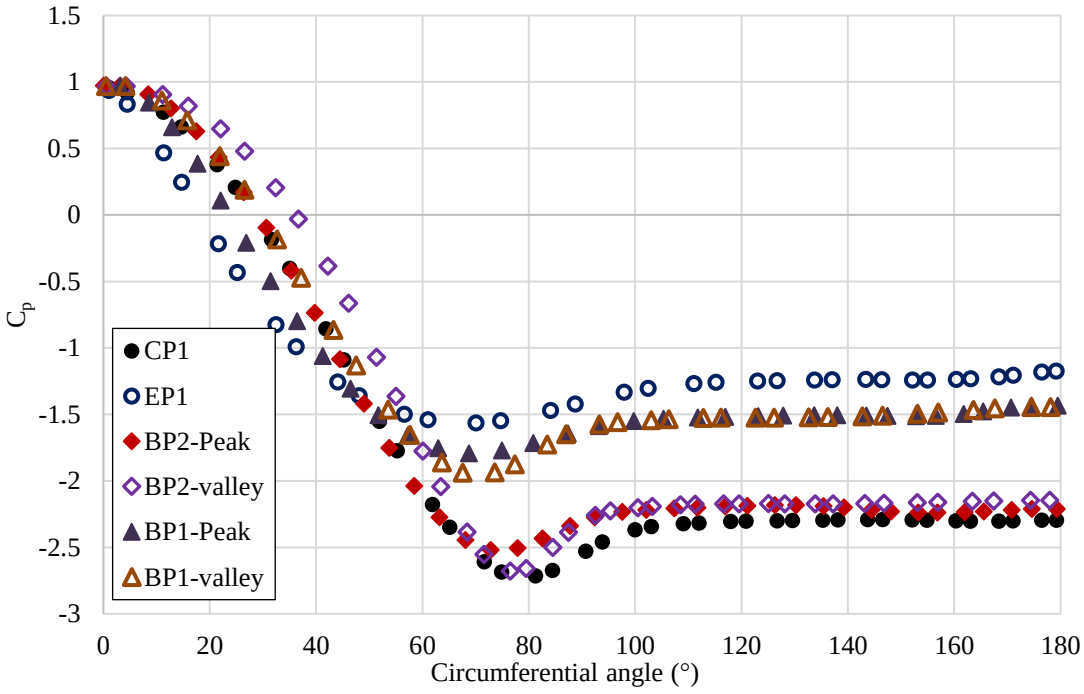

Figure 4.14 Row 1 pin circumferential C_p data for Re = 15,500

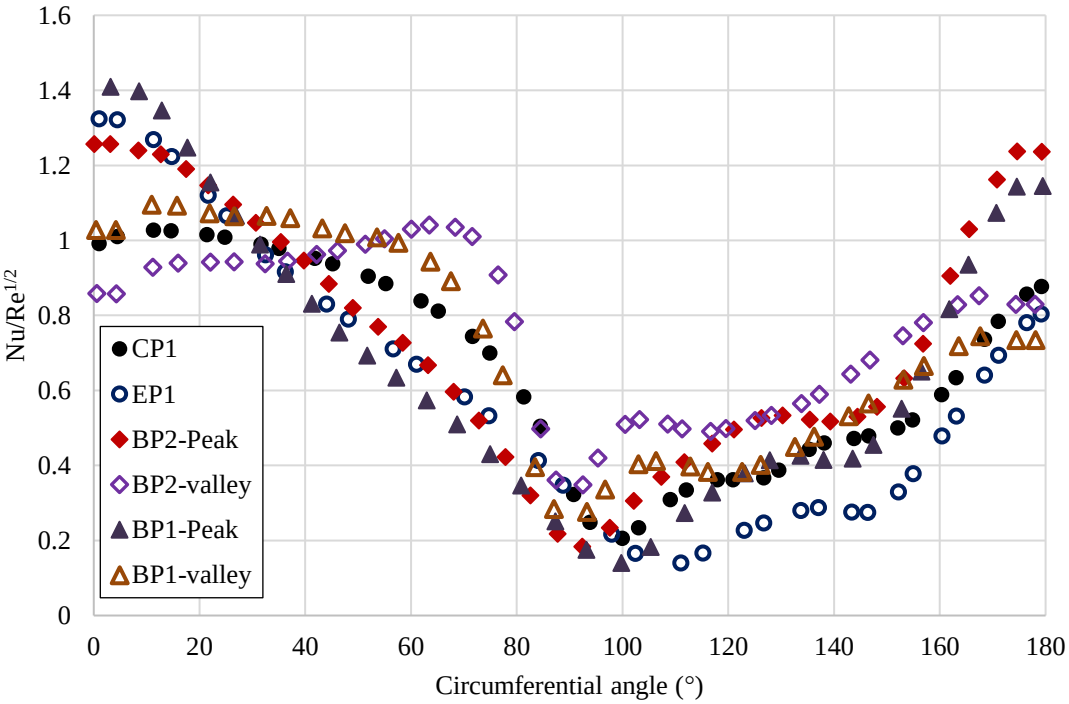

Figure 4.15 Row 1 pin circumferential Frossling number data for Re = 15,500

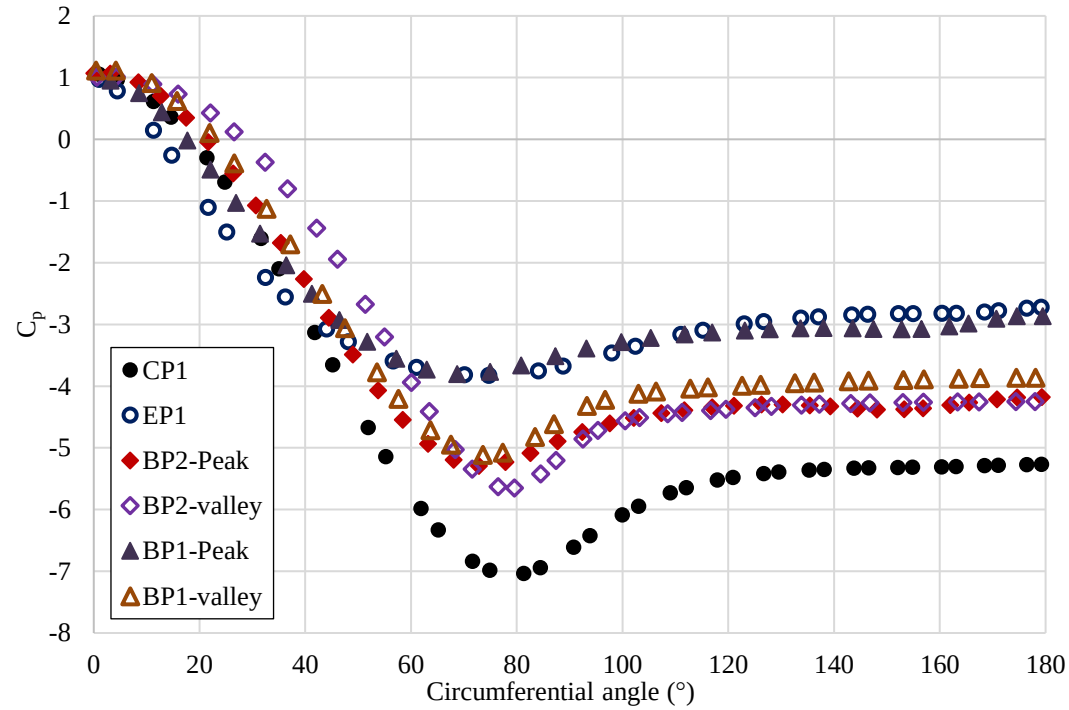

Figure 4.16 Row 1 pin circumferential C_p data for Re = 15,500

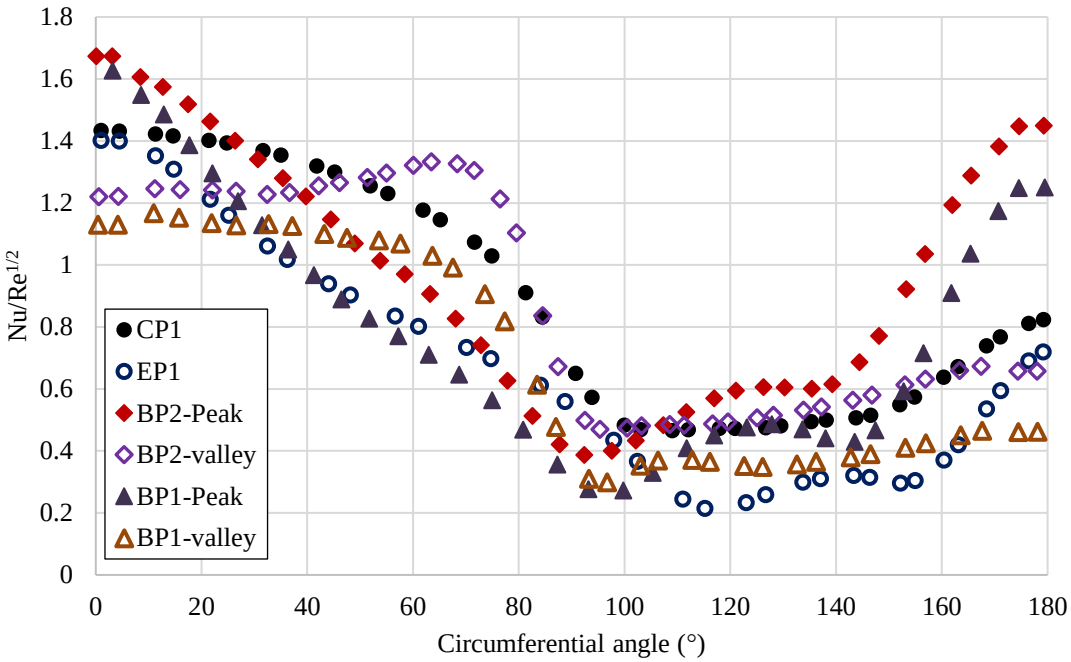

Figure 4.17 Row 5 pin circumferential Frossling number data for Re = 15,500

Figure 4.14 – Figure 4.17 represents pin circumferential data for Reynolds number of 15,500. These results are similar to the results discussed for Reynolds number of 5,200, with BP1 being the poor performer in comparison to BP2.

4.1.3. Pin Surface Average Nusselt Number

Pin surface average Nusselt number is normalized with respect to Reynolds number, ergo the Frossling number is in comparing the heat transfer augmentation in different rows of pins. Figure 4.18 represents the surface average Frossling number for Reynolds number of 2,700. As seen in row 1 circumferential data, due to the higher Nusselt number in the leading edge stagnation region and the secondary stagnation region at the side for pins BP1 and BP2, relates to the increase in surface average Frossling number. Overall due to the presence of the undulations on the bio pins surface we can see augmentation in surface average Nusselt number for pins BP1 and BP2.

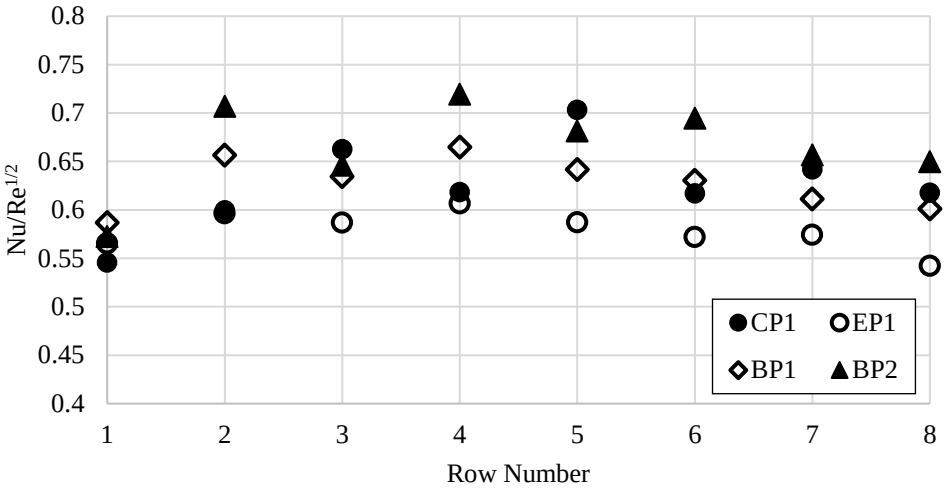

Figure 4.18 Pin surface average Frossling number for Re = 2,700

BP2 is the overall best performer with a maximum difference of 18% in comparison to pin CP1 at row 2. CP1 outperforms the bio pin BP2 at row 3 and row 5 with a difference of 3%, due to the increase in Nusselt number at the stagnation region and the trailing edge of the pin as seen in row 5 circumference data. EP1 is the worst performer being the most aerodynamic in shape.

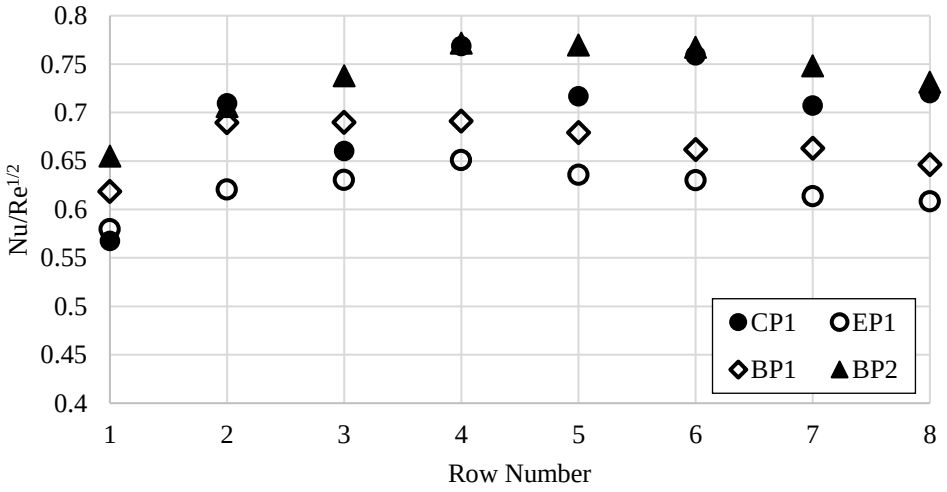

Figure 4.19 Pin surface average Frossling number for Re = 5,200

Figure 4.19 represents the surface average Frossling number for Reynolds number of 5,200. The results are mostly similar to the lower Reynolds number case, with BP2 being the overall best performer. Figure 4.20 represents the surface average Frossling number for Reynolds number of 15,500. As the velocity of the flow is increased, we can see that the pins with circular structure dominate the augmentation of heat transfer at the pin surface, as seen in literature the circular cylindrical pins have higher pin surface average Nusselt number in comparison to the slender more aerodynamically shaped pins such as an elliptical pin.

The circular shape of the pin accelerates the flow to a higher velocity around its circumference leading to increase in the Nusselt number and also leading to earlier flow separation. Hence the turbulence caused due to the flow separation increases the heat transfer but at the cost of increase in pressure drop which will be discussed in the next section. BP2 being a bio pin based on circular dimensions has better performance in comparisons to CP1 due to presence of the undulation creating local heat transfer augmentation.

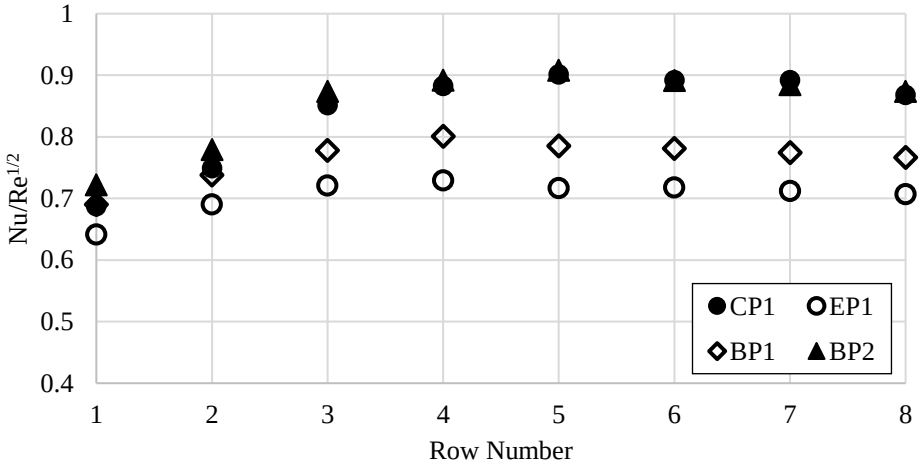

Figure 4.20 Pin surface average Frossling number for Re = 15,500

4.1.4. Pressure Drop Along the Channel

Time averaged static pressure data are obtained from averaging data in a plane between each row of pins and also the inlet. The pressure drop is calculated based on pressure drop between each plane and the inlet ($P_{inlet} - P$). Figure 4.21 – Figure 4.23 represents the pressure drop across the channel for Reynolds numbers of 2,700, 5,200 and 15,500.

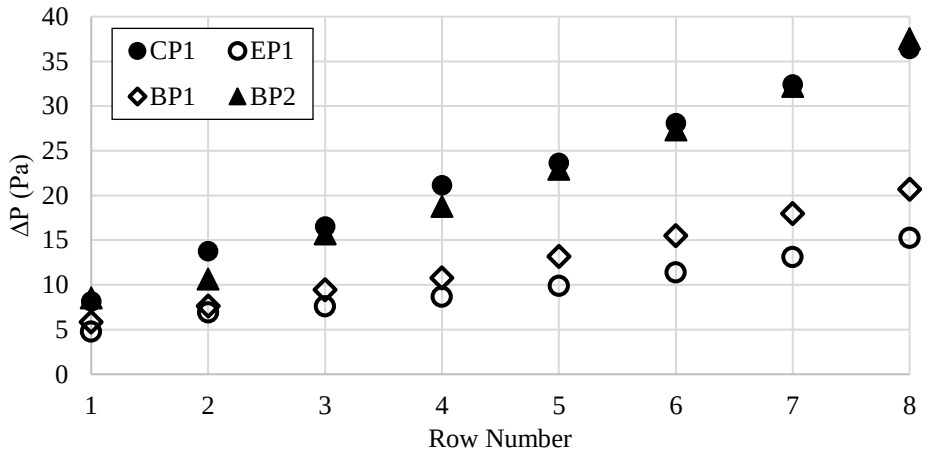

Figure 4.21 Pressure drop along the channel for Re = 2,700

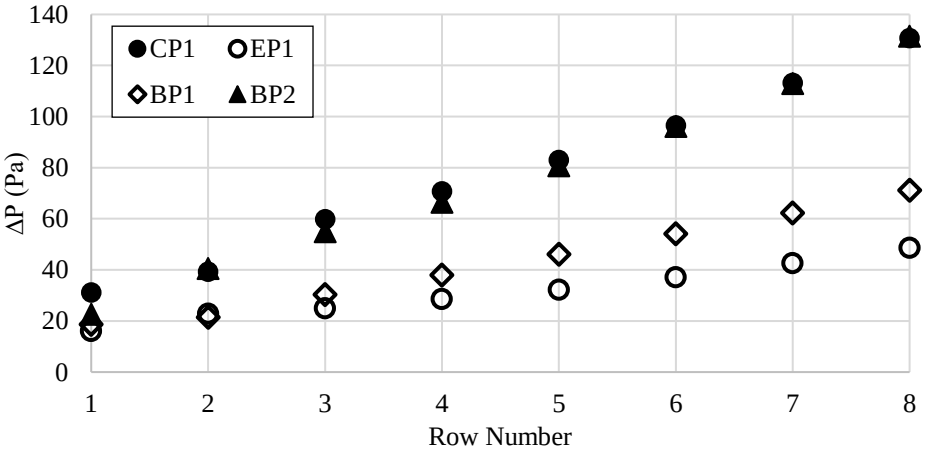

Figure 4.22 Pressure drop along the channel for Re = 5,200

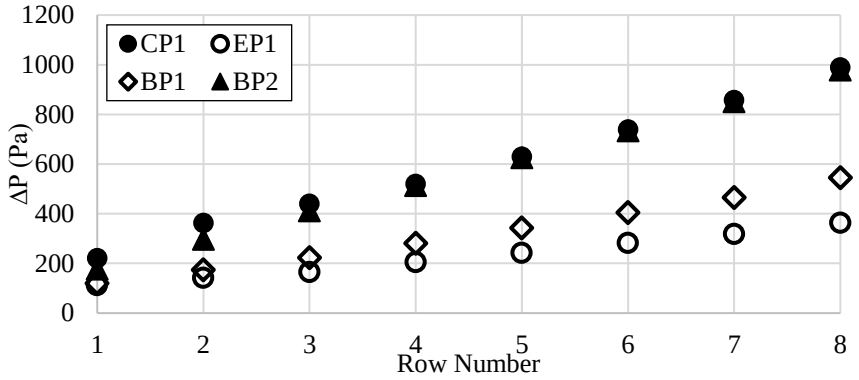

Figure 4.23 Pressure drop along the channel for Re = 15,500

As discussed before, pins which are based out of circular dimensions have greater pressure drop in comparison to pins which are more aerodynamic in shape like EP1. Less aerodynamic pin like CP1 creates pronounced periodic wake shedding which leads to large drop in total pressure. As the flow moves through the domain there is an increase in flow mixing due to wake shedding from each row of pins leading to a greater pressure drop in the channel. Bio pins BP1 and BP2 decreases the magnitude of wake shedding, which leads to reduced pressure loss, leading to reduced pressure drop in the channel, which can be seen from comparing BP1 and EP1 in Figure 4.21 – Figure 4.23, since both are based on elliptical shapes.

4.1.5. Reynolds Number Effects

Reynolds number effects are studied at three different categories, endwall average Nusselt number, pin surface average Nusselt number and Channel average Nusselt number which are compared against friction factor. All the Nusselt number values are normalized with respect to respective data from CP1. The channel average Nusselt number is an area weighted average between the endwall and the pins. Figure 4.24 – Figure 4.26 shows the result for the three categories mentioned above for Re of 2,700.

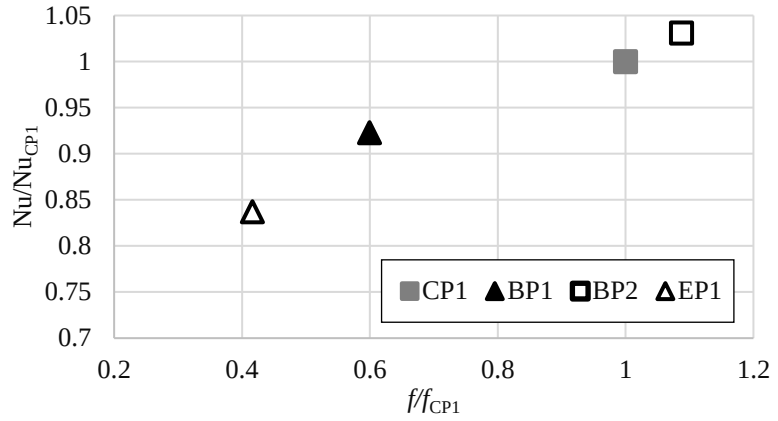

Figure 4.24 Channel average Nusselt number vs friction factor for Re = 2,700

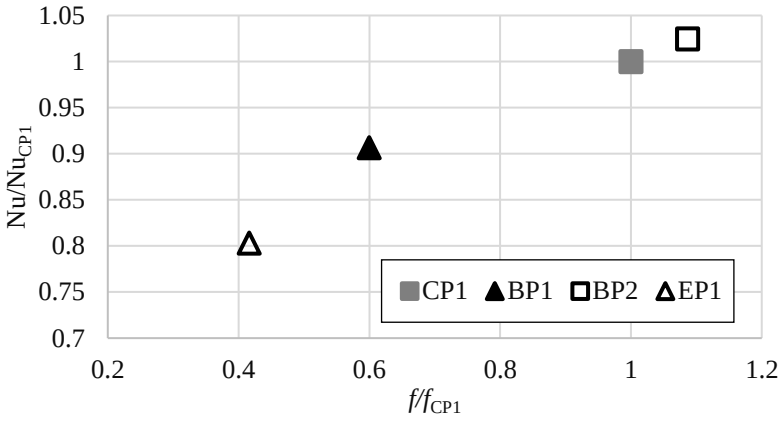

Figure 4.25 Endwall average Nusselt number vs friction factor for Re = 2,700

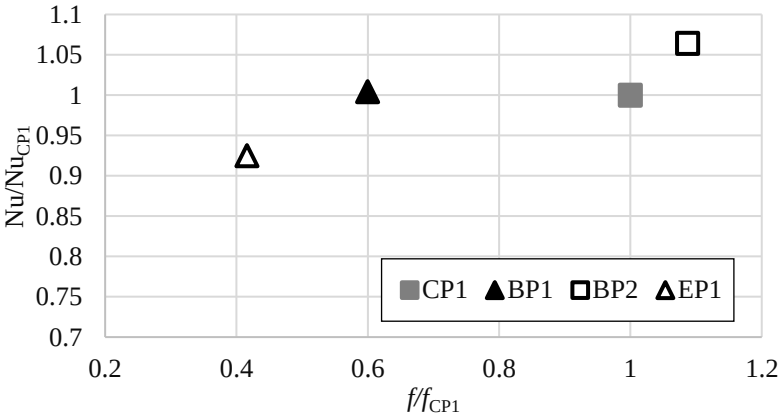

Figure 4.26 Pin surface average Nusselt number vs friction factor for Re = 2,700

Since the Nusselt number and friction factor are normalized with respect to CP1, any data point above CP1 in the y axis means it performs well in heat transfer and any data point to the left of CP1 in the x axis means it performs well in pressure drop.

From Figure 4.25 we can see that the bio pin BP1 in comparison to CP1 performs well in terms of friction factor by 40% and has a deficit in heat transfer performance by 9%. The same pin BP1 in comparison to EP1 has 14% increase in heat transfer performance and 43% decrease in friction factor performance. For BP2, in comparison to CP1 has 2% increase in heat transfer performance and 10% decrease in friction factor performance. The elliptical pin EP1 in comparison to CP1 has 58% increase in friction factor performance and 20% decrease in heat transfer performance.

As seen in endwall Nusselt number results the pin BP2 has an enhancement in heat transfer in the wake region, due to complex flow structures in the wake combined with lower momentum in the flow. BP1 occasionally outperforms CP1 mostly behind pin 2 and 4, but performs immensely better in pressure drop due to the elliptical cross sections combined with the undulations which reduces the magnitude of the wake.

From Figure 4.26, we can see that the bio pins BP1 and BP2 outperforms CP1 and EP1 in terms of thermo-hydrodynamic aspect due to reasons discussed in the pin surface average Nusselt number results. BP1 performs 40% better in terms of pressure drop while maintain the same heat transfer performance as CP1. In terms of channel average data as seen in Figure 4.24, the results are mostly similar to Figure 4.25, as the gains seen in pin surface Nusselt number are significantly less impactful when the surface area of the end wall constitutes greater to the average. Figure 4.27 – Figure 4.29 shows the result for the three categories for Re of 5,200.

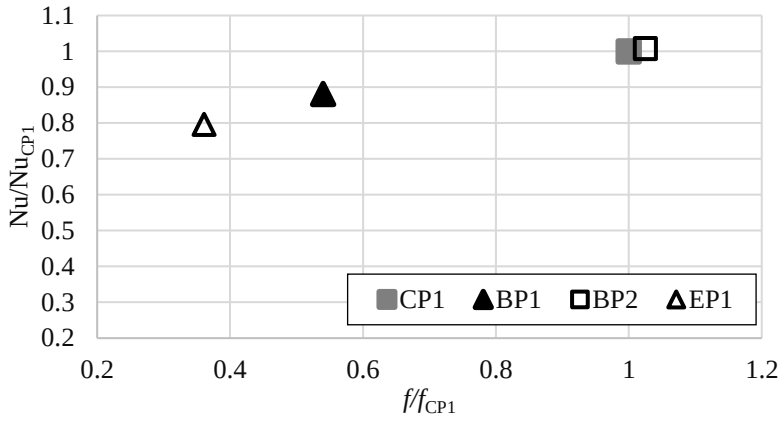

Figure 4.27 Channel average Nusselt number vs friction factor for Re = 5,200

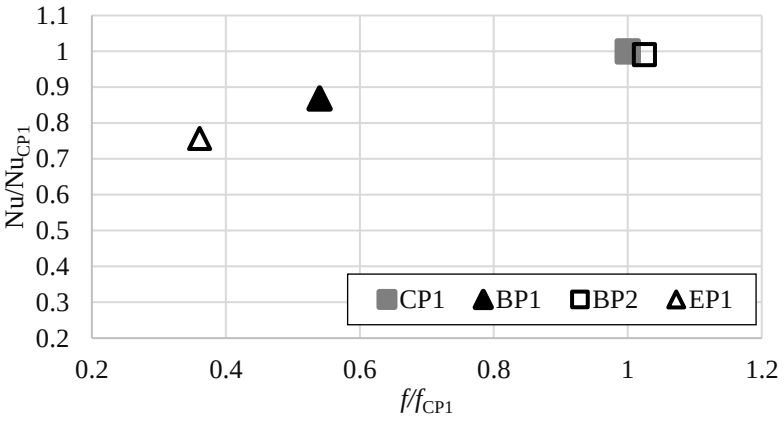

Figure 4.28 Endwall average Nusselt number vs friction factor for Re = 5,200

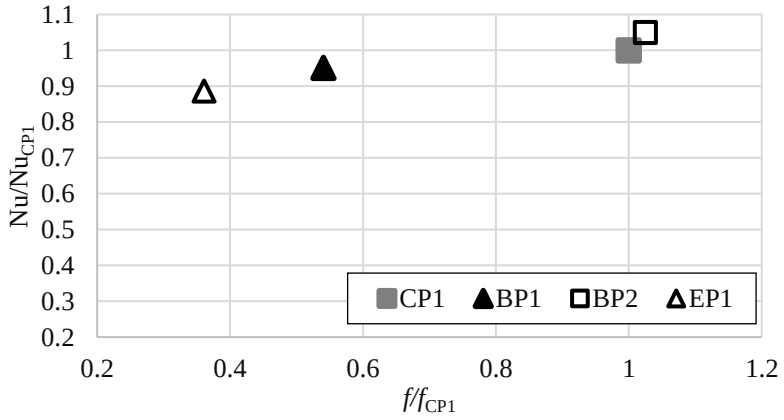

Figure 4.29 Pin surface average Nusselt number vs friction factor for Re = 5,200

From Figure 4.27 – Figure 4.29, we see that in comparison to lower Reynolds number case there is shift in performance, about 5% decrease in heat transfer and 6% improvement in friction factor. This can be seen for all pins and for all categories. Since the data is normalized with results from CP1, it is understood that as the momentum of the flow is increased the cylindrical pin CP1 have more pronounced periodic wake shedding which contributes to greater enhancement in heat transfer at the cost of increase in pressure drop.

Whereas the bio pins BP1 and BP2 don't have an large increase in heat transfer as the momentum of the flow is increased, in comparison to CP1, but there is an improvement in friction factor, this suggest that the complex wake structure still retains its form even in high Reynolds number cases and contributes to reduction in pressure loss.

Pin EP1 has the same trend as seen in other pins, since this pin is more aerodynamic than other pins it does improve in friction factor in comparison to CP1, but the periodic wake shedding is not as pronounced as seen in CP1, which leads to the reduction in heat transfer.

The same trend can be seen for a higher Reynolds number case of 15,500 with the only difference that the magnitude increase in friction factor and decrease in heat transfer performance becomes less prominent in comparison to the Reynolds number case of 5,200. This suggest that, if the Reynolds number is further increased the magnitude shift in performance will eventually become stagnant. Figure 4.30 – Figure 4.32 shows the result for the three categories for Re of 15,500.

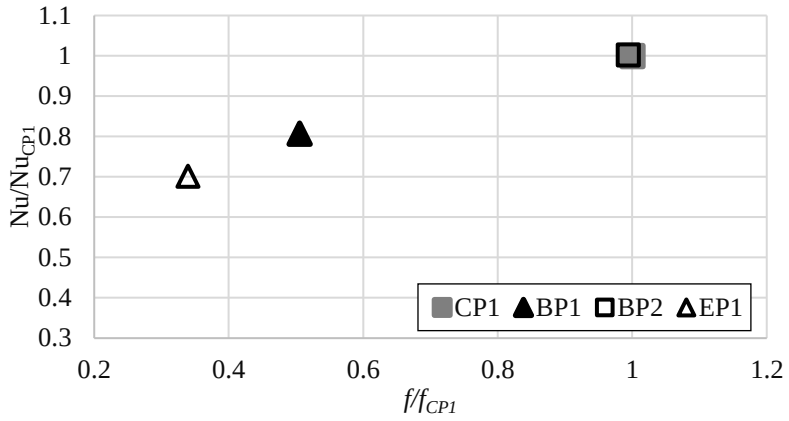

Figure 4.30 Channel average Nusselt number vs friction factor for Re = 15,500

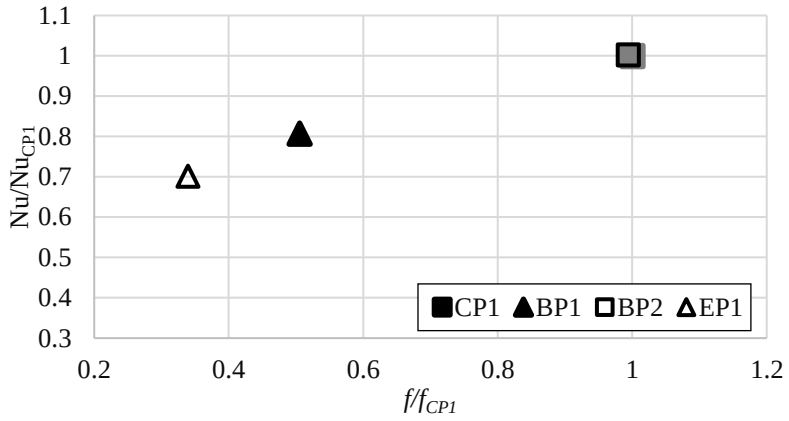

Figure 4.31 Endwall average Nusselt number vs friction factor for Re = 15,500

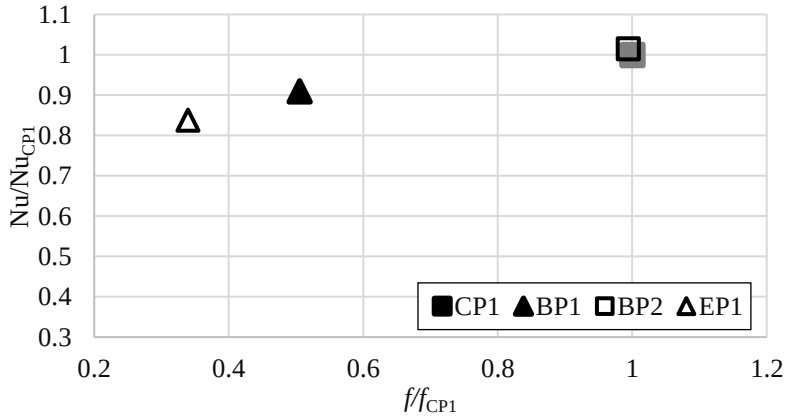

Figure 4.32 Pin surface average Nusselt number vs friction factor for Re = 15,500

4.1.6.Turbulent Kinetic Energy

Turbulent kinetic energy data are obtained from averaging data in a plane between each row of pins at a solution time of 3 seconds. The TKE data is normalized with respect to inlet velocity squared. Figure 4.33 – Figure 4.35 represents the TKE data across the channel for Reynolds numbers of 2,700, 5,200 and 15,500.

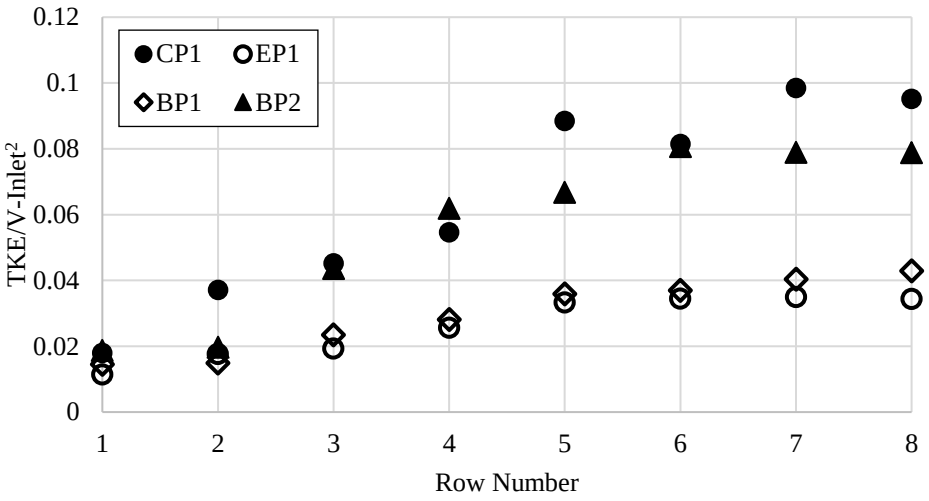

Figure 4.33 TKE along the channel for Re = 2,700

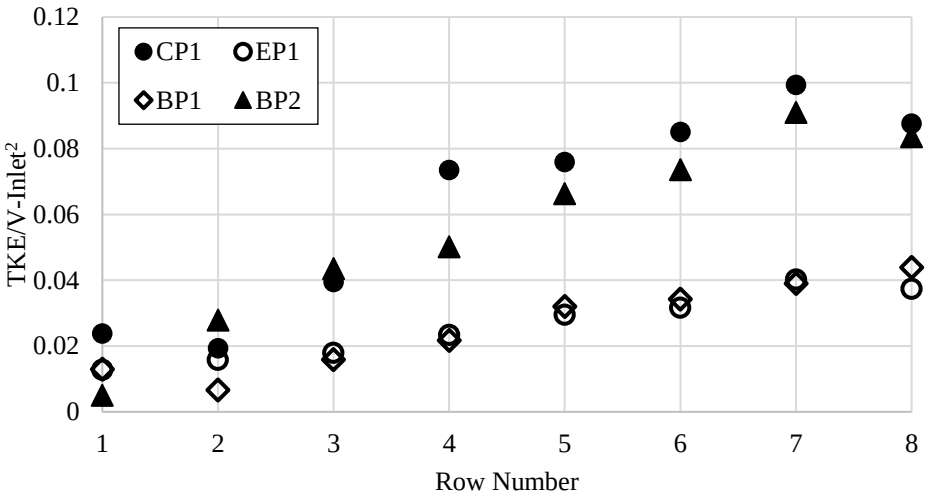

Figure 4.34 TKE along the channel for Re = 5,200

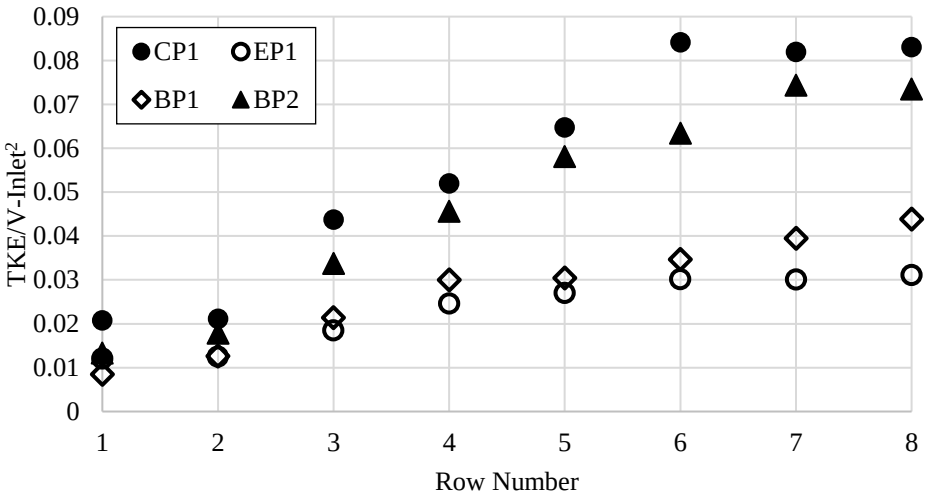

Figure 4.35 TKE along the channel for Re = 15,500

From these figures it is clear that the turbulence created by the cylindrical pin CP1 in a channel is the more predominant in comparison to other pins. Since BP2 is a bio pin of cylindrical nature it is comes second to CP1. Comparing EP1 and BP1, since they are both elliptical in nature, it is evident that BP1 contributes to less turbulence in the channel than EP1. Figure 4.36 – Figure 4.38 looks at TKE data behind row 1 and row 5 in the axial direction. The data is collected 0.023 m behind from the pin center.

In Figure 4.36 at row 1 it is seen that all the pins have the same TKE value, this suggest that the velocity is not adequate enough for the first row of pins to have vortex shedding, the wake created by the pins are held in a recirculation region and doesn't undergo vortex shedding. But as the flow gets accelerated in between the pins and also due to the turbulence mixing downstream of the channel, the pins in the subsequent rows undergo wake shedding as seen in Figure 4.36 at row 5. The magnitude of the wake in the axial direction is larger in CP1, followed by BP2, BP1 and finally EP1, as seen in the pressure drop and the TKE data in the previous sections.

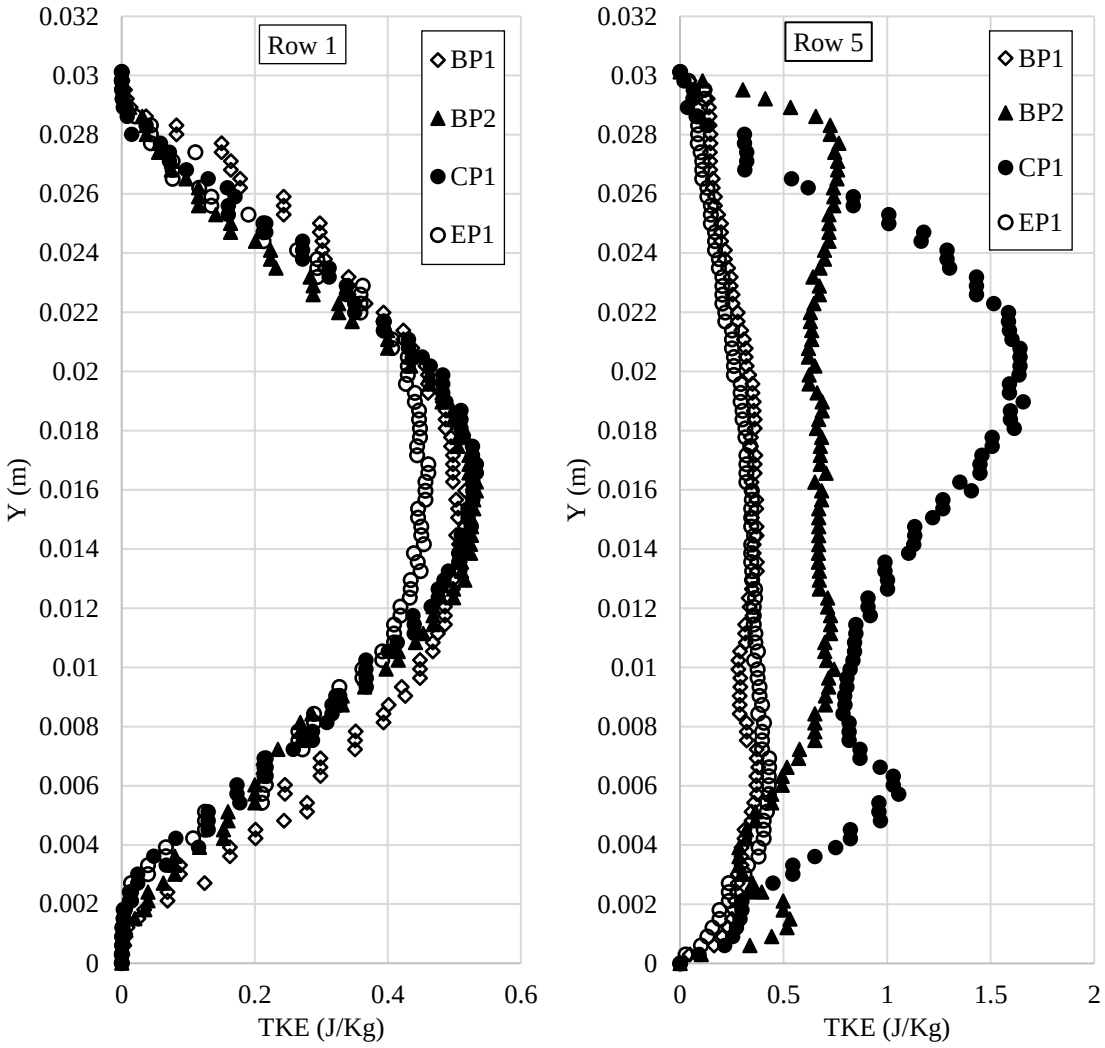

Figure 4.36 TKE – axial direction for Re = 2,700

In Figure 4.37 for row 1 pin, it is seen that for a Reynolds number of 5,200 the result for CP1 is the same as seen in the previous Reynolds number case. But for the bio pins we can see the presence of the undulations create a wake structure which is undulated in the axial direction mimicking the peak and the valley in the pin structure. Having less wake strength in the core flow as seen in the undulated wake promotes less total pressure loss, but still the endwall interaction remains the same as seen with the other pin structures leading to the same endwall Nusselt number performance as seen in other pins.

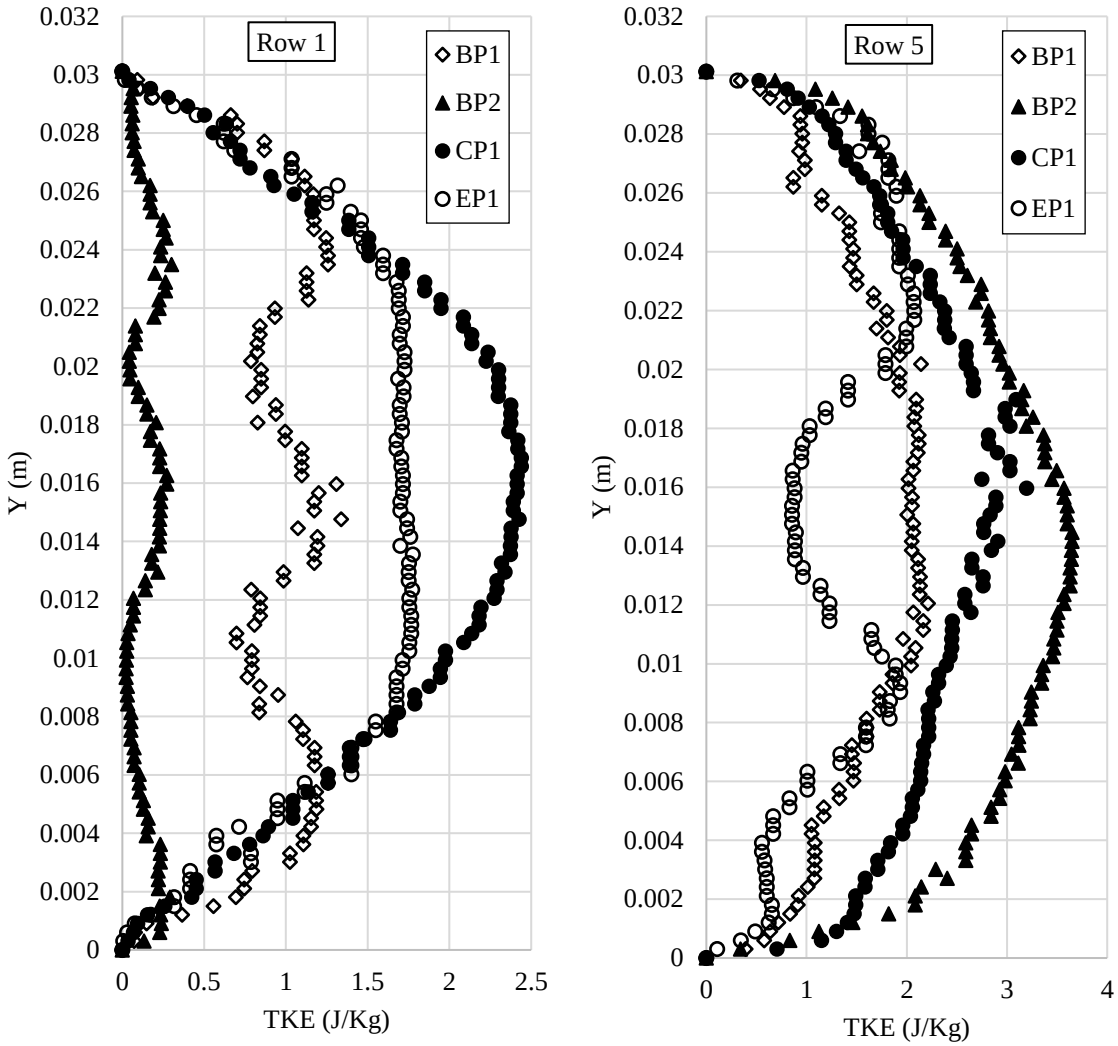

Figure 4.37 TKE – axial direction for Re = 5,200

For row 5 pin we can see that the TKE is higher near the endwall for pin BP2 suggesting an enhancement in the endwall Nusselt number which can also be seen in the endwall Nusselt number results in Figure 4.3, but this enhancement is at the cost of having an higher magnitude in turbulence intensity at the core flow of the wake, which might contribute to the pressure loss.

BP2 has the lowest turbulence levels in core region behind row 1, which can also be seen in Figure 4.34 suggesting that the presence of the undulations decrease the

magnitude of the wake in the axial and also in the streamwise direction due to added vorticity component by the presence of the undulation as seen in literature. For higher Reynolds number of 15,500 as seen in Figure 4.38, we can see that the pins with circular cross sections (BP2 and CP1) have a larger magnitude in the wake in comparison to pin with elliptical cross section (BP1 and EP1).

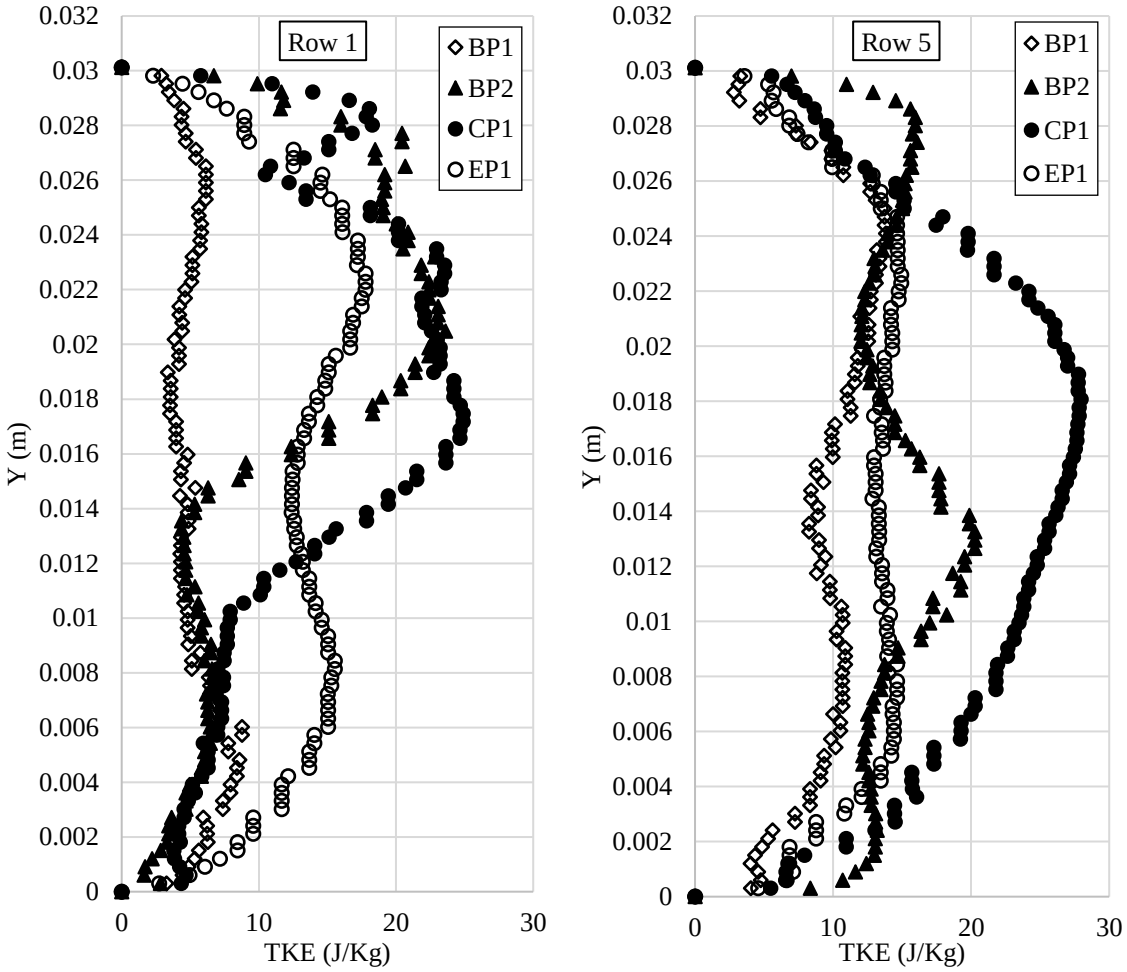

Figure 4.38 TKE – axial direction for Re = 15,500

At row 1, with respect to core flow to end wall interaction we can see that the pin CP1 and BP1 has higher turbulence level near the end wall this would enhance the heat

transfer at wake region of the endwall as seen in Figure 4.4. Figure 4.39 and Figure 4.40 represents the TKE values in the spanwise direction 0.023 m behind the pin center for row1 and row 5.

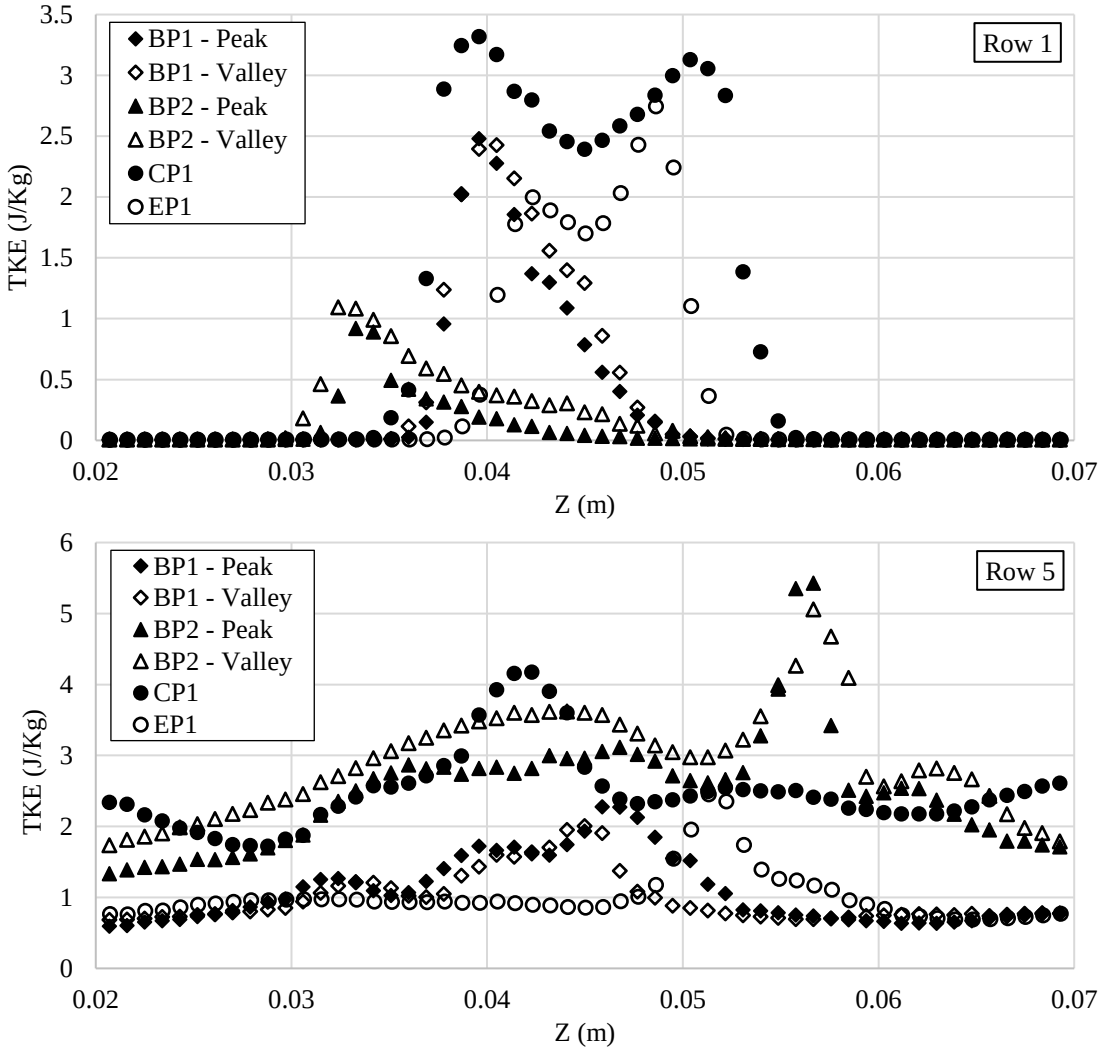

Figure 4.39 TKE – spanwise direction for Re = 5,200

From both figures we can see that pin CP1 and EP1 has a wider wake behind row 1. The wake structure created by the peak and valley section of the pins are same in structure while valley section of the wake is larger in magnitude behind both row 1 and 5.

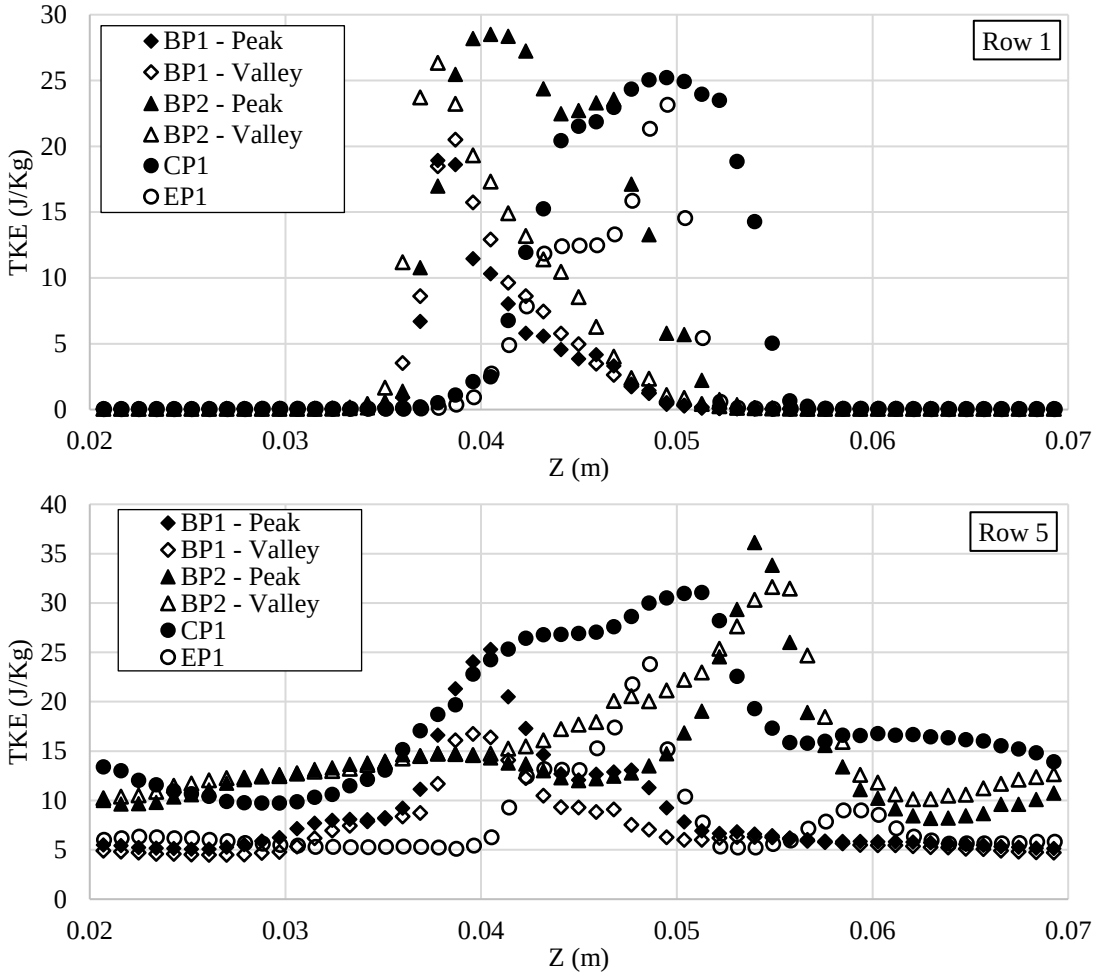

Figure 4.40 TKE – spanwise direction for Re = 15,500

The wake structure in the spanwise direction combined with the axial direction shows us that the magnitude of the wake created behind row 5 by CP1 is larger followed by BP1, BP2 and finally EP1, which can also be seen in the pressure drop and TKE results. This suggest that the aero-thermal performance of the bio pins which are seen in row 1 are washed out in the subsequent rows downstream due to turbulence mixing. Figure 4.41 – Figure 4.48 represents the contour plot of instantaneous (taken at 3 seconds solution time) TKE and vorticity for all the pins, for the sake of brevity only Reynolds number of 15,500 is shown.

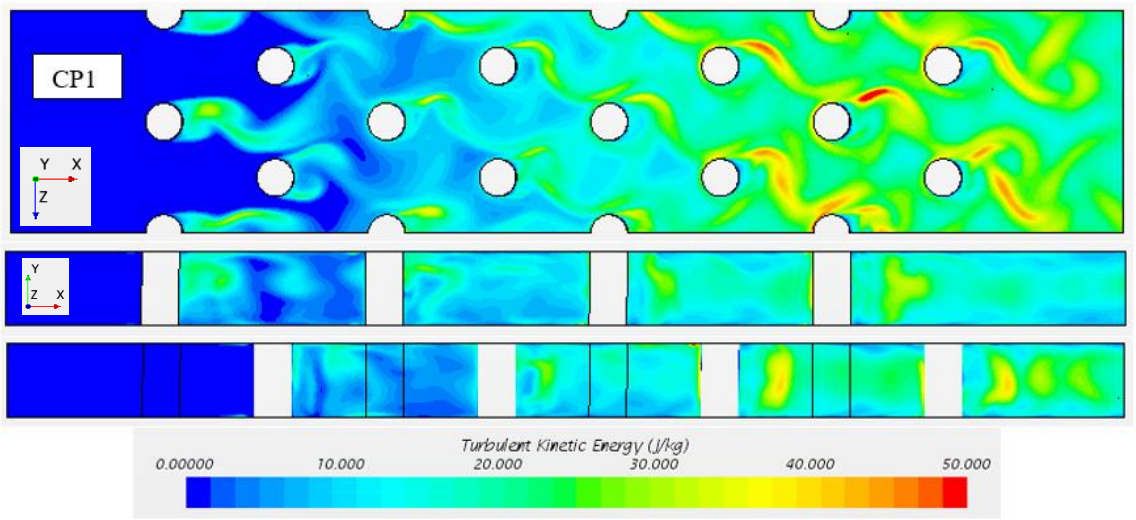

Figure 4.41 CP1 – TKE contour for Re = 15,500

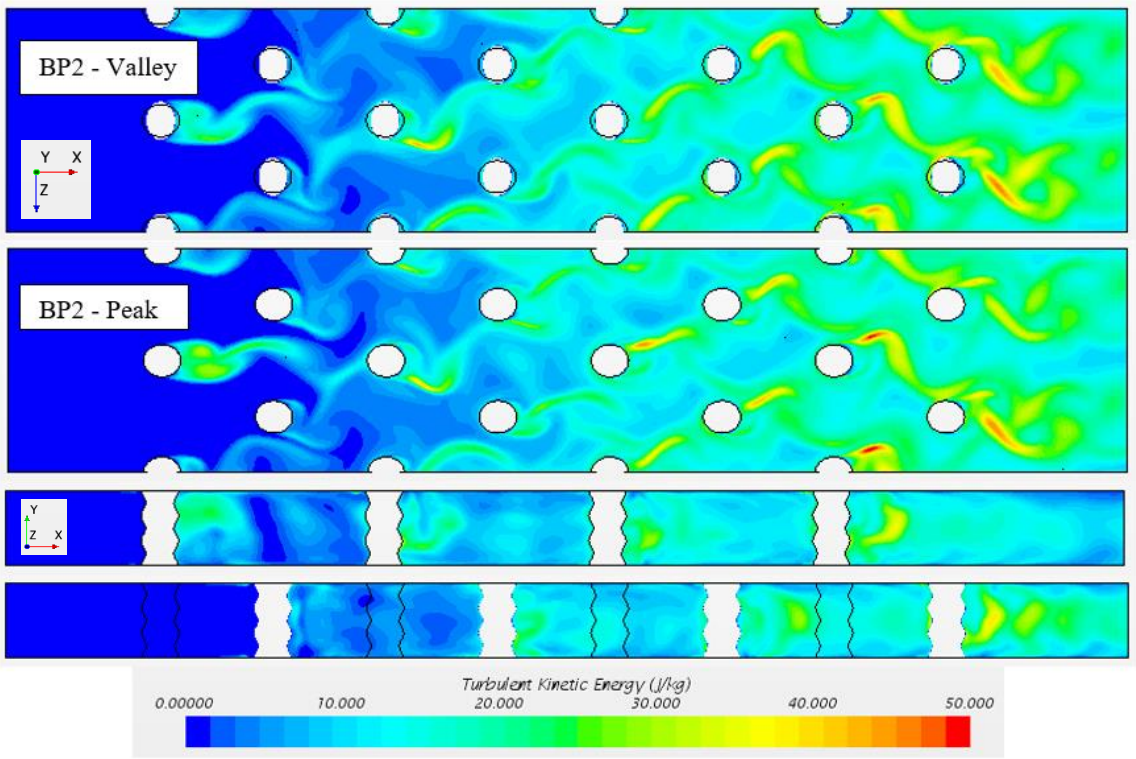

Figure 4.42 BP2 – TKE contour for Re = 15,500

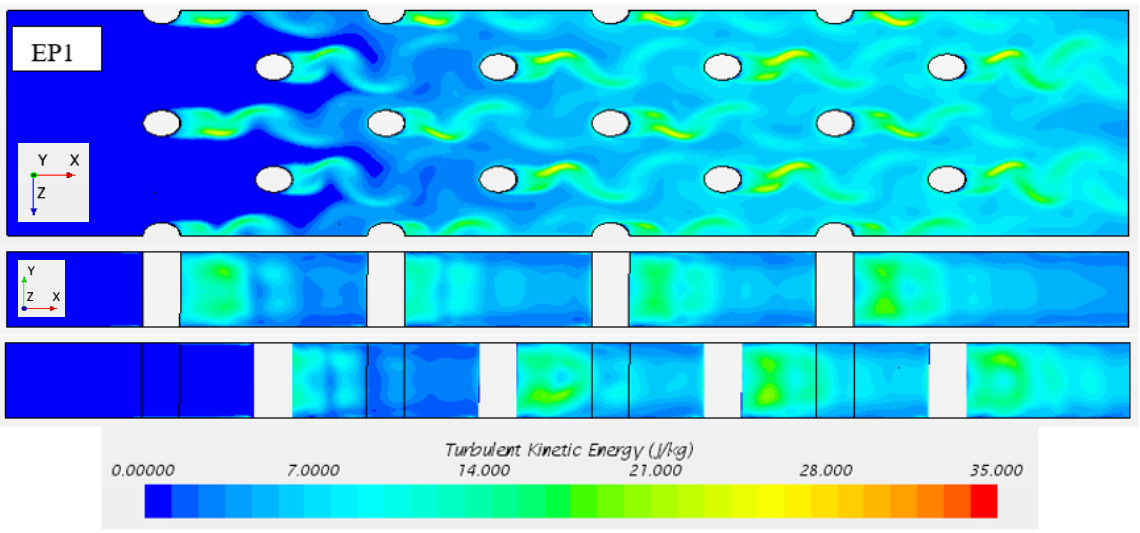

Figure 4.43 EP1 – TKE contour for Re = 15,500

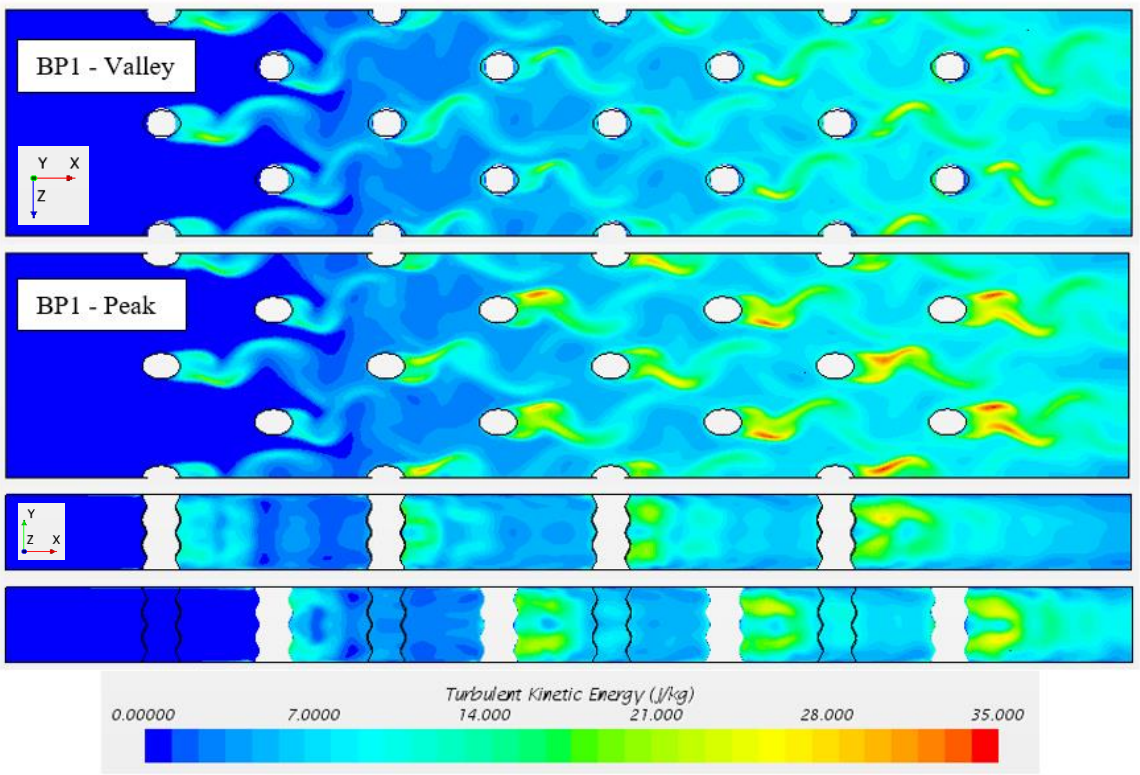

Figure 4.44 BP1 – TKE contour for Re = 15,500

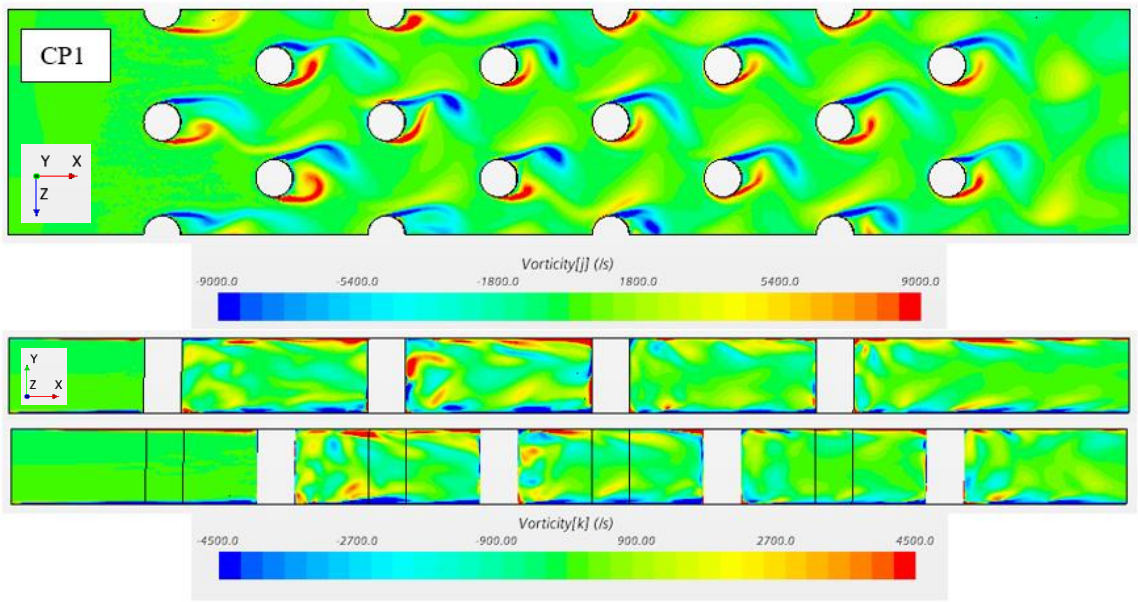

Figure 4.45 CP1 – Vorticity contour for Re = 15,500

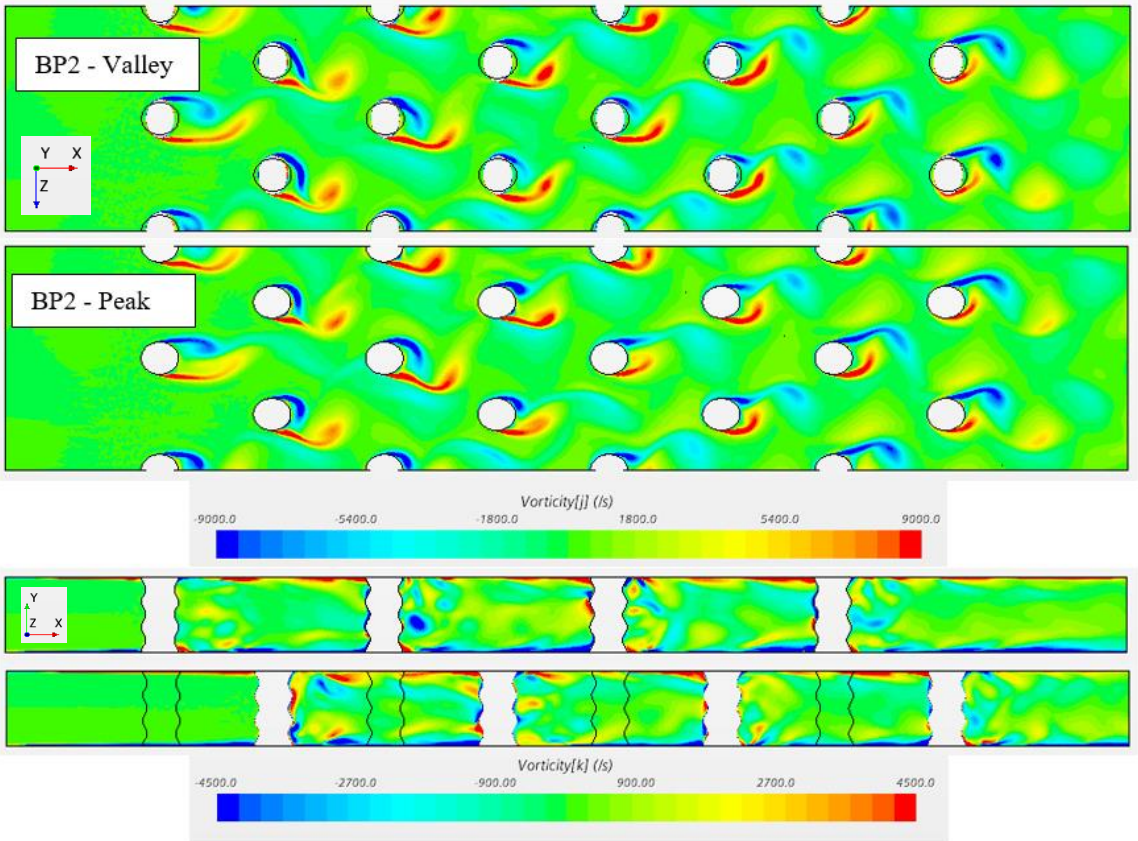

Figure 4.46 BP2 – Vorticity contour for Re = 15,500

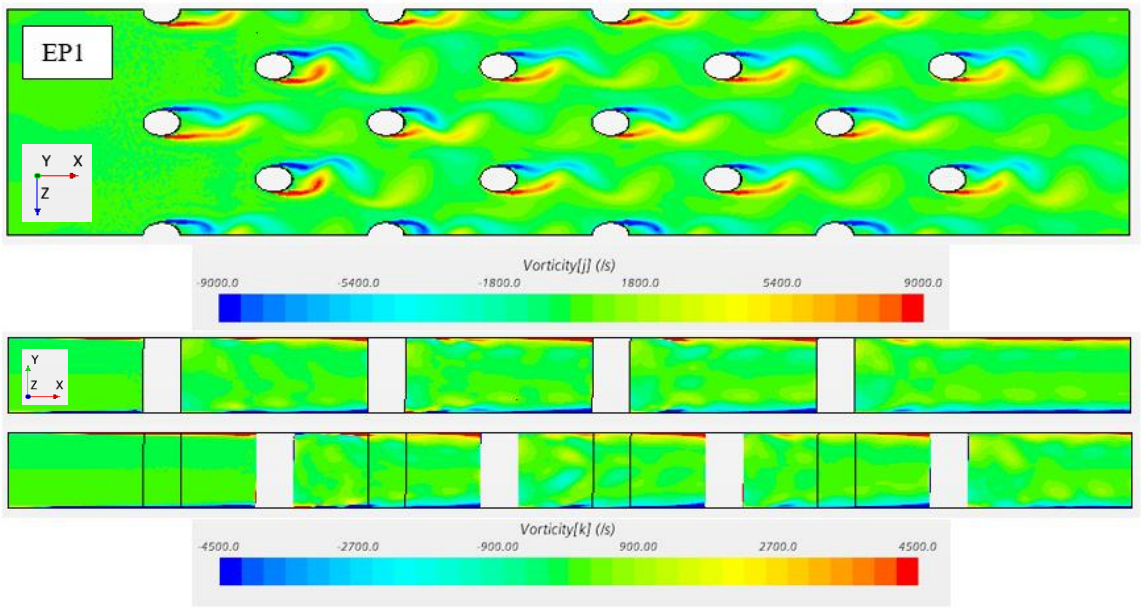

Figure 4.47 EP1 – Vorticity contour for Re = 15,500

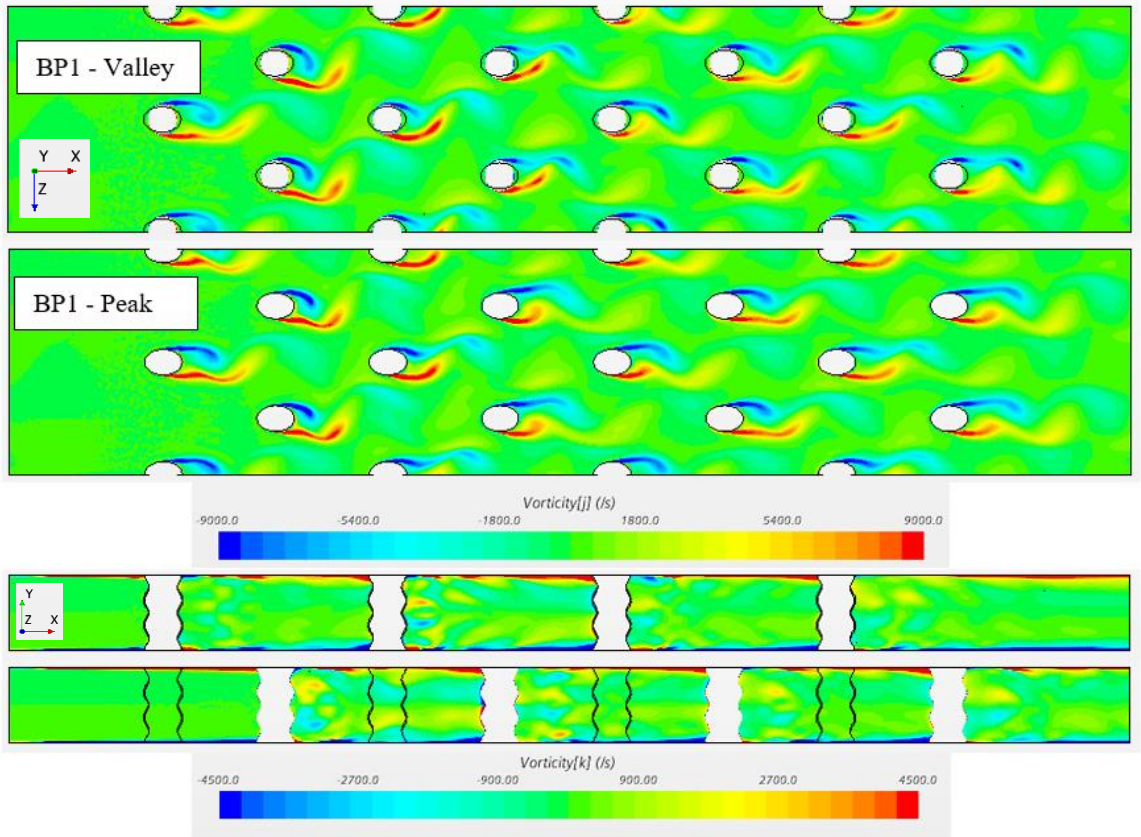

Figure 4.48 BP1 – Vorticity contour for Re = 15,500

In the vorticity contour the right side of the contour bar represents anticlockwise rotation and the left side of the contour bar represents clockwise rotation. From the contour plots we can see that the bio pins BP1 and BP2 does create wake shedding as supposed to breaking down the wake seen in literature. This could be due to the fact that the pins are heavily undulated as supposed to the natural design of the whisker geometry. Due to these heavy undulations the structure of the pin behaves more like a cylinder and ellipse at different cross section locations. But having these undulation does contribute to the reduction in pressure loss does attest to the fact that these undulation does reduce the magnitude of the wake as seen BP2 and BP1 when compared with CP1.

4.1.7. Spectral Analysis

The pressure data is obtained in time at a point in the domain center 22.5 mm behind rows 1, 3 and 5. The simulation was run for 3 seconds and the data used was the last 2 seconds at 5000 samples a second. The amplitude spectrum of the pressure fluctuations is then plotted with frequency for a Reynolds number case of 5,200. For the sake of brevity only one Reynolds number case number is discussed. Plotting the pressure fluctuations will give two dominant frequencies for the pin, one related to the drag and the other related to the lift. The frequency for the drag will be twice that of the lift.

From Figure 4.49 – Figure 4.51 we can see that behind row 1 for pin CP1 there are two dominant frequency, 100 Hz for lift and 200 Hz for Drag and its respective harmonics. The amplitude for these frequencies is smaller in comparison to row 3 and 5 suggesting that there is no presence of wake shedding, which was also seen in TKE results discussion, also depending on the length of recirculation zone the amplitude of lift and drag frequency would higher or lower in comparison to each other.

For BP2 we can see a dominant frequency of 200 Hz behind row 1 and a frequency of 100 Hz at a smaller amplitude corresponding to lift, suggesting that the presence of the undulations does reduce the lift forces as mentioned in the literature. The amplitude of 200 Hz is higher in comparison to CP1, since as seen from previous results there is a presence of wake shedding in BP2.

For row 1 elliptical pin EP1, two frequencies 149 Hz (for lift) and 295 Hz (for drag) can be seen. The amplitude of these frequencies is small compared to other pins suggesting a smaller wake size and subsequent reduction in pressure due to instabilities in the wake.

For BP1 we see 117 Hz frequency due to lift and 234 Hz frequency due to drag. The amplitude is larger in comparison to EP1 and smaller in comparisons to BP2 which fits the trend in pressure drop results seen previously.

The Lift frequency corresponds to vortex induced vibrations, lower the frequency lower the vortex induced vibrations. The frequency for drag relates to the drag created by the pin structure and corresponds to the pressure loss due to the instabilities in the wake. From the data in Row 1 we can see that the frequency for lift is lower for all the pins except for BP2, the drag is higher in BP2 in comparison to other pins, which corresponds to the pressure data seen before.

In subsequent rows 3 and 5, we can see based on the amplitude of pressure fluctuations the bio pins BP1 and BP2 in comparison to CP1 does have a reduction in wake size and hence contribute to reduction in turbulent mixing downstream of the channel, which is also seen in previous results.

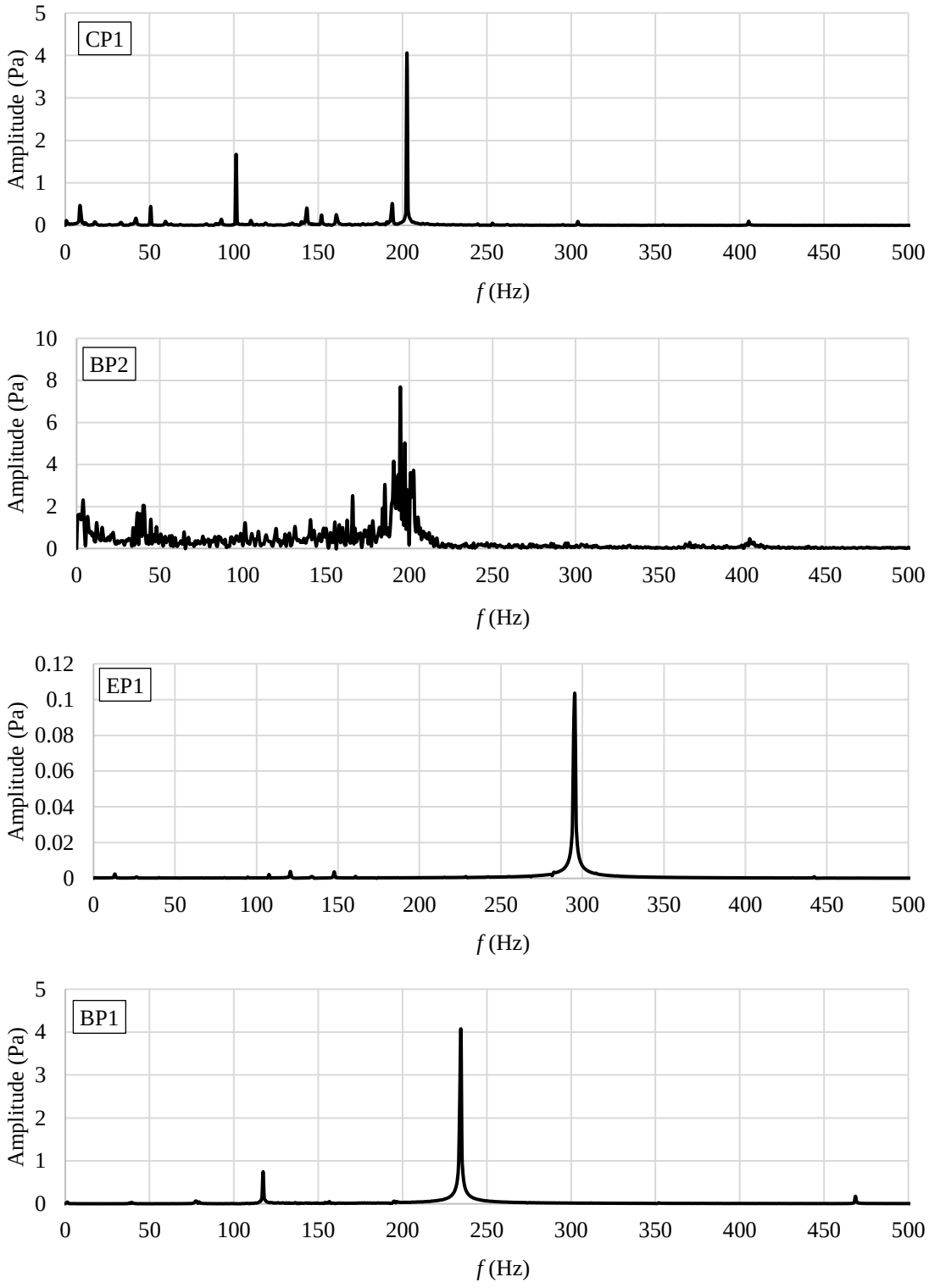

Figure 4.49 PSD: Row 1 for Re = 5,200

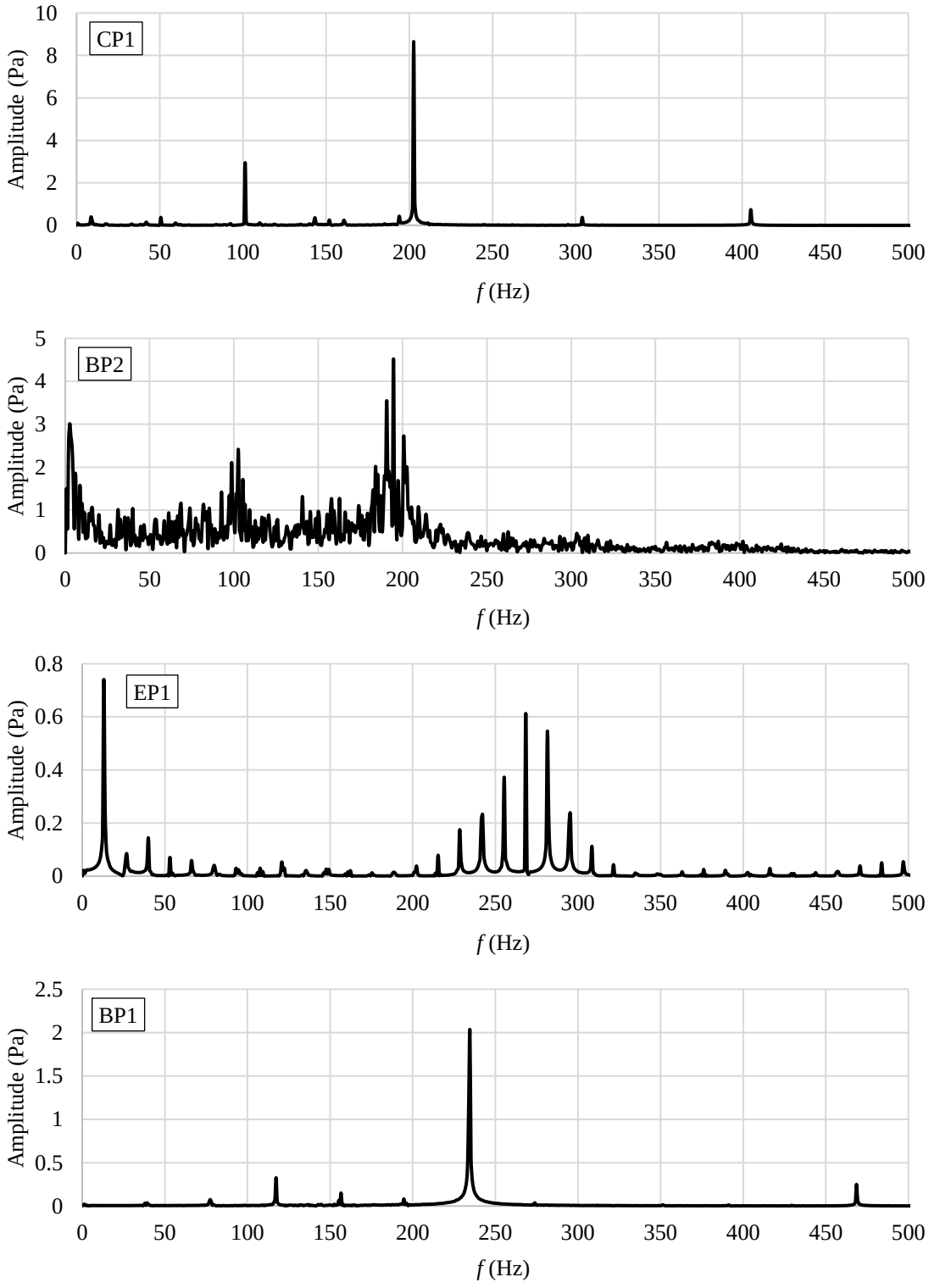

Figure 4.50 PSD: Row 3 for Re = 5,200

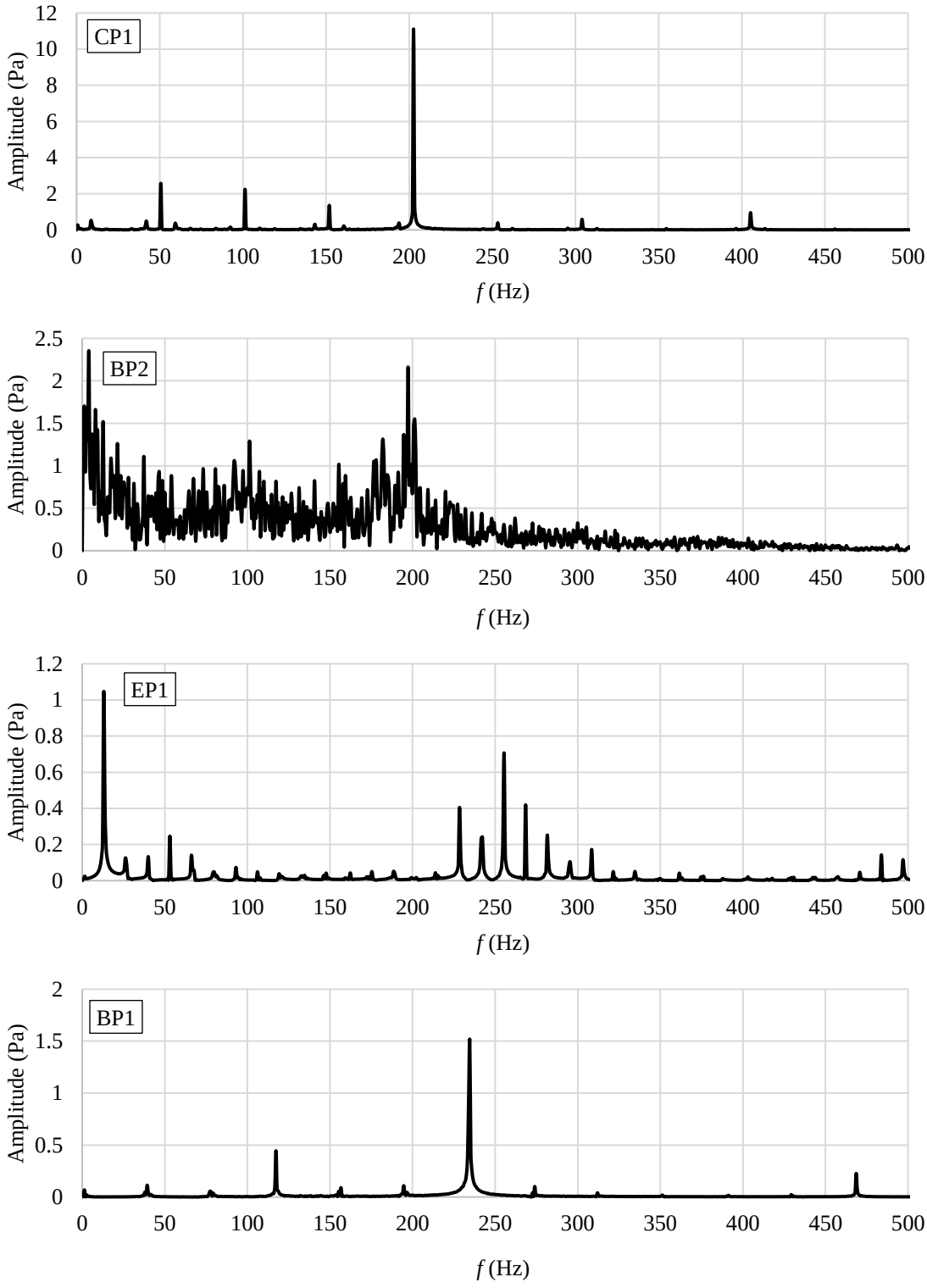

Figure 4.51 PSD: Row 5 for Re = 5,200

4.2. Computational study – Final pin design

As seen from the results in the initial pin design the presence of heavy undulation on the pin surface leads to periodic wake instabilities as supposed to non-periodic broken down complex structured wake seen in literature. Whereas if we look upon a harbor seal whisker the undulations are subdued, hence the final pin design is an exact replica of a scaled up harbor seal whisker structure.

4.2.1. Endwall Nusselt number

Figure 4.52 and Figure 4.53 shows the spanwise average endwall Nusselt number for group 1, 2 and 3 of the final pin design. The Nusselt number data for the pin fin channel are normalized with respect to data from a smooth channel. From Figure 4.52 we can see that G1C is the best performing pin which is also known from literature that cylindrical pins have better performance in terms of endwall heat transfer.

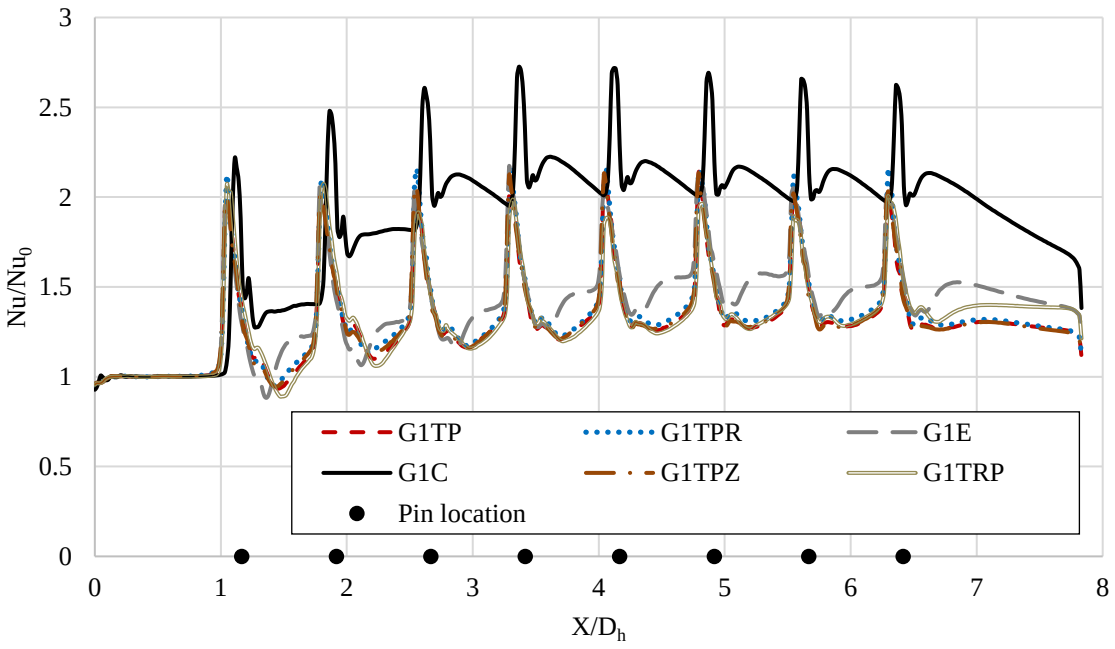

Figure 4.52 Spanwise average endwall Nusselt number for group 1 pins

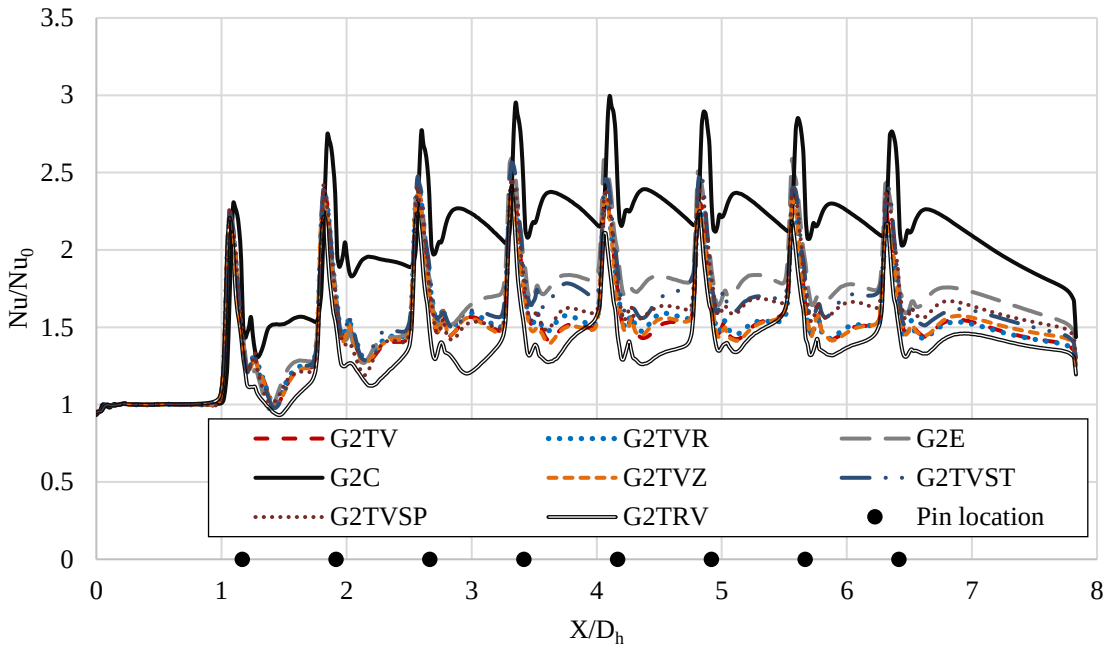

Figure 4.53 Spanwise average endwall Nusselt number for group 2 and 3 pins

A good comparison for the bio pins would be with the elliptical pin G1E due to the similar elliptical cross section in pin shape. The bio pins G1TP, G1TPR and G1TPZ has identical endwall heat transfer performance. Pin G1TRP has a similar performance in comparison to other bio pins. This shows that the angle of the undulations has no effect on the endwall performance and also increasing the number of peaks in the pins only increases the Nusselt number in the wake region of the final pin. Pin G1E on comparison to the bio pins have marginally better performance, especially in the wake region of the endwall after each pin. This suggest that the core flow for G1E has a more predominant wake structure which increases the endwall Nusselt number.

In Figure 4.53, again we can see that G2C is the best performing pin. The bio pins G2TV, G2TVR and G2TVZ has identical performance, this again shows that the angle of the undulations has negligible effect on endwall heat transfer. Pin G2TRV in comparison

to other bio pins has a reduction in endwall heat transfer by ~ 14 %. Pin G2E on comparison to the bio pins have better performance in the wake region of the endwall after third row of pins, with a maximum difference of ~23 % in heat transfer. Pin G2TVST and G2TVSP has a similar endwall heat transfer performance. In comparison to pin G2TV, they have better endwall heat transfer from row 4, with an average difference of ~11 – 13%. This suggest that removing the undulation on at least one of the pin directions increases the size of the wake leading to an increase in endwall heat transfer.

4.2.2. Pin Surface Average Nusselt number

Figure 4.54 and Figure 4.55 shows the pin surface average endwall Nusselt number for group 1, 2 and 3 of the final pin design. The pin surface average Nusselt number are averaged across the rows and normalized to get Frossling number.

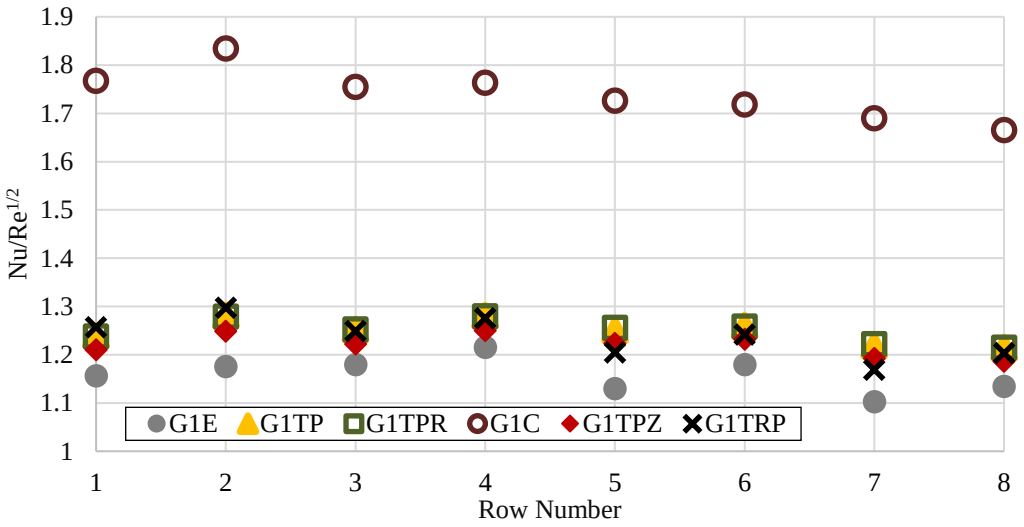

Figure 4.54 Group 1: Row average Nusselt number

In Figure 4.54, we can see that G1C is the best performing pin which is also known from literature that cylindrical pins have better performance in terms of heat transfer. The

bio pins G1TP and G1TPR has identical performance, this shows that the orientation of the undulations doesn't affect the surface average Nusselt number. Pin G1TPZ has a marginal decrease in Nusselt number in comparison to G1TP, this shows that the angle of the undulations locally creates a pseudo stagnation region on the side leading to the increase in Nusselt number.

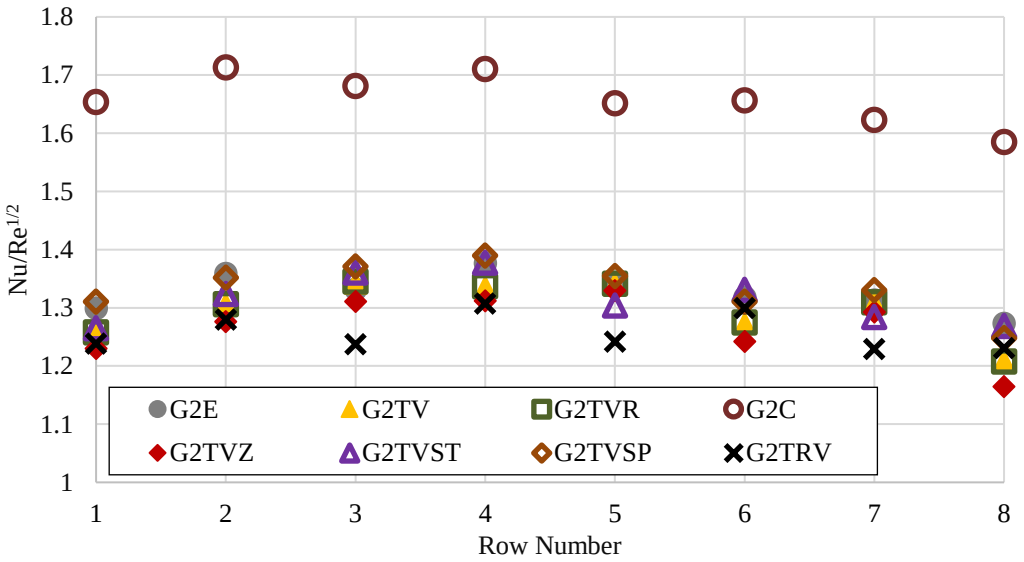

Figure 4.55 Group 2 and 3: Row average Nusselt number

Pin G1TRP has a similar performance in comparison to other bio pins, having one more peak and valley undulations increases the local peaks in the surface contour thereby increase the pin surface average Nusselt number. Pin G1E being the lowest performer in this group, since it has the lowest minor diameter throughout the axial direction which leads to less flow acceleration around the pin circumference.

In Figure 4.55, again we can see that G2C is the best performing pin. The bio pins G2TV and G2TVR has identical performance. Pin G2TVZ has a marginal difference

overall in comparison to G2TV. Pin G2TRV in comparison to other bio pins has a similar performance for rows 1, 2 and 4, marginal difference in rows 6 and 8 and a reduction in heat transfer in rows 3, 5 and 7. In this case the two of the three valley regions are at the wall intersection, this surface pattern seems not ideal for an increment in undulations in the axial direction. Hence this pattern gives the pin overall two valley regions and two peak regions, and as we have seen before the flow acceleration around the peak regions are lower in comparison to the valley regions leading to a reduction in surface average Nusselt number.

Pin G2E in comparison to other bio pins has similar heat transfer in rows 3, 5 and 7 and a marginal increase in rows 1, 2, 4, 6 and 8. As seen from the structure the pin G2E has the largest minor diameter throughout the axial direction leading to better flow acceleration thereby increasing the heat transfer. Pin G2TVST has a similar heat transfer performance in comparison to pin G2TV, with a maximum difference of ~ 4.5 % in rows 6 and 8. Pin G2TVSP which only has the spanwise undulation in comparison to G2TV performs significantly well after row 5 with a maximum increment in heat transfer of 17%. This shows that the undulation in the spanwise direction is more important than the undulation in the streamwise direction for the improvement in heat transfer.

4.2.3. Pressure Drop

A plane section is created 20 mm behind each pin in the channel and the time averaged static pressure in measured in each plane section. The pressure drop is calculated between each plane section from the inlet section. Data in row 1 is the pressure drop between inlet and the plane section behind first row of pins. Similarly row 2 is the pressure drop between plane section behind 2 and inlet section. The pressure drop data is

normalized by the pressure drop data in a smooth channel. Figure 4.56 and Figure 4.57 shows the pressure drop data for group 1, 2 and 3 pins.

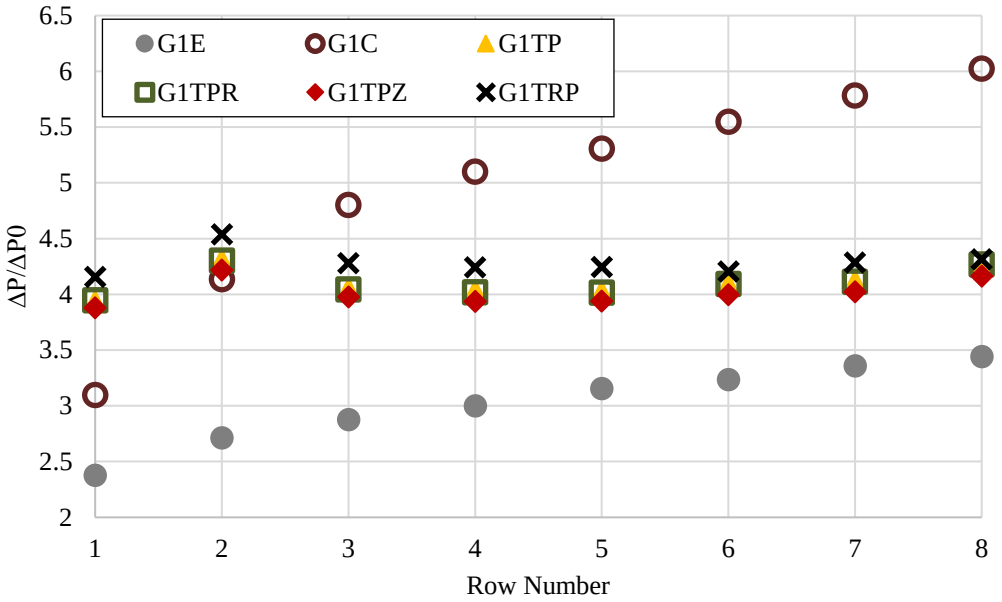

Figure 4.56 Group 1: Pressure drop along the channel

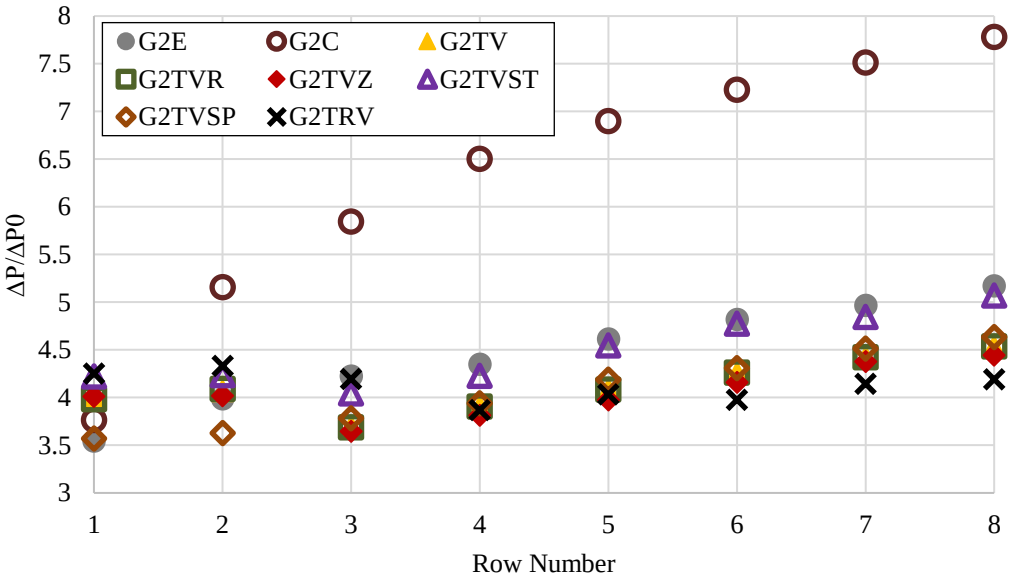

Figure 4.57 Group 2 and 3: Pressure drop along the channel

In Figure 4.56, we can see that G1C is the least performing pin in this group, as documented in literature cylindrical pins are good heat transfer characteristics at the expense of pressure drop. The bio pins G1TP, G1TPR and G1TPZ has identical pressure drop data, which shows that the angle and orientation of the undulations does not affect the pressure drop across the channel.

Pin G1TRP has a marginal increase in pressure drop in comparison to other bio pins, indicating that increasing the number of undulations in the pin apart from what nature intended does not bode to the aerodynamic aspect of the pin design. This could be due to the fact that when the half period between the undulations is decreased the pins structure works more as individual elliptical cross section at local sections of the pin decreasing the effect of the added vorticity component, which is also seen in the initial pin design data. Pin G1E has better performance in comparison to other pins, due to the given fact that this pin has the smallest minor diameter leading to reduction in wake size.

In Figure 4.57, we can see that G2C is the least performing pin. The bio pins G2TV, G2TVR and G2TVZ has identical performance. Pin G2TRV has a marginal increase in pressure drop for the first three rows of pins, identical performance in rows 4 and 5 and reduction in pressure drop in rows 6, 7 and 8. This deviation from the pin in group 1 could be due to the fact that the pin G2TRV overall has 2 valley regions and two peak regions unlike the pin G1TRP which has the two valley regions near the middle of the channel. Having two peak regions in the core flow for pin G2TRV significantly aides in the pressure drop performance due to the slimmer cross sectional area of the peak sections.

G2E has higher pressure drop compared to bio pins since this pin has the largest

minor diameter. The bio pins in comparison to G2E has overall 8 – 10% lower pressure drop. Pin G2TVSP has a similar pressure drop in comparison to pin G2TV, except for rows 1 and 2 which sees a reduction in pressure drop by 16%. Pin G2TVSt in comparison to G2TV has similar pressure drop for rows 1 and 2 and about 8 – 10% increase in pressure drop for rows 3 onwards. This shows that removing the undulation in the spanwise direction increase the pressure drop as the flow moves downstream of the channel.

4.2.4. Thermal Performance

Figure 4.58 – Figure 4.60 shows the average endwall Nusselt number, pin surface average Nusselt number and channel average Nusselt number in comparison to friction factor for group 1 of the final pin design. The Nusselt number and friction factor data for the pin fin channel are normalized with respect to data from a smooth channel, except for pins surface average in that case the Nusselt number is normalized with respect to square root of Reynolds number to get Frossling number.

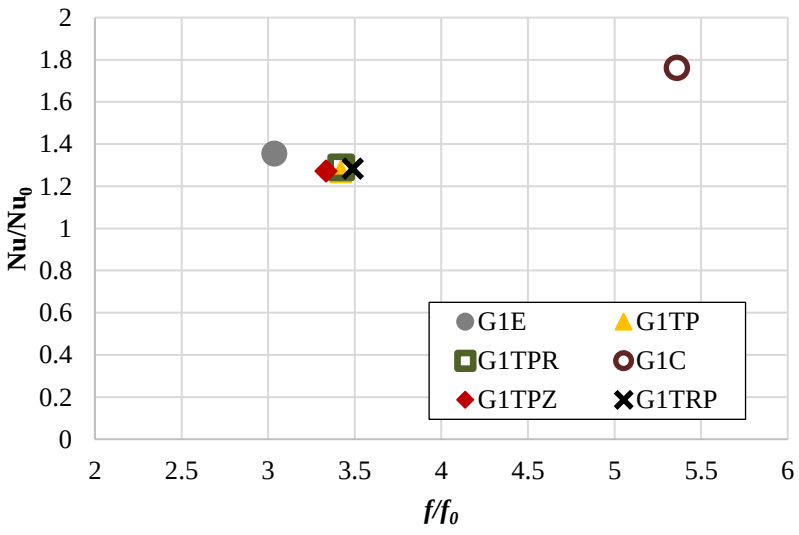

Figure 4.58 Endwall average Nusselt number for Group 1 pins

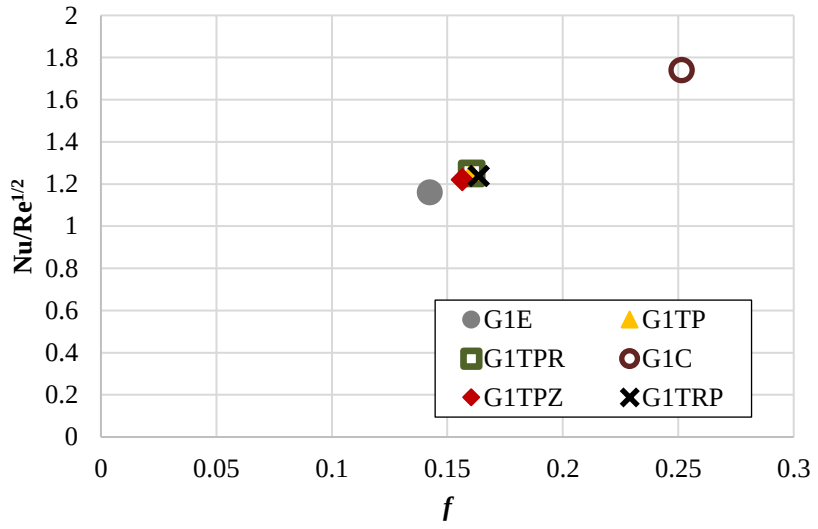

Figure 4.59 Pin surface average Nusselt number for Group 1 pins

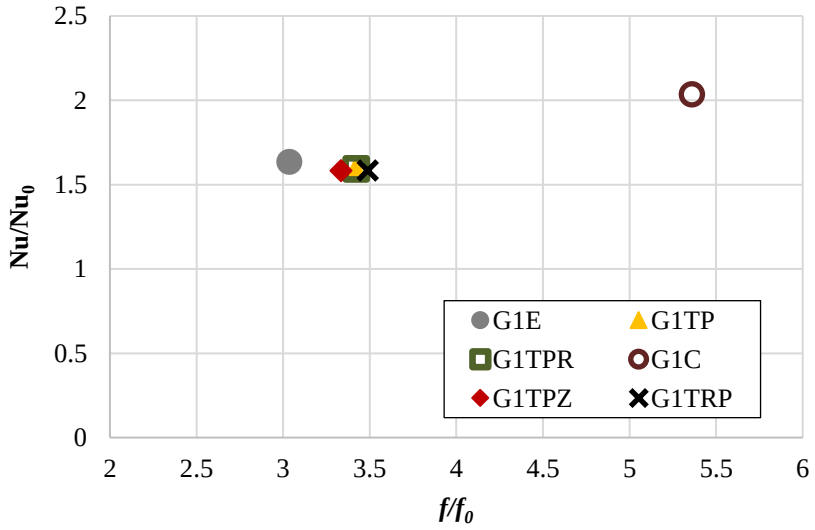

Figure 4.60 Channel average Nusselt number for Group 1 pins

From Figure 4.59, we can see that the presence of the undulations cause an increase in pin surface average Nusselt in comparison to G1E, which was also seen in previous results. As seen before in spanwise average endwall Nusselt number and pressure drop results, we can see in Figure 4.58 that the pin G1E is the best performer in this category

in comparison to bio pins.

In Figure 4.60, we can see pins G1TP and G1TPR have identical performance. Pin G1TPZ has a marginal improvement in friction factor by 0.6% in comparison to G1TP and G1TPR. This again shows that the inclination of the undulation does not affect the performance of the pins. Pin G1TRP has a marginal increase in friction factor on comparison to the other bio pins. Pin G1C is the better performer in terms of heat transfer at the cost of friction factor performance. It can be clearly seen that pin G1E (elliptical pin) is the better performer in this segment when comparing against the bio pins, with an improvement of 9% in friction factor and 3% improvement in heat transfer and in comparison to the G1C, it has an 43% improvement in friction factor at the cost of 19% in heat transfer.

Figure 4.61 – Figure 4.63 shows the average endwall Nusselt number, pin surface average Nusselt number and channel average Nusselt number in comparison to friction factor for group 2 and 3 of the final pin design.

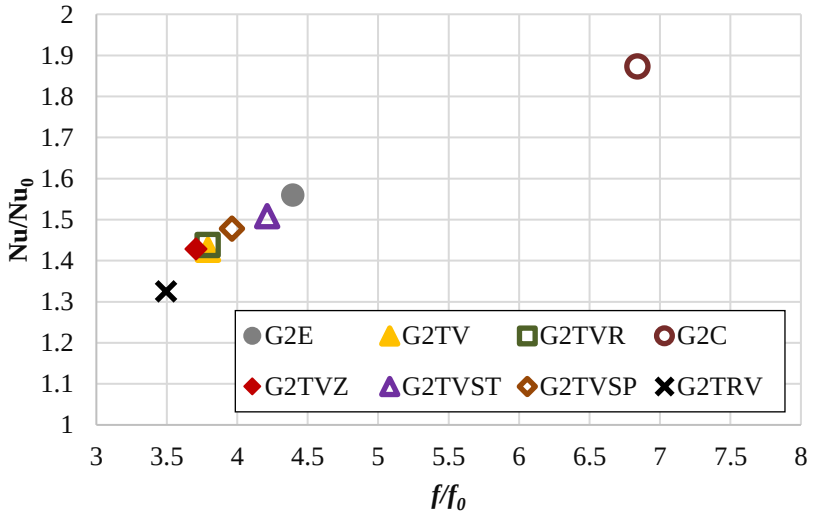

Figure 4.61 Endwall average Nusselt number for Group 2 and 3 pins

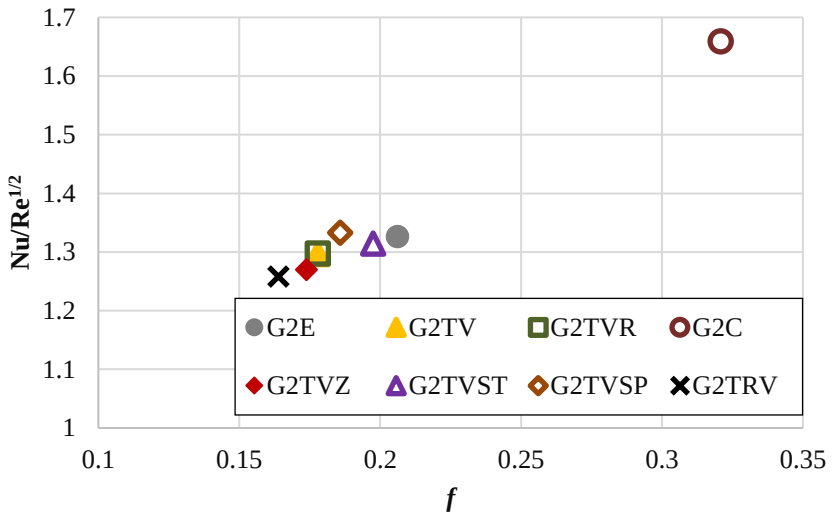

Figure 4.62 Pin surface average Nusselt number for Group 2 and 3 pins

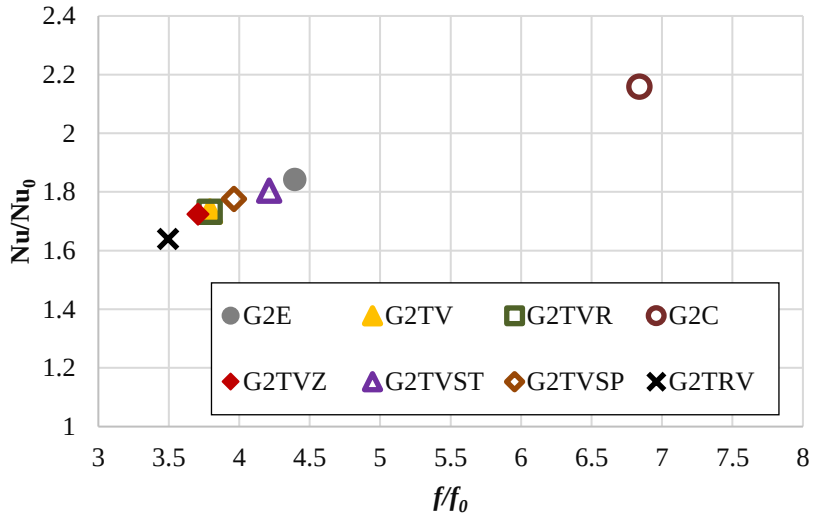

Figure 4.63 Channel average Nusselt number for Group 2 and 3 pins

In Figure 4.62 for pin surface Nusselt number, pin G2TV in comparison to pin G2E has a 14% improvement in friction factor at a cost of about 6% in heat transfer. As discussed before the pin G2E has the maximum minor diameter giving rise to increase in pin surface average Nusselt number. The performance of pin G2TV and G2TVR are

identical, and the pin G2TVZ has a marginal difference in comparison to G2TV and G2TVR, this shows us that the angle and orientation of the undulation doesn't contribute much to the pin surface average Nusselt number. Pin G2TVSP in comparison to G2E has a marginal improvement in heat transfer with a 10% improvement in friction factor, this shows that the spanwise undulation is important in decreasing the pressure drop caused by the pin structure. Pin G2TVSP in comparison to G2E has a similar performance in heat transfer with a marginal improvement in friction factor.

From Figure 4.61 and Figure 4.63 we can see that the results are similar. In Figure 4.63, we can see pins G2TV and G2TVR have identical performance. Pin G2TVZ has a marginal improvement in friction factor in comparison to G2TV and G2TVR. This again shows that the inclination of the undulation does not affect the performance of the pins. Pin G2TRV has a ~6% improvement in friction factor at the cost of 5% decrease in heat transfer on comparison to the G2TV. Pin G2C is the better performer in terms of heat transfer at the cost of friction factor performance. The bio pins G2TV, G2TVR and G2TVZ is the better performer when comparing against G2E, with an improvement of ~15.5 % in friction factor at the cost of 6.5 % in heat transfer and in comparison to G2C, it has a 45 % improvement in friction factor at the cost of 20 % in heat transfer.

The bio pin G2TRV on comparison to G2E has an improvement of ~20.5 % in friction factor at the cost of ~11% in heat transfer and in comparison to G2C, it has a 49 % improvement in friction factor at the cost of 24 % in heat transfer. Pins G2TVST and G2TVSP has similar heat transfer performance with a difference of 4% on comparison to G2TV. G2TVST has an increase in friction factor by 11% on comparison to G2TV. G2TVSP has an increase in friction factor by 4.5% on comparison to G2TV. This shows

that by removing either the spanwise or the streamwise undulation there is a significant increase in pressure drop in the channel.

4.2.5. Turbulent Kinetic Energy Along the Channel

A plane is created 20 mm behind the center of the pins in the channel, and time averaged TKE value is plotted for points behind each row for group 1, 2 and 3 pins. The TKE value is normalized with respect to velocity squared. Figure 4.64 and Figure 4.65 shows the TKE values across the channel for the different group of pins.

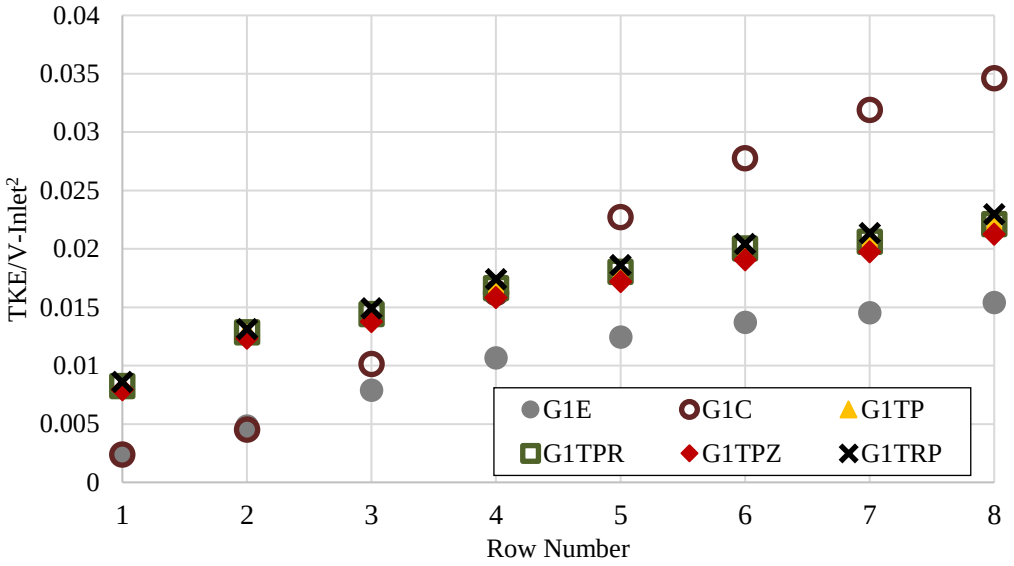

Figure 4.64 TKE – Group 1

From the above figure it can be seen that the group 1 bio pins have a higher turbulence mixing behind the pins in comparison to G1E. This difference in magnitude is similar to the pressure drop results discussed before. Also as discussed before we can see that the angle and orientation of the undulation doesn't affect the performance of the pins.

From Figure 4.65 we can see that the bio pins G2TV, G2TVR and G2TVZ are

identical in performance. As seen in G2TVST and G2TVSP, removing at least one of the undulations increases the turbulence magnitude in the channel. The pin G2TRV, which has more undulation has a marginal increase in turbulence downstream of the pins in the first 3 rows of the channel. As seen in pressure drop results pins G2C and G2E have larger wake with periodic shedding leading to increase in turbulence mixing downstream of the channel.

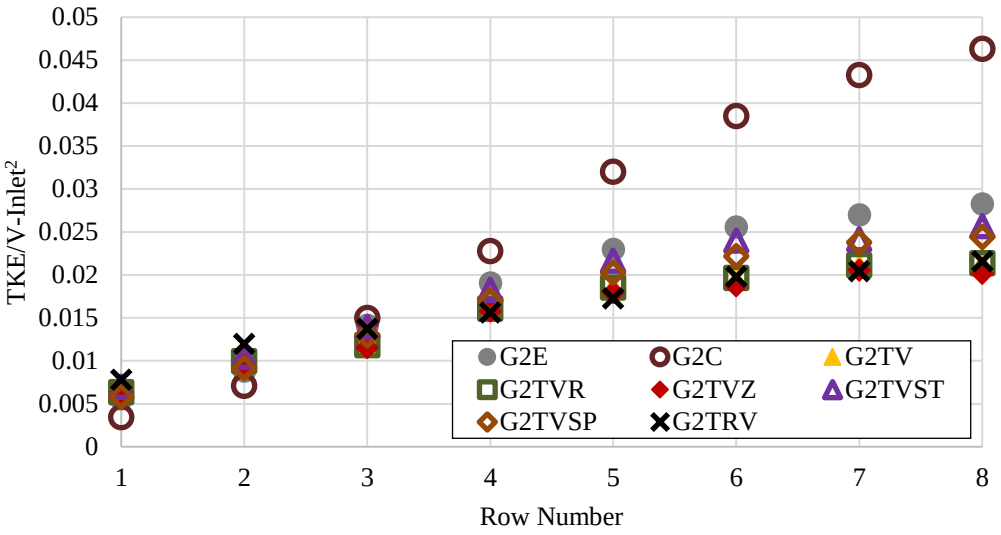

Figure 4.65 TKE – Group 2 and 3

As seen in these results group 2 pins performs well in respective categories in comparison to the pure elliptical pin G2E. Hence from this point onwards for the sake of brevity only pins G2E, G2C, G2TV and G2TRV will be discussed.

4.2.6. Pin Circumferential Data

For the sake of brevity only row 1 and row 5 circumferential data for pin surface Nusselt number, coefficient of pressure and wall shear stress will be discussed. Figure

4.66 – Figure 4.71 represents the above mentioned data for row 1 and row 5 pins for G2E, G2C, G2TV and G2TRV.

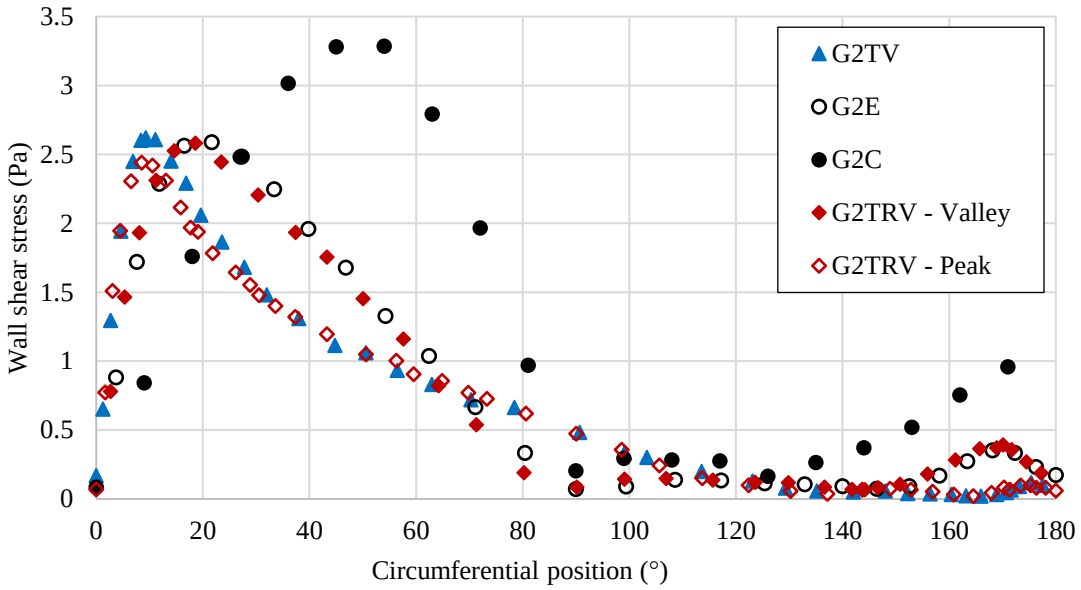

Figure 4.66 Row 1 pin circumferential wall shear stress

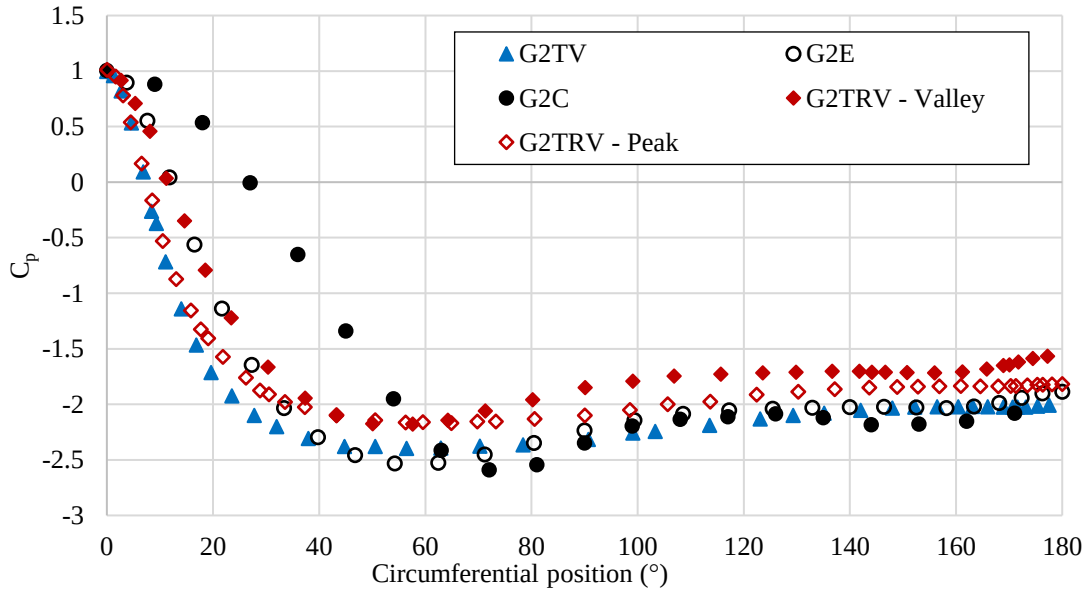

Figure 4.67 Row 1 pin circumferential coefficient of pressure

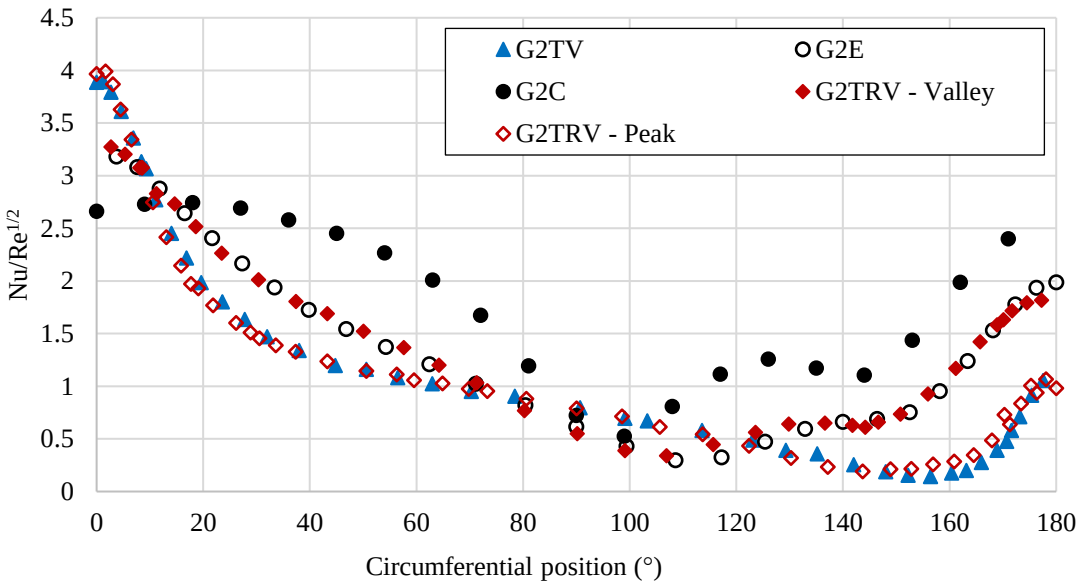

Figure 4.68 Row 1 pin circumferential Frossling number

The pin circumferential data is obtained from a center plane for G2C, G2E and G2TV, the center plane of pin G2TV has the peak ellipse. For pin G2TRV, data from the center plane represents the valley ellipse and since this pin shape contains more undulations another plane is created at the peak ellipse to obtain data.

From Figure 4.66, it is seen from the wall shear stress data that the wall shear stress values for G2TV is similar to G2TRV – peak, since both section have peak ellipse, flow separation can be found at an angle of around 160° for G2TV and 140° for G2TRV. Similarly shear stress data for G2E and G2TRV – valley are similar due to their similar circumferential cross section, flow separation angle is noted to be around 90°. Pin G2C has a flow separation angle about 90°. As the flow goes around the circumference of the cylinder it accelerates faster due to the steep angle of the pin circumference leading to a higher value in wall shear stress. The flow separation angle and the magnitude of flow velocity can also be seen in pin circumferential C_p data in Figure 4.67.

In Figure 4.68 we can see that pin G2C has higher overall heat transfer performance before separation in comparison to other pins due the higher magnitude in flow acceleration. Also, after separation the pin G2C has the higher heat transfer performance due to the larger magnitude wake created by the pin structure. This gives the cylindrical pin the best heat transfer performance at the cost of pressure drop as seen before.

Since the bio pins are elliptical in nature a good comparison would be with the pure elliptical pin. In Figure 4.68 we cans see that stagnation heat transfer for pin G2TV and G2TRV – Peak are higher in comparison to G2E and G2TRV – valley, since the leading edge of the peak ellipse is smaller in radius compared to valley ellipse, it leads to an increase in stagnation Nusselt number. Since G2C has the leading edge with a bigger radius, it has the lowest stagnation heat transfer performance.

The valley ellipse section performs better in terms if hear transfer due to being less slender that the peak ellipse. Hence pin G2TV which has a peak ellipse at the center plane and transitions to valley ellipse towards the bottom and the top wall outperforms the pin G2TRV which has two peak ellipse and almost two valley ellipse. This can be seen in the Pin surface average Nusselt number results discussed before.

Figure 4.69 represents time averaged wall shear stress for row 5 pins. Since this result is time averaged the stagnation point and the separation point are not represented by zero Pascal, due to turbulence in the channel leading to change in stagnation points over time in the leading edge of the pins. From the figure we can see that there is a decrease in magnitude in wall shear stress towards the leading edge of pins G2C and G2TRV in comparison to other two pins. This indicates that the pins G2C and G2TRV has increase in turbulence mixing in the channel compared to pins G2TV and G2E. The separation

point for pin G2C is increased to 117°, for pin G2TV it's around 160°, for pins G2E it's at 100° and for pin G2TRV the separation angle is between 100° – 140°.

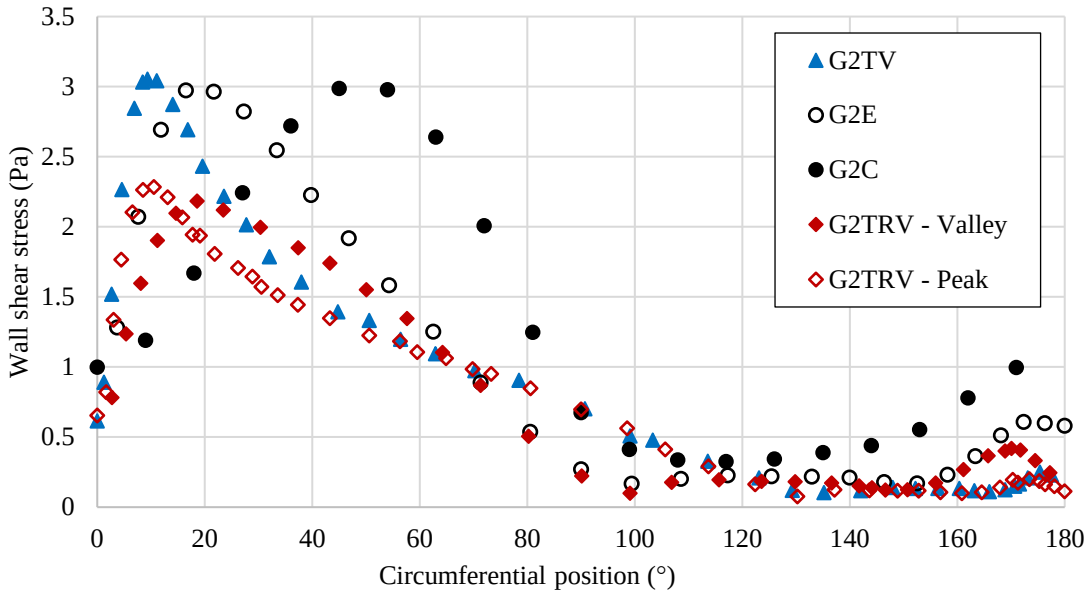

Figure 4.69 Row 5 pin circumferential wall shear stress

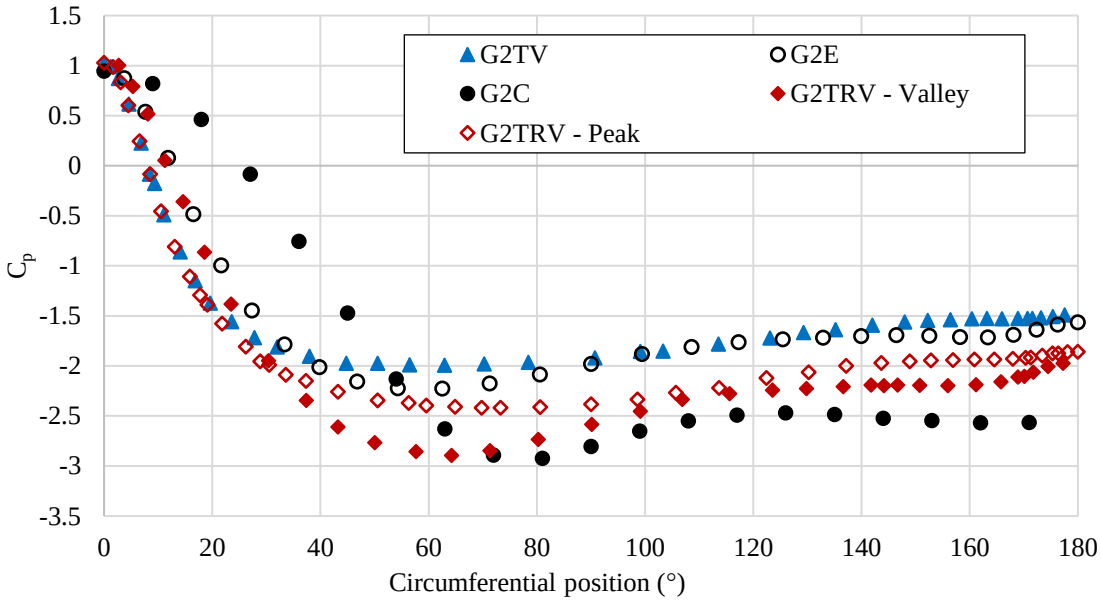

Figure 4.70 Row 5 pin circumferential coefficient of pressure

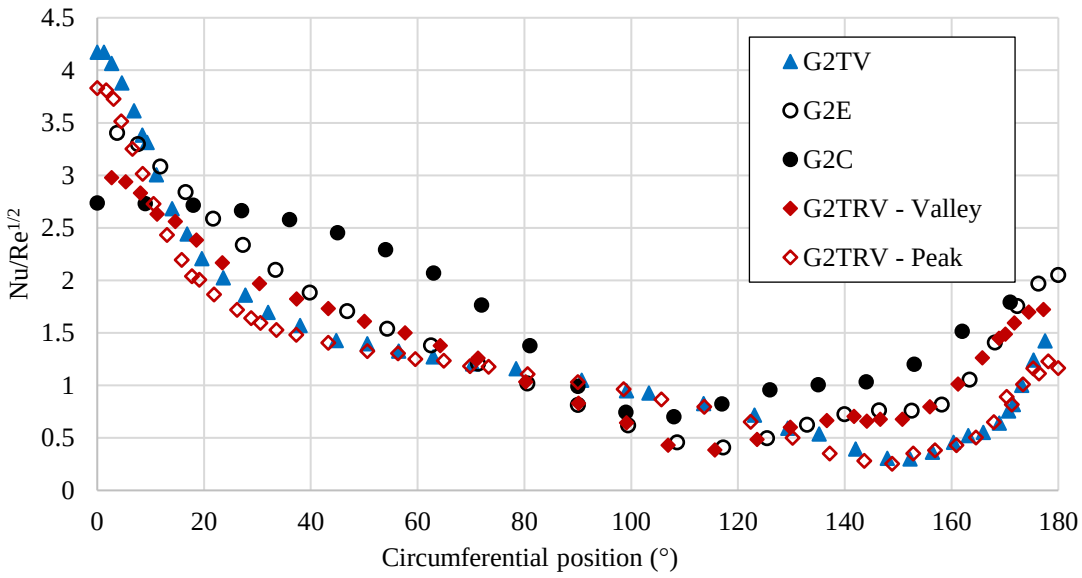

Figure 4.71 Row 5 pin circumferential Frossling number

In Figure 4.70 we can see that the pressure loads are increased for pin G2E and G2TV in comparison to pin and G2C, whereas in row 1 pins it was almost the same towards the leading the trailing edge. This indicates that pins G2E and G2TV has lower pressure loss along the channel. The flow separation angle is noted to be the same as seen in wall shear stress results. In Figure 4.71 for the pins surface heat transfer results the trends are almost similar to row 1 results. The main notable difference is the increase in stagnation and the trailing edge heat transfer in pin G2TV and pin G2TRV – peak in comparison to the other pins.

4.2.7. Turbulent Kinetic Energy

The TKE is plotted from bottom to the top wall, located by a line probe 20 mm from the center of the pin for rows 1, 3, 5 and 7, as seen in Figure 4.72 – Figure 4.75. In Figure 4.72 , we can see that at the given location behind row 1 pin the turbulence intensity from

the wake in the axial direction is smallest for G2C and highest for G2TRV. In G2TV it can be seen that the turbulence intensity is higher near the top and the bottom wall and there is a reduction in strength in the core flow, which is an ideal situation needed to have less pressure drop and improve heat transfer near the wall. G2E has the second smallest turbulence intensity in the axial direction.

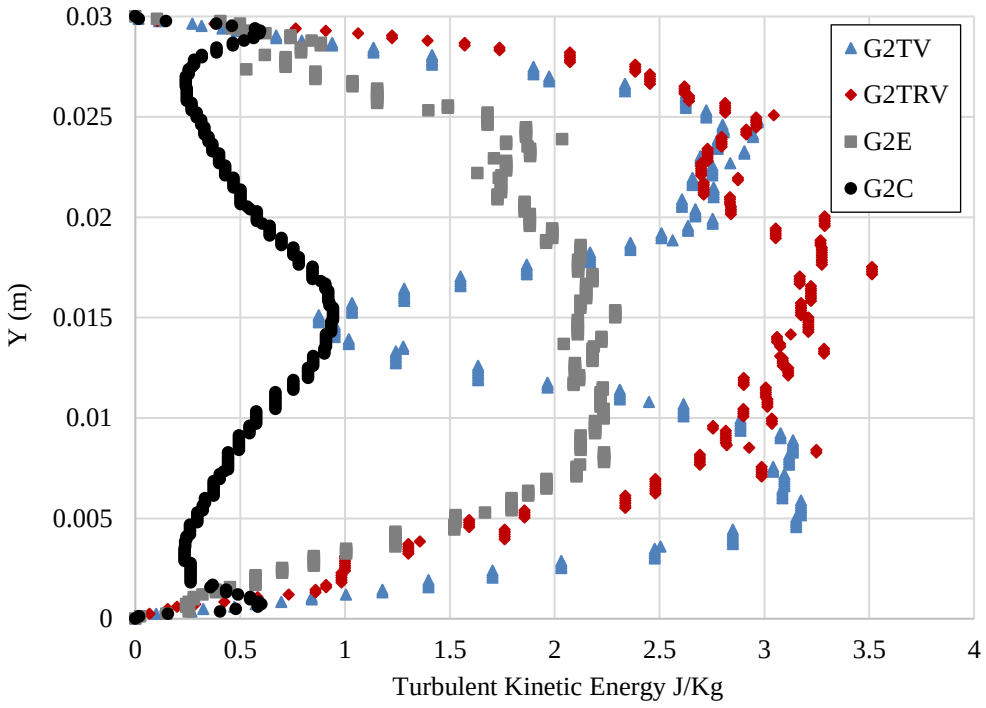

Figure 4.72 TKE behind row 1

In Figure 4.73, behind row 3 pin, the trend is similar to the one seen in Figure 4.72, G2C having the smallest turbulence intensity and G2TRV having the largest turbulence intensity. The trend seen in G2TV behind row 1 pin is not seen behind row 3 pin, the turbulence intensity of the wake is more towards the core flow.

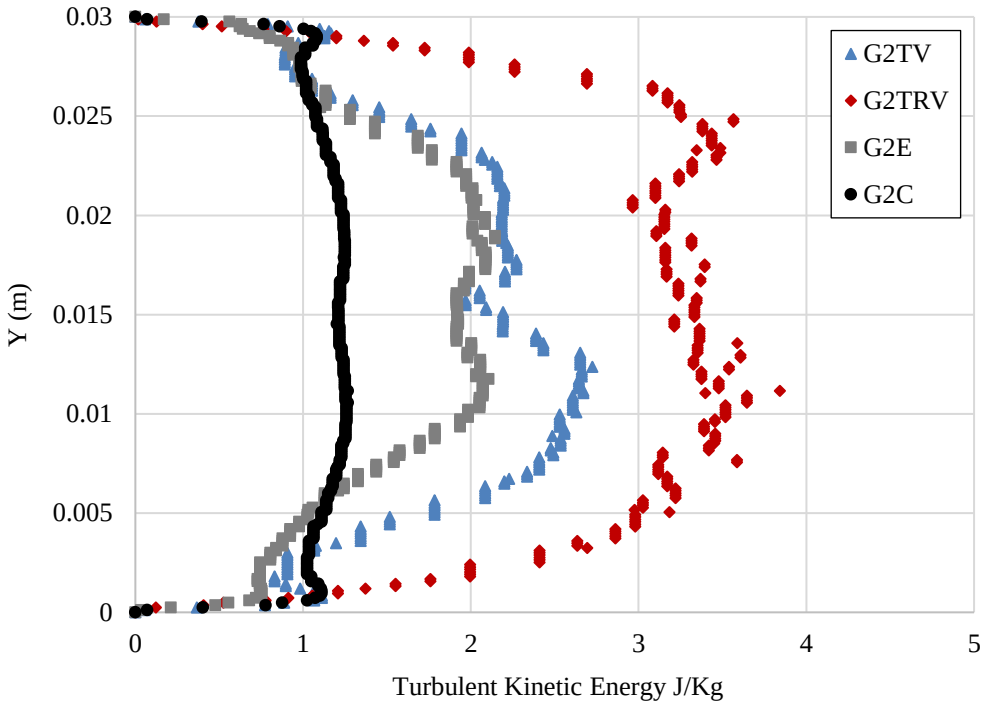

Figure 4.73 TKE behind row 3

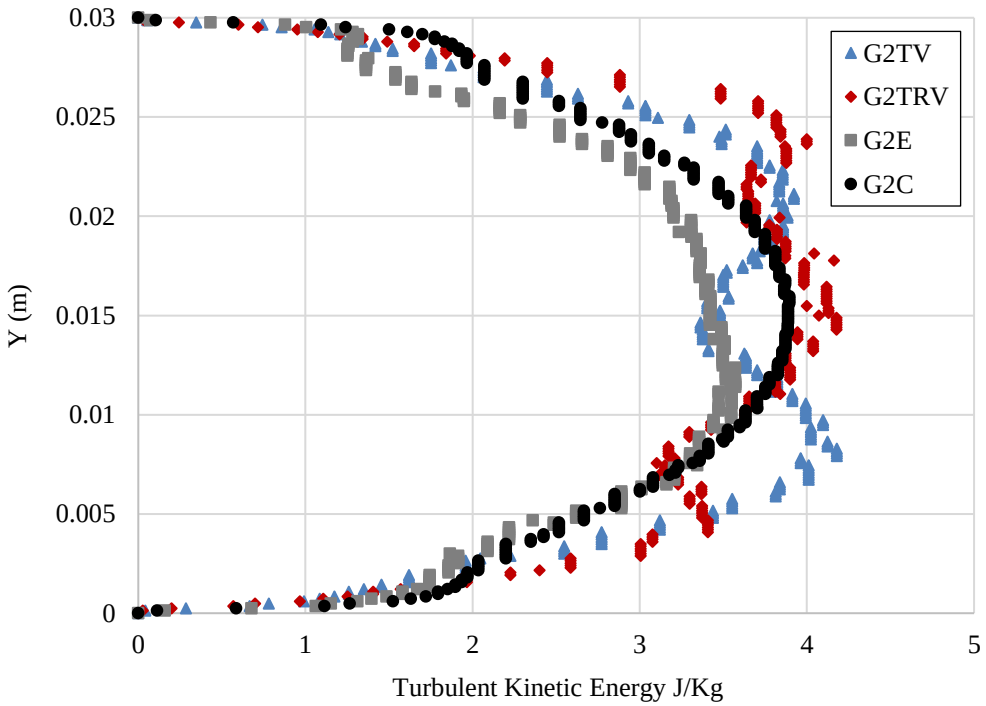

Figure 4.74 TKE behind row 5

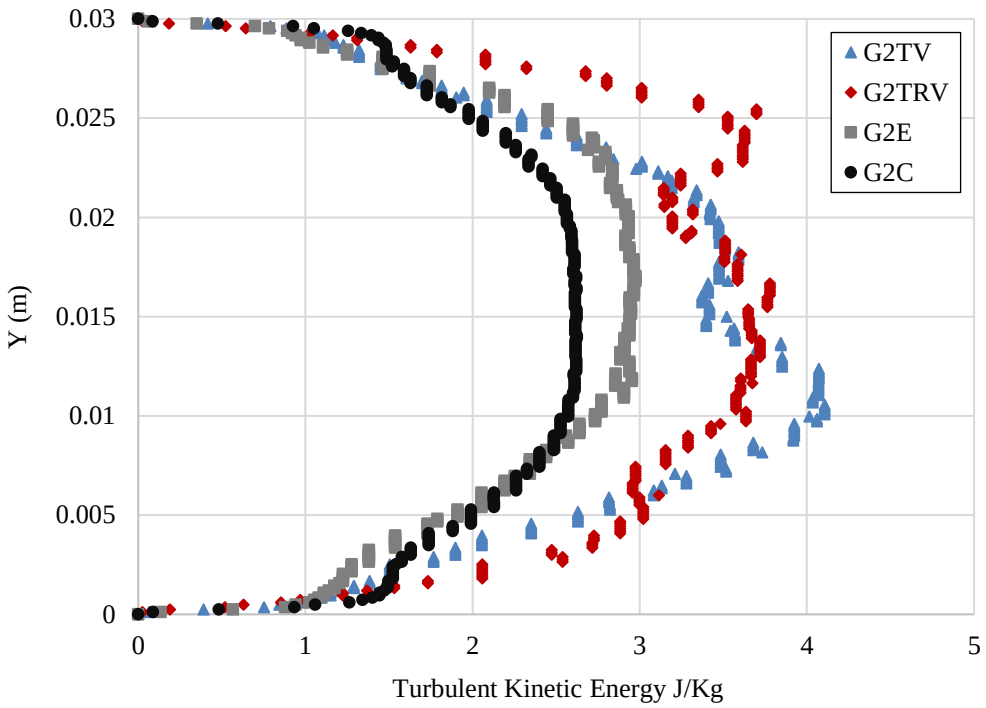

Figure 4.75 TKE behind row 7

In Figure 4.74, behind row 5 pin, the turbulence intensity for the 4 cases of pins are almost similar. In comparison to Figure 4.72 and Figure 4.73, G2C has an increase in magnitude which relates to a stronger wake in the axial direction. In Figure 4.75, behind row 7 pin the G2TV and G2TRV has the same turbulence intensity. G2C has a reduction in the magnitude of turbulence intensity in comparison to the previous figure.

From Figure 4.72, Figure 4.73 and Figure 4.75, it seems that the pin G2C has the less turbulence intensity overall in the core flow, but in comparing these results to the contour plots Figure 4.78 – Figure 4.81, we can see that in the contour plot the turbulence intensity increase downstream of the flow domain for G2C in comparison to the other pin cases. This suggest that the wake created by the cylindrical pins G2C is much wider in comparison to the other pins, which can be seen in Figure 4.76.

Figure 4.76, the TKE is plotted along the width of the channel from one periodic boundary to the other, located by a line probe 0.02 m from the center of the pin for row 7. From Figure 4.76, it is seen that the wake is wider and has a higher range of turbulence intensity for G2C. Followed by G2E, G2TRV and G2TV. For G2TV the wake is narrower and has less turbulent intensity promoting less pressure drop. Furthermore, looking the wake of G2TRV we can see that behind the peak region (G2TRV – Peak) the wake characteristic are similar to G2TV, since G2TV has a peak elliptical structure at the center.

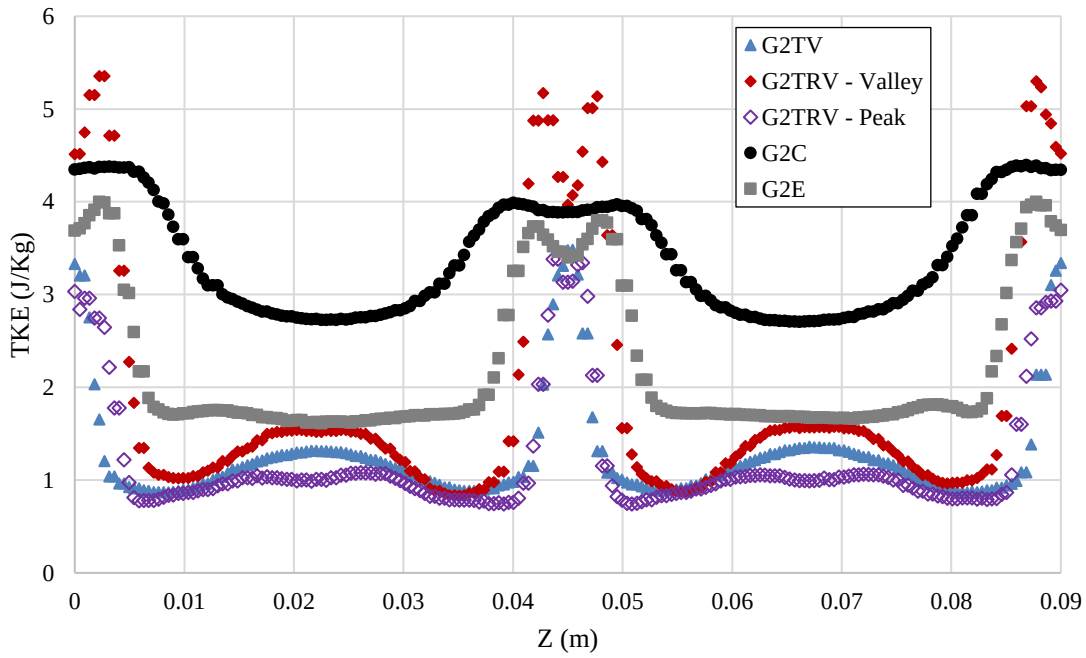

Figure 4.76 Spanwise TKE data behind row 7

4.2.8. Contour Plots

Figure 4.77 shows the mean of endwall Nusselt number for pins G2E, G2C, G2TV and G2TRV. From the figure we can see that the periodic wake structure from the

cylindrical pin enhances the end wall Nusselt number in the wake region. Same goes for pin G2E. But for pin G2TV we can see that the end wall Nusselt number in the wake region is reduced in comparison to G2E, this is due to the fact that pin G2TV has a reduction in wake magnitude due to the undulations on its surface.

For pin G2TRV having more peaks and valleys on the pin surface leads to a lower end wall Nusselt number in the wake region, this is due to the interaction of the core flow to the enwall being broken down due to the presence of the undulation with smaller half period between them. Also the magnitude of the horseshoe vortex is reduced in this case.

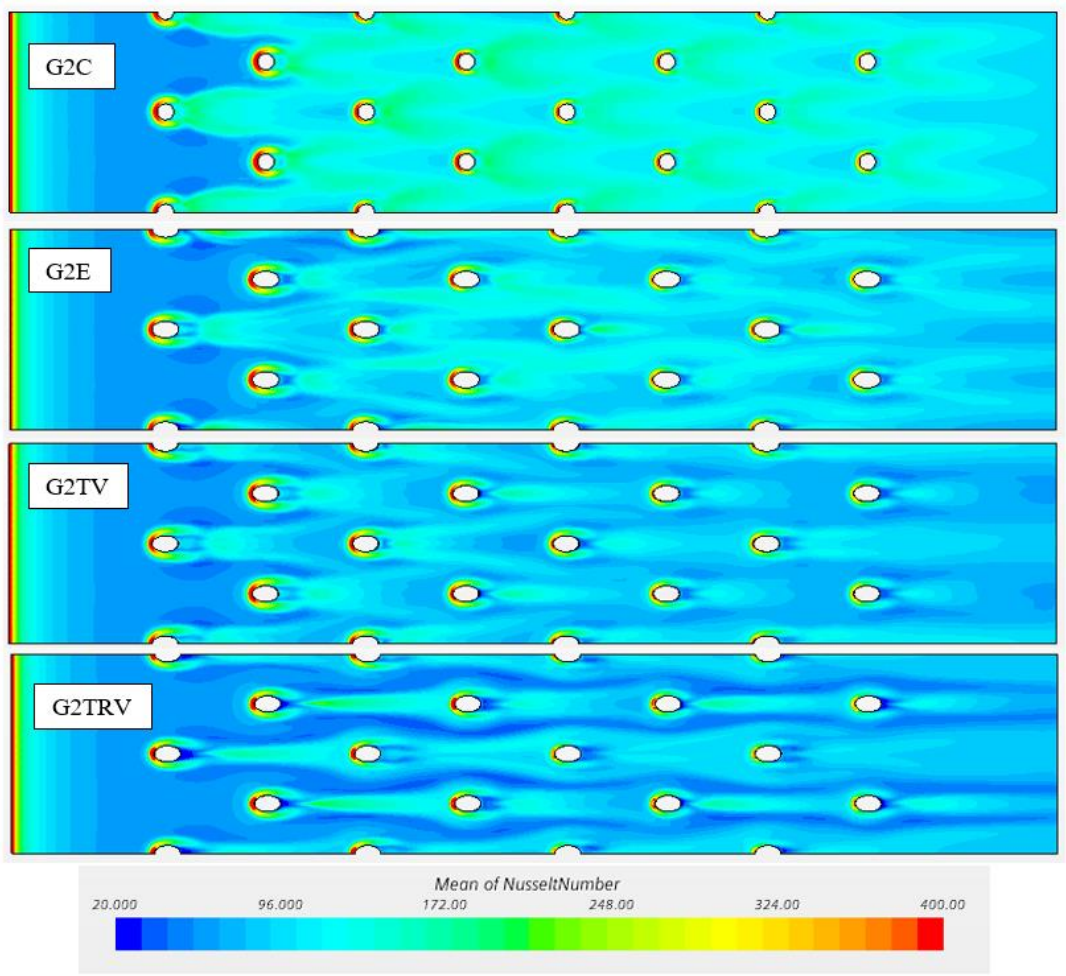

Figure 4.77 Mean of endwall Nusselt number

Figure 4.78 – Figure 4.81 shows the TKE data for the pins geometries. Figure 4.82 – Figure 4.85 shows the vorticity data for these pins. The TKE and vorticity data are obtained at 3 second in solution time. In vorticity contour the blue represesnts clockwise rotation and red represents anticlockwise rotation of the vortex. From the TKE contour we can see that the pin G2C and G2E has periodic wake shedding.

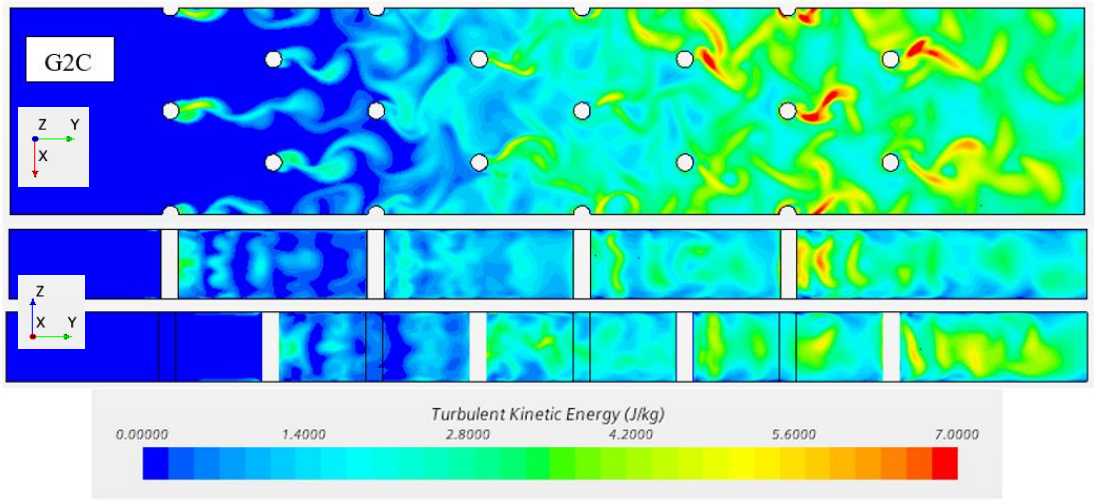

Figure 4.78 TKE – G2C

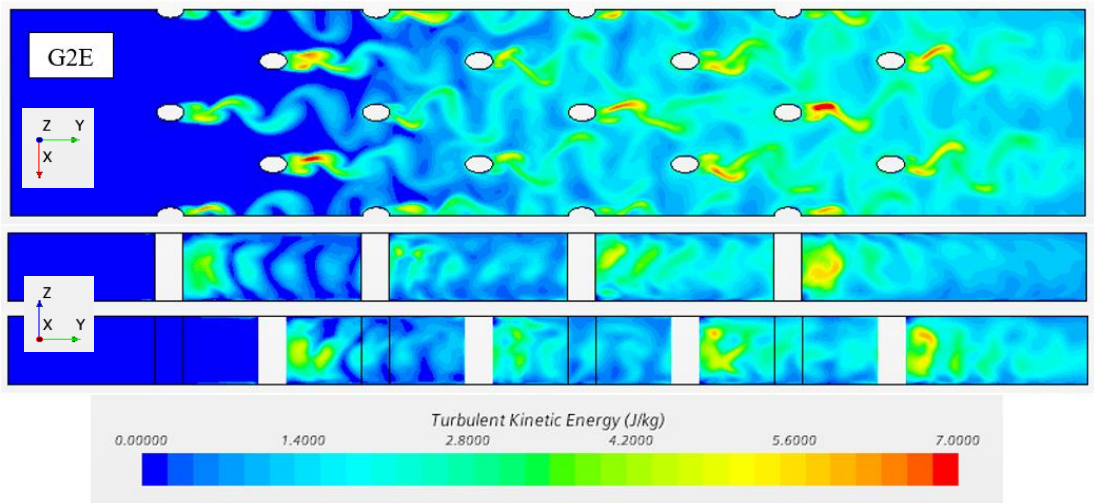

Figure 4.79 TKE – G2E

But looking at pin G2TV we can see that the wake shedding is not periodic and also smaller in magnitude this represents the information presented in the literature. The same goes for pin G2TRV, since it has peaks and valley near the core flow, looking at the respective planes we can see no periodic wake shedding.

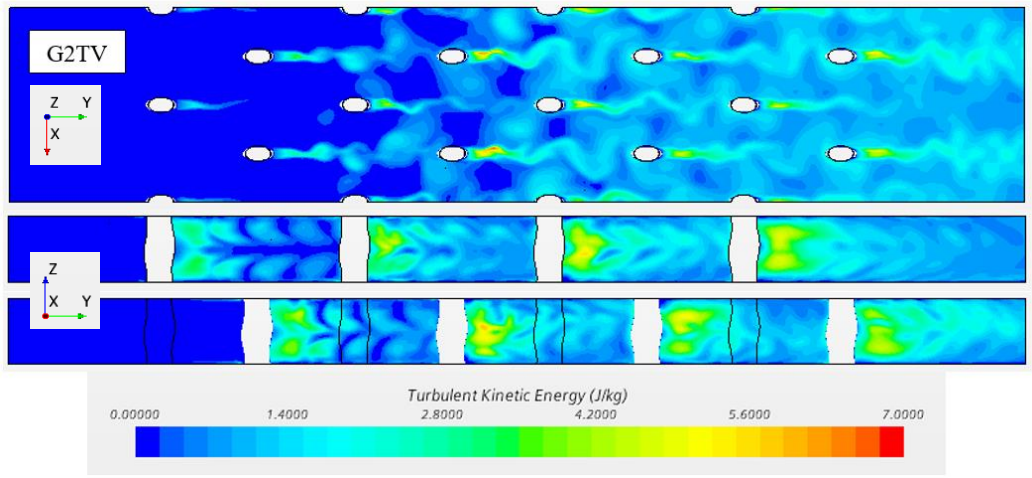

Figure 4.80 TKE – G2TV

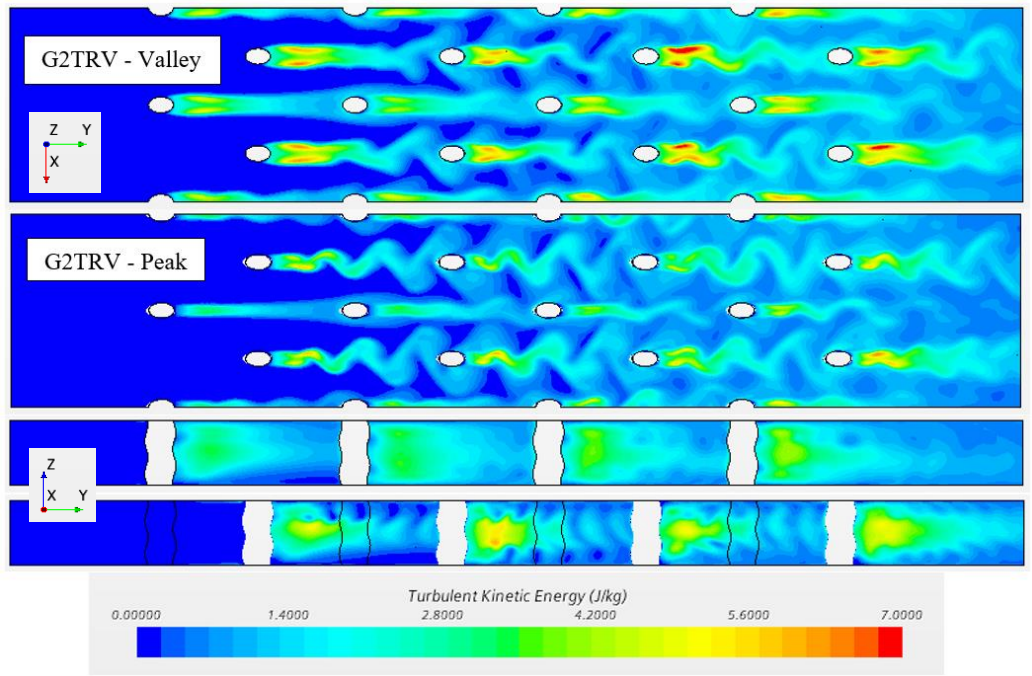

Figure 4.81 TKE – G2TRV

Also the valley region has a wider wake in comparison to peak region, this suggest that the wake near the walls are wider compared to wake near the center for both G2TV and G2TRV, this improves the pressure loss in the channel while maintaining the endwall heat transfer.

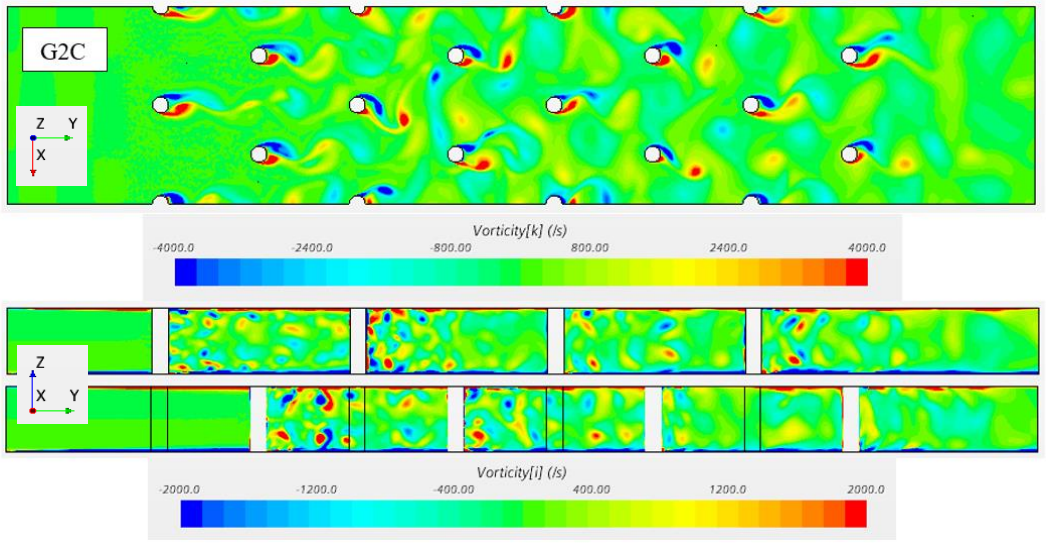

Figure 4.82 Vorticity – G2C

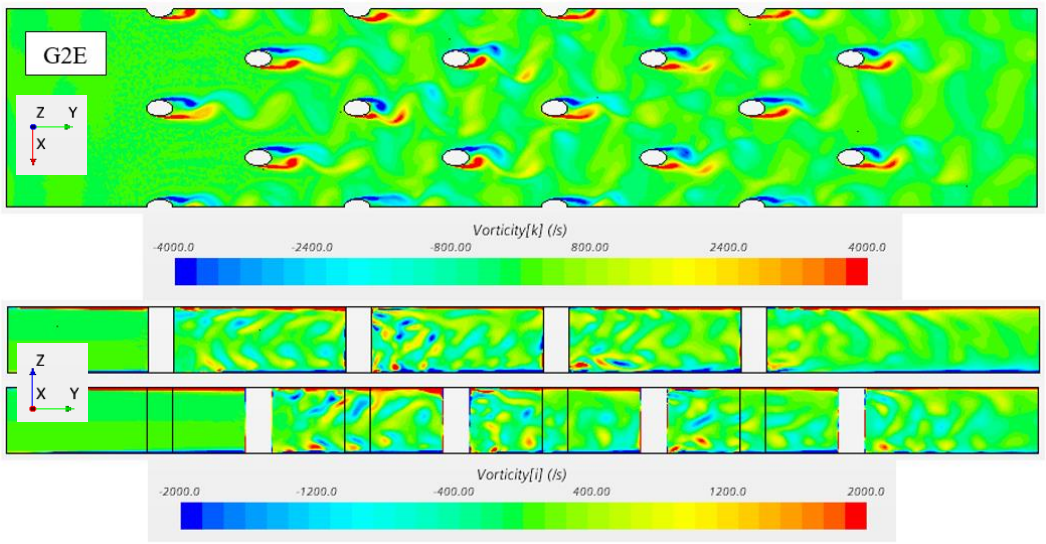

Figure 4.83 Vorticity – G2E

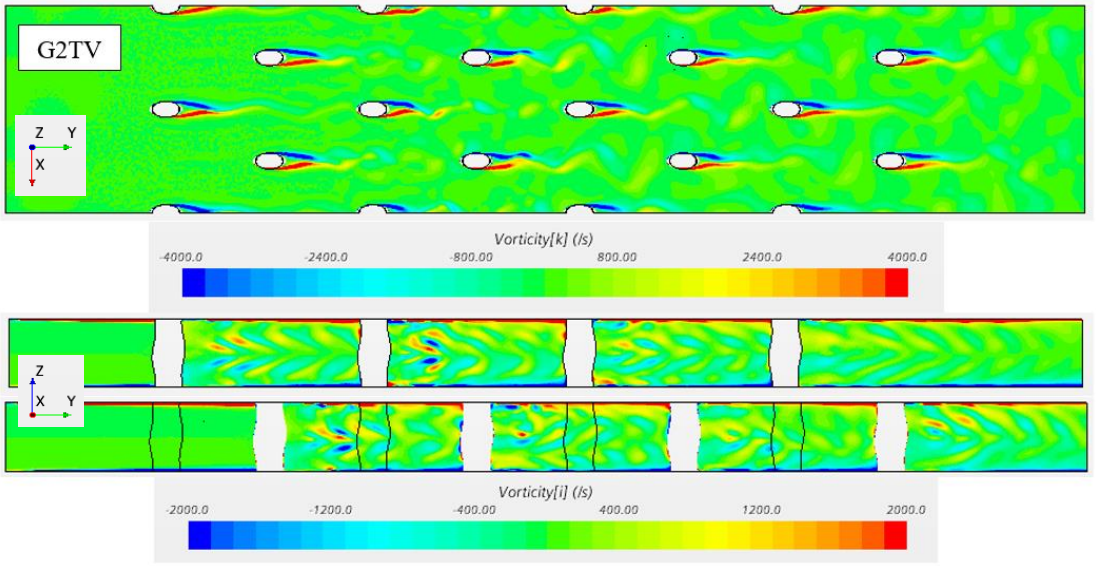

Figure 4.84 Vorticity – G2TV

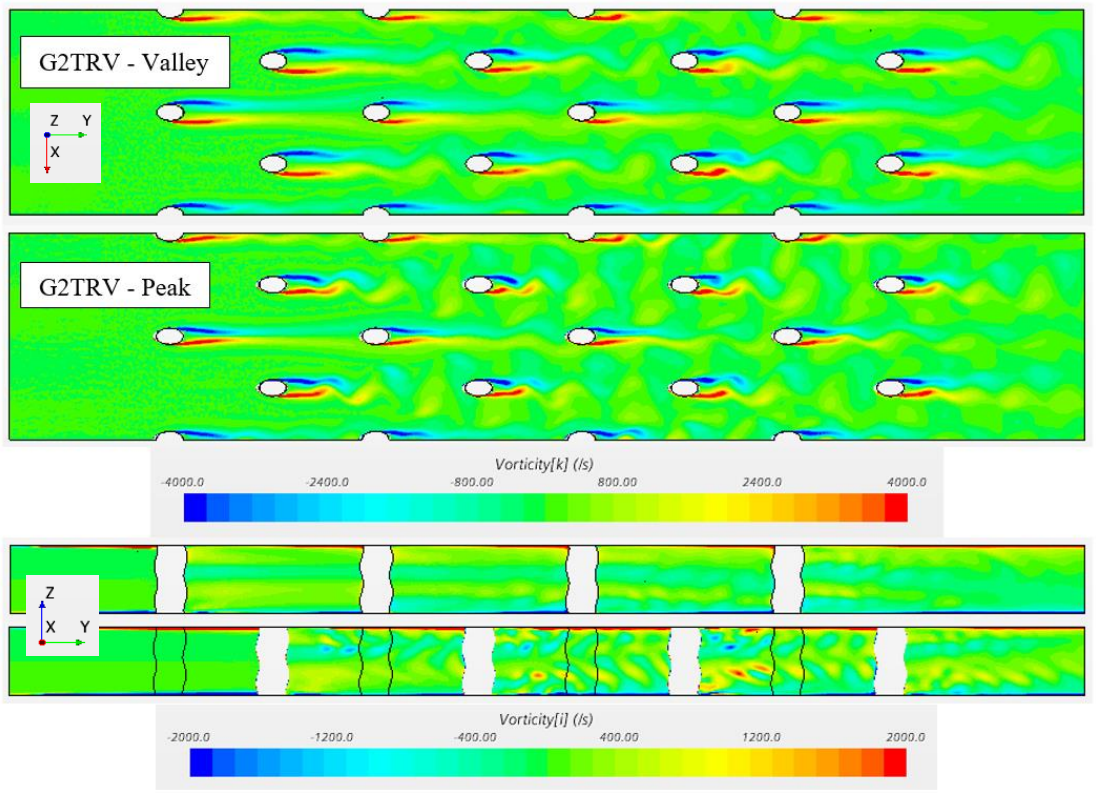

Figure 4.85 Vorticity – G2TRV

From the vorticity contour plots we can see that pins G2C and G2E has periodic vortex shedding but pins G2TV and G2TRV does not have periodic vortex shedding. This is similar to the discussion presented in the TKE contours. Looking at the vorticity contours in the axial direction we can see that in the wake region of pin G2C, the rotation of flow vortex near the end wall due to the horseshoe vortex interaction to the core flow. This contributes to the enhancement of heat transfer but at the cost of pressure drop. We can also see the same phenomenon for pin G2E but with reduction in magnitude. From pins G2TV and G2TRV the vortex structure is at an inclined angle for the axial direction of the pin this is due to the presence of the undulation of the pin.

4.2.9. Spectral Analysis

Local velocity magnitude data is obtained in time at a point 20 mm behind rows 1, 3, 5 and 7. The simulation was run for 3 seconds and the data used was the last 2 seconds at 10000 samples a second. The amplitude spectrum of the velocity magnitude fluctuations is then plotted with frequency. Plotting the velocity magnitude fluctuations will give two dominant frequencies for the pin, one related to the drag and the other related to the lift. The frequency for the drag will be twice that of the lift. Figure 4.86 and Figure 4.87 shows the FFT for lift and drag force on pin G2TV in row 1.

From the two figures we can see that the pin generates a lift of 219 Hz and drag of 438 Hz. As discussed before the frequency of drag is twice the lift. Figure 4.88 shows the amplitude spectrum of the velocity magnitude fluctuations for pin G2TV. From the row 1 data we can see two frequencies 222 Hz and 441 Hz, as mentioned before they represent lift and drag. As we move down steam in the channel we can see from the FFT data, that the amplitude of the frequency is retained for row 3 and 5, except row 7. This suggest

that there is a reduction in turbulence mixing downstream of the channel.

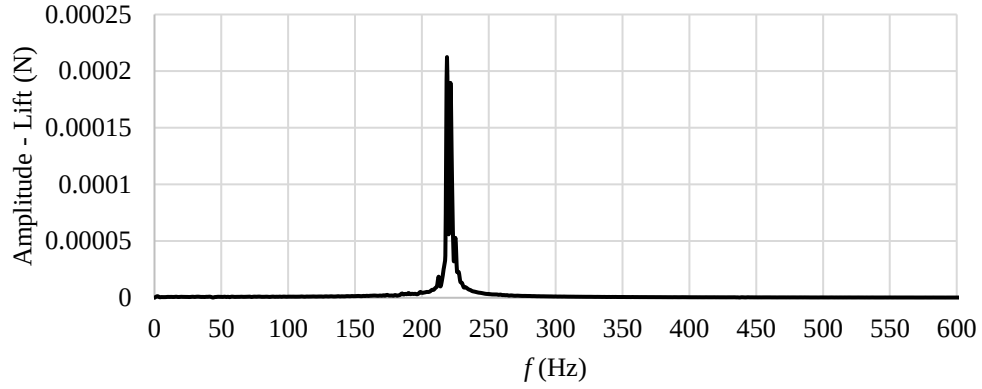

Figure 4.86 FFT – Lift on pin G2TV

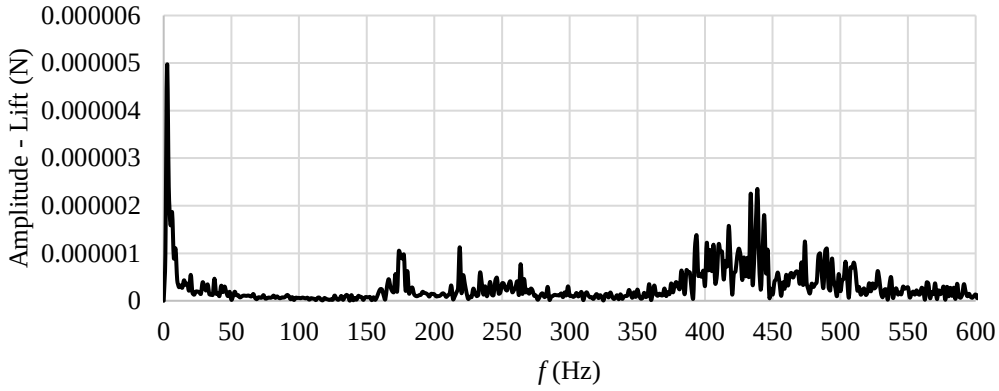

Figure 4.87 FFT – Drag on pin G2TV

Figure 4.89 represents FFT data for pin G2TRV. From the figure we can see that multiple frequencies are resolved by FFT, suggesting that the wake created by the pin is broken down. As we move down steam in the channel we can see from the FFT data that the amplitude of the frequency is retained, suggesting that there is no vortex mixing, which leads to reduction in turbulence mixing downstream of the flow domain.

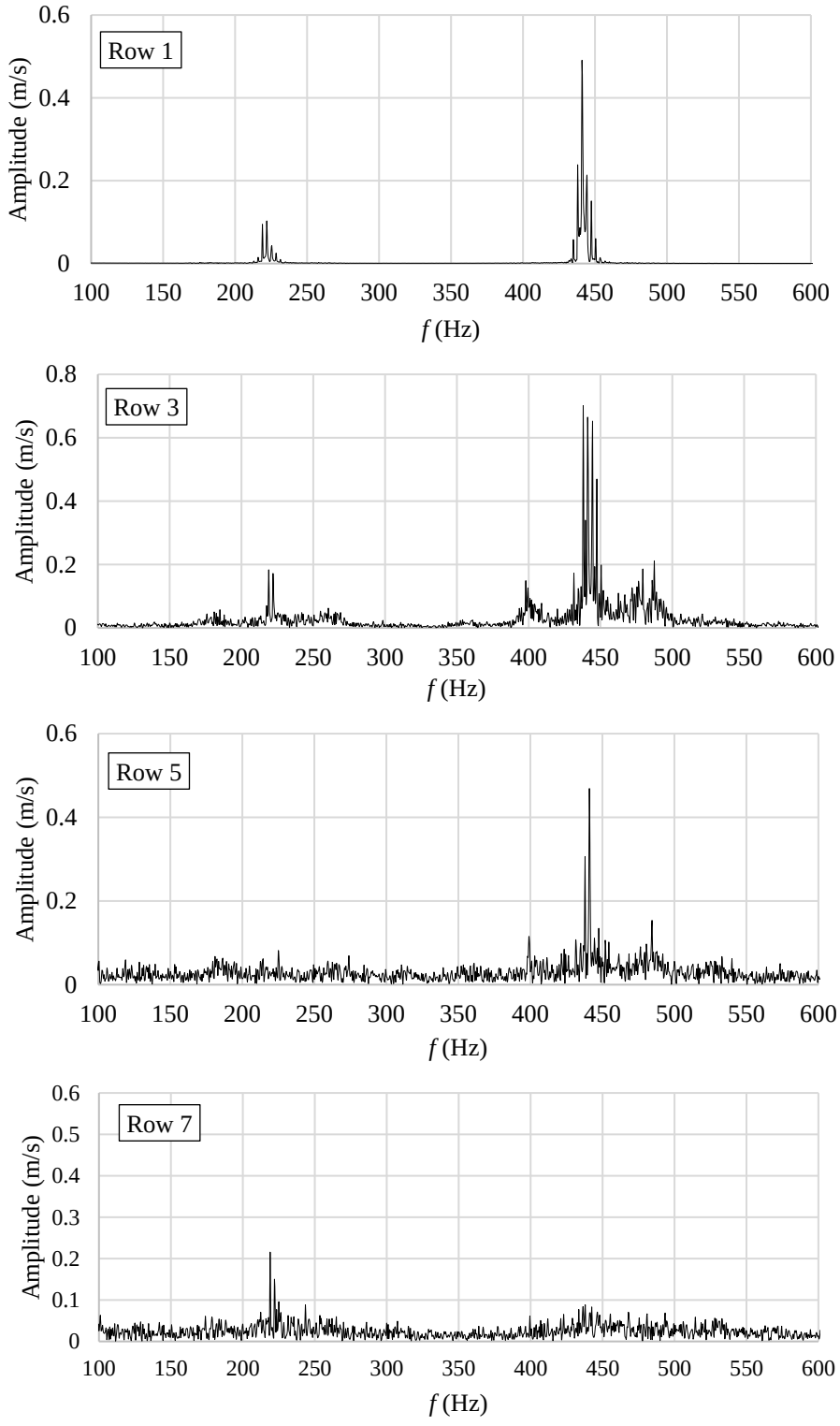

Figure 4.88 FFT – G2TV

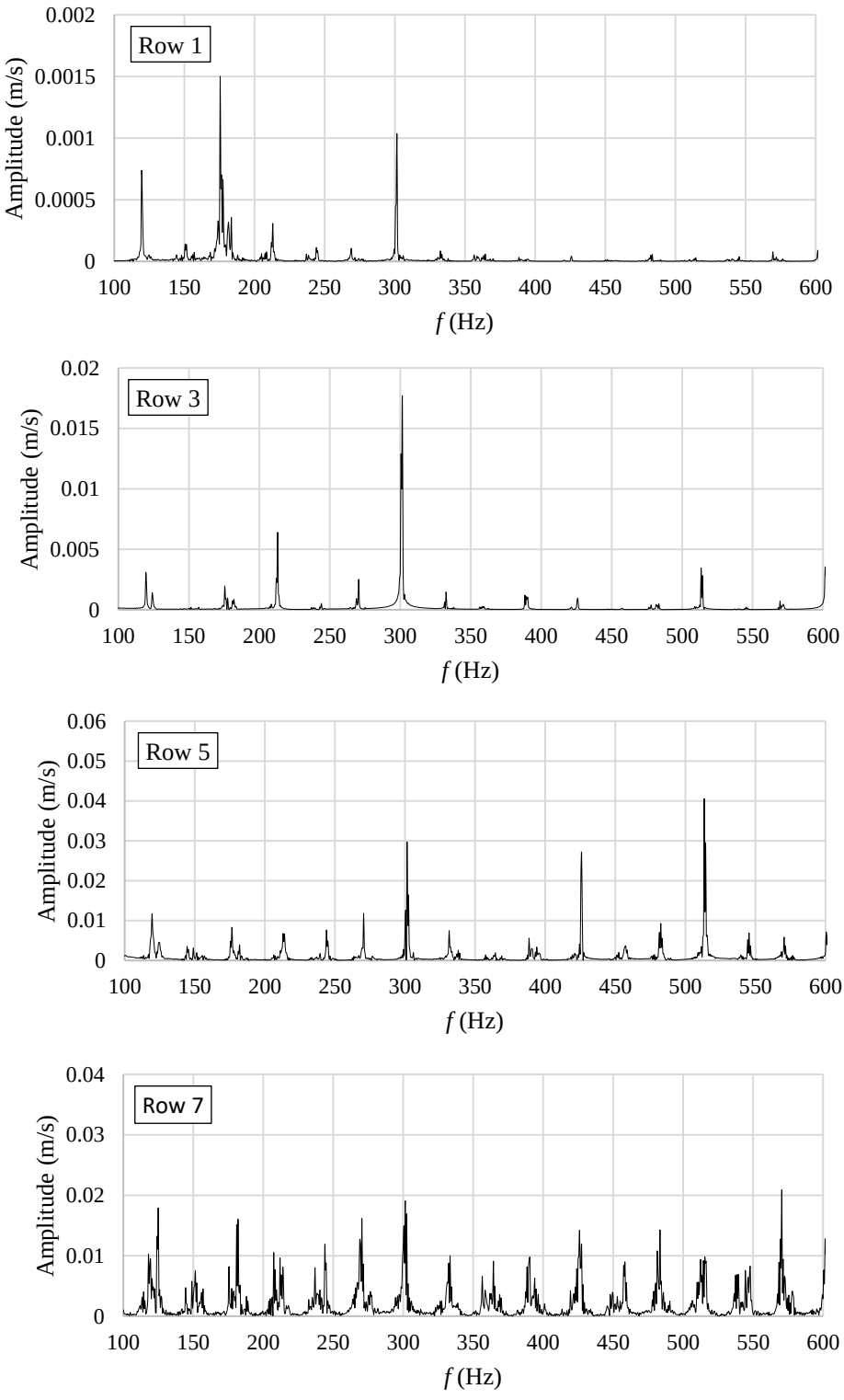

Figure 4.89 FFT – G2TRV

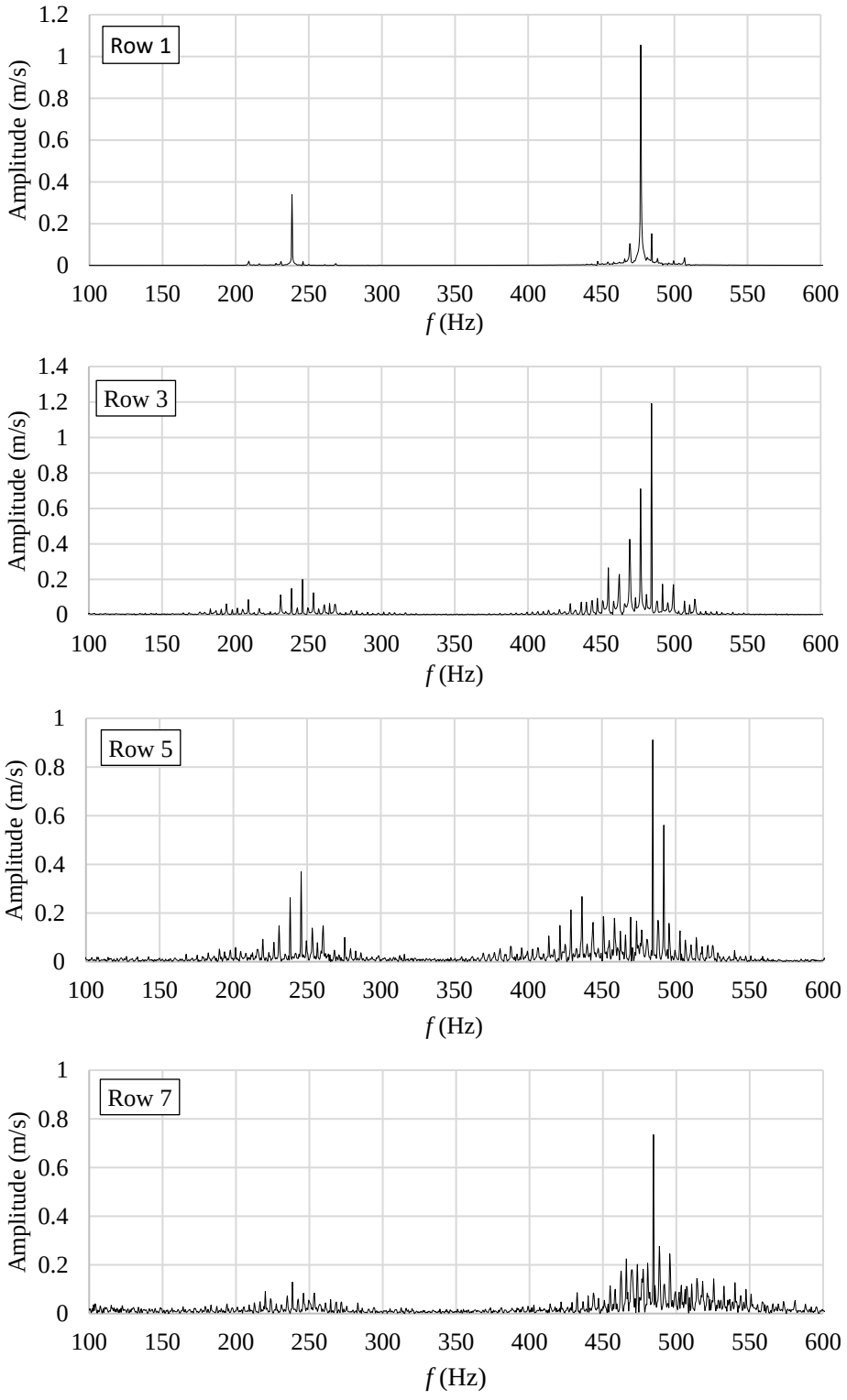

Figure 4.90 FFT – G2E

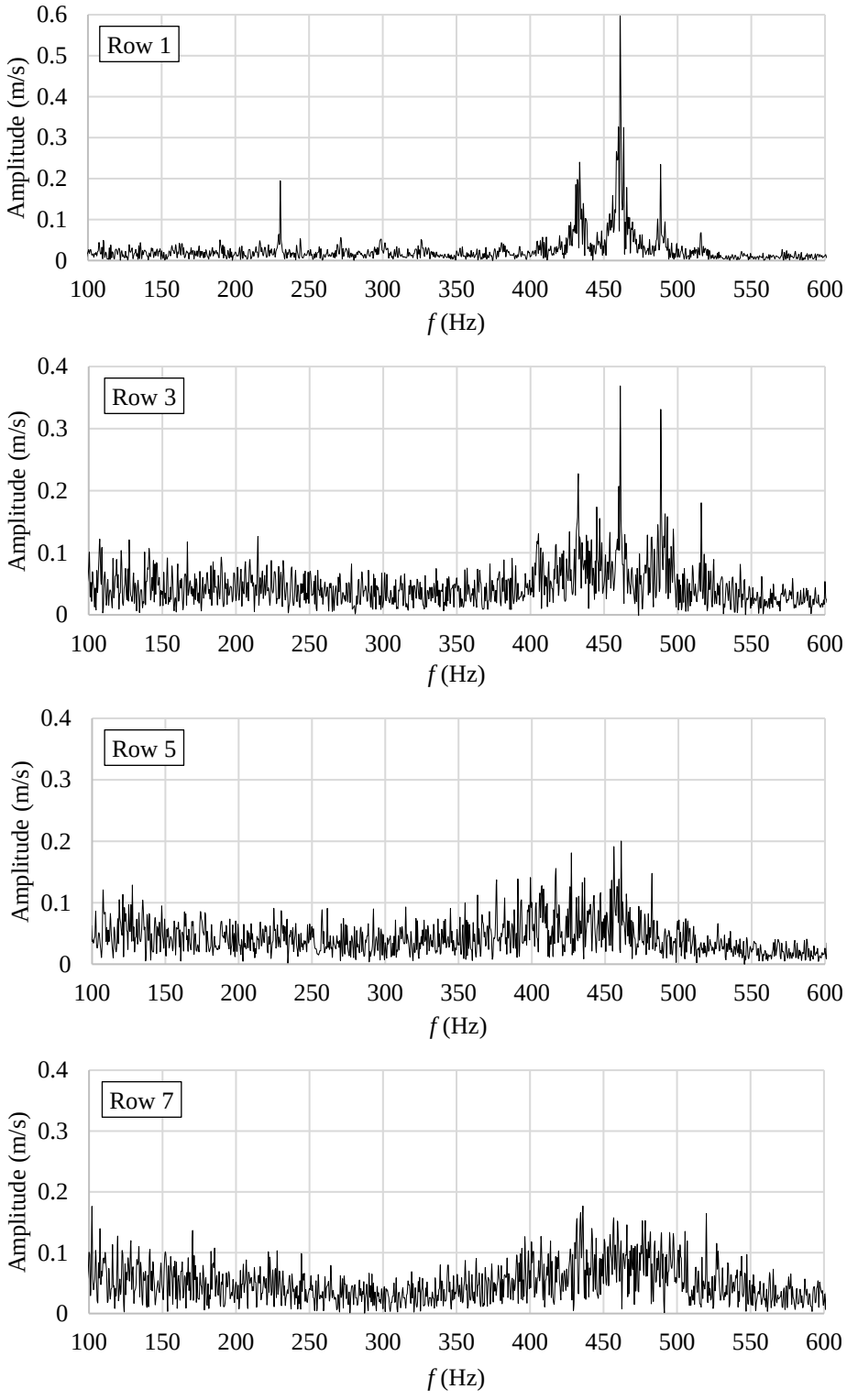

Figure 4.91 FFT – G2C

Figure 4.90 represents the FFT data for pin G2E. From the figure we can see that the two frequencies are picked up behind row 1 pin, 238 and 477 Hz. As we move down steam in the channel we can see from the FFT data of the figure, that the amplitude of the frequency gets reduced, except for data behind row 3 in which it can be seen that the amplitude is higher suggesting that the wakes are pronounced similar to the pins in row 1. At the data behind row 7, it can be seen that the frequency of the wake shedding is captured by the FFT, but when compared with data behind row 1 pin, the amplitude is reduced. This suggest that even though there is turbulence mixing happening downstream, the wakes are distinguishable.

Figure 4.91 shows the FFT data for pin G2C. From the figure we can see that the harmonics of the frequency in the data behind the row 1 pin, is given by 230 and 460 Hz. These represent the wake shedding corresponding to lift and drag forces from the pins. As we move down steam in the channel, we can see from the FFT data of the figure, that the amplitude of the frequency gets reduced. At the data behind row 5 and 7, it can be seen that amplitude of the shedding frequency is reduced but has a broader frequency range. This is due to the increase in turbulence mixing that increases downstream of the flow domain.

On comparing the FFT data for the four pins design we can see that pin G2C has more turbulence mixing downstream of the channel, this can be also seen in the contour plots. Pin G2E is similar to pin G2C it does have an increase in magnitude as the flow moves downstream but not as much as G2C hence the wake shedding frequencies of the pins are preserved downstream of the channel. Same could be said for pin G2TV but in comparison to G2E there is a reduction of drag force as seen from the plots and the wake

structure contributes to reduction in turbulence mixing downstream of the channel. Pin G2TRV has multiple frequencies suggesting a complex wake structure due to having more undulations on the axial direction. These complex wake structure reduce the turbulence mixing in the channel leading to a reduction in static pressure loss across the channel.

4.2.10. Array Sensitivity

To determine the effect of array dimensions on the pin design the spanwise and streamwise directions are changed from 0.045 m to 0.02394 m in the spanwise and streamwise direction. This sensitivity study is done for pins G2TV, G2TRV, G2E and G2C for the same Reynolds number of 30,000. Figure 4.92 shows the endwall average Nusselt number result.

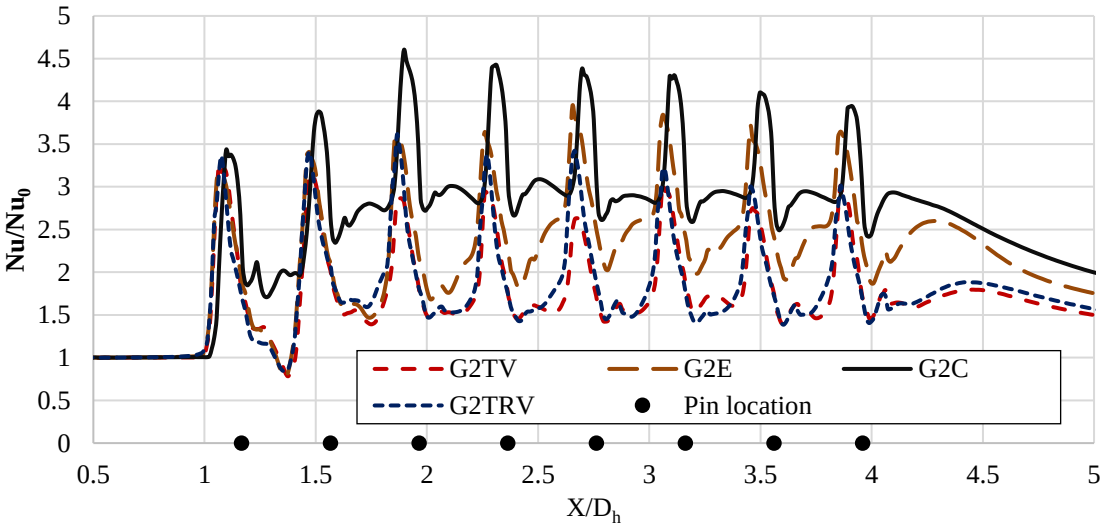

Figure 4.92 Endwall average Nusselt number – reduced array dimensions

From the figure we can see that the heat transfer performance of the pins G2TV and G2TRV are almost identical. This deviates from the previous results (Figure 4.53) in

which the pin G2TRV had a reduction in endwall heat transfer in comparison to G2TV. This indicates that uniqueness of pins individual wake structure which contributes to the endwall heat transfer are washed out when the array dimensions are reduced. Figure 4.93 shows the contour plot for mean of Nusselt number contour for endwall heat transfer.

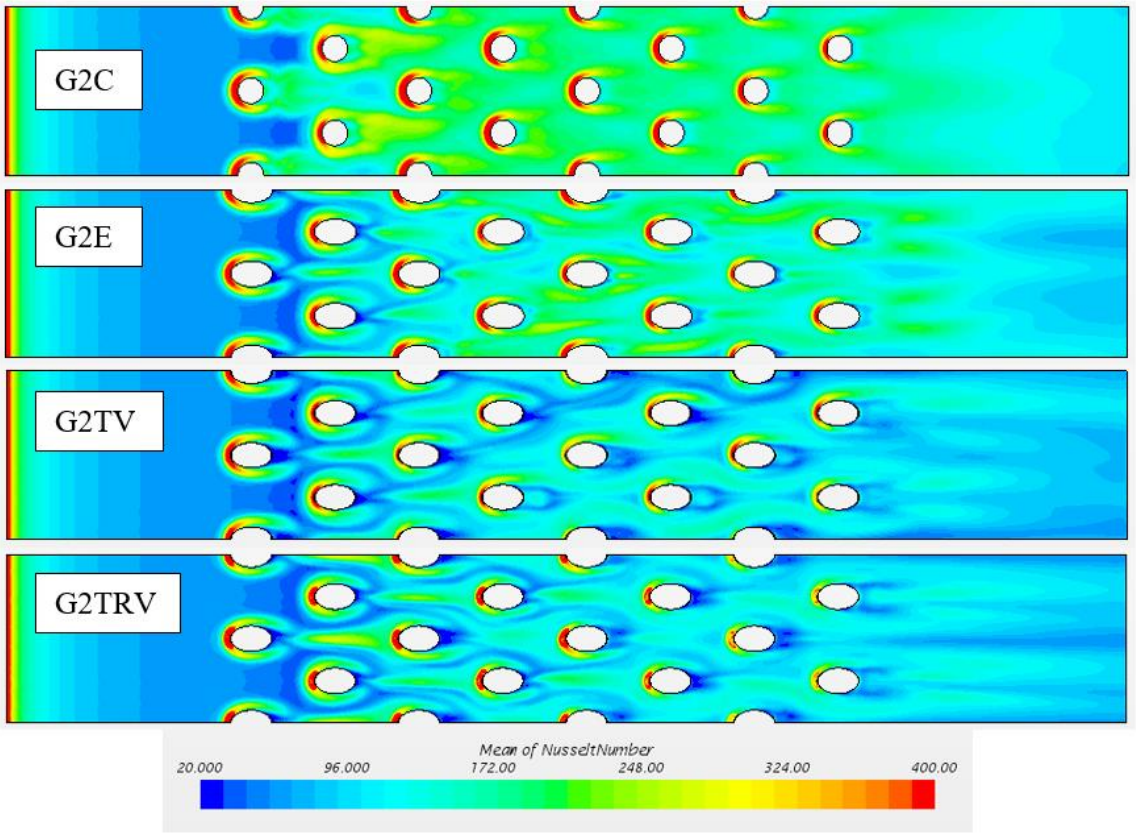

Figure 4.93 Endwall Nusselt number contour – reduced array dimensions

From the contour plot we can see that G2TV and G2TRV has almost the same result, except in G2TRV there is an moderate enhancement in heat transfer at the leading edge of the pins which can also be seen in the spanwise average results. In comparison to the previous array dimension contour plot (Figure 4.77) we can see that the flow accelerating between the pins compresses the endwall wake structure for the pins G2TV and G2TRV.

Figure 4.94 shows the pins surface average Nusselt number result. The results are normalized to obtain Frossling number. It can be seen from the figure that having a reduction in array dimensions has a significant effect on the pin surface average Nusselt number for pins G2TV and G2TRV. In this case pin G2TRV takes advantage of the increase in undulations on its surface as the blockage ratio of the channel is increased.

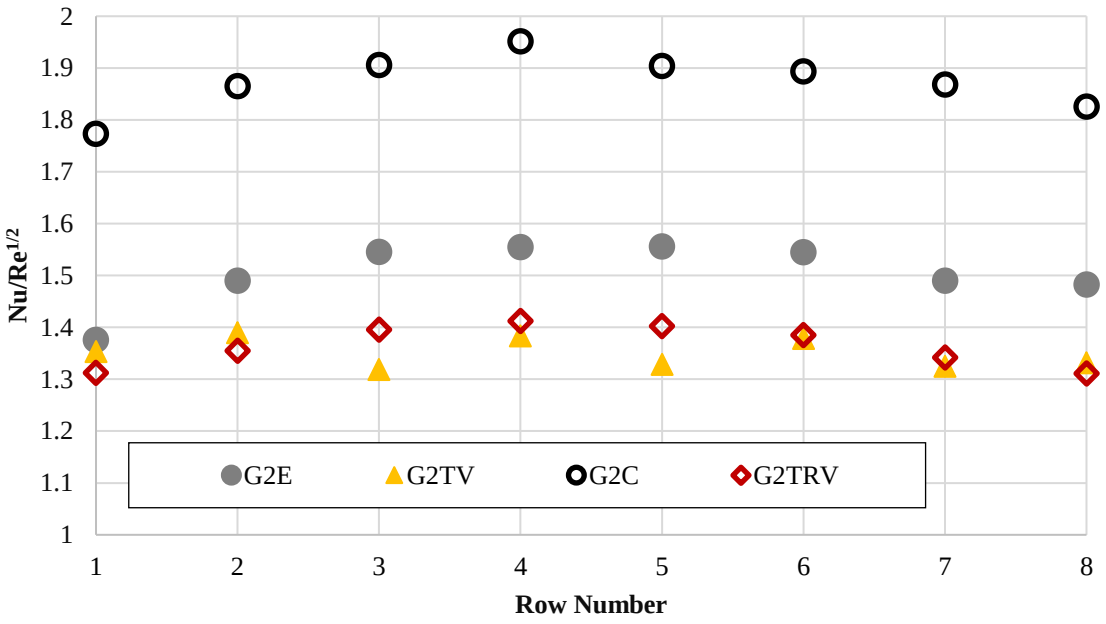

Figure 4.94 Pin surface average Nusselt number – reduced array dimension

Figure 4.95 shows the pressure drop across the channel. It can be seen from the results, that the bio pins still maintain the reduction in pressure loss in the channel in comparison to previous results (Figure 4.57). A major notable change is that the difference between the pressure drop for pin G2TV and G2TRV is subtle in this case due to the wake structure for these pins almost being the same as the spanwise direction is reduced.

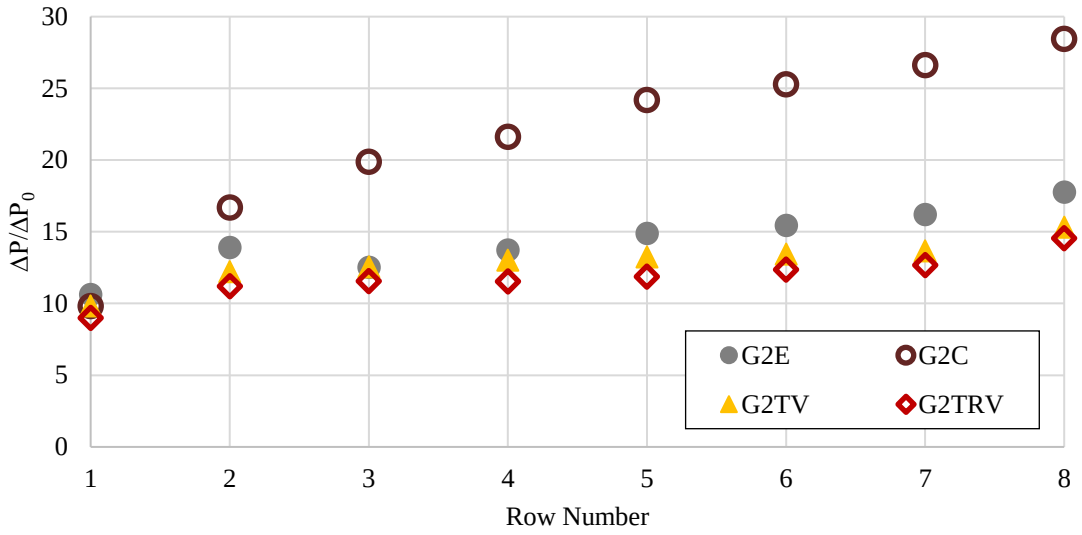

Figure 4.95 Pin surface average Nusselt number – reduced array dimension

Figure 4.96 – Figure 4.98 shows the average endwall Nusselt number, pin surface average Nusselt number and channel average Nusselt number in comparison to friction factor The Nusselt number and friction factor data for the pin fin channel are normalized with respect to data from a smooth channel, except for pins surface average in that case the Nusselt number is normalized to get Frossling number.

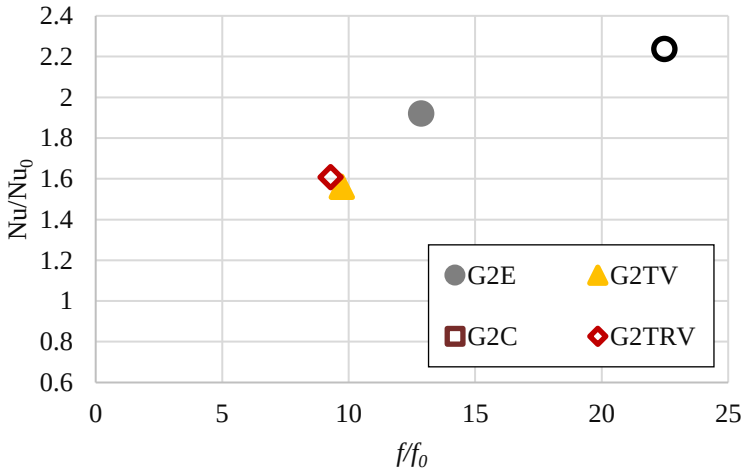

Figure 4.96 Endwall thermal performance

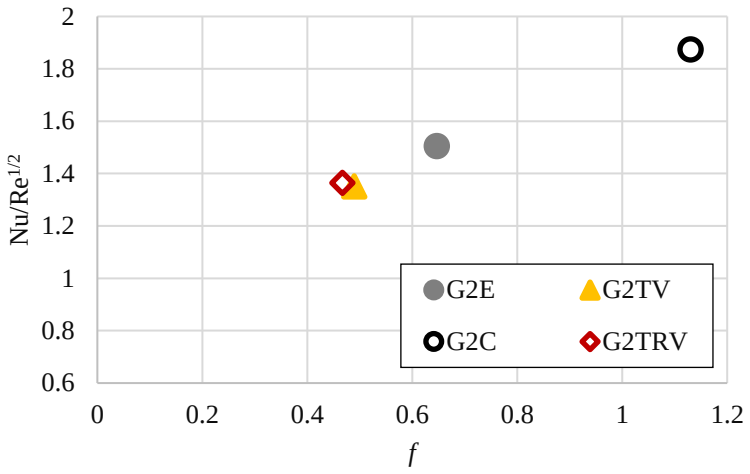

Figure 4.97 Pin thermal performance

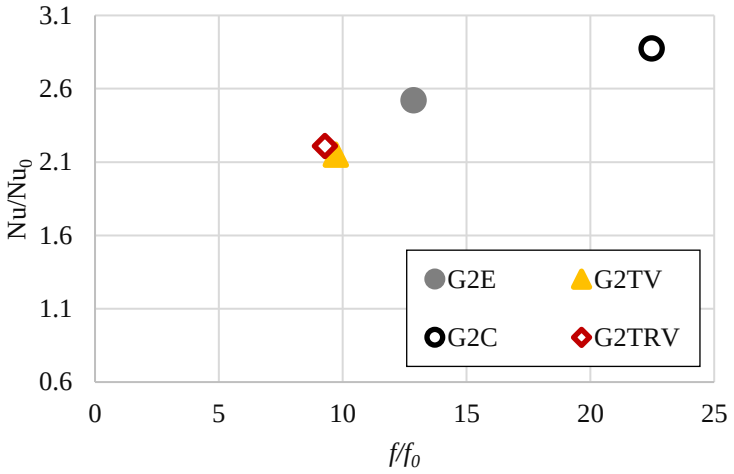

Figure 4.98 Channel average thermal performance

From Figure 4.97 we can see that the difference between pin G2TRV and G2TV as seen before is considerably reduced with both pins having the same heat transfer with G2TRV having a 4% improvement in friction factor. This is reflected from the results discussed above. In comparison to pin G2E the bio pin G2TRV has a 27% improvement in friction factor at the cost of 10% in heat transfer. Looking at the endwall heat transfer

from Figure 4.96, we can see that pin G2TRV having a 4.6% improvement in friction factor and 3.2% improvement in heat transfer. In comparing pin G2TRV and G2E we can see that pin G2TRV has a 28% improvement in friction factor at the cost of 16% in heat transfer. The average of these results is reflected in the area weighted channel average results presented in Figure 4.98.

A plane is created 20 mm behind the center of the pins in the channel, and time averaged TKE value is plotted for points behind each row, as shown in Figure 4.99. The TKE value is normalized with respect to velocity squared. The results (trend) are identical in comparison to previous TKE results shown in Figure 4.65.

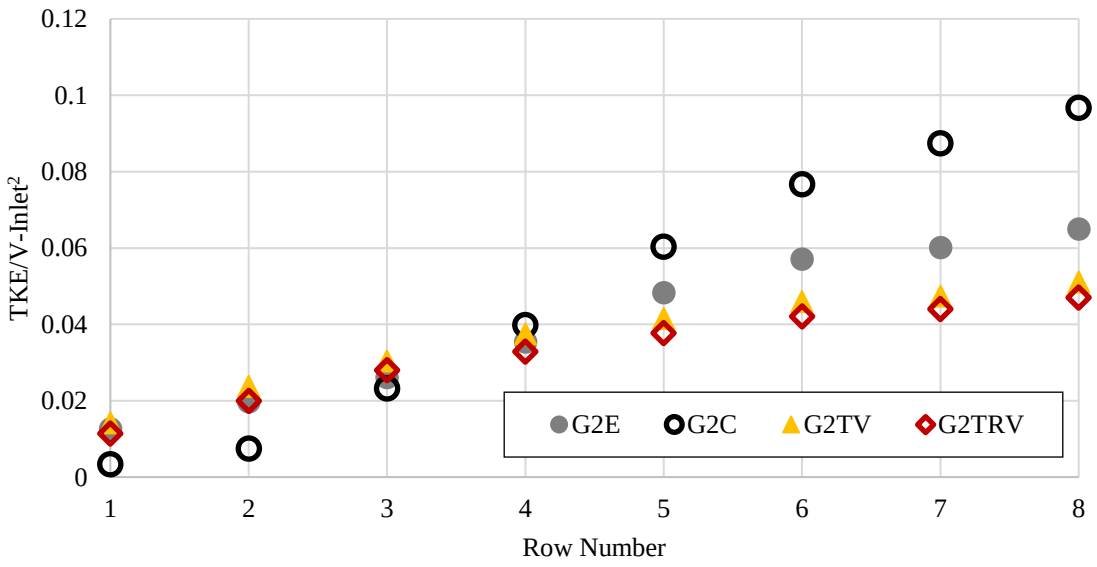

Figure 4.99 TKE across the channel for reduced array dimension

Figure 4.100 shows the TKE contour obtained at 3 second in solution time. From the figure we can see that the results are similar to the contours seen in previously from Figure 4.78 – Figure 4.81.

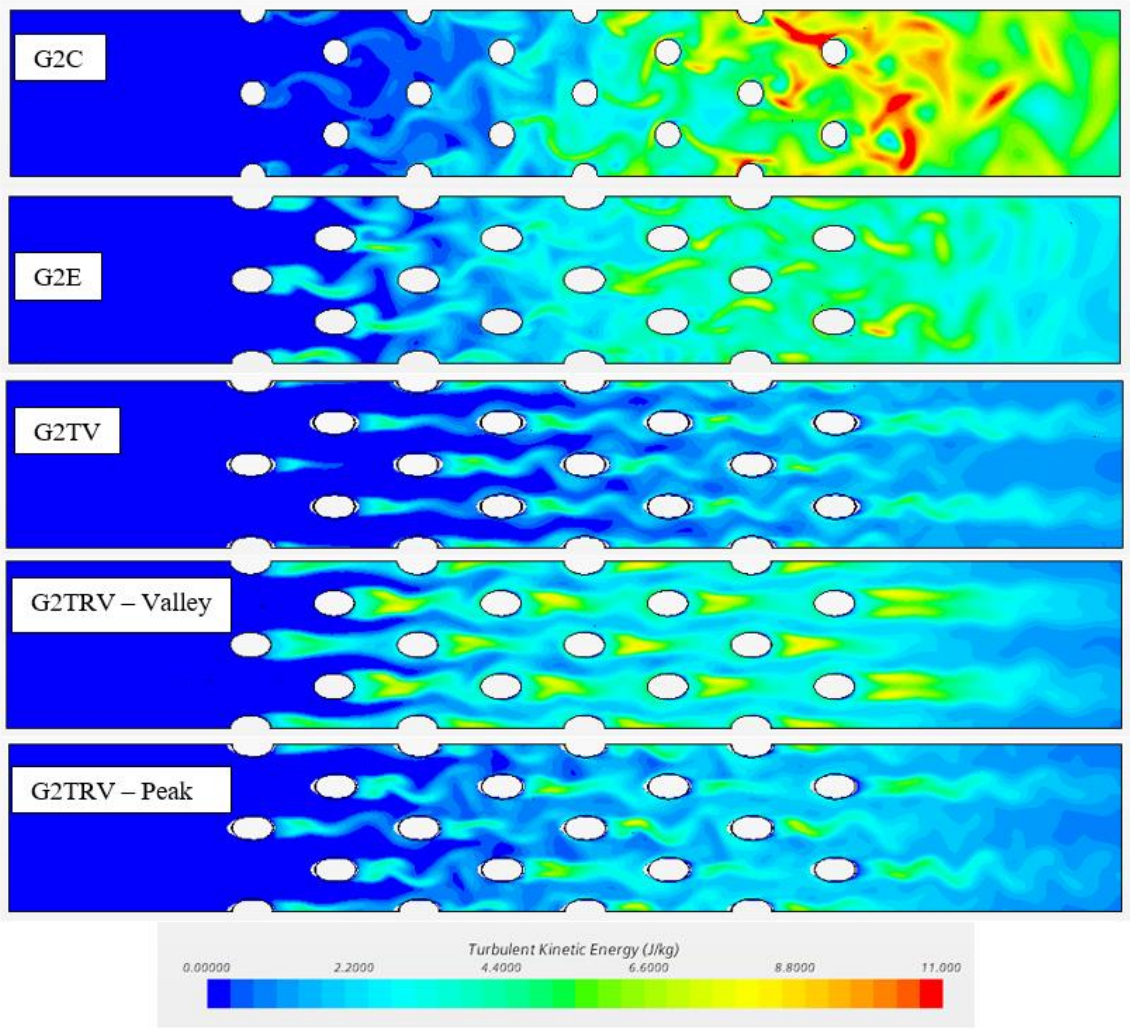

Figure 4.100 TKE contour for reduced array dimensions

This shows that the wake structure is still maintained at the core flow, but as seen in endwall Nusselt number result in Figure 4.92, due to the reduction in array size the horseshoe vortex drastically affects the wake interaction with the endwall, leading to a much narrower wake region at the endwall.

4.2.11. Infinite Pin

The top and bottom wall of the channel were set to symmetry boundary conditions in

order to simulate an infinite pin configuration. This is done to remove the wall effect on the pin and evaluate the pin thermal performance. Figure 4.101 shows the comparison between the wall bounded pins with the infinite pin configuration for pins G2TV, G2TRV and G2E.

From the figure it can be seen that by removing the top wall and the end wall the pin heat transfer is increased. Additionally, the heat transfer augmentation increases from row 1 to row 3 and then stays almost constant whereas in wall bounded pins the heat transfer decreases after row 3. This could be due to the absence of core flow to wall interaction which thereby increases the ability for the pins to extract the heat effectivity as the flow moves downstream in the channel.

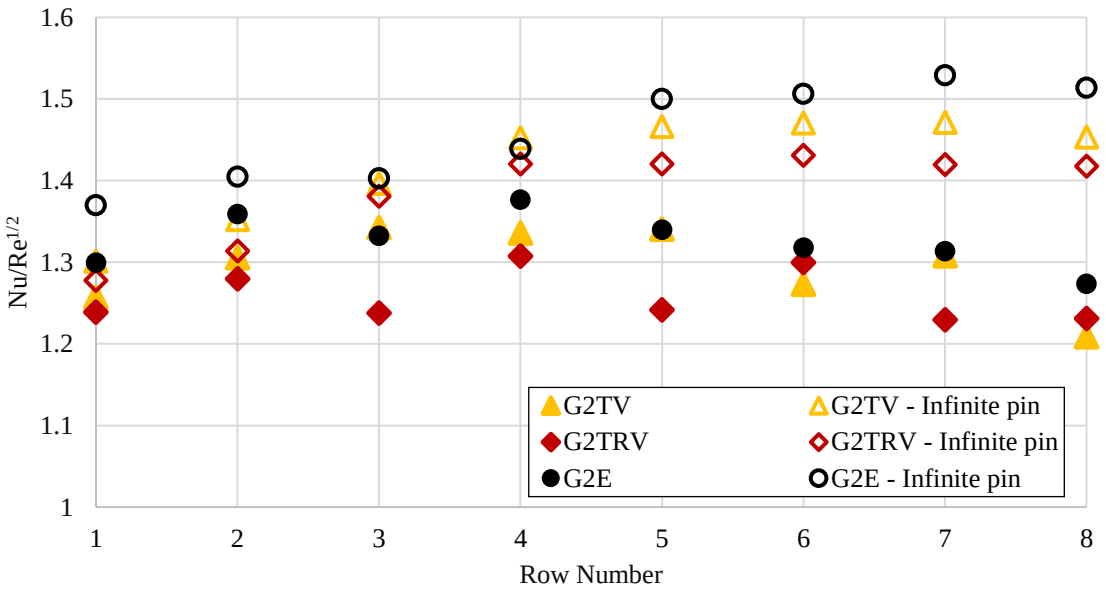

Figure 4.101 Infinite pin – pin surface average Nusselt number

Figure 4.102 shows the pressure drop across the channel. For the results we can see that the pressure drop trend is similar to wall bounded pins, but with the wall removed

there is a reduction in the magnitude of pressure drop. This is due to the absence of wall shear stress from the bottom and the top wall leading to the static pressure loss in the flow.

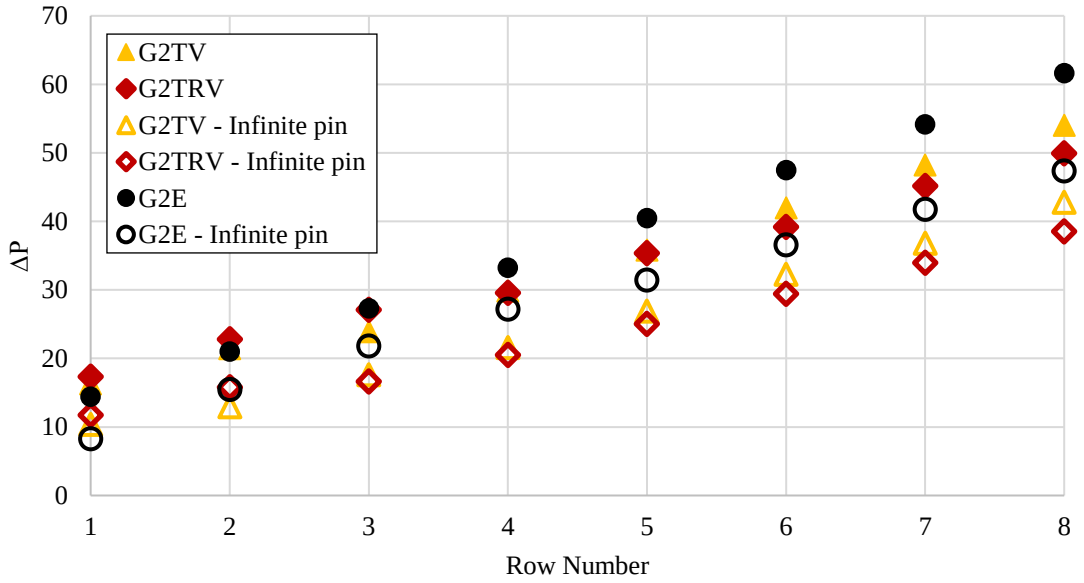

Figure 4.102 Infinite pin – Pressure drop across the channel

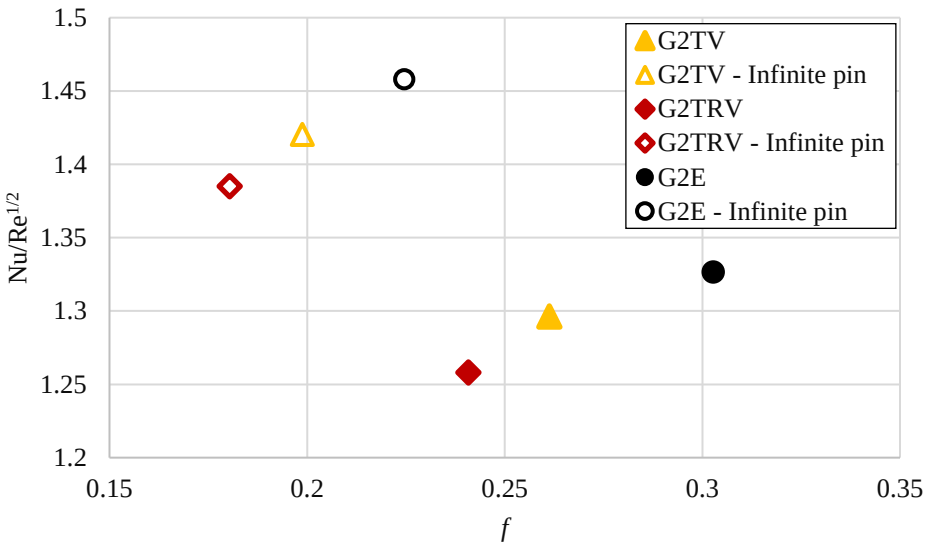

Figure 4.103 Infinite pin – Thermal performance

Figure 4.103 shows the thermal performance comparison of the infinite pin with the wall bounded pins. From the figure we can see that by removing the walls there is an improvement in thermal performance and friction factor by 10% and 24%, this is relevant to the results from the above two figures.

4.2.12. Reynolds Number Effects

A Reynolds number case of 15,000 was done for the wall bounded pins and compared to the Reynolds number case of 30,000 to see the Reynolds number effects on the pins. The 30,000 Reynolds number case is for an inlet velocity of 3.925 m/s.

Figure 4.104 – Figure 4.106 shows the average endwall Nusselt number, pin surface average Nusselt number and channel average Nusselt number in comparison to friction factor for Reynolds number case of 15,000 and 30,000.

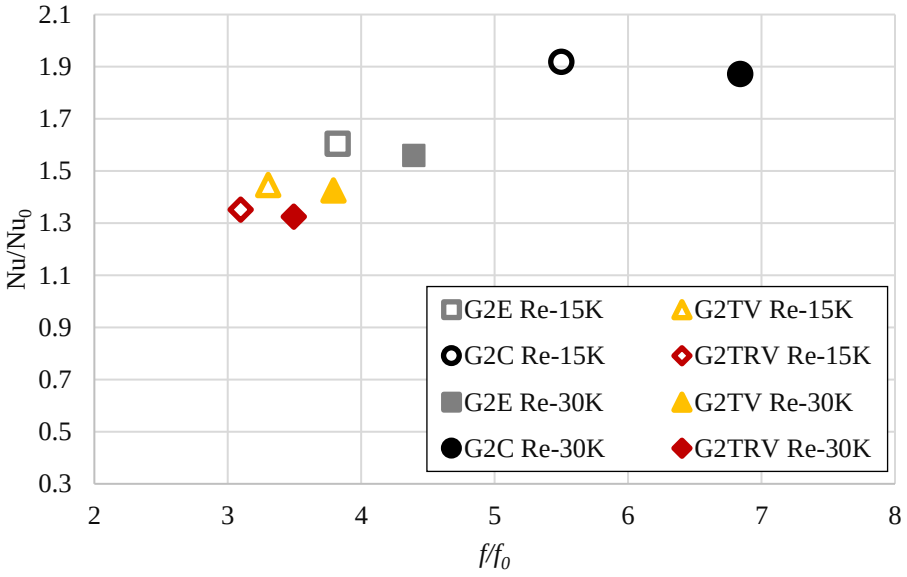

Figure 4.104 Nu vs f – Enwall average Nusselt number

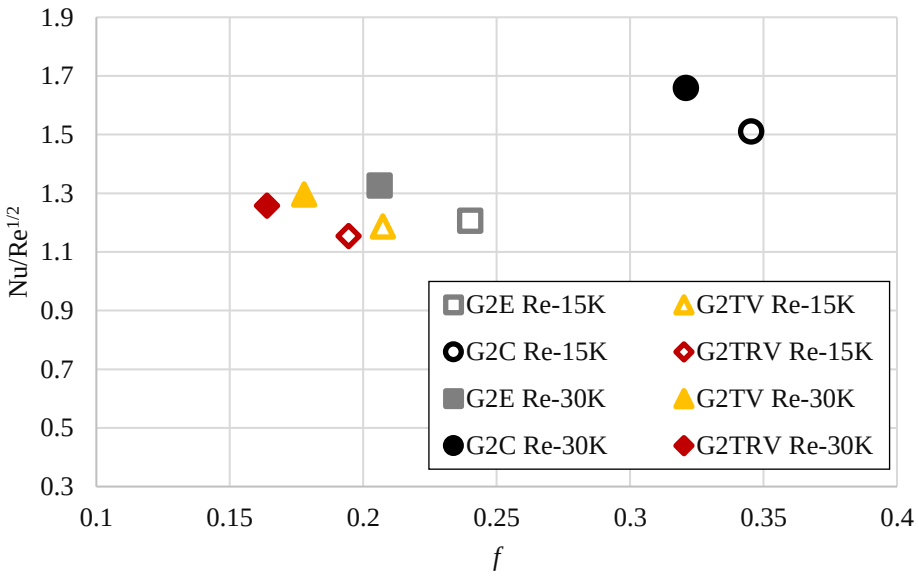

Figure 4.105 Nu vs f – Pin surface average Nusselt number

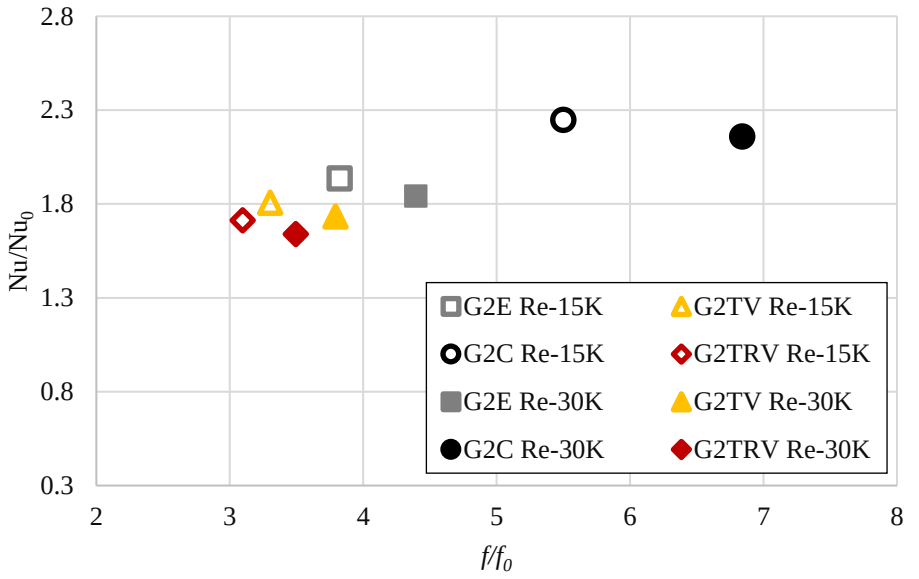

Figure 4.106 Nu vs f – Channel average Nusselt number

The Nusselt number and friction factor data for the pin fin channel are normalized with respect to data from a smooth channel, except for pins surface average in that case

the Nusselt number is normalized to get Frossling number. A lower Reynolds number is chosen for this study to maintain the already present mesh conditions. From Figure 4.105 we can see that the trend remains the same for a lower Reynolds number case, with a reduction in magnitude for pin surface average Nusselt number.

Looking at the endwall Nusselt number result in Figure 4.104, it can be seen that the normalized results for Reynolds number of 15,000 show a marginal increase in heat transfer performance with a higher reduction in pressure drop, most notably the cylindrical pin G2C. This shows us that with respect to the smooth channel case the lower Reynolds number case performs better. An average of these results are seen in the channel average Nusselt number in Figure 4.106.

4.2.13. Engineered Pin Designs Based on Bio Pin Geometries

The characteristic of the undulations are applied to the elliptical and cylindrical pin structures to see that effect in the aero-thermal performance. The pin shapes in this study is shown in Figure 4.107. The purpose of this design is to incorporate the best of cylindrical and elliptical pin structures into one pin design. As cylindrical pins are better at endwall heat transfer the bottom and top part of the pins are circular shapes and the center part of the pin is elliptical shape as elliptical pins are better in reducing pressure drop in the channel.

The design NC1 has the circular shape at the bottom and the top with the same diameter as G2C, and the elliptical shape at the center has the same major diameter as peak ellipse with the minor diameter of valley ellipse. The pin design NC2 has the same circular dimension as NC1, but the elliptical shape has the minor diameter of peak ellipse and the major diameter of valley ellipse.

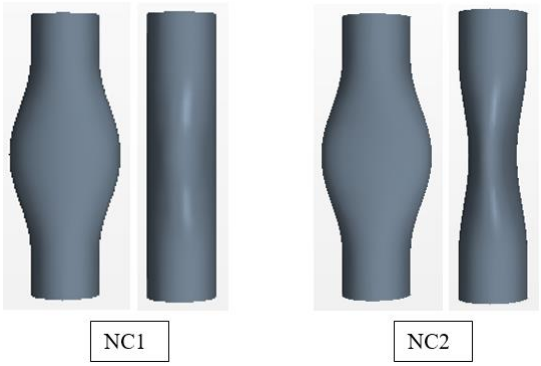

Figure 4.107 NC1 and NC2 geometry

Figure 4.108 shows the spanwise average Nusselt number for NC1 and NC2, they are compared with G2C, G2E and G2TV. From the results we can see that even though the bottom and the top of the pin has the same circular geometry the end wall results are influenced by the shape of the pin center as this contributes to the core flow to endwall interaction leading to heat transfer augmentation on the side and the wake region of the pin. This is also affected by the minor diameter of the pin center as seen by pin NC2.

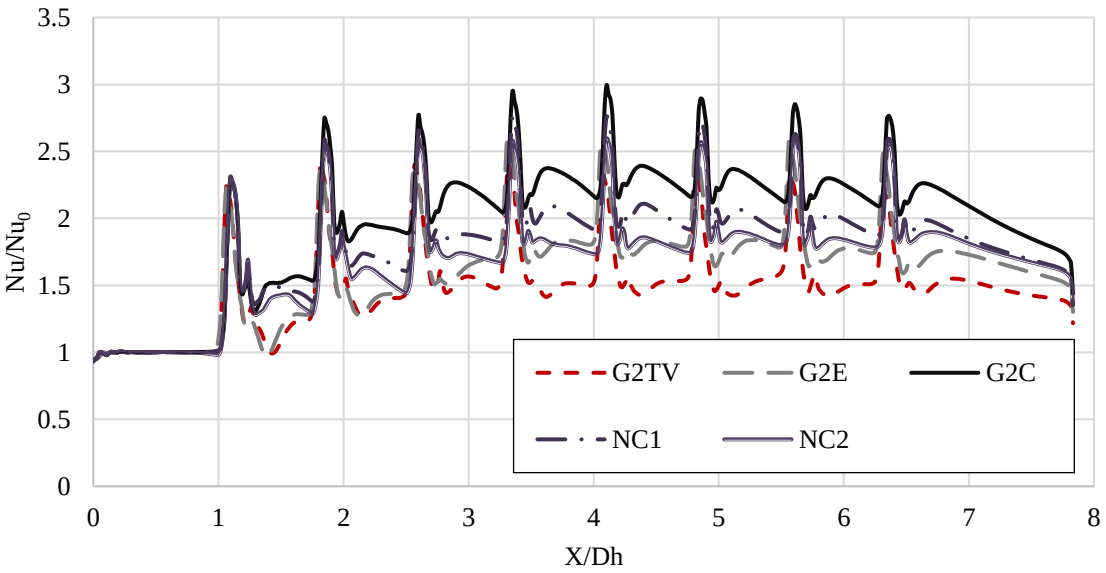

Figure 4.108 Spanwise average Nusselt number for pin NC1 and NC2

Figure 4.109 shows the pin surface average Nusselt number for NC1 and NC2. As seen from the endwall results a similar discussion can be made for pin surface average Nusselt number. As the center of the pin is slenderer the flow acceleration is much less in comparison to pin G2C, this leads to a reduction in Nusselt number. As pin NC2 has a narrower shape at the center than the pin NC1, it has a reduction in pin surface average Nusselt number as seen in Figure 4.109.

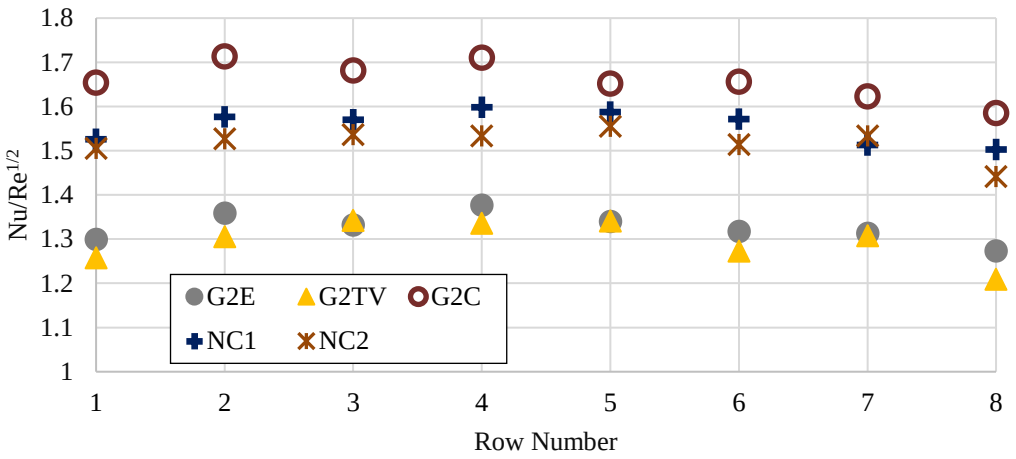

Figure 4.109 Pin surface average Nusselt number for pin NC1 and NC2

Looking at the pressure drop results from Figure 4.110 we can see that pin NC2 which has the same center dimension as the elliptical pin G2E, has almost the same pressure loss in the channel as compared to pin G2E. This shows that the pressure drop in the channel is adversely affected by the characteristic of the core flow, which gets affected by the center shape of the pin. As NC1 having the same minor diameter of G2C, its performance lies right between G2C and G2E, and the larger major diameter of the pin center helps the flow to separate later leading to a reduction in wake size which contributes to the reduction in pressure drop.

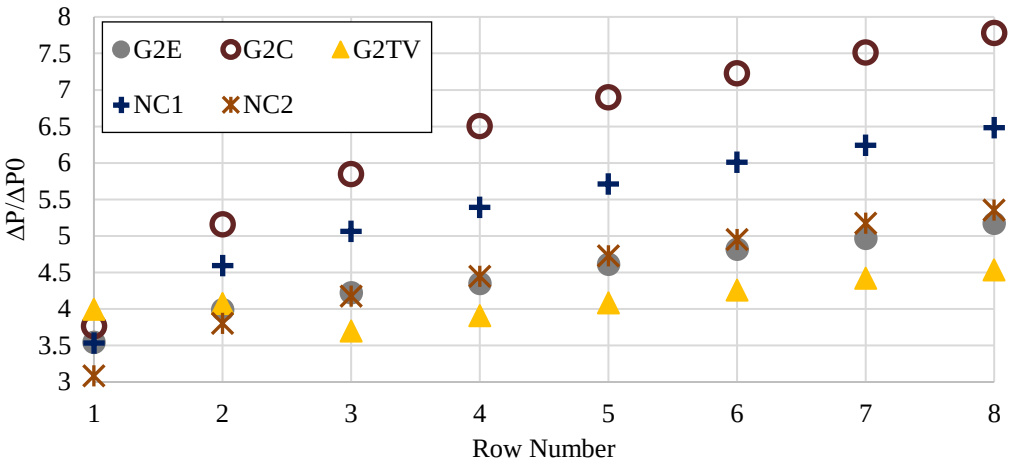

Figure 4.110 Pressure drop across the channel for pin NC1 and NC2

Figure 4.111 – Figure 4.113 shows the average endwall Nusselt number, pin surface average Nusselt number and channel average Nusselt number in comparison to friction factor for pins NC1 and NC2. The Nusselt number and friction factor data for the pin fin channel are normalized with respect to data from a smooth channel, except for pins surface average in that case the Nusselt number is normalized to get Frossling number.

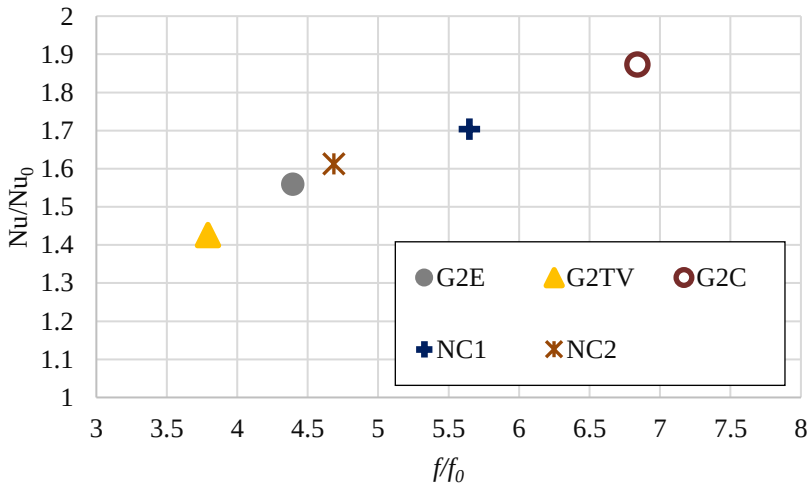

Figure 4.111 Endwall Nusselt number for pin NC1 and NC2

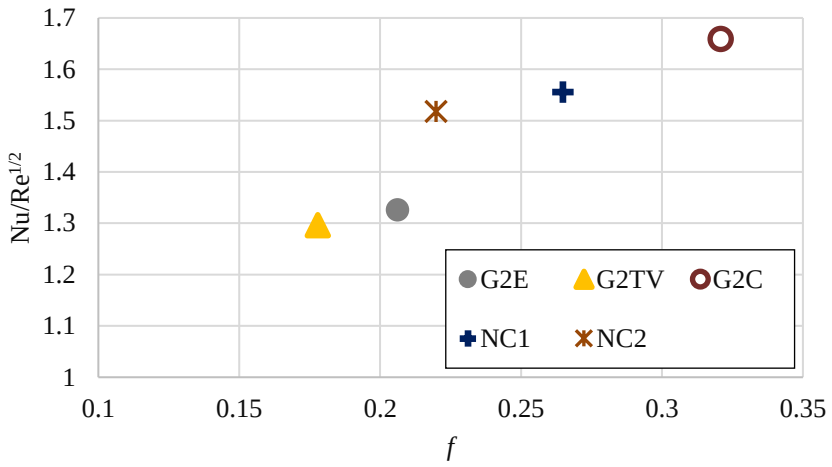

Figure 4.112 Pin average Nusselt number for pin NC1 and NC2

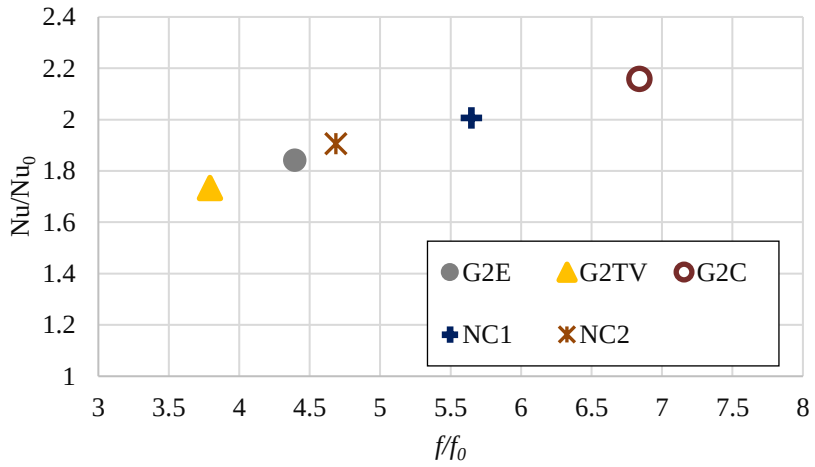

Figure 4.113 Channel average Nusselt number for pin NC1 and NC2

As seen from the pin surface average and the pressure drop results, looking at Figure 4.112 we can see that pin NC2 has an increment in heat transfer by 14% at a cost of 7% in friction factor. And as discussed before pin NC1 is right in the middle of the performance of G2E and G2C, with 17% improvement in friction factor at a cost of 6.6% in heat transfer. Where as in endwall thermal performance from Figure 4.111, we can see that the performance of NC1 and NC2 are linear with respect to G2C and G2E.

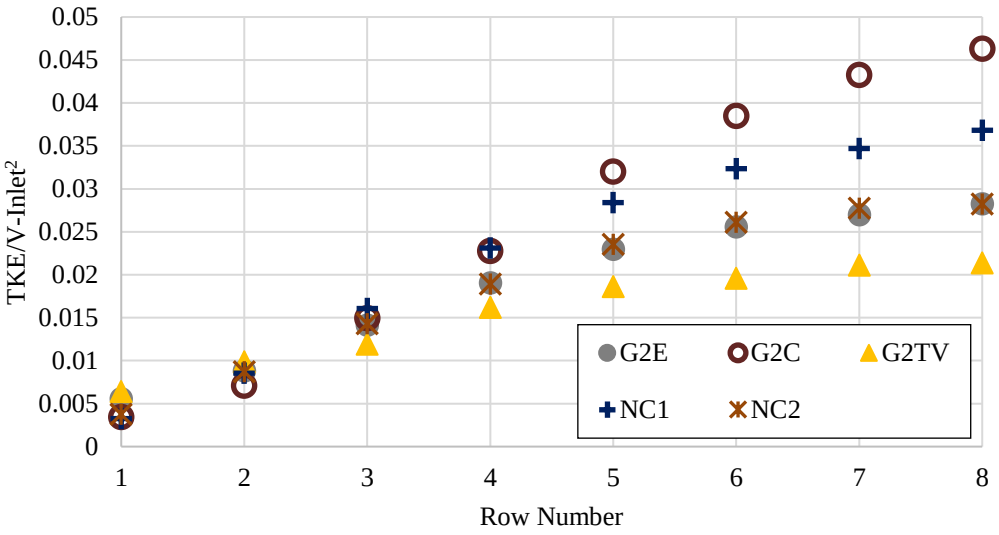

Figure 4.114 TKE across the channel in NC1 and NC2

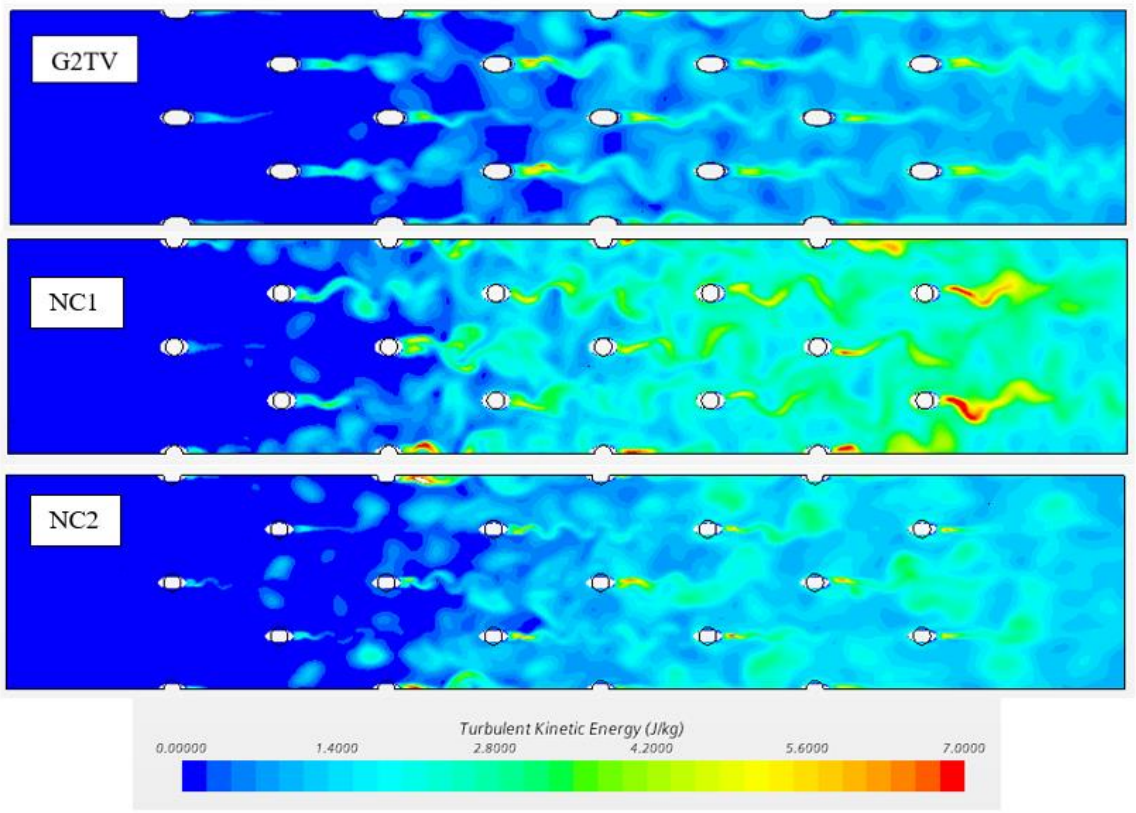

Figure 4.115 TKE contour for NC1 and NC2

Figure 4.114 shows the TKE results across the channel for NC1 and NC2. A plane is created 20 mm behind the center of the pins in the channel, and time averaged TKE value is plotted for points behind each row. From the figure we can see that the TKE trend are similar to the pressure drop trend as seen in Figure 4.110.

Figure 4.115 shows the TKE contour for pin NC1 and NC2 at 3 second solution time. From the TKE contours we can see that by having the characteristic of undulation in the streamwise and spanwise direction does aide in the reduction of wake size as seen in NC2. The result from this section shows that TKE and flow acceleration are the primary contributors to heat transfer.

4.2.14. Laminar Case Study

Laminar case study was conducted for the pins with symmetry boundary conditions on the top and the bottom wall (infinite pin) to determine the effects of having and not having turbulence fluctuations in the flow domain and its effects on pin surface heat transfer. The pins used in this study are G2TV and G2TRV. The Nusselt number is normalized to get Frossling number. Figure 4.116 shows the comparison for a laminar case and a turbulence model for pin surface average thermal performance.

From the figure we can see that from switching from the turbulence model to laminar, we see a decrease in heat transfer performance from row 4 pins. This is due to the absence of turbulence fluctuations. In comparison to literature for a wall bounded pin setup the heat transfer performance on the pins plateaus out after row 4 pins this could be seen in the next section, this behavior could be seen in the turbulence case form the figure. According to the literature by Williamson (1996), the Reynolds number used in the study (with respect to pin diameter not with the 2H) is within the shear – layer

transition regime (Re_D = 1000 to 200,000).

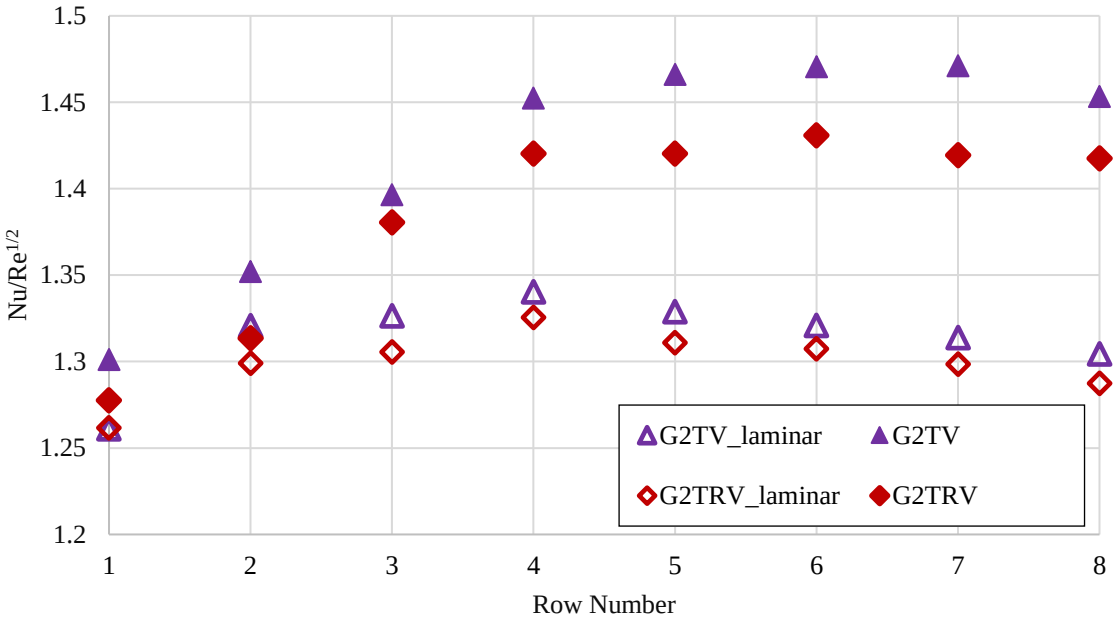

Figure 4.116 Pin surface average Nusselt number laminar case

In this regime the flow around the cylinder has a turbulent transition point at which the shear layer separates leading to the Kelvin – Helmhotz instability and creation of Karman vortices, which are turbulent. In a pin fin channel flow these vortices lead to flow mixing and the turbulence fluctuation in those flow structure leads to the augmentation of heat transfer on the pin surface downstream of the non-wall bounded pins (Williamson, 1996).

This is seen in turbulence model of RANS even in infinite pin configuration. Whereas in the laminar case there is a reduction of heat transfer rate as we move downstream. This suggest the use of turbulence model is more appropriate in modelling a bank of pins which are not bounded by top and bottom walls, but a more detailed study with

experimental comparison needs to be done to properly understand the relation between the heat transfer characteristic and CFD models in an infinite pin configuration.

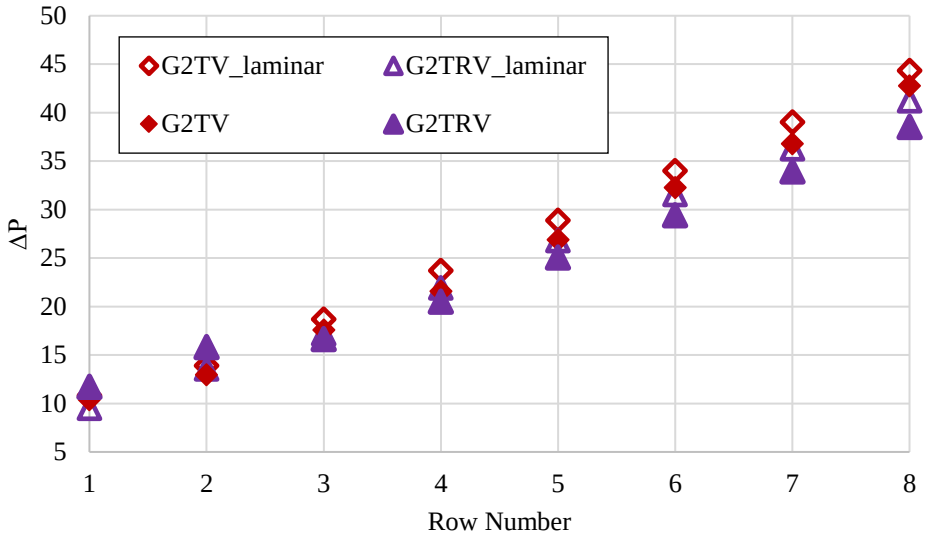

Figure 4.117 Pressure drop across the channel for laminar case

Figure 4.117 shows the pressure drop across the channel for a laminar case in comparison to turbulence model. From the figure we can see that using a laminar case does affect the pressure drop results. As pressure drop is calculated by the averaging a plane section between each pin rows, the absence of turbulence fluctuation does contribute to the loss of static pressure across the bank of pin fins.

Figure 4.118 shows the thermal performance of the laminar case with the turbulence model. From the figure we can see that the difference between the fluid model cases for pin G2TV is 11% for friction factor and 6% for heat transfer, and about percentage 8% in friction factor and heat transfer rate for pin G2TRV.

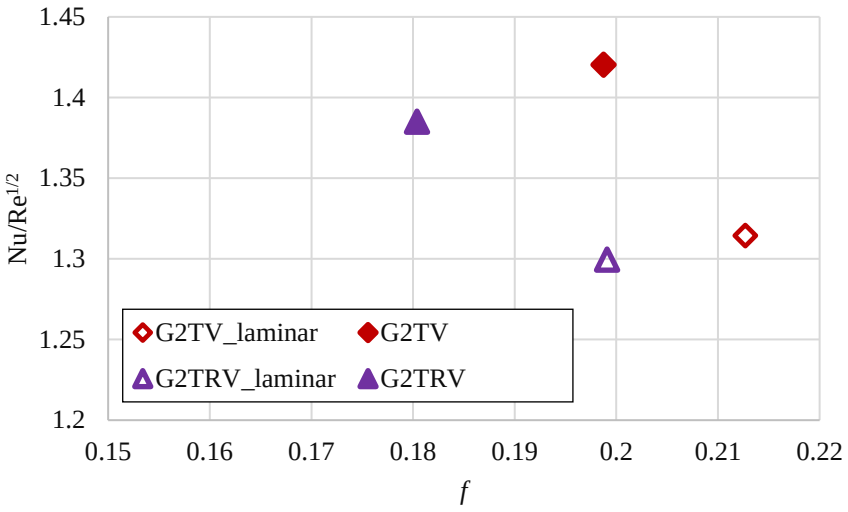

Figure 4.118 Thermal performance of laminar case

4.3. Experimental Results – Initial Pin Design

The initial pin design consists of pins CP1, EP1, BP1 and BP2. Due to experimental limitations only pins CP1, BP1 and BP2 were studied, and the Reynolds number used in CFD could not be matched, instead three Reynolds numbers 2,000, 4,000 and 12,000 was used in this preliminary experimental study. The Reynolds number is based on the inlet velocity of 2.15 m/s, 4.15 m/s and 12.5 m/s, CP1 diameter (0.15 m) and the inlet cross sectional area of the test section.

4.3.1. Test Setup Validation

Initially the test setup is validated with the results from literature to give confidence in the measurement techniques used in this study, also at the same time the ESM technique is validated with results from literature. Ames, Dvorak & Morrow (2005) obtained midline circumferential distribution of Nusselt number for a single pin through rows 1-5 of a staggered pin-fin array in the form of Frossling Number ($Nu/Re^{1/2}$) for Reynolds numbers of 3,000, 10,000 and 30,000. This circumferential distribution was averaged in

order to obtain a single value of Nusselt number for each row and Reynolds number with a reported uncertainty of ± 6% (Ames, Dvorak & Morrow, 2005). The experimental setup with pin CP1 was run for 3 Reynolds numbers, 3000, 10,000 and 30,000. The Reynolds number were calculated based on the maximum velocity to match literature.

The uncertainty in this experiential study is calculated by using root sum square method (Moffat, 1998; Prasad & Ricklick, 2017). The uncertainty for the three Reynolds number 3,000, 10,000 and 30,000 are calculated to be ± 2.4%, ± 1.1% and ± 1%. The uncertainty for pin surface average Nusselt number for the three Reynolds number are calculated to be ± 6.5%, ± 5.6% and ± 5.6%. The uncertainty for average endwall Nusselt number for the three Reynolds number are calculated to be ± 9.4%, ± 8.7% and ± 8.2%. The uncertainty for Frossling number for the three Reynolds number are calculated to be ± 6.6%, ± 5.6% and ± 5.6%. The uncertainty for channel average Nusselt number for the three Reynolds number are calculated to be ± 6%, ± 5.3% and ± 5% (Pai, Prasad & Ricklick, 2020). Figure 4.119 – Figure 4.121 show the comparison between Ames's data and the analytical solution for the cases.

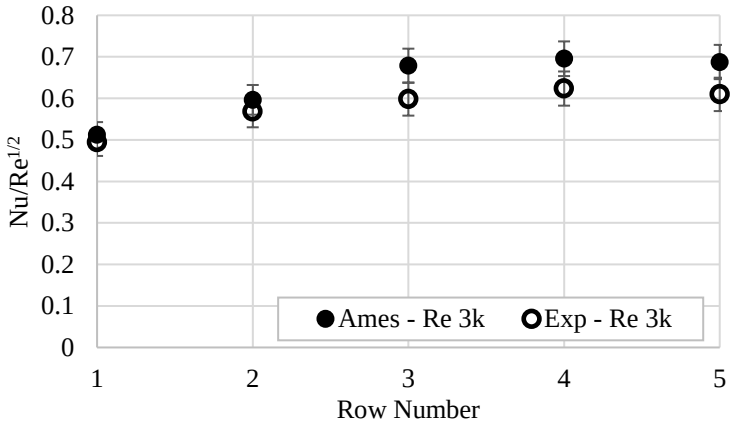

Figure 4.119 Comparison of analytical solution with Ames for Re = 3,000 (Pai et al., 2020).

In Figure 4.119, ‘Exp’ represents experimental data computed from endwall temperatures using ESM method. The values obtained are in close agreement with Ames’s data. The highest and lowest percentage difference in Frossling number is about 11% obtained for row 5 and 3.5% for row 1 (Pai et al., 2020).

In Figure 4.120, for 10,000 Reynolds number case, we see that the highest and lowest percentage difference in Frossling number is about 33% for row 1 and about 0.23% for row 5 in comparison to Ames’s data. From rows 3 – 5 the experimental data is in good agreement with Ames. This gives validity to the ESM method (Pai et al., 2020).

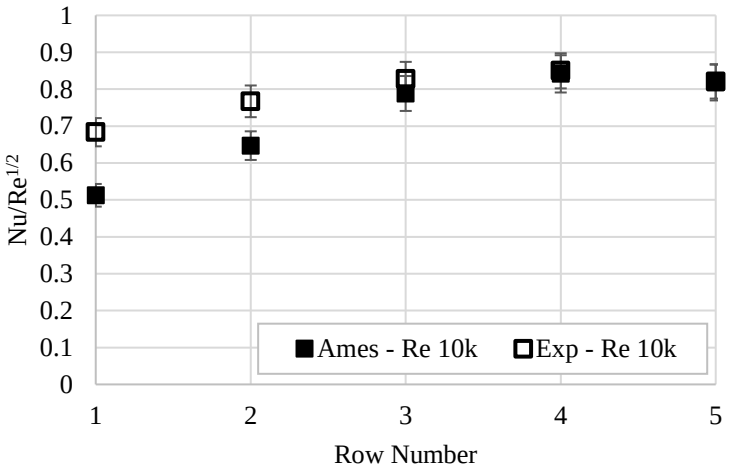

Figure 4.120 Comparison of analytical solution with Ames for Re = 10,000 (Pai et al., 2020).

In Figure 4.121, we see that all rows are in good agreement with Ames’s data. The highest and lowest percentage difference in Frossling number is about 8.7% for row 3 and about 1% for row 4 in comparison to Ames (Pai et al., 2020). The analytical solution with its uncertainty error range presented in these figures are within the uncertainty range given by Ames. It is evident from these results that ESM is in good agreements with

Ames' experimental data (Pai et al., 2020).

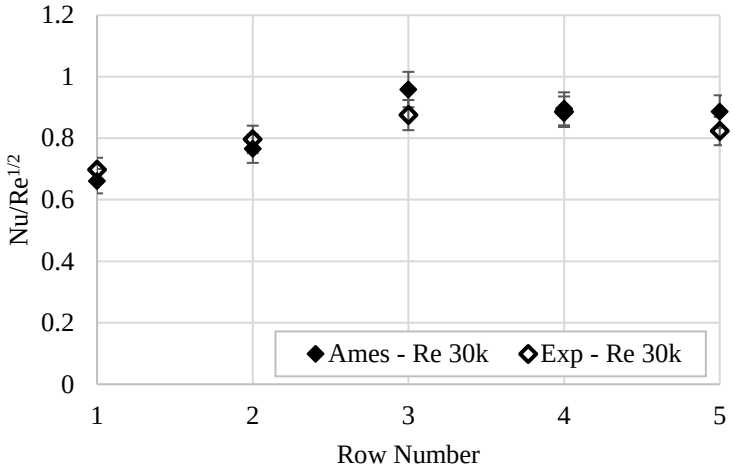

Figure 4.121 Comparison of analytical solution with Ames for Re = 30,000 (Pai et al., 2020).

Figure 4.122 and Figure 4.123 are plots of the pin, endwall and channel averaged Nusselt numbers for the different Reynold's number cases, compared to the previous work done by Ames et al. (2007), Metzger & Haley (1982) and VanFossen (1982).

From Figure 4.122 it becomes clear that the pin surface Nusselt numbers are higher than the endwall by about 20 – 40%, which is consistent with previous findings of Chyu et al. (1999), VanFossen (1982), Dabagh & Andrews (1992) It should be noted that pin surface average Nusselt number shown in Figure 4.122 is an average of the 8 rows of pin surface average Nusselt number that were obtained using the ESM in the previous section and also from Ames' experimental data (Pai et al., 2020).

The experimental pin average Nusselt number for the different Reynold's number cases were compared to the data from Ames et al. (2007). The experimental pin data has good agreement with Ames et al. (2007), with a maximum and minimum percentage

difference of 7.3% and 6.3% (Pai et al., 2020). On comparison, the experimental endwall Nusselt number has good agreement with the data from Ames et al. (2007), Metzger & Haley (1982) and VanFossen (1982). The uncertainty for Ames experimental endwall data was given to be ± 9%.

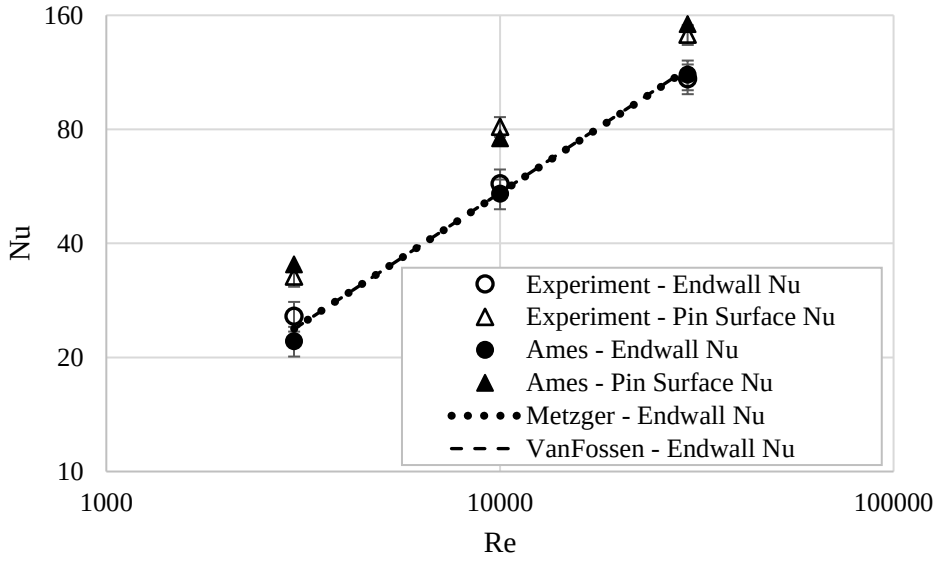

Figure 4.122 Comparison of average endwall and pin Nusselt numbers (Pai et al., 2020).

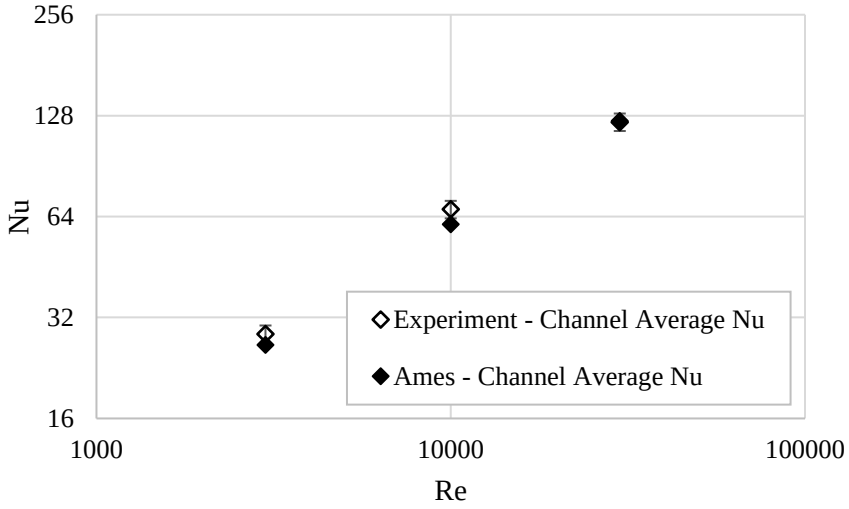

Figure 4.123 Comparison of Channel average Nusselt number (Pai et al., 2020).

In Figure 4.123 the channel average Nusselt number data presented, is thus an area weighted average, weighing in the contribution of the pin and endwall based on the corresponding area, assuming all 56 pins saw a heat transfer coefficient equal to the average of the 12 pins tested in the present study (Pai et al., 2020).From Figure 4.123, we can see that the area weighted channel average of the Nusselt number is in close agreement with Ames et al. (2007). On comparison, the maximum and minimum percentage difference was about 10.7% and 0.8% (Pai et al., 2020).

4.3.2. Endwall Nusselt Number

Figure 4.124 shows the endwall Nusselt number contour post processed from TSP for Reynolds number of 12,000. Figure 4.125 – Figure 4.127 shows the spanwise average endwall Nusselt number for the pins CP1, BP1 and BP2 for three Reynolds number 2,000, 4,000 and 12,000.

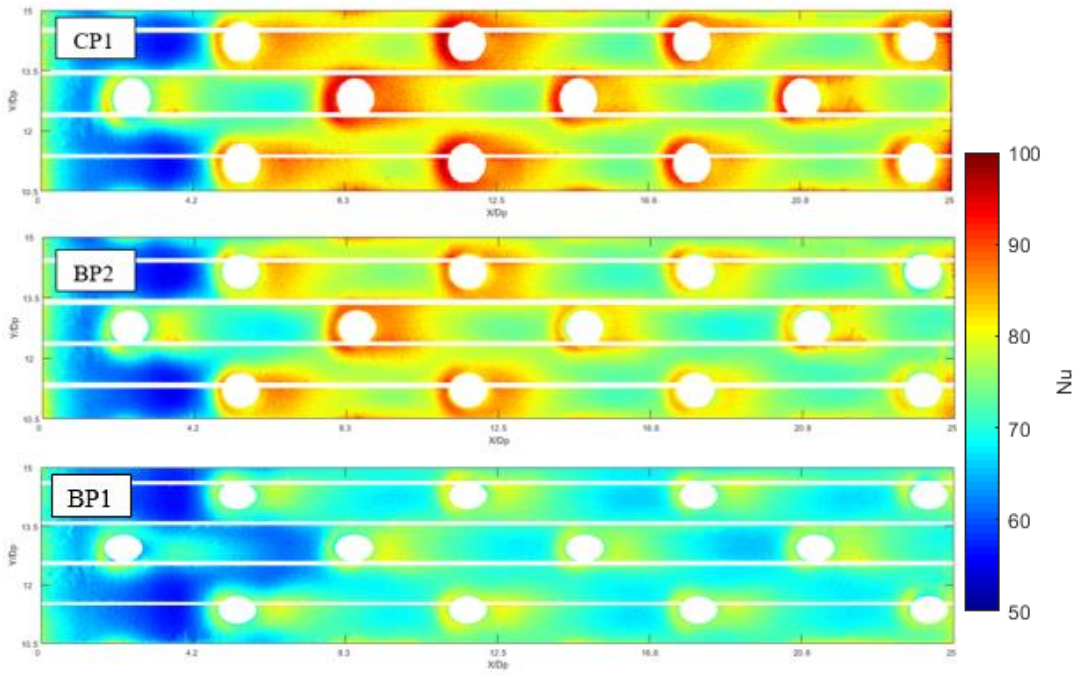

Figure 4.124 Endwall Nusselt number contour for Reynolds number = 12,000

The Nusselt number result is normalized to get Frossling number. From the Nusselt number contour we can see that the best performing pin is the cylindrical pin CP1, followed by BP2 and BP1. Looking at the wake created by the first row of pins on the endwall, we can see that the cylindrical pin CP1 has a wider wake region, endwall wake region is similar to CP1 and BP1 the elliptical pin has a narrower wake region leading to a lower heat transfer rate.

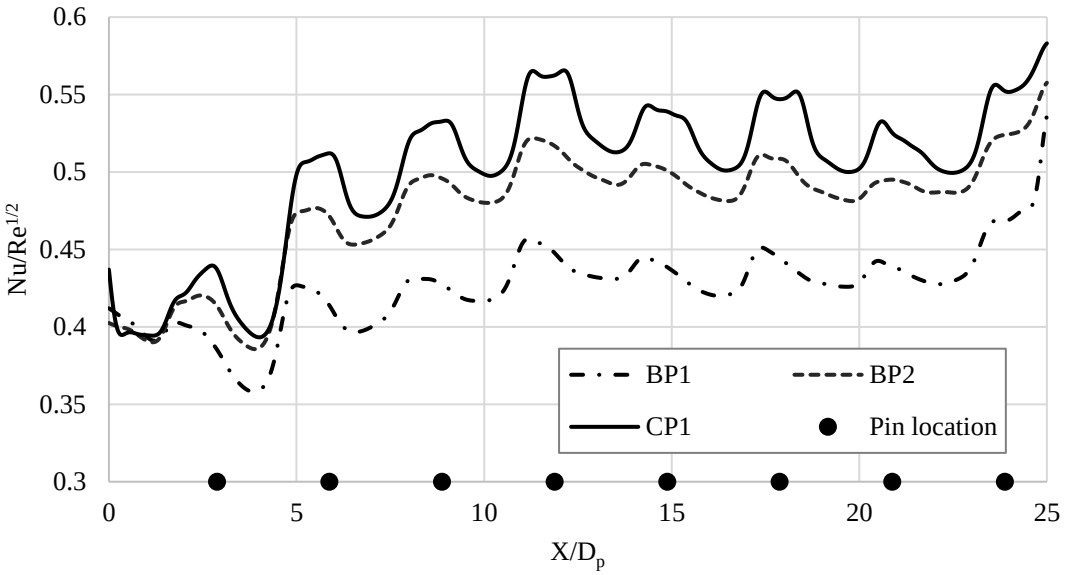

Figure 4.125 Spanwise average endwall Nusselt number for Reynolds number = 2,000

As the flow moves through the channel the magnitude of the wake generated by the pins affect the flow mixing in the channel leading to different augmentation of heat transfer rates as seen in the Figure 4.124. This is also seen in the computational study for the initial pin design. From Figure 4.125 – Figure 4.127 we can see that for all Reynolds number cases, pin CP1 is the best performer followed by pin BP2 and BP1. This trend was also captured by the computational study for higher Reynolds number case.

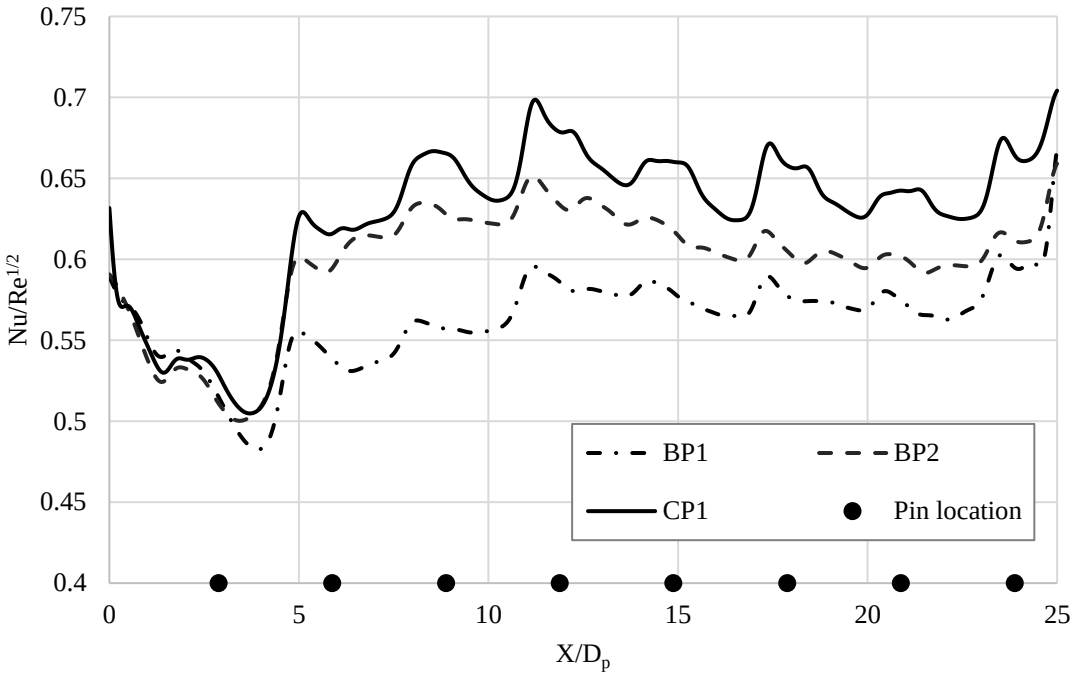

Figure 4.126 Spanwise average endwall Nusselt number for Reynolds number = 4,000

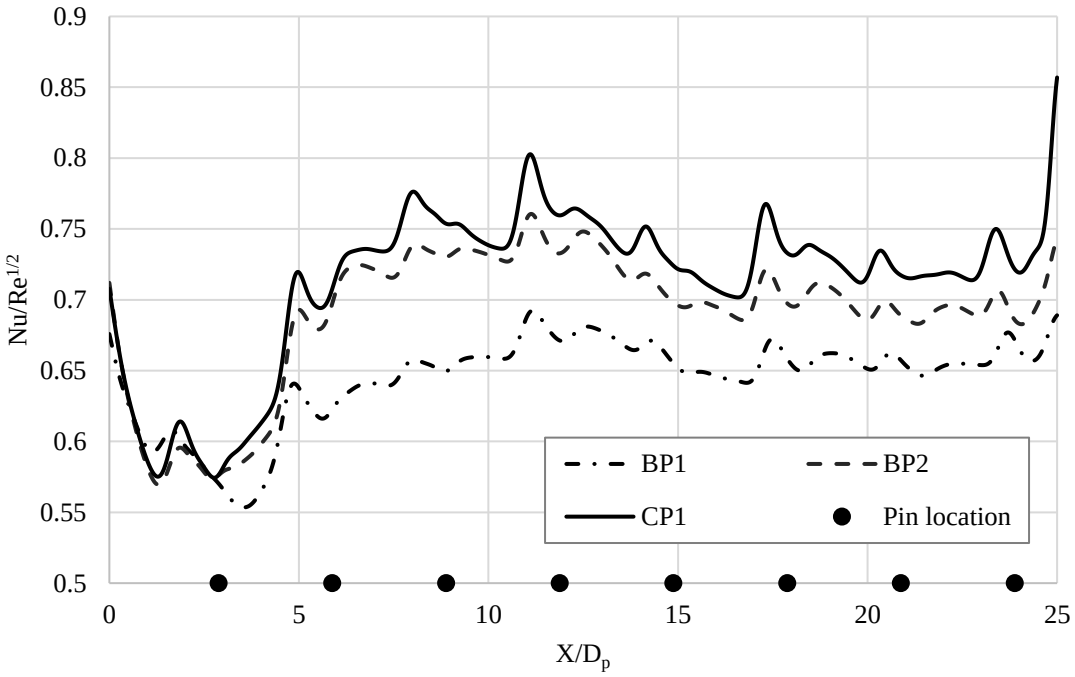

Figure 4.127 Spanwise average endwall Nusselt number for Reynolds number = 12,000

4.3.3. Pressure Drop Along the Channel

The pressure data are obtained from the side wall in the test section. Each port is located between two rows of pins, first port is located before the first row and the last port is located after the last row. The pressure drop across the channel is calculated based on the difference between the first port and the subsequent port similar to the computational study. Figure 4.128 – Figure 4.130 shows the pressure drop data. The experimental uncertainties are approx. 11%, 7% and 5% for Reynolds number case of 2000, 4000 and 12000.

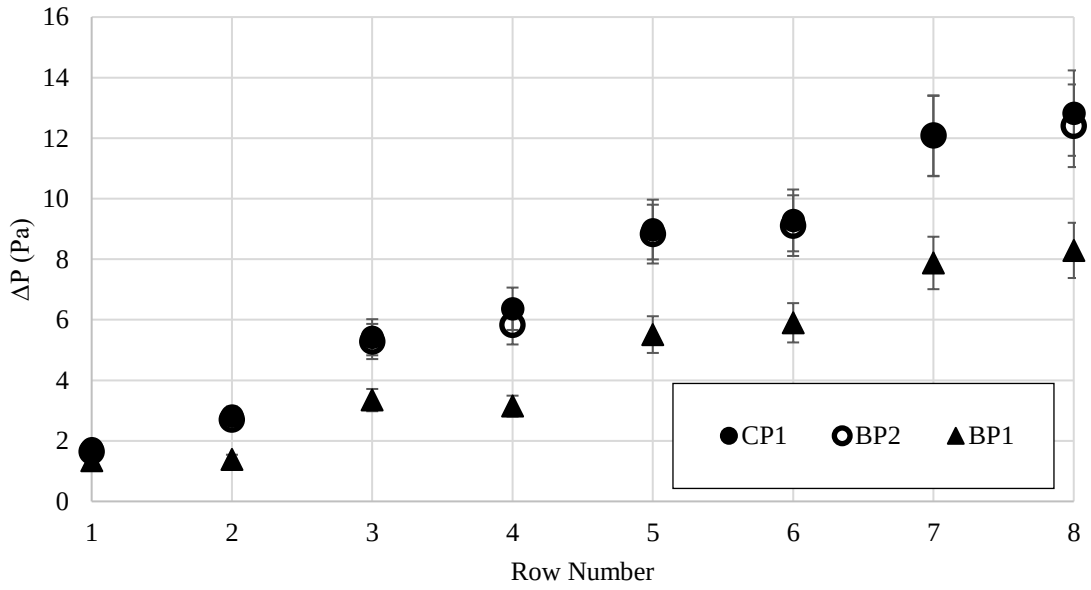

Figure 4.128 Pressure drop along the channel for Reynolds number = 2,000

From these figures we can see that the pressure drop across the channel for the three pins are similar for all the Reynolds number, with pin CP1 and BP2 having the highest pressure drop flowed by pin BP1. Since pin CP1 and BP2 are cylindrical in nature the wake produced by these pins are larger in magnitude compared to pin BP1 which in

elliptical in nature this leads to a reduction in static pressure loss across the channel.

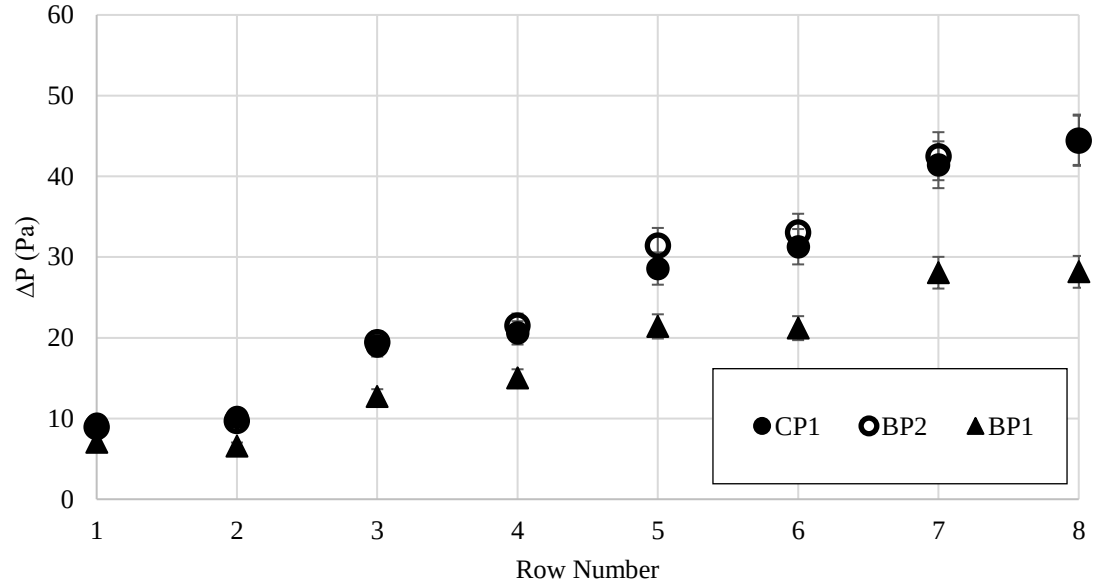

Figure 4.129 Pressure drop along the channel for Reynolds number = 4,000

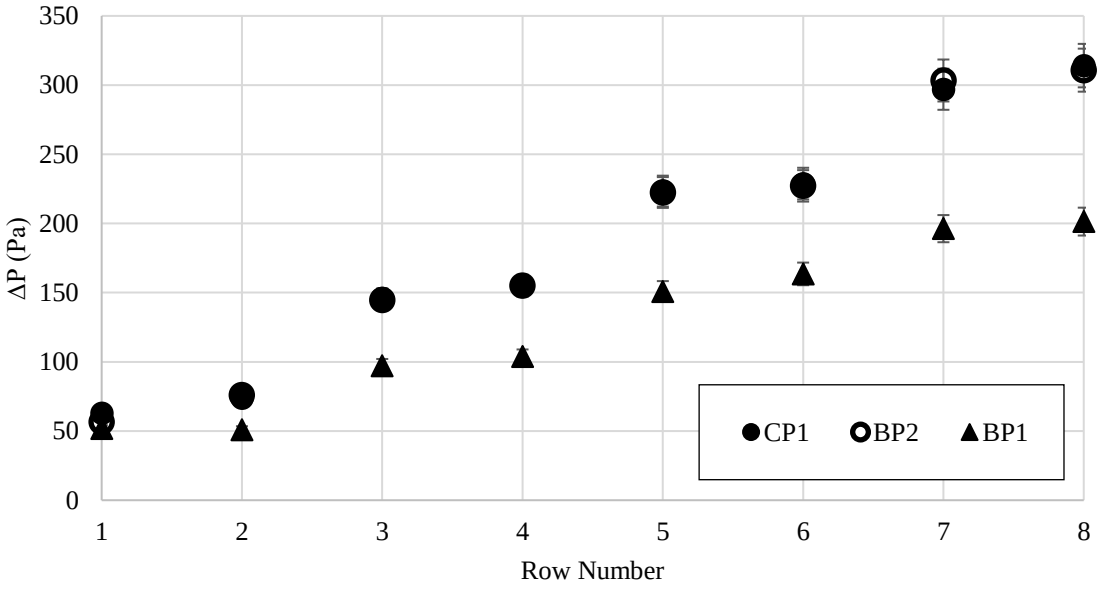

Figure 4.130 Pressure drop along the channel for Reynolds number = 12,000

4.3.4. Reynolds Number Effects

Figure 4.131 shows the Nusselt number variation across different Reynolds number. From this result, it can be seen that the heat transfer performance between pin CP1 and BP1 is maintained between 10 – 15%. Whereas BP2 has almost the same performance as CP1. The uncertainty in the results is approx. 9.6% for Reynolds number of 2,000 and approx. 9.1% for Reynolds number case of 4,000 and 12,000. The Reynolds number has an uncertainty of approx. 3% overall.

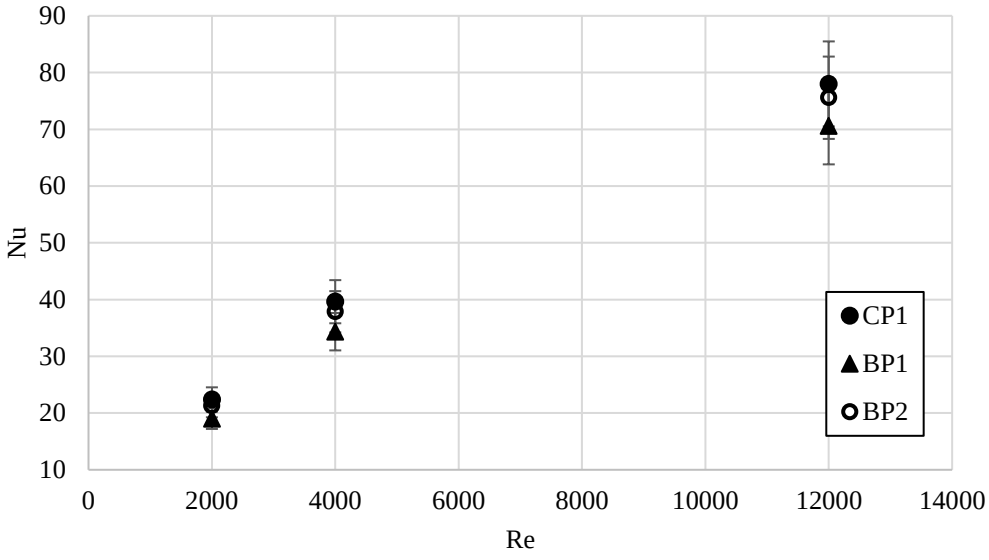

Figure 4.131 Nusselt number over various Reynolds number

Figure 4.132 – Figure 4.134 shows the thermal performance of the pins for the three Reynolds number. The experimental uncertainties are approx. 10% for normalized Nusselt number and 9% for normalized friction factor for Reynolds number case of 2,000, 9% and 5% for Reynolds number case of 4,000, and 9.3% and 3.5% for Reynolds number case of 12,000.

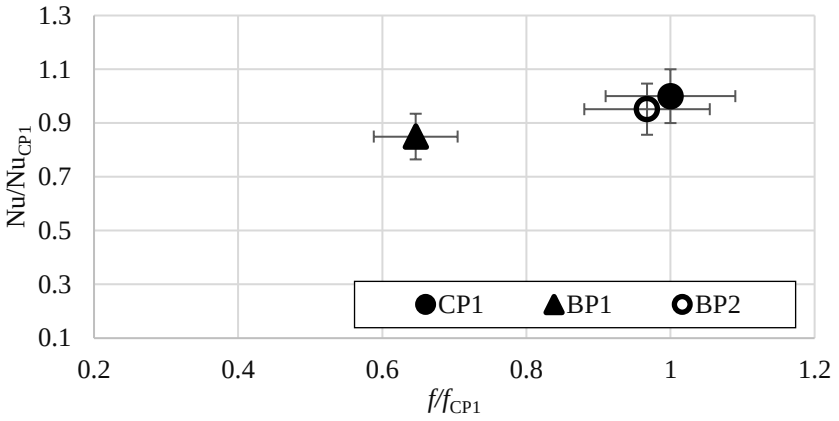

Figure 4.132 Thermal performance for Reynolds number = 2,000

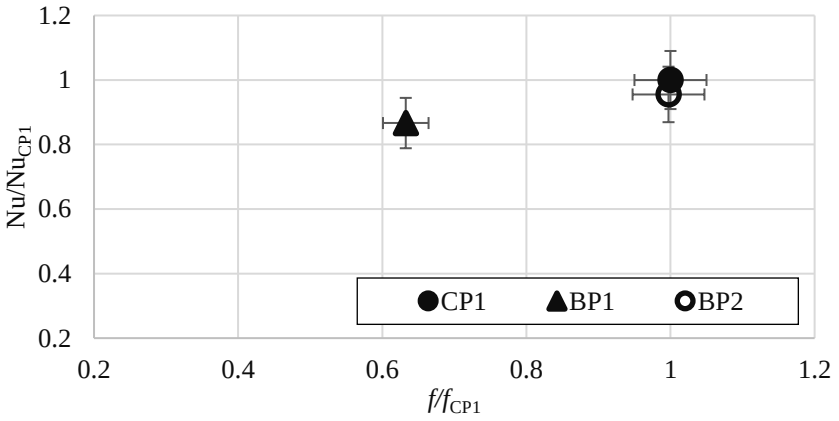

Figure 4.133 Thermal performance for Reynolds number = 4,000

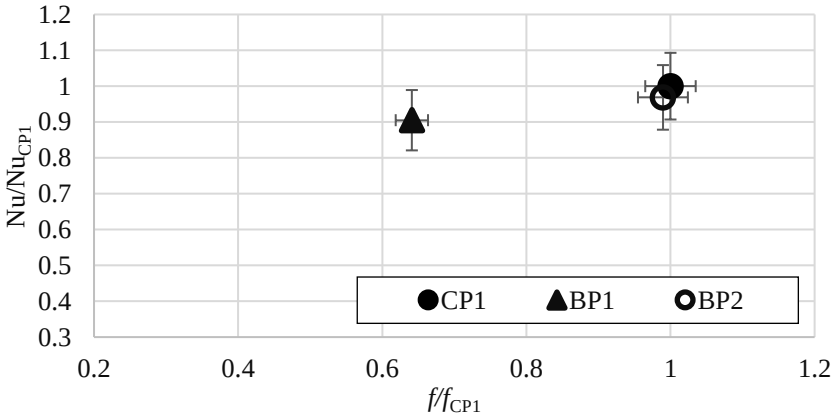

Figure 4.134 Thermal performance for Reynolds number = 12,000

Since the Nusselt number and friction factor are normalized with respect to CP1, any data point above CP1 in the y axis means it performs well in heat transfer and any data point to the left of CP1 in the x axis means it performs well in pressure drop.

In terms of thermal performance standpoint we cans see from the results above that the pin BP1 in comparison to CP1 has approximately 36 % improvement in friction factor at the cost of 10 % in heat transfer for Reynolds number of 12,000. This is similar in comparison to the computational study which shows 50% improvement in friction factor at the cost of 19 % in heat transfer for the higher Reynolds number case.

4.3.5. Spectral Analysis

Pressure data is obtained from the Kulite pressure probes in time at 22.5 mm behind rows 1, 3 and 5 for a duration of 10 seconds with 2000 samples a second. The amplitude spectrum of the pressure fluctuations is then plotted with frequency for a Reynolds number case of 12,000. For the sake of brevity only one Reynolds number case number will be discussed. Plotting the pressure fluctuations will give two dominant frequencies for the pin, one related to the drag and the other related to the lift as explained in the computational study. The frequency for the drag will be twice that of the lift.

Figure 4.135 shows the FFT data for row 1 of pin CP1. Initially as seen in the figure there is a lot of noise in the lower frequency ranges which is attributed to the inlet (entrance) section, cropping the x axis gives a better range of the amplitude. Figure 4.136 – Figure 4.138 shows the FFT analysis for pin CP1, BP1 and BP2. From Figure 4.136 we can see that there are two main frequency in the spectrum around 210 Hz and 415 Hz corresponding to lift and drag generated by the pin. These are present in all three rows 1, 3 and 5.

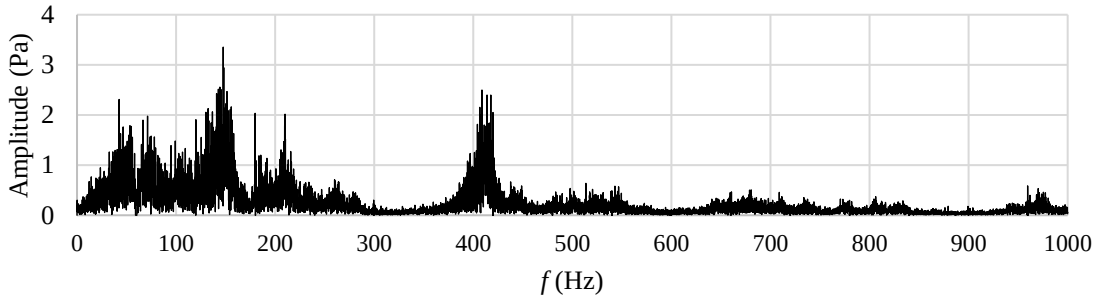

Figure 4.135 FFT experiment – CP1 row 1

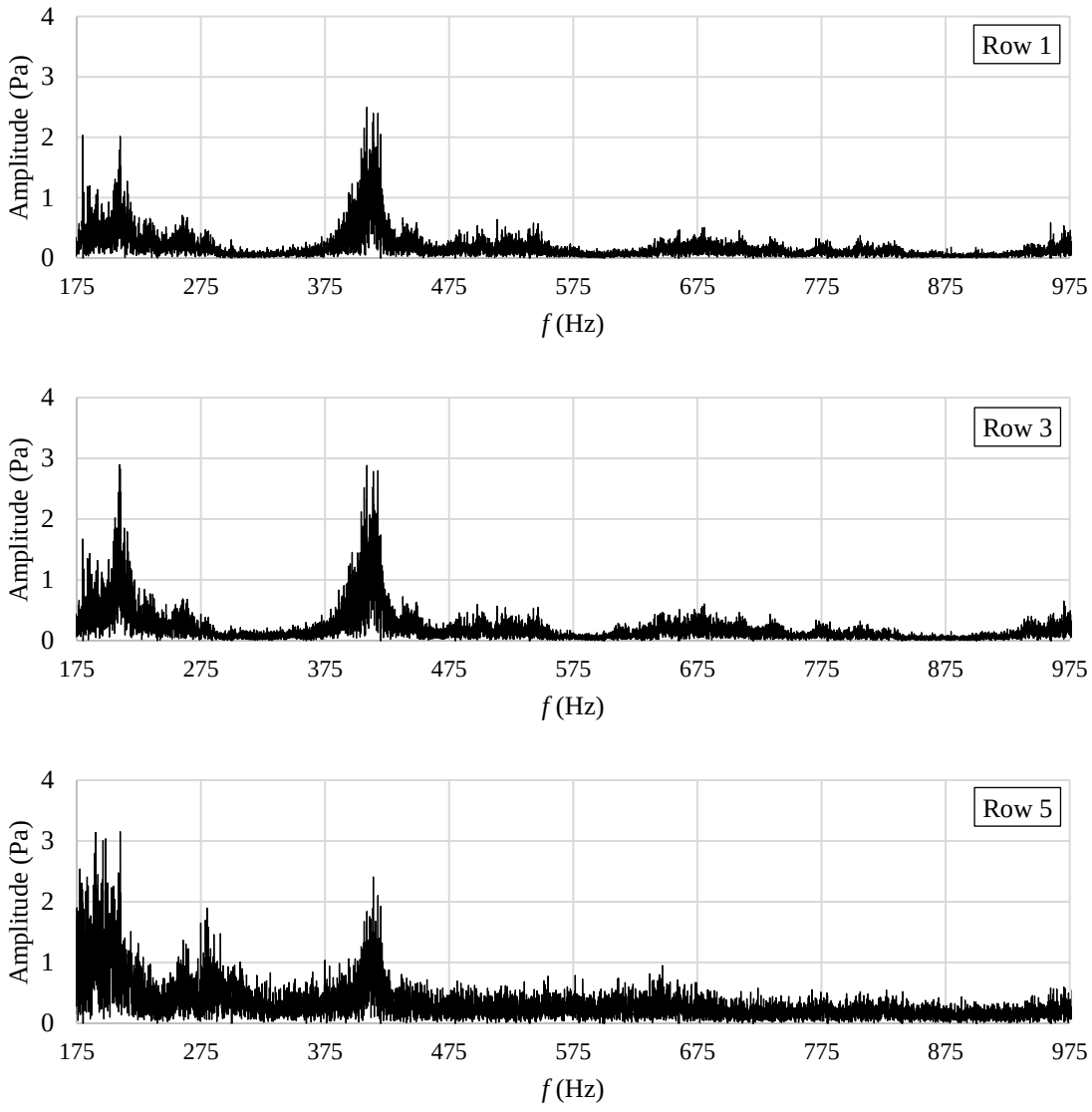

Figure 4.136 Experiment FFT – CP1

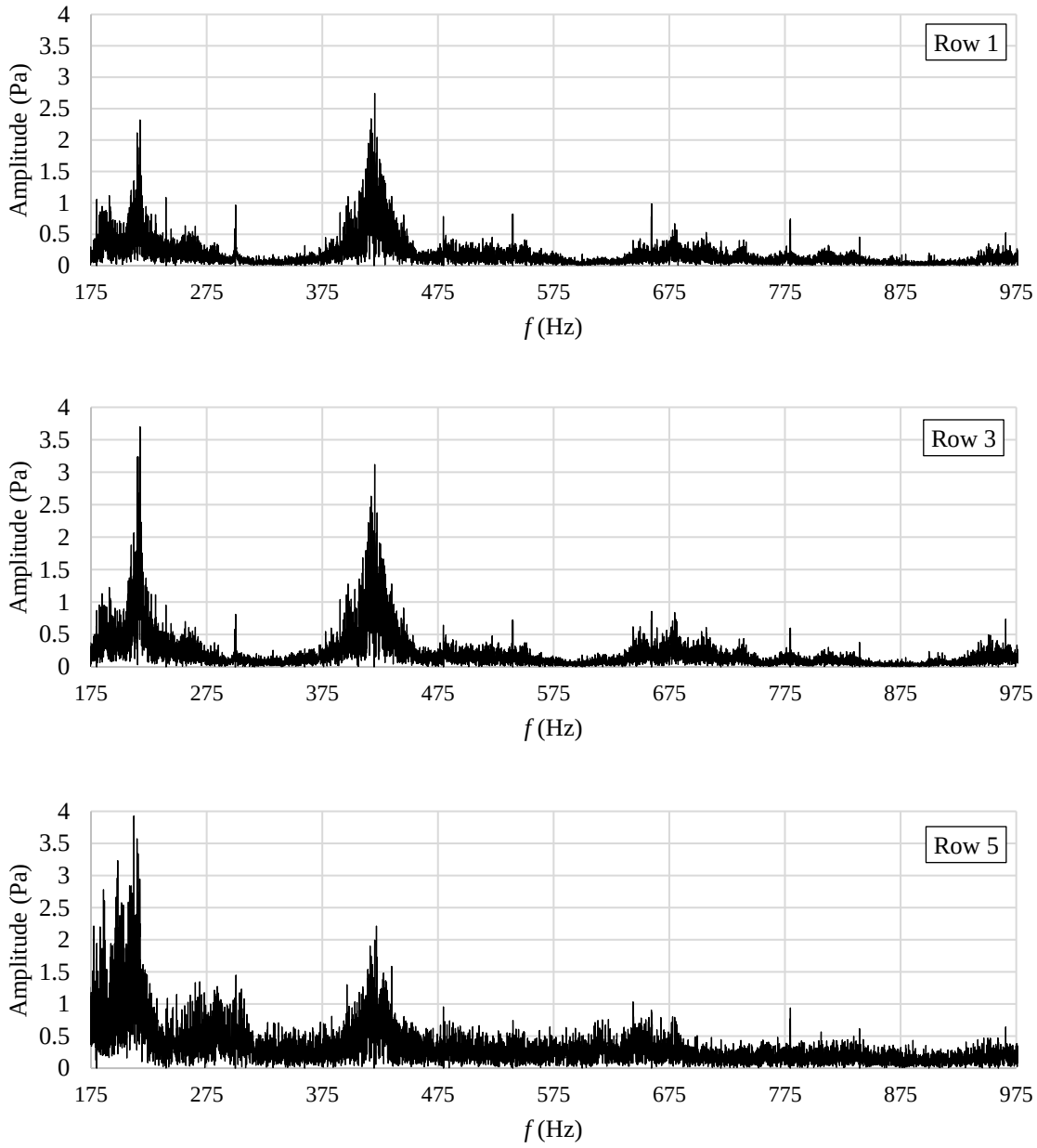

Figure 4.137 Experiment FFT – BP2

From Figure 4.137 we can see that there are two main frequency in the spectrum around 215 Hz and 420 Hz corresponding to lift and drag generated by the pin. These are present in all three rows 1, 3 and 5. These results were similar to the results seen in CP1, as seen in the steady state results the performance of pin CP1 and BP2 are similar.

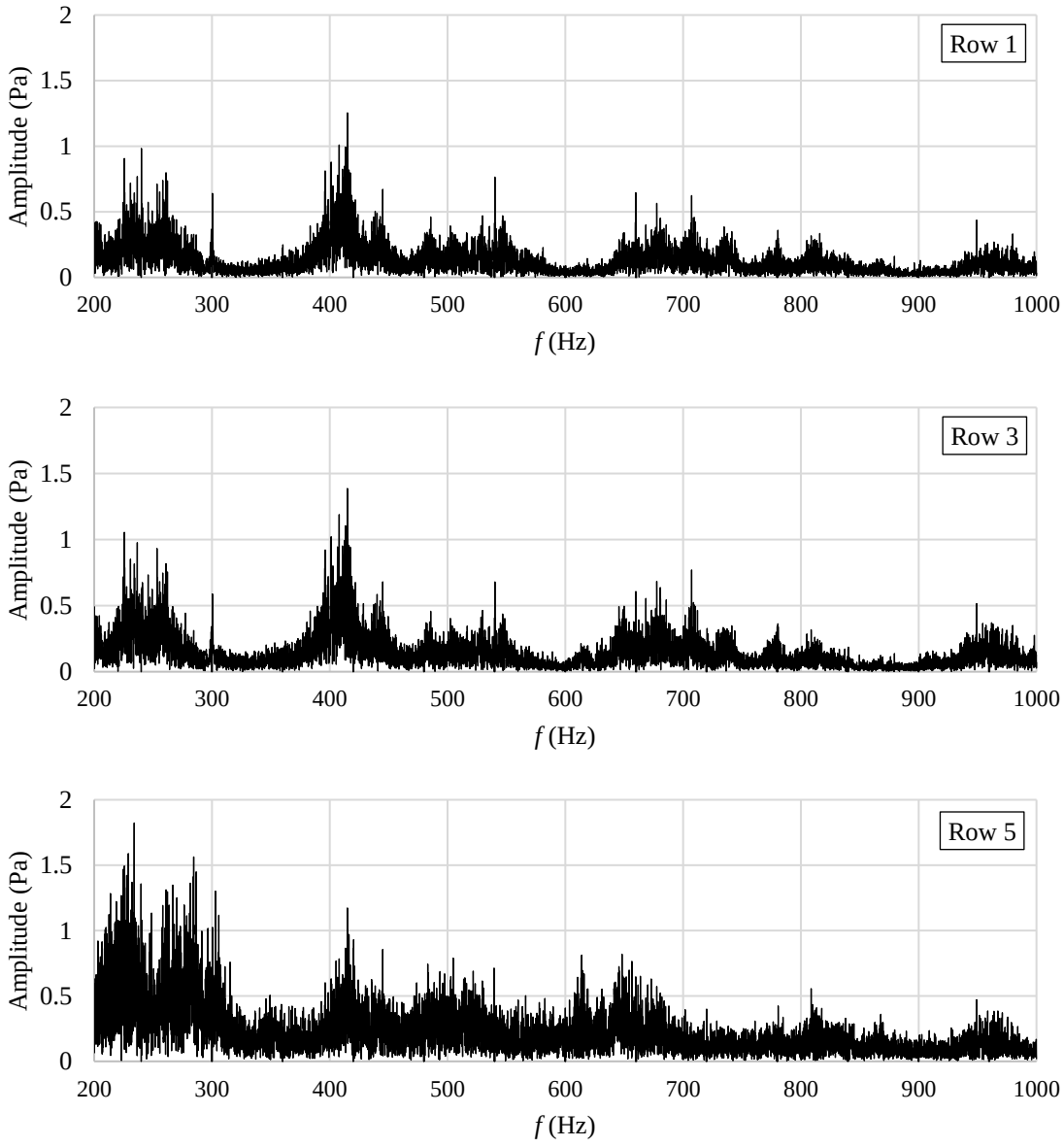

Figure 4.138 Experiment FFT – BP1

From Figure 4.138 we can see that there are two main frequency in the spectrum around 240 Hz and 415 Hz corresponding to lift and drag generated by the pin. These are present in all three rows 1, 3 and 5. In comparison to CP1 and BP1, we can see the amplitude of the frequencies are smaller suggesting a reduction in lift and drag generated by the pins, hence the magnitude of the wake is smaller.

4.4. Experimental Results – Final Pin Design

The final pin design consists of pins from group 1, 2 and 3. From the computational study we saw that the performance of group 2 and 3 pins is better than group 1 pins. Hence the thermal performance group 2 pins are evaluated experimentally. Due to experimental limitations only pins G2TV, G2E and G2TRV were studied for Reynolds numbers 15,000, 30,000, 60,000 and 85,000. The Reynolds number is based on the inlet velocity and characteristic diameter of 2H.

Table 4.1 shows the comparison of mass flux used in the CFD simulation and the experimental setup, and they are within 5% of each other. Hence for this study a comparison could be made with the computational study for Reynolds number of 15,000 and 30,000. A notable difference between the experimental and the computational setup is that the latter has an inlet section to fully develop the flow hydro dynamically, whereas the CFD setup does not have an inlet section. In order to have a proper comparison for heat transfer results, the results from the experiment and CFD are normalized with respect to data from G2E.

Table 4.1

Mass flux comparison

Reynolds number	CFD ($Kg/m^2.s$)	Experiment ($Kg/m^2.s$)	% difference
15,000	4.62	4.55	1.52
30,000	9.24	8.84	4.33

4.4.1. Endwall Nusselt number

A smooth channel test was done in order to establish confidence in the results obtained from our test setup and measurement techniques before progressing further. The

spanwise averaged Nusselt number for smooth channel was compared with Gnielinski correlation (Gnielinski, 1976) as shown in equation 42.

$$Nu_D = \frac{(f/8)(Re_D - 1000)Pr}{1 + 12.7(f/8)^{1/2}(Pr^{2/3} - 1)} \quad (42)$$

Where *f* is the friction factor which is calculated using Darcy–Weisbach equation (Equation 32). This correlation is valid for $0.5 < Pr < 2000$ and $3000 < Re_D < 5 \times 10^6$. Figure 4.139 shows the spanwise average Nusselt number for the smooth channel test. As we can see for the figure that there is a deviation at the starting, this is due to the absence of a heated inlet section. Since heating begins at the start of the test section, the impact of thermal development of the flow is seen up to approximately at an X/D_h of 4, at this point we can say that the flow becomes fully thermally developed. Comparing the result to the correlation we can see that the spanwise average is in good agreement, well within 10% of given uncertainty.

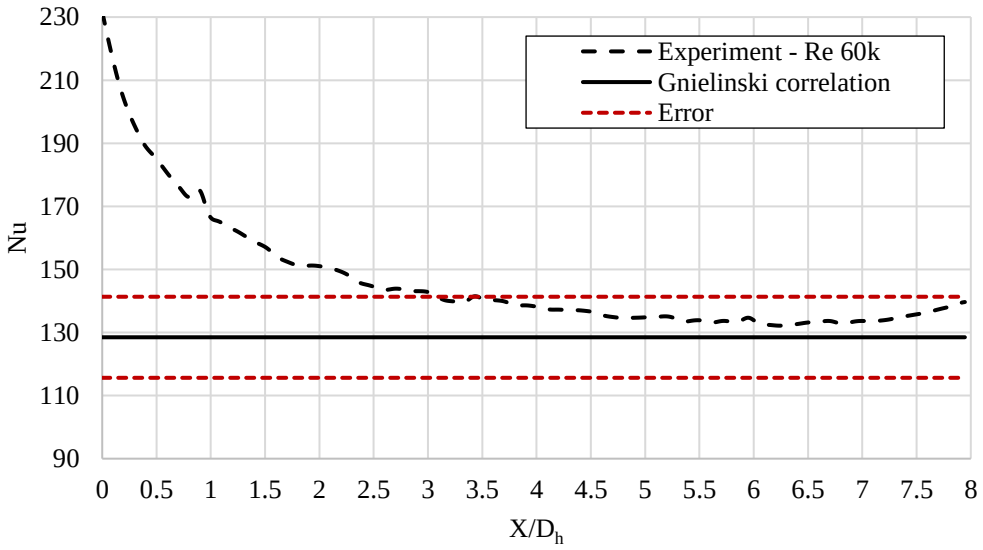

Figure 4.139 Spanwise average Nusselt number for Smooth channel

Figure 4.140 shows the post processed image of TSP for a smooth channel test. The white lines in the contour are the space between the strips which are discarded in post processing, as these regions are not subjected to the given heat flux.

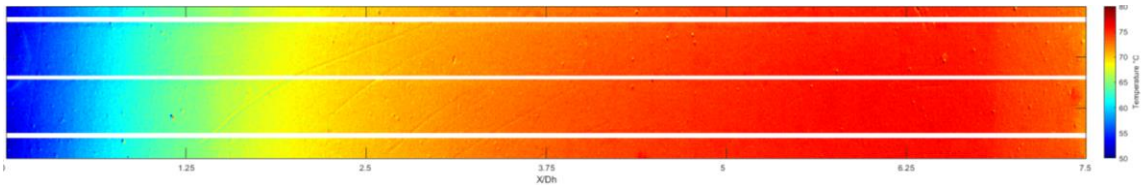

Figure 4.140 Temperature contour (TSP)

Figure 4.141 shows the end wall Nusselt number contour for Re of 30,000. From the figure we can see that behind row 1 the wake region is much narrower for pin G2TRV in comparison to the other pins, this trend can be seen almost behind every row for G2TRV. We can also see the same behavior in CFD contour results shown in Figure 4.77. Looking at the data downstream of the channel we can see that pin G2E has an increase in magnitude of heat transfer compared to other two pins.

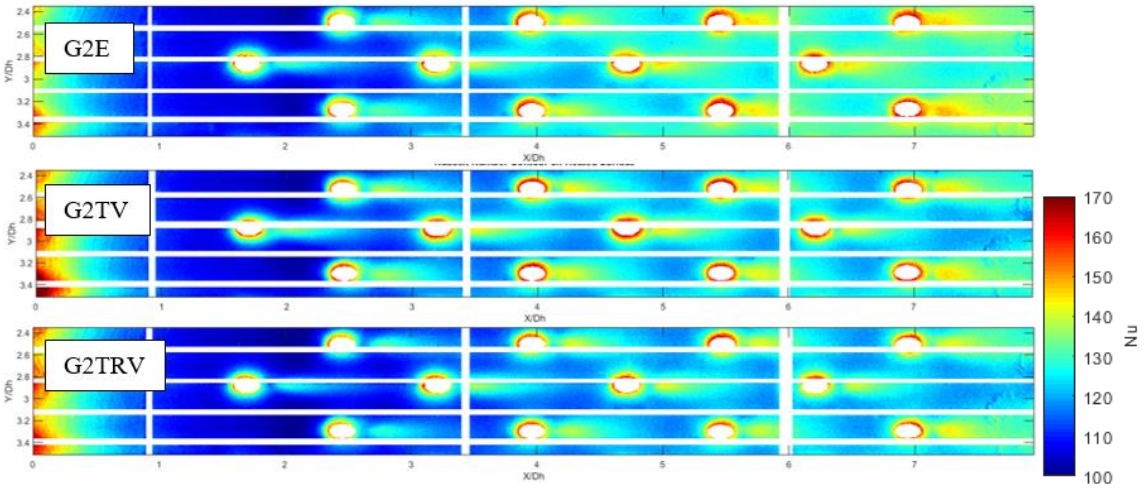

Figure 4.141 Nusselt number contour for Re = 30,000

As explained in the CFD results this is due to pin G2E having a higher magnitude of flow mixing compared to other pins, related to the structure of each pins wake. Figure 4.142 – Figure 4.145 show the spanwise average endwall Nusselt number for all 4 Reynolds number. The results are normalized to obtain Frossling number.

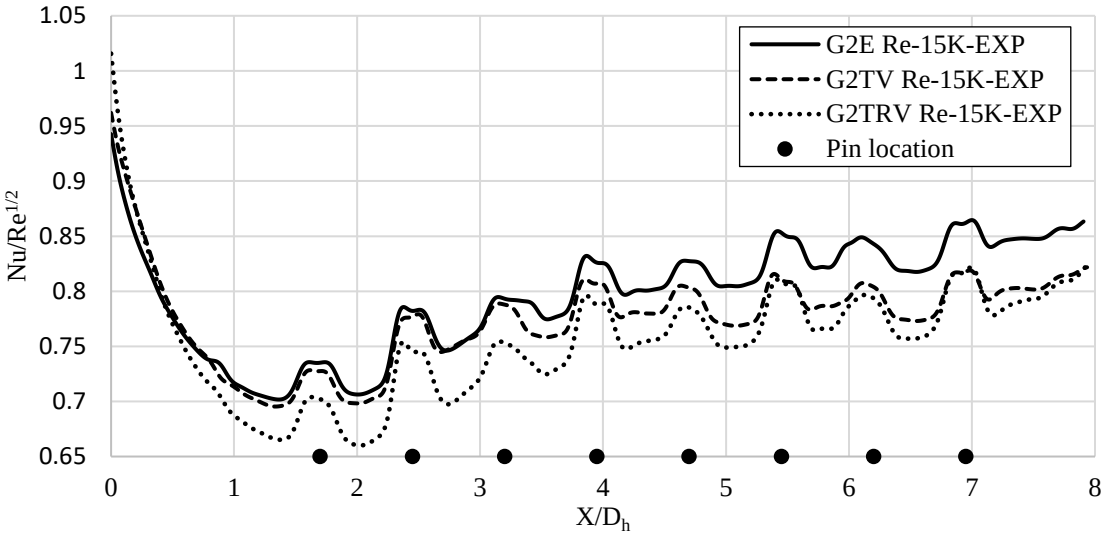

Figure 4.142 Spanwise average Nusselt number for Re = 15,000

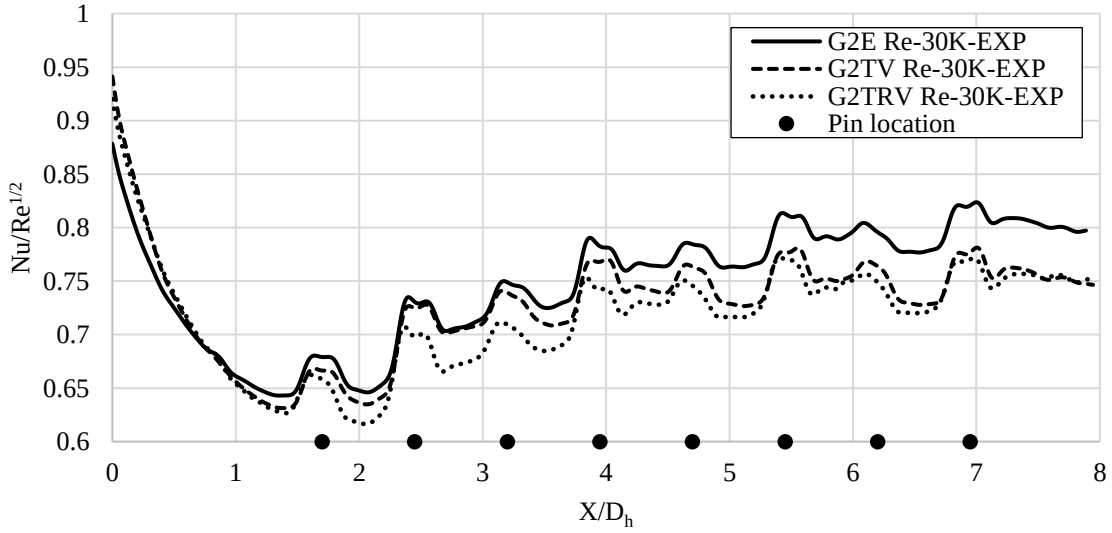

Figure 4.143 Spanwise average Nusselt number for Re = 30,000

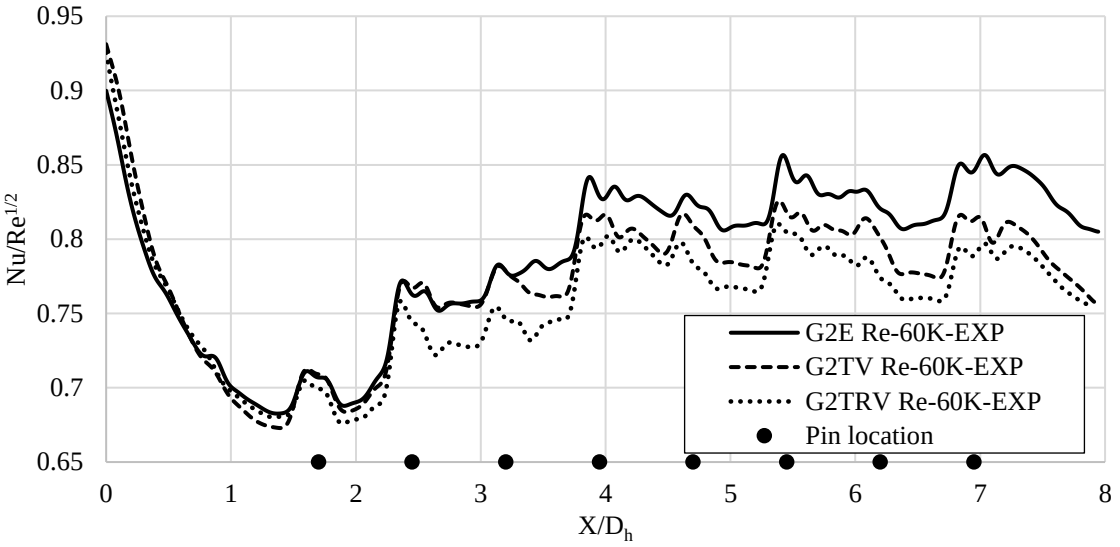

Figure 4.144 Spanwise average Nusselt number for Re = 60,000

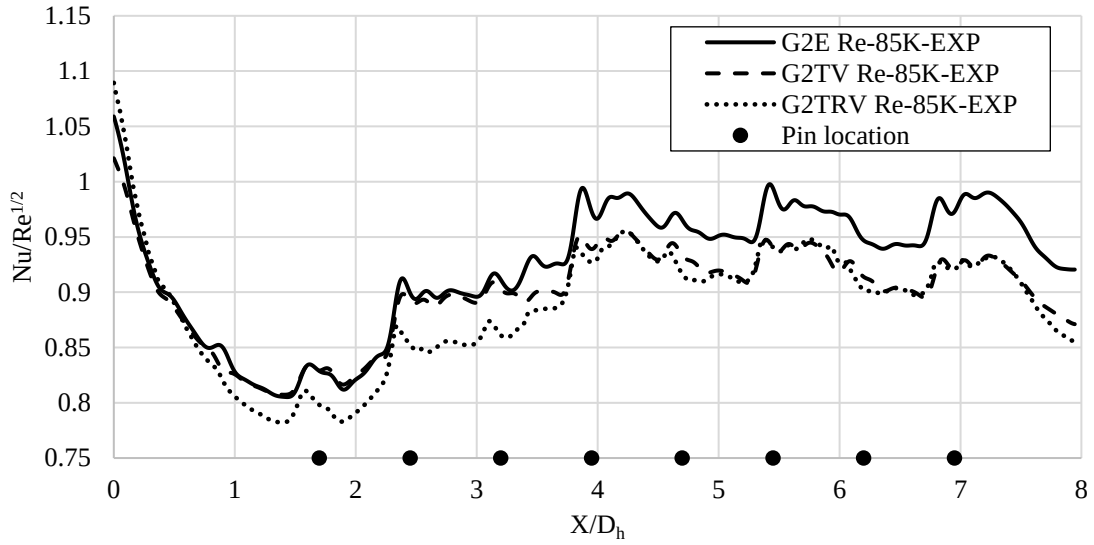

Figure 4.145 Spanwise average Nusselt number for Re = 85,000

From the spanwise results, we can see that as the Reynolds number is increased the difference between the spanwise average Nusselt number for pin G2TV and G2TRV decreases after Row 3. This is due to fact that as the momentum in the flow is increased the magnitude of flow mixing downstream of the channel is increased as well, leading to

loss of uniqueness of the pin wake structure.

On comparing between the bio pins and pin G2E, we can see that the pin G2E still has a better heat transfer augmentation downstream of the channel. This is due to G2E having periodic wake shedding which leads to an increase in turbulence fluctuations at the endwall as the flow moves through the channel. But the bio pins G2TV and G2TRV having reduction in wake size due to the presence of the undulation leads to a reduction in magnitude of flow mixing downstream of the channel thereby leading to the reduction in endwall Nusselt number.

4.4.2. Pressure Drop Along the Channel

The pressure data are obtained from the side wall in the test section. Each port is located between two rows of pins, first port is located before the first row and the last port is located after the last row. The pressure drop across the channel is calculated based on the difference between the first port and the subsequent port similar to the computational study. Figure 4.146 – Figure 4.151 shows the comparison of pressure drop data for experiment and CFD results for Reynolds number case of 15,000 and 30,000, with experimental uncertainties of 7% and 5.5%.

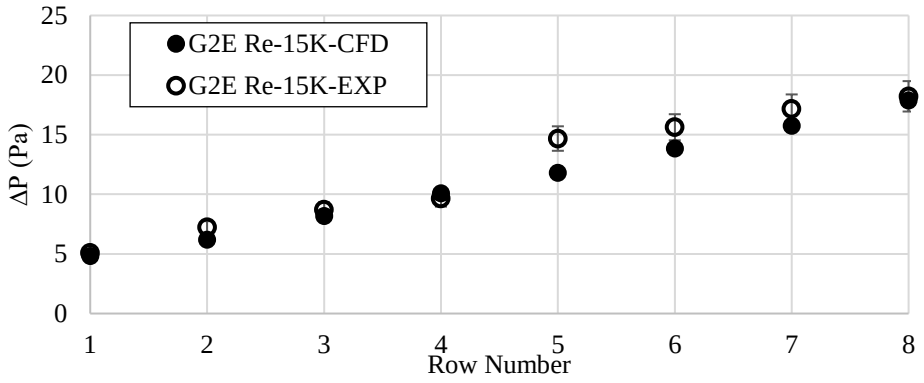

Figure 4.146 Pressure drop along the channel for G2E – Re = 15,000

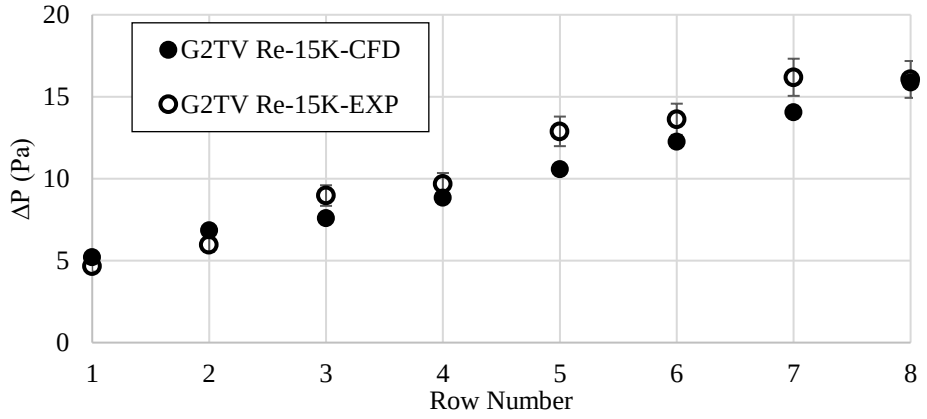

Figure 4.147 Pressure drop along the channel for G2TV – Re = 15,000

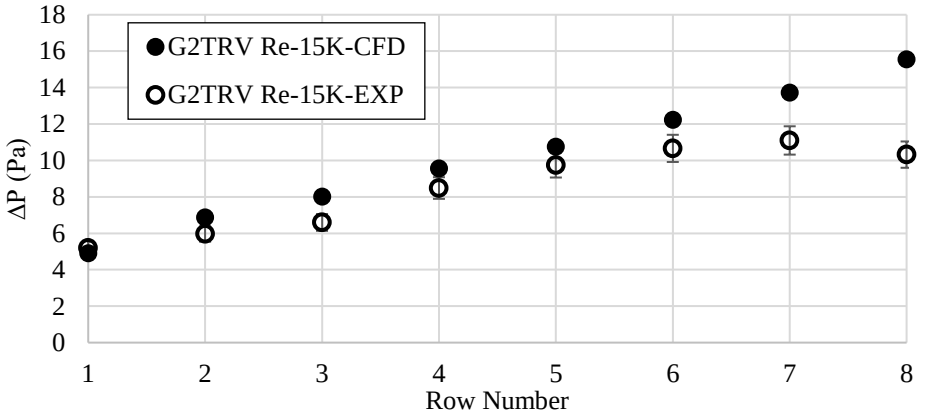

Figure 4.148 Pressure drop along the channel for G2TRV – Re = 15,000

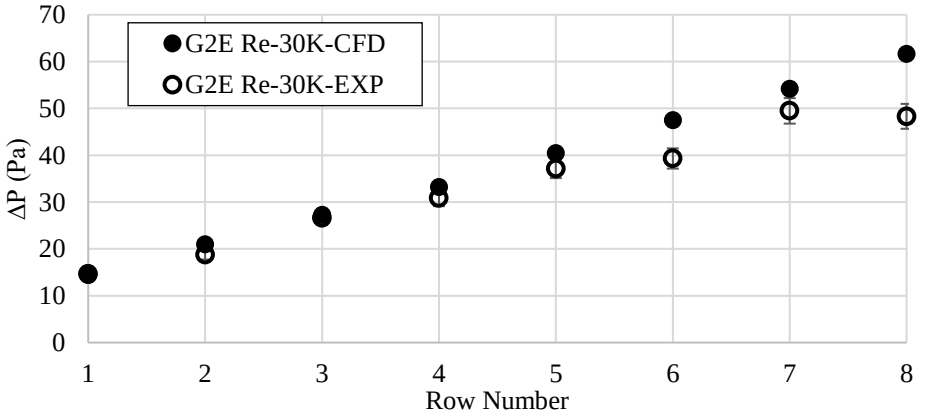

Figure 4.149 Pressure drop along the channel for G2E – Re = 30,000

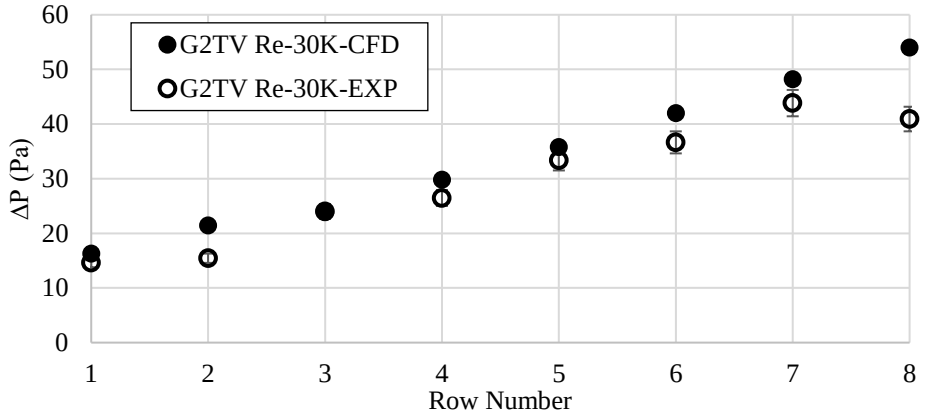

Figure 4.150 Pressure drop along the channel for G2TV – Re = 30,000

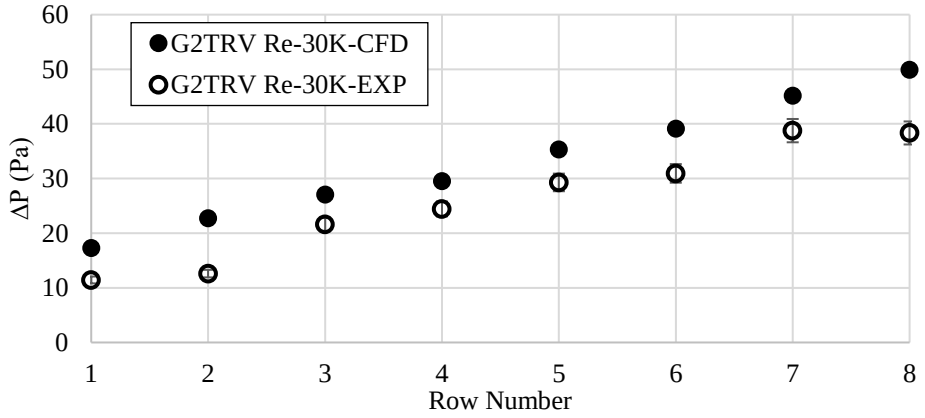

Figure 4.151 Pressure drop along the channel for G2TRV – Re = 30,000

From the above data we can see that the pressure drop results from experiment are in good agreement with the CFD results. Figure 4.152 – Figure 4.155 shows the pressure drop comparison of the pins for all 4 Reynolds number. The uncertainties in the results are 7%, 5.5%, 4% and 3.3% for Reynolds number case of 15000, 30000, 60000 and 85000. From these results we can see that as the Reynolds number is increased the magnitude difference between the static pressure loss for pin G2TV and G2TRV decreases for the same reason explained in endwall Nu results.

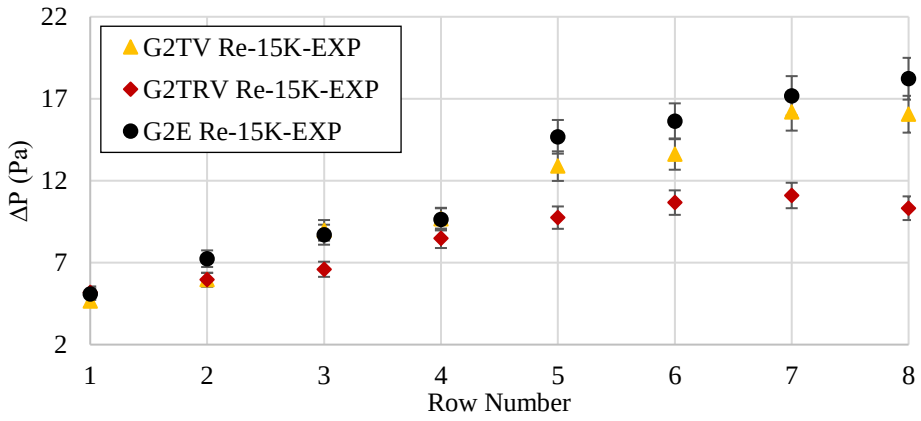

Figure 4.152 Pressure drop along the channel for Re = 15,000

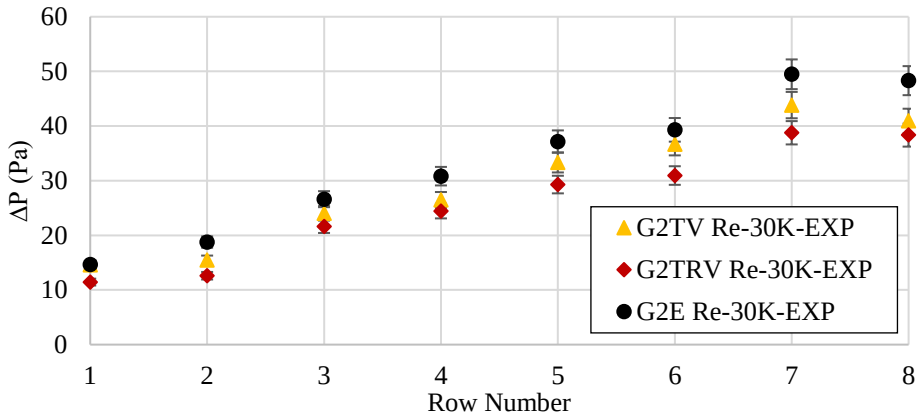

Figure 4.153 Pressure drop along the channel for Re = 30,000

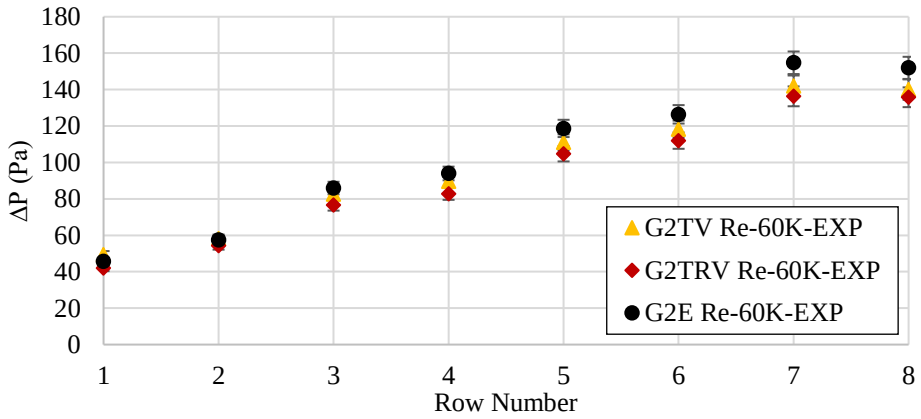

Figure 4.154 Pressure drop along the channel for Re = 60,000

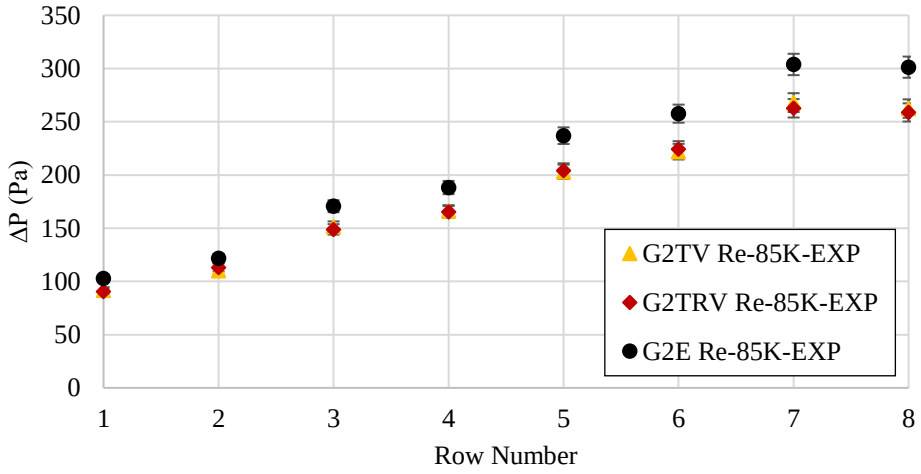

Figure 4.155 Pressure drop along the channel for Re = 85,000

Also as explained previously G2E has the periodic wake shedding which leads to larger pressure drop in the channel compared to the bio pins which have reduction in the wake magnitude leading to decrease in static pressure loss. This can be seen in the pressure drop results.

4.4.3. Pin Surface Nusselt Number

The ESM methodology as explained before was utilized to predict the pin surface average Nusselt number. One challenge with this methodology is that, while using the pin parameter 'm' in the equation to calculate heat transfer coefficient 'h', one would encounter pin cross sectional area and perimeter. This methodology was developed and tested for uniform cross section area of the pin. In this case the bio pins have varying cross section (A_c) and perimeter (p). In order to account for this an effective cross sectional area and perimeter is calculated, as shown in equation 43 and 44.

$$p = \frac{Surface\ area}{Height} \tag{43}$$

$$A_c = \frac{Volume}{Height} \tag{44}$$

This methodology was implemented for pins G2E, G2TV and G2TRV at Reynolds number of 60,000. The Nusselt number is normalized to get Frossling number, as shown in Figure 4.156. The uncertainty in the results is approx. 4.5% for G2TV, G2TRV and G2E. From the figure we can see that the heat transfer on the pins surface increases to row 3 – 4 and gradually decreases, this is seen in CFD results Figure 4.55.

This is due to the increase in bulk temperature of the core flow as the flow moves downstream of the channel. This increase in bulk temperature is due to heat extraction from walls leading to a decrease in heat transfer on the pin surface. Also as seen in CFD results the pin G2E performs better in pin surface heat transfer in comparison to the bio pins, with G2TV and G2TRV almost being the same in performance.

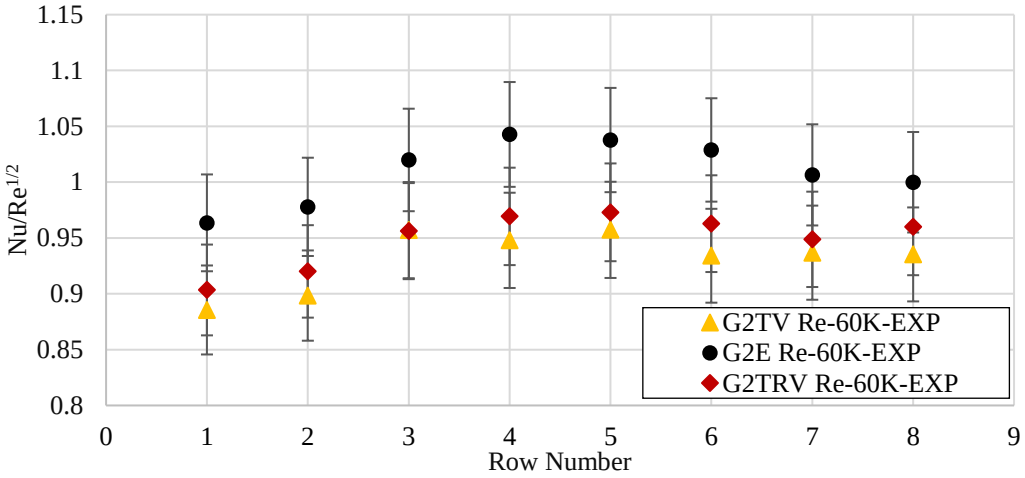

Figure 4.156 Pin row average Nusselt number for Re = 60,000

4.4.4. Reynolds Number Effects

Figure 4.157 shows the Nusselt number variation across different Reynolds number.

From this result, it can be seen that the difference between the heat transfer performance is maintained between 1 – 2%. With G2E being the best performer follower by G2TV and G2TRV. The uncertainty is the results are approx. 9.4% for Reynolds number case of 15,000 and 30,000 and approx. 8.5% for Reynolds number case of 60,000 and 85,000. The uncertainty in the Reynolds numbers is approx. 2.8%.

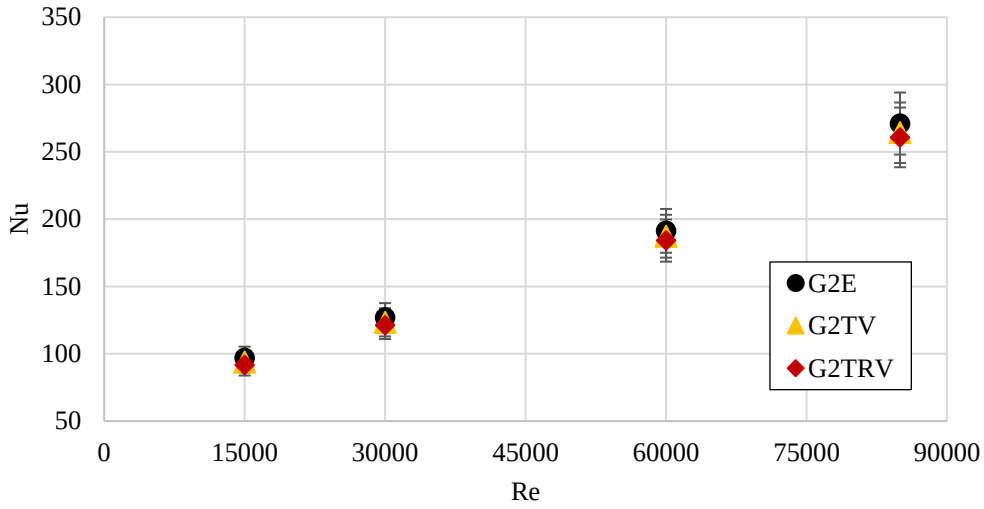

Figure 4.157 Endwall Nusselt number over Reynolds number

Figure 4.158 – Figure 4.159 shows the comparison of thermal performance results from CFD and experiment for pins G2TV and G2TRV. The uncertainty in the results are approx. 9% for the normalized Nusselt number and about 4% for normalized friction factor for Reynolds number of 15,000. And for 30,000 Reynolds number case it is about 10% and 3.5%. The pins G2TV and G2TRV are normalized with respect to G2E. Since the Nusselt number and friction factor are normalized with respect to G2E, any data point above G2E in the y axis means it performs well in heat transfer and any data point to the left of G2E in the x axis means it performs well in pressure drop.

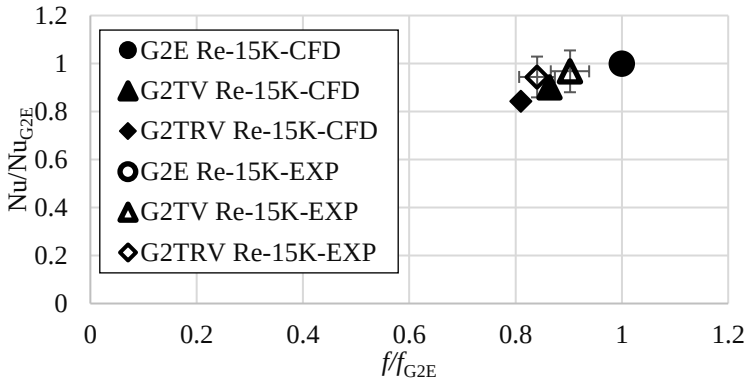

Figure 4.158 Thermal performance comparison for Re = 15,000

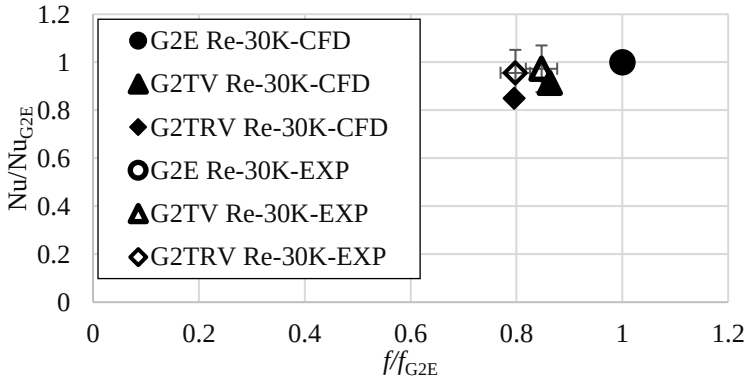

Figure 4.159 Thermal performance comparison for Re = 30,000

From the above two figures we can see that the results are in good agreement with each other with a maximum difference of 35% in friction factor and 10% in Nusselt number for Reynolds number of 15,000 and <1% in friction factor and 11% in Nusselt number for Reynolds number of 30,000. Figure 4.160 shows the thermal performance for the three pins at various Reynolds number. The uncertainty in the results are approx. 10% for normalized Nusselt number and approx. 5% for normalized friction factor for Reynolds number of 15,000. For Reynolds number of 30,000 its 11.5% and 3.3%, for 60,000 its 8.5% and 3% and for 90,000 its 9.5% and 2.7%.

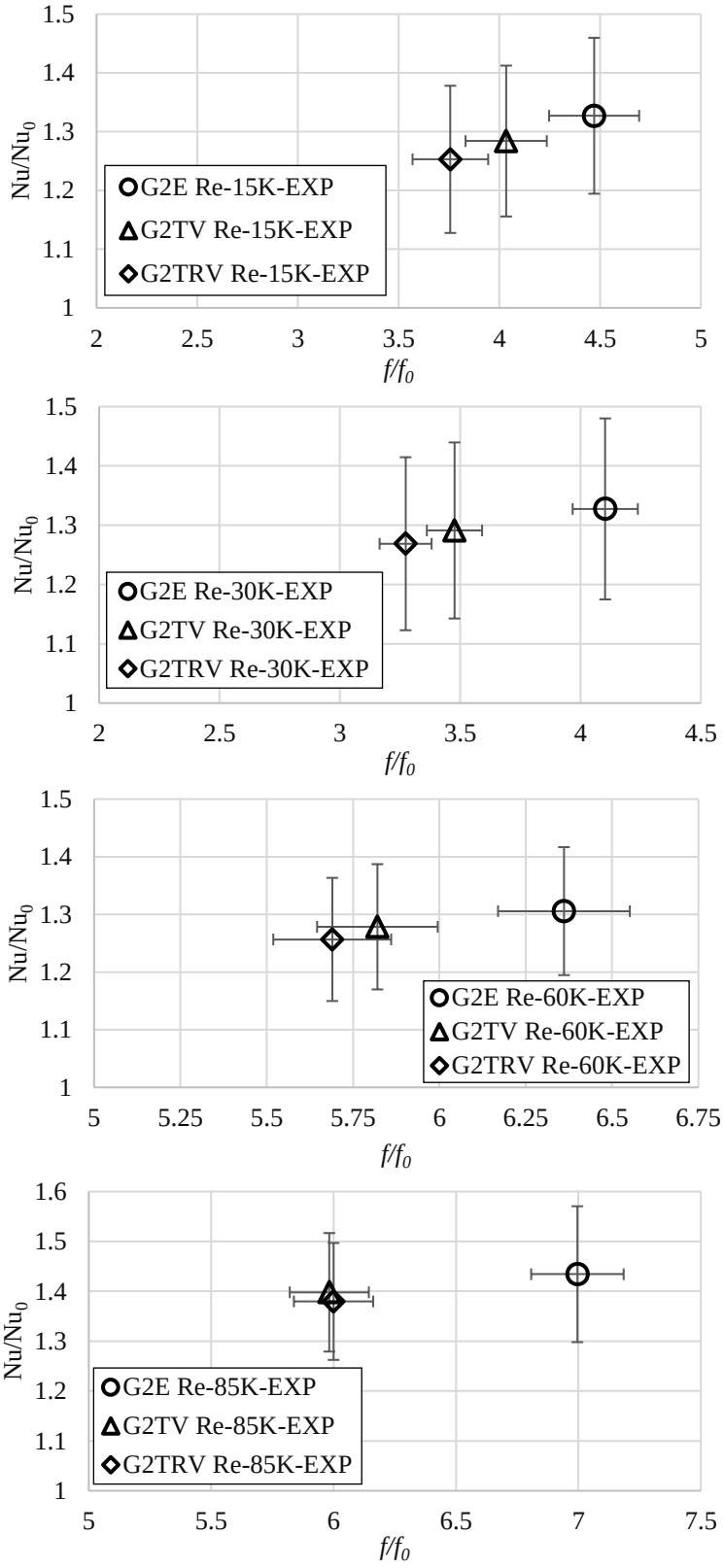

Figure 4.160 Thermal performance at various Reynolds number

The Nusselt number and factor values in Figure 4.160 are normalized with respect to smooth channel data. From this result we can see that thermal performance trend is similar to the trend seen in CFD results. One notable difference is that for a high Reynolds number of 85,000 the thermal performance of G2TV and G2TRV are the same. And also, the difference in heat transfer between G2E and the bio bins decreases from 5.5% to 3.5% as the Reynolds number is increased, with an overall improvement in friction factor performance by 14%.

4.4.5. Spectral Analysis

Pressure data is obtained from the Kulite pressure probes in time at 17 mm behind rows 1 and 5 for a duration of 10 seconds with 2000 samples a second. The amplitude spectrum of the pressure fluctuations is then plotted with frequency for a Reynolds number case of 30,000. Plotting the pressure fluctuations will give two dominant frequencies for the pin, one related to the drag and the other related to the lift as explained in the computational study. The frequency for the drag will be twice that of the lift. Initially the pressure fluctuation for smooth channel data is plotted with respect to their frequency to determine the frequencies not related to the pins later on.

Figure 4.161 shows the FFT data for smooth channel pressure fluctuations. From the figure we can see a lot of noise in the lower frequency ranges, which are attributed to the inlet section. The frequencies around 500 to 650 Hz is caused by the blower used in the experiment. The frequencies around 220 Hz and 260 Hz and its harmonics could be due to the noise generated by another test section connected to the by bass flow of the blower. Hence the lower frequencies before 200 Hz can be cropped, to better represent the data. Figure 4.162 – Figure 4.163 shows the FFT data for the pins at row 1 and row 5.

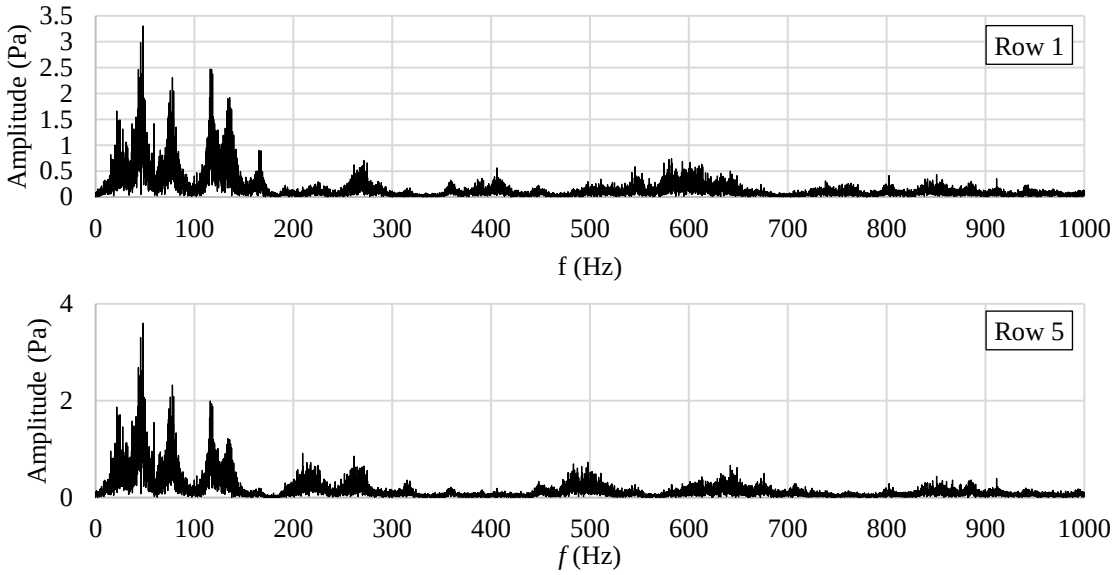

Figure 4.161 FFT – Smooth channel

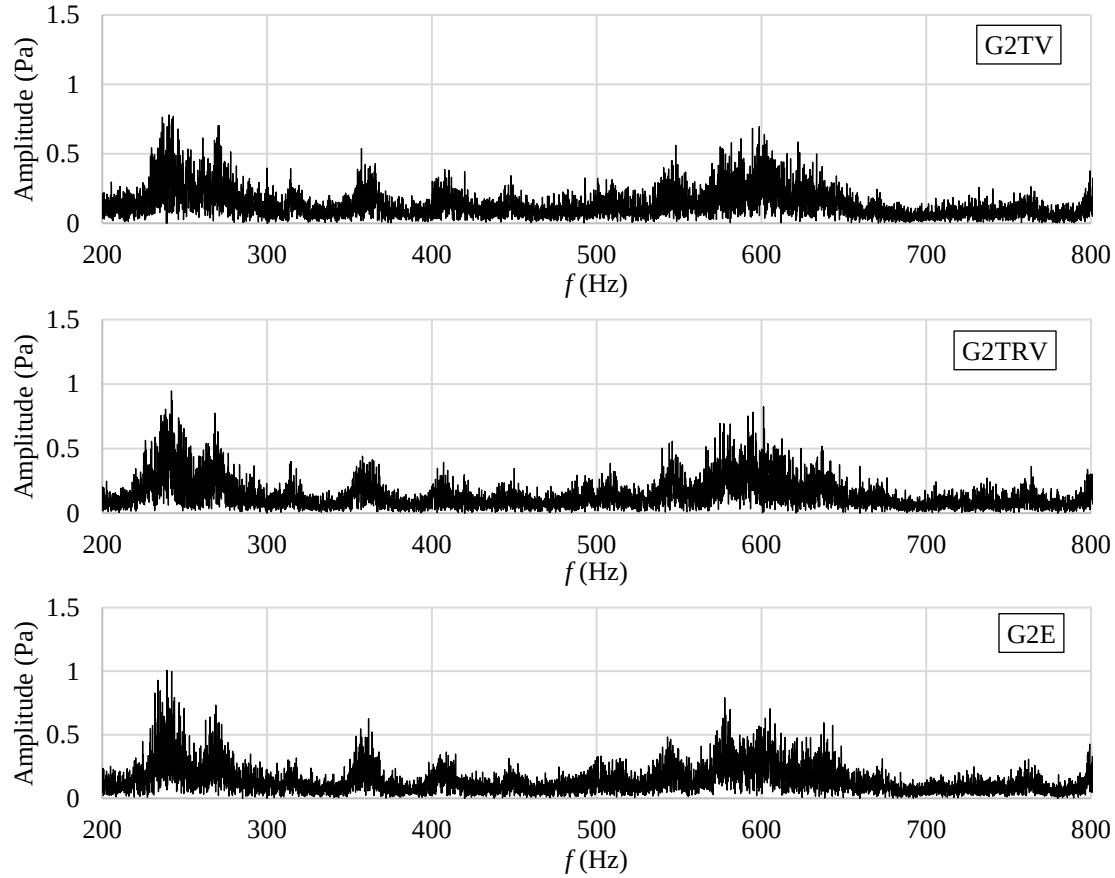

Figure 4.162 FFT – Row 1

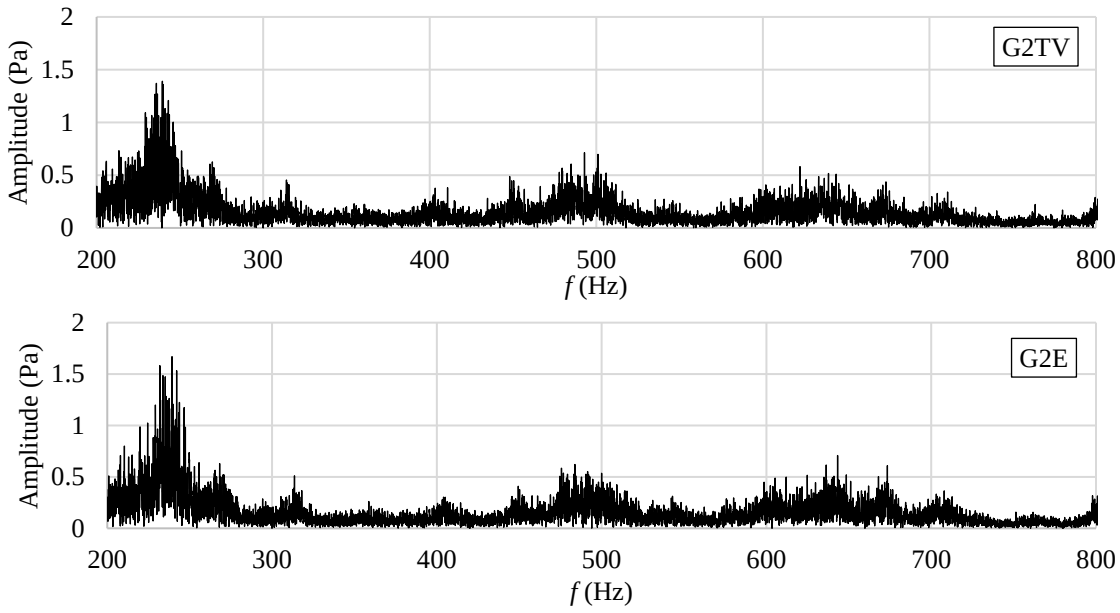

Figure 4.163 FFT – Row 5

From CFD results the frequencies obtained for G2TV are 225 and 450 Hz. Looking at Figure 4.162, we see that a dominant frequency around 225 Hz which is mixed with other noise signals as seen in smooth channel data. The harmonics of 225 Hz which is 450 Hz is also seen in the data. For pin G2E, the dominant frequency of about 238 Hz is seen in the FFT data which also aligns with CFD results, but the harmonic of this frequency is not picked up in the signal. For pin G2TRV the frequencies are almost similar to pin G2TV. Looking at row 5 data, we see a shift in magnitude of frequencies.

4.4.6. Turbulence Intensity

Turbulence intensity (TI) is calculated from the velocity fluctuations for pin G2TV and G2E in the axial plane of the pin taken at 17 mm behind the pin center. Figure 4.164 shows the TI data behind row 1 and row 5 pin. From Figure 4.164, looking at the turbulence intensity contour for pin G2TV behind row 1, we can see that in comparison to pin G2E there is an increase in magnitude of TI near the endwall and reduction in

magnitude at the center region, this aids in heat transfer near the endwall and reduces pressure drop in the flow.

We can also see that TI is higher throughout the wake region, suggesting that the wake is broken down as seen in literature. As the flow moves downstream, the flow gets accelerated through the channel leading to an increase in the size of the wake, but the bio pin G2TV in comparison to G2E still keeps the shape of the wake with higher TI near the endwall than at the center region. This leads to the reduction in pressure loss in the channel while maintaining the heat transfer at the endwall.

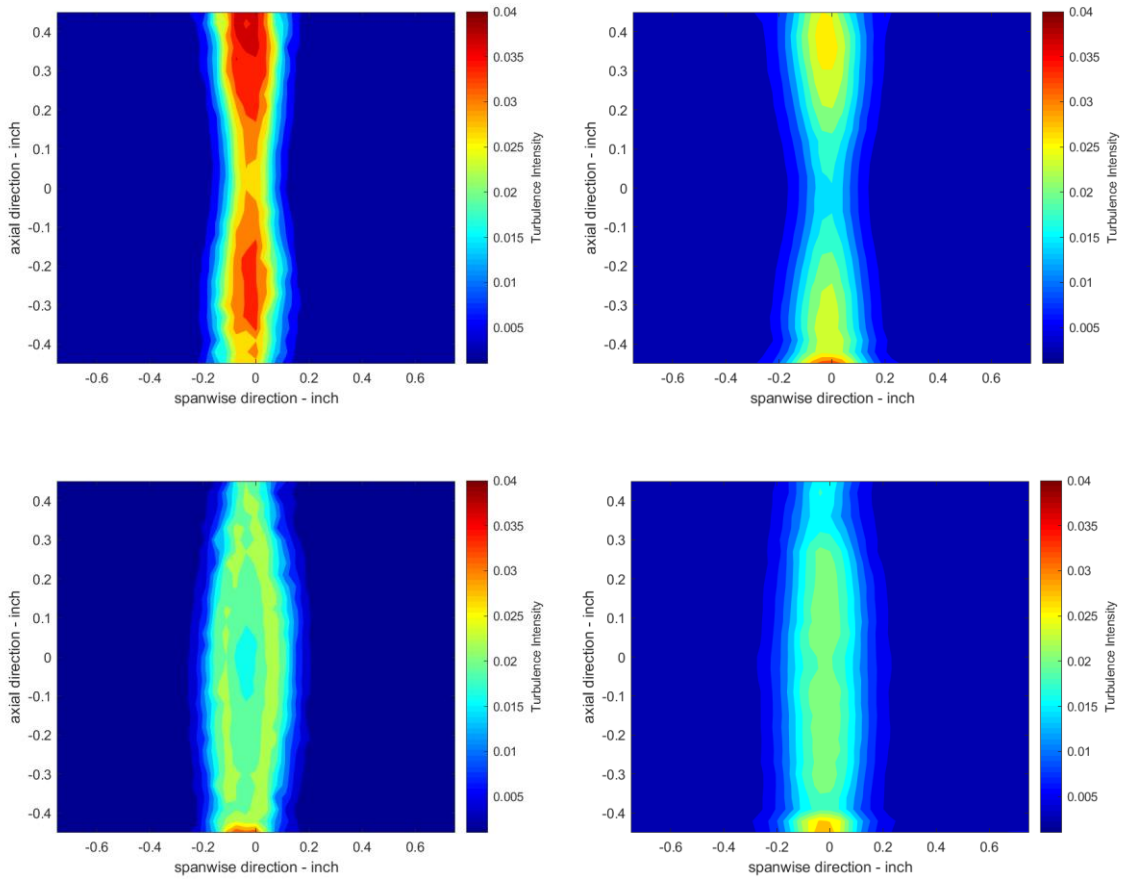

Figure 4.164 TI for pin G2TV (top) and G2E (bottom) behind row 1 (left) and 5 (right) pin

5. Conclusions

The objective of this study has been to characterize and compare the aero-thermal behavior of bio-inspired pin geometries with a standard circular and elliptical pin fin for different Reynolds number. As mentioned in the methodology two set of pin designs were made and each one having its own group. The initial pin design has the bio pins BP1 and BP2 and the conventional pins CP1 (cylindrical) and EP1 (elliptical), with BP1 being the bio pin with elliptical structure and BP2 being the bio pin with cylindrical structure. Both these pins BP1 and BP2 are non-uniformly scaled up versions of the actual whisker geometry. Whereas the final pin design is a scaled up version of the actual whisker geometry, this is done to study the effect of the actual whisker shape in thermal performance.

The behavior of the pin design in aero-thermal performance was done by comparing the spanwise average Nusselt number on the end-wall, row-wise pin surface average Nusselt number, circumferential distribution of Nusselt number and pressure coefficient and also a comparison of friction factor. The results of the entire study have been summarized in the tables given below.

The results are in terms of channel average, endwall average and pin surface average enhancement ratios normalized with respect to the baseline case. From the given enhancement ratios, a greater value indicates a better performance. The enhancement ratios are given in terms of thermal performance at constant pressure drop and at constant pumping power respectively, the latter is the one with the denominator raised to one third. Table 5.1 shows the thermal performance numbers for the initial pin design obtained from the computational study.

Table 5.1

Initial pin design – CFD – Thermal Performance

Re	Case	Endwall average		Pin surface average		Channel average	
		$\frac{\frac{Nu}{Nu_{CP1}}}{\frac{f}{f_{CP1}}}$	$\frac{\frac{Nu}{Nu_{CP1}}}{\left(\frac{f}{f_{CP1}}\right)^{1/3}}$	$\frac{\frac{Nu}{Nu_{CP1}}}{\frac{f}{f_{CP1}}}$	$\frac{\frac{Nu}{Nu_{CP1}}}{\left(\frac{f}{f_{CP1}}\right)^{1/3}}$	$\frac{\frac{Nu}{Nu_{CP1}}}{\frac{f}{f_{CP1}}}$	$\frac{\frac{Nu}{Nu_{CP1}}}{\left(\frac{f}{f_{CP1}}\right)^{1/3}}$
2,700	CP1	1	1	1	1	1	1
	BP1	1.511	1.075	1.673	1.191	1.538	1.094
	BP2	0.9426	0.997	0.979	1.035	0.949	1.003
	EP1	1.9284	1.075	2.222	1.239	2.012	1.121
5,200	CP1	1	1	1	1	1	1
	BP1	1.608	1.066	1.762	1.169	1.631	1.082
	BP2	0.966	0.983	1.024	1.041	0.983	0.999
	EP1	2.096	1.063	2.452	1.242	2.205	1.118
15,000	CP1	1	1	1	1	1	1
	BP1	1.596	1.013	1.798	1.141	1.596	1.013
	BP2	1.008	1.004	1.021	1.017	1.008	1.004
	EP1	2.066	1.006	2.467	2.467	2.066	1.006

In Table 5.1 the enhancement ratios are normalized with respect to results from CP1, so a value greater than 1 indicates better performance in comparison to CP1. From the table we can see that pin EP1 and BP1 are performing better than pin CP1 in terms of thermal performance at constant pressure drop and pumping power, with a maximum difference of about 100% for pin EP1 and 54% for BP1 at constant pressure drop and about 12% for pin EP1 and 11% for pin BP1 for constant pumping power.

Table 5.2 shows the thermal performance result for the initial pin design from the experimental study. This similar to the results seen in the computational study. The bio pin BP1 performs better in comparison to CP1 in terms of thermal performance at constant pressure drop and pumping power, with a maximum difference of 40% and 10% respectively. This shows that in comparing the initial pin design group of pins the best

performing pin is EP1 followed by BP1 and BP2. Having the undulation on the pins benefits in terms of reduction in pressure drop at a small cost of heat transfer.

Table 5.2

Initial pin design – Experiment – Endwall thermal performance

Re	Case	$\frac{\frac{Nu}{Nu_{CP1}}}{\frac{f}{f_{CP1}}}$	$\frac{\frac{Nu}{Nu_{CP1}}}{\left(\frac{f}{f_{CP1}}\right)^{1/3}}$
2,000	CP1	1	1
	BP1	1.314	0.983
	BP2	0.984	0.962
4,000	CP1	1	1
	BP1	1.369	1.009
	BP2	0.958	0.956
12,000	CP1	1	1
	BP1	1.412	1.049
	BP2	0.978	0.972

Table 5.3 show the thermal performance results for the final pin design from the computational study. The enhancement ratios are normalized with respect to smooth channel data and cylindrical pin data. Hence a pin which has a higher value is the better performer. From group 1 pins in the final pin design, we can see that the cylindrical pin G1C and the elliptical pin G1E are the better performer in comparison to the bio pins. The angle of the undulations cause a difference of 3% in thermal performance at constant pressure drop and 1% in thermal performance at constant pumping power requirement.

Looking at the performance of group 2 and 3 pins, we can see that the bio pins are the best performer in comparison to G2E and G2C with a maximum difference of 37% in thermal performance at constant pressure drop. As seen before the angle of the

undulations doesn't affect the results significantly. Removing the streamwise or the spanwise undulation decreases the thermal performance at constant pressure drop by 5% for pin G2TVST and by <1% for pin G2TVSP, but in terms of thermal performance at constant pumping power there is an increase in performance by 1%. Increasing the number of undulations on the pin increases the magnitude of thermal performance at constant pressure drop by a small amount but decreases the performance at constant pumping power by 3%. For the pins inspired from the bio pins design, pin NC1 and NC2, both have a decrease in performance at constant pressure drop but have an increase in performance for constant pumping power by 2.5%.

Table 5.3

Final pin design – CFD – Thermal performance – Re = 30,000

Case	Endwall average		Pin surface average		Channel average	
	$\frac{\frac{Nu}{Nu_0}}{\frac{f}{f_0}}$	$\frac{\frac{Nu}{Nu_0}}{\left(\frac{f}{f_0}\right)^{1/3}}$	$\frac{\frac{Nu}{Nu_C}}{\frac{f}{f_C}}$	$\frac{\frac{Nu}{Nu_C}}{\left(\frac{f}{f_C}\right)^{1/3}}$	$\frac{\frac{Nu}{Nu_0}}{\frac{f}{f_0}}$	$\frac{\frac{Nu}{Nu_0}}{\left(\frac{f}{f_0}\right)^{1/3}}$
G1C	0.328	1.006	1	1	0.379	1.162
G1E	0.446	0.936	1.176	0.805	0.537	1.128
G1TP	0.371	0.843	1.126	0.834	0.465	1.057
G1TRP	0.368	0.846	1.092	0.820	0.454	1.044
G1TPR	0.377	0.856	1.124	0.834	0.465	1.057
G1TPZ	0.381	0.851	1.127	0.821	0.474	1.059
G2C	0.273	0.986	1	1	0.315	1.137
G2E	0.355	0.952	1.244	0.926	0.419	1.125
G2TV	0.375	0.914	1.408	0.950	0.456	1.111
G2TVR	0.379	0.922	1.410	0.951	0.456	1.111
G2TVZ	0.385	0.922	1.412	0.938	0.465	1.113
G2TRV	0.379	0.873	1.483	0.948	0.469	1.080
G2TVST	0.358	0.934	1.286	0.931	0.428	1.117
G2TVSP	0.372	0.933	1.387	0.963	0.448	1.122
NC1	0.301	0.956	1.135	0.999	0.355	1.126
NC2	0.344	0.963	1.335	1.037	0.406	1.139

Table 5.4 show the thermal performance results for the final pin design from the computational study for a lower Reynolds number of 15,000. A similar conclusion could be drawn for this case as well, with the bio pins performing 8% better in terms of thermal performance at constant pressure drop but has a 2% decrease in thermal performance at constant pumping power.

Table 5.4

Final pin design – CFD – Thermal performance – Re = 15,000

Case	Endwall average		Pin surface average		Channel average	
	$\frac{\frac{Nu}{Nu_0}}{\frac{f}{f_0}}$	$\frac{\frac{Nu}{Nu_0}}{\left(\frac{f}{f_0}\right)^{1/3}}$	$\frac{\frac{Nu}{Nu_C}}{\frac{f}{f_C}}$	$\frac{\frac{Nu}{Nu_C}}{\left(\frac{f}{f_C}\right)^{1/3}}$	$\frac{\frac{Nu}{Nu_0}}{\frac{f}{f_0}}$	$\frac{\frac{Nu}{Nu_0}}{\left(\frac{f}{f_0}\right)^{1/3}}$
G2C	0.348	1.087	1	1	0.408	1.273
G2E	0.419	1.026	1.148	0.901	0.506	1.237
G2TV	0.437	0.971	1.308	0.931	0.547	1.212
G2TRV	0.436	0.927	1.356	0.925	0.553	1.174

Table 5.5 shows the thermal performance result for the final pin design from the experimental study. The thermal performance data is normalized with respect to smooth channel data, hence a higher value indicates better performance. From the results we can see that the bio pins perform better in comparison to elliptical pin G2E in terms of thermal performance at constant pressure drop and pumping power, with a maximum difference of 11% and 13% for the lower Reynolds number case. As the harbor seal whisker is elliptical in nature a good comparison would be with respect to the conventional elliptical pin G2E and from the results we can see that the bio pins perform better in this comparison.

Table 5.5

Final pin design – Experiment – Endwall thermal performance

Re	Case	$\frac{\frac{Nu}{Nu_0}}{\frac{f}{f_0}}$	$\frac{\frac{Nu}{Nu_0}}{\left(\frac{f}{f_0}\right)^{1/3}}$
15,000	G2E	0.296	0.098
	G2TV	0.318	0.106
	G2TRV	0.333	0.111
30,000	G2E	0.323	0.107
	G2TV	0.371	0.123
	G2TRV	0.387	0.129
60,000	G2E	0.205	0.068
	G2TV	0.219	0.073
	G2TRV	0.221	0.076
85,000	G2E	0.205	0.068
	G2TV	0.233	0.077
	G2TRV	0.229	0.076

Hence it can be seen from this study that the pin geometries inspired from harbor seal whiskers do have the potential to improve thermal performance. Furthermore, the impact of endwall heat transfer, pin surface heat transfer and pressure drop in the channel are related to the magnitude of wake created by the pins, flow acceleration and turbulence mixing in the channel. This is based on the pin shape and design considered in this current study, hence other engineered pin designs apart from NC1 and NC2 can be implemented such as, helical strake on a circular cylinder. Helical strakes are used in cylindrical towers to minimize flow induced vibrations by reducing the wake size generated by these towers.

As discussed in the literature review, numerous studies have been carried out on pin shapes, such as oblong pins, teardrop shaped pins, NACA airfoil shaped pins, triangular pins and so on. This shows that there are other engineering designs and also other

potential nature designs available to be implemented in a pinfin channel configuration for a thermal management purpose, with harbor seal whisker pin designs being one more potential solution.

REFERENCES

Ames, F. E., & Dvorak, L. A. (2006). Turbulent transport in pin fin arrays: experimental data and predictions. *Journal of Turbomachinery, 128(1),* 71-81.

Ames, F.E., Nordquist, C. A. & Klennert, L.A. (2007). Endwall heat transfer measurements in a staggered pin fin array with an adiabatic pin. *ASME Turbo Expo: Power for Land, Sea, and Air*, pp. 423-432. Montreal, Canada. 14-17 May.

Asknature. Retrieved from https://asknature.org/

Barlow, J., Rae, W., & Pope, A. (1999). *Low-speed wind tunnel testing* (Third edition). Hoboken, NJ: John Wiley & Sons.

Beem, H., Dahl, J., & Triantafyllou, M. (2011). Harbor Seal Vibrissa Morphology Reduces Vortex Induced Vibrations. *64th Annual Meeting of the APS Division of Fluid Dynamics.* 56(18). Baltimore, MD. 20-22 November.

Beem, H., & Triantafyllou, M. (2012). Seal whisker-inspired circular cylinders reduce vortex-induced vibrations. *65th Annual Meeting of the APS Division of Fluid Dynamics.* 57(17). San Diego, CA. 18-20 November.

Beem, H., & Triantafyllou, M. (2015). Exquisitely sensitive seal whisker-like sensors detect wakes at large distances. Cornell University open-access repository. *https://arxiv.org/abs/1501.04582*

Beem, H. (2016). Seal whiskers inspire marine technology. Retrieved from https://www.whoi.edu/oceanus/feature/seal-whiskers-inspire-marine-technology/

Bejan, A., & Almogbel, M. (2000). Constructal T-shaped fins. *International Journal of Heat and Mass Transfer, 43(12),* 2101-2115.

Bejan, A., & Kraus, A. (2003). *Heat transfer handbook*. Hoboken, NJ: John Wiley & Sons.

Bell, J. H., Schairer, E. T., Hand, L. A., & Mehta, R. D. (2001). Surface pressure measurements using luminescent coatings. *Annual Review of Fluid Mechanics, 33,* 155-206.

Benyus, J. M. (1997). Biomimicry: Innovation inspired by nature. New York City, NY: HarperCollins Publishers LLC.

Biome Renewables. Retrieved from: http://biome-renewables.com/

Bernstein, J., Bravato, A., Ealy, B., & Ricklick, M. (2013). Fabrication and analysis of porous superalloys for turbine components using laser additive manufacturing.

49th AIAA/ASME/SAE/ASEE Joint Propulsion Conference. San Jose, CA. 14-17 July.

Boyce, M.P. (2006). *Gas Turbine Engineering Handbook* (pp. 47-48). Gulf Professional Publishing (3rd edition).

Bunker, R. S. (2006). Gas turbine heat transfer: 10 remaining hot gas path challenges. *ASME Turbo Expo 2006: Power for Land, Sea, and Air,* p.1-14. Barcelona, Spain. 8-11 May.

Chyu, M., & Goldstein, R. (1991). Influence of an array of wall-mounted cylinders on the mass transfer from a flat surface. *International Journal of Heat and Mass Transfer, 34(9),* 2175–2186

Chyu, M. K., Hsing, Y. C., Shih, T. P., & Natarajan, V. (1999). Heat transfer contributions of pins and endwall in pin-fin arrays: effects of thermal boundary condition modeling. *Journal of Turbomachinery, 121(2), 257-263.*

Ciha, K. T. (2014). Pressure loss through multiple rows of various short pin array geometries & a survey of pressure loss and heat transfer through multiple rows of short pin arrays. *University Turbine Systems Research (USTR) Industrial Fellowship Program 2014 Final Report*.

Dabagh, A., & Andrews, G.E. (1992). Pin-Fin Heat Transfer: Contribution of the Wall and the Pin to the Overall Heat Transfer. *ASME 1992 International Gas Turbine and Aeroengine Congress and Exposition.* Cologne, Germany. 1-4 June.

Delibra, G., Hanjalić, K., Borello, D., & Rispoli, F. (2010). Vortex structures and heat transfer in a wall-bounded pin matrix: LES with a RANS wall-treatment. *International Journal of Heat and Fluid Flow,* 31(5), 740-753.

DeLuca, A. M. (2013). Aerodynamic performance and particle image velocimetery of piezo actuated biomimetic manduca sexta engineered wings towards the design and application of a flapping wing flight vehicle (Order No. 3601061). Available from ProQuest One Academic. (1466272561).

Downs, J. P., & Landis, K. K. (2009). Turbine Cooling Systems Design: Past, Present and Future. *Turbo Expo: Power for Land, Sea, and* Air. Orlando, FL. 8-12 June.

Fernandes, R., Ricklick, M., Prasad, A., & Pai, Y. (2017). Benchmarking reynolds averaged navier–stokes turbulence models in internal pin fin channels. *Journal of Thermophysics and Heat Transfer, 31*(4), 976-982.

Fish, F. E., Weber, P. W., Murray, M. M., & Howle, L. E. (2011). The tubercles on humpback whales' flippers: Application of bio-inspired technology. *Integrative and Comparative Biology, 51(1),* 203-213.

Goh, A.L. and Ooi, K.T., (2016). Nature-inspired Inverted Fish Scale microscale passages for enhanced heat transfer. *International Journal of Thermal Sciences, 106*, 18-31.

Gnielinski, V. (1976). New equations for heat and mass transfer in turbulent pipe and channel flow. Int. Chem. Eng., 16(2), 359-368.

Han, J. C. (2004). Recent studies in turbine blade cooling. *International Journal of Rotating Machinery*, *10*(6), 443-457.

Hans, H., Alvarado, V. Y., Thekoodan, D., Jianmin, M., & Triantafyllou, M. (2011). A whisker sensor: role of geometry and boundary conditions. *64th Annual Meeting of the APS Division of Fluid Dynamics.* 56(18). Baltimore, MD. 20-22 November.

H. Hans, J. Miao, G. Weymouth, & M. Triantafyllou. (2013). Whisker-like geometries and their force reduction properties. *2013 MTS/IEEE OCEANS.* Bergen, Norway.10-13 June.

Hanke, W., Witte, M., Miersch, L., Brede, M., Oeffnet, J., Michael, M., Hanke, F., Leder, A., & Dehnhardt, G. (2010). Harbor seal vibrissa morphology suppresses vortex-induced vibrations. *Journal of Experimental Biology, 213(15),* 2665-2672.

Huang, Z., Hwang, Y., & Radermacher, R. (2017). Review of nature-inspired heat exchanger technology. *International Journal of Refrigeration, 78,* 1-17.

Iacovides, H., & Launder, B. E. (2007). Internal blade cooling: the Cinderella of computational and experimental fluid dynamics research in gas turbines. *Proceedings of the Institution of Mechanical Engineers, Part A: Journal of Power and Energy*, *221*(3), 265-290.

Kim, K., & Moon, M. (2009). Optimization of a stepped circular pin-fin array to enhance heat transfer performance. *Heat and Mass Transfer = Wärme- Und Stoffübertragung., 46(1),* 63–74.

Kirsch, K. L., Ostanek, J. K., & Thole, K. A. (2013). Comparison of pin surface heat transfer in arrays of oblong and cylindrical pin fins. *Journal of Turbomachinery, 136(4),* 041015.

Kondo, Y., Matsushima, H., & Komatsu, T. (2000). Optimization of pin-fin heat sinks for impingement cooling of electronic packages. *Journal of Electronic Packaging, 122(3),* 240-246.

Kottapalli, A. G. P., Asadnia, M., Miao, J. M., & Triantafyllou, M. S. (2015, January). Harbor seal whisker inspired flow sensors to reduce vortex-induced vibrations. *2015 IEEE 28th IEEE International Conference on Micro Electro Mechanical Systems (MEMS).* pp. 889-892. Estoril, Portugal. 18- 22 January.

Lawson, S.A., Thrift, A.A., Thole, K.A. & Kohli, A. (2011). Heat transfer from multiple row arrays of low aspect ratio pin fins. *International Journal of Heat and Mass Transfer, 54*(17-18), 4099-4109.

Lee, D.H., Ha, M.Y., Balachandar, S. & Lee, S. (2004). Numerical simulations of flow and heat transfer past a circular cylinder with a periodic array of fins. *Physics of Fluids*, *16*(5), 1273-1286.

Metzger, D. E., & Haley, S. W. (1982). Heat transfer experiments and flow visualization for arrays of short pin fins. A*SME 1982 International Gas Turbine Conference and Exhibit*. London, England. 18-22 April.

Lee, C. S., Shih, T. I. P., Bryden, K. M., & Dennis, R. A. (2019). Effects of High Heating Loads on Unsteady Flow and Heat Transfer in a Cooling Passage With a Staggered Array of Pin Fins. *ASME Turbo Expo 2019: Turbomachinery Technical Conference and* Exposition. Phoenix, AZ. 17-21 June.

Liu, Y., Tian, L., & Barbastathis, G. (2013). Study of a seal whisker–inspired flow sensor using compressive holography. *Digital Holography and Three-Dimensional Imaging*. pp. DTh4A-5. Kohala Coast, HI. 21-25 April.

Miersch, L., Hanke, W., Wieskotten, S., Hanke, F. D., Oeffner, J., Leder, A., Brede, M., Witte, M., & Dehnhardt, G. (2011). Flow sensing by pinniped whiskers. *Philosophical Transactions. Biological Sciences*, *366*(1581), 3077-3084.

Miklosovic, D. S., Murray, M. M., Howle, L. E., & Fish, F. E. (2004). Leading-edge tubercles delay stall on humpback whale (Megaptera novaeangliae) flippers. *Physics of fluids*, *16*(5), L39-L42.

Murphy, C. T., Eberhardt, W. C., Calhoun, B. H., Mann, K. A., & Mann, D. A. (2013). Effect of angle on flow-induced vibrations of pinniped vibrissae. *PloS One*, *8(7)*.

U.S. Department of Energy-National Energy Technology Laboratory (NETL) (2006). *Gas Turbine Handbook.* Retrieved from https://www.netl.doe.gov/coal/turbines/handbook

Pai, Y., Prasad, A., & Ricklick, M. (2020). Extended surface heat transfer coefficients via endwall temperature measurements. *Journal of Thermophysics and Heat Transfer, 34(1),* 101-108.

Paniagua, L., Lehmkuhl, O., Oliet, C., and Pérez-Segarra, C.D. (2014), Large Eddy Simulations (LES) on the Flow and Heat Transfer in a Wall-Bounded Pin Matrix. *Numerical Heat Transfer, Part B: Fundamentals*, *65(2),* 103-128.

Pent, J. M., Kapat, J. S., & Ricklick, M. (2009). Comparison of Pressure Drop and Endwall Heat Transfer Measurements to Flow Visualization Testing of Solid and

Porous Pin Fin Arrays. *ASME International Mechanical Engineering Congress and Exposition, 43826,* pp. 2101-2111. Lake Buena Vista, FL. 13-19 November.

Sautner, M., Clouser, S., and Han, J.C. (1993). Determination of Surface Heat Transfer and Film Cooling Effectiveness in Unsteady Wake Flow Conditions. *AGARD Conference Proceedings 527*, pp. 6-1 - 6-12. Retrieved from https://www.sto.nato.int/publications/AGARD/Forms/AllItems.aspx

Settles, Gary S., Douglas A. Kester, and Lori J. Dodson-Dreibelbis. (2003). The external aerodynamics of canine olfaction. *Sensors and sensing in biology and engineering* (pp. 323-335). Vienna, Austria: Springer.

Shyam, V., Ameri, A., Poinsatte, P., Thurman, D., Wroblewski, A., and Snyder, C. (2015). Application of Pinniped Vibrissae to Aeropropulsion. *Proceedings of ASME Turbo Expo 2015*, Montreal, Quebec, Canada. 15–19 June.

Thompson, M., Burnett, J., Batra, A., Ixtabalan, D., Tran, D., Rodriguez, A., and Steele, B. (2015). Experimental Design of a Flapping Wing Micro Air Vehicle through Biomimicry of Bumblebees. *Proceedings of AIAA SciTech 2015*. Kissimmee, FL. 5-9 January.

Tullius, J., Tullius, T., and Bayazitoglu, Y. (2012). Optimization of short micro pin fins in minichannels. *International Journal of Heat and Mass transfer*, 55, 3921-3932.

Uzol, O., Camci, C. (2005). Heat Transfer, Pressure Loss and Flow Field Measurements Downstream of a Staggered Two-Row Circular and Elliptical Pin Fin Arrays. *Journal of Heat Transfer*, 127(5), 458-471.

VanFossen, G. J. (1982). Heat Transfer Coefficients for Staggered Arrays of Short Pin Fins. *Journal of Engineering for Gas Turbines and Power*, 104(2), 268-274.

Volstad, N., and Boks, C. (2012). On the use of Biomimicry as a Useful Tool for the Industrial Designer. Sustainable Development, 20(3), 189-199.

Wadley Research Group. Retrieved from https://www2.virginia.edu/ms/research/wadley/high-temp.html

Whalepower Corporation. Retrieved from https://whalepowercorp.wordpress.com/

Weymouth, G., and Triantafyllou, M. (2011). Numerical Study of Seal Whisker Vibrations. *64th Annual Meeting of the APS Division of Fluid Dynamics*. 56(18). Baltimore, MD. 20-22 November.

Williamson, C. H. (1996). Vortex dynamics in the cylinder wake. *Annual review of fluid mechanics*, *28*(1), 477-539.

PUBLICATIONS

Fernandes, R., Ricklick, M., Prasad, A., & Pai, Y. (2017). Benchmarking Reynolds Averaged Navier–Stokes Turbulence Models in Internal Pin Fin Channels. *Journal of Thermophysics and Heat Transfer*. 31(4), 976-982.

Krishna, K., Prasad, A., & Ricklick, M. A. (2018). Preliminary Numerical Investigation on the interaction of an Impinging Jet with Cylinder Wake. *2018 AIAA Aerospace Sciences Meeting*. pp. 0389. Kissimmee, FL. 8-12 January.

Pai, Y., Prasad, A., Fernandes, R., & Ricklick, M. A. (2017). Preliminary Investigation of Bio-Inspired Cylinders for Improved Thermal Performance of Internal Cooling Channels. *53rd AIAA/SAE/ASEE Joint Propulsion Conference*. pp. 4977. Atlanta, GA. 10-12 July.

Pai, Y., Prasad, A., & Ricklick, M. (2019). Extended Surface Heat Transfer Coefficients via Endwall Temperature Measurements. *Journal of Thermophysics and Heat Transfer*. 34 (1), 101-108.

Prasad, A., & Ricklick, M. A. (2020). Preliminary Experimentation on Wall Bounded Harbor Seal Whisker Inspired Pin Geometries. *AIAA Propulsion and Energy 2020 Forum.* pp. 3695. Virtual Conference. 24-28 August.

Prasad, A., & Ricklick, M. A. (2020). Unsteady Behavior of Wall Bounded Harbor Seal Whisker Inspired Pin Geometries. *AIAA Scitech 2020 Forum.* p.0633. Orlando, FL. 6-10 January.

Prasad, A., & Ricklick, M. A. (2019). Effect of Surface Pattern for Harbor Seal Whisker Inspired Pin Geometries for Enhanced Heat Transfer. *AIAA Propulsion and Energy 2019 Forum.* pp. 4177. Indianapolis, IN. 19-22 August.

Prasad, A., Pai, Y., Ogbebor-Evans, O., & Ricklick, M. A. (2018). Investigation of Bio-Inspired Pin Geometries for Enhanced Heat Transfer Applications. *2018 Joint Propulsion Conference.* pp. 4429. Cincinnati, OH. 9-11 July.

Prasad, A., & Ricklick, M. A. (2017). A Detailed Uncertainty Analysis of Heat Transfer Experiments using Temperature Sensitive Paint. *55th AIAA Aerospace Sciences Meeting*. pp. 1283. Grapevine, TX. 9-13 January.

Shrestha, S., Prasad, A., & Ricklick, M. A. (2018). Internal Cooling of Rotating and Non-Rotating Channels with Rib Turbulators. *2018 AIAA Aerospace Sciences Meeting.* pp. 0392. Kissimmee, FL. 8-12 January.

APPENDIX

A.1. Reynolds Number for a Harbor Seal Whisker

Harbor seals can swim up to 12mph, hence using dynamic similarity of Reynolds number (Equation 45 and Equation 46) the velocity used in this study was calculated for the final pin design.

$$Re_1 = Re_2 \tag{45}$$

Where Re_1 is the Reynolds number of the actual seal whisker and Re_2 is the scaled up version of the seal whisker geometry for the final pin design study. The condition for Re_1 is sea water and the conditions for Re_2 is air.

$$\frac{\rho_1 V_1 L_{C1}}{\mu_1} = \frac{\rho_2 V_2 L_{C2}}{\mu_2} \tag{46}$$

Where L_{C1} and L_{C2} are the characteristic length scale for Re_1 and Re_2. Since the whiskers are scaled uniformly in all dimensions for the final pin design,

$$L_{C2} = 12 \times L_{C1} \tag{47}$$

Hence the velocity for the scaled version of the whisker is calculated to be approx. 7.1 m/s, therefore in the computational study 3.925 m/s and 7.85 m/s inlet velocity conditions were used.

A.2. 3D Printed Harbor Seal Whisker Geometries

The bio pins, both the initial pin design and the final pin design geometries are 3D printed using Shapeways 3D printing services. The material used are Nylon 12, and Aluminum alloy and steel alloy for pins which are internally heated. Figure A.1 – Figure A.2 shows the 3D printed geometries for the experiment.

Figure A.1 3D printed geometries – Initial Pin Design

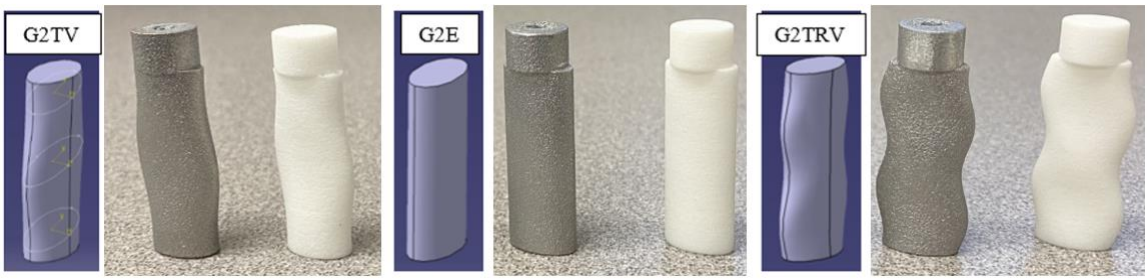

Figure A.2 3D printed geometries – Final Pin Design

A.3. Time step

The time step for the CFD simulations are calculated based on the shedding frequency of the pin geometries. The shedding frequency (*f*) is calculated based on the Strouhal number (*St*).

$$f = \frac{St \times V}{D_C} \tag{48}$$

Where V is the flow velocity and D_c is the characteristic diameter based on the pin diameter. Time period (T) of the wake shedding is given by,

$$T = \frac{1}{f} \tag{49}$$

In order to capture the unsteadiness of the wake generated by the pin geometries the time step (*t*) used in the simulation is given by,

$$t = \frac{T}{20} \tag{50}$$

For the final pin design, the time step calculated for an elliptical geometry is about 0.28 – 0.29 ms and for the cylindrical geometry is about 0.183 – 0.22 ms. Hence a time step of 0.1 ms is used for all cases.

A.4. Plots

Figure A.3 – Figure A.10 shows the plots for the CFD results of final pin design with result from G2C removed to properly show the difference in comparison with the bio and elliptical pins.

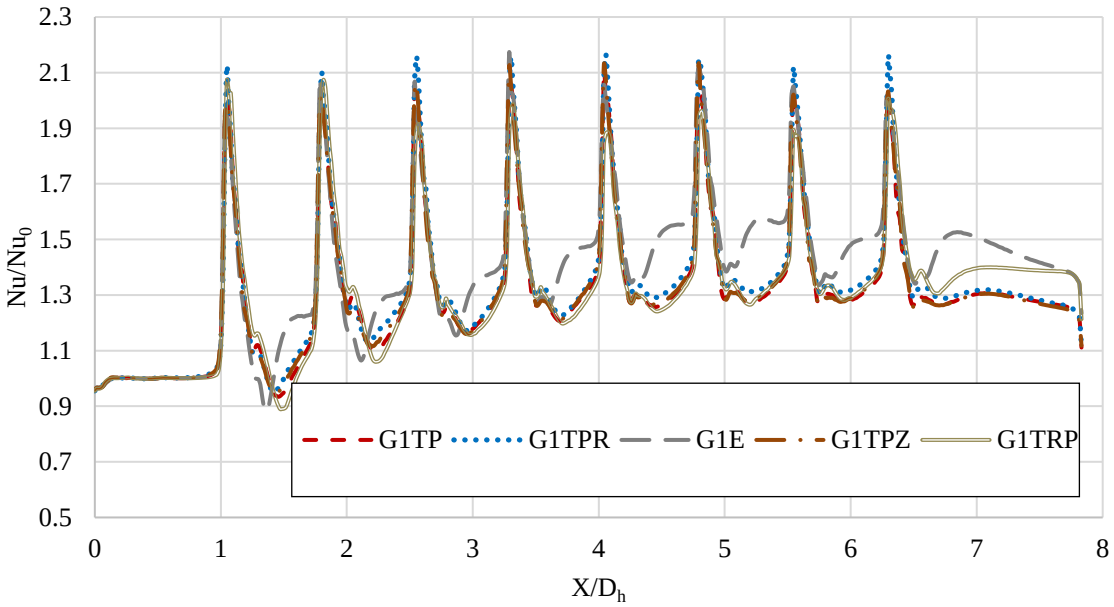

Figure A.3 Spanwise average endwall Nusselt number for group 1 pins

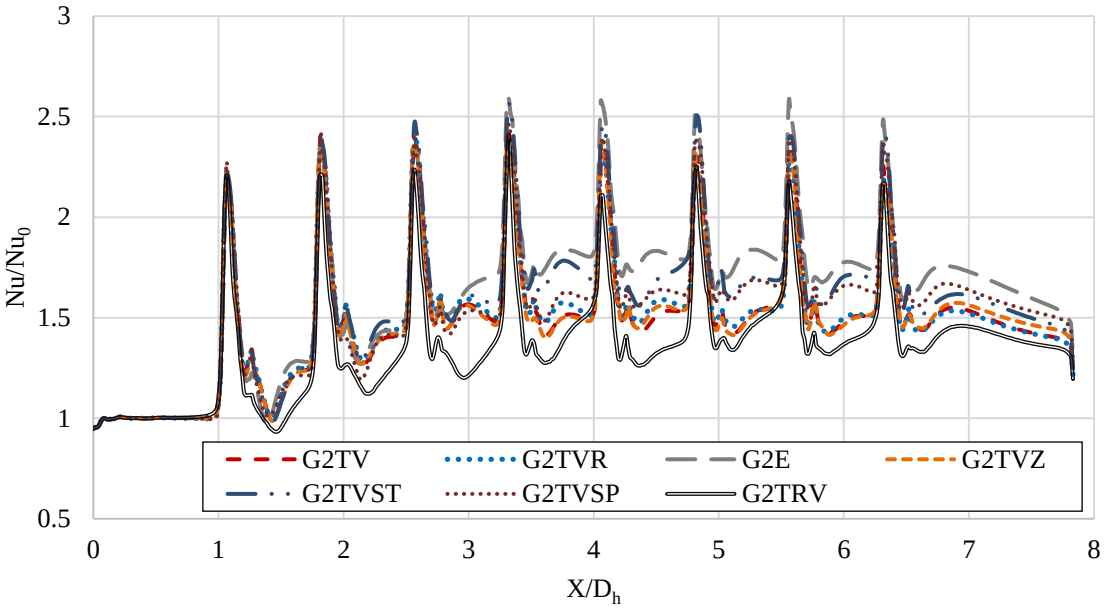

Figure A.4 Spanwise average endwall Nusselt number for group 2 and 3 pins

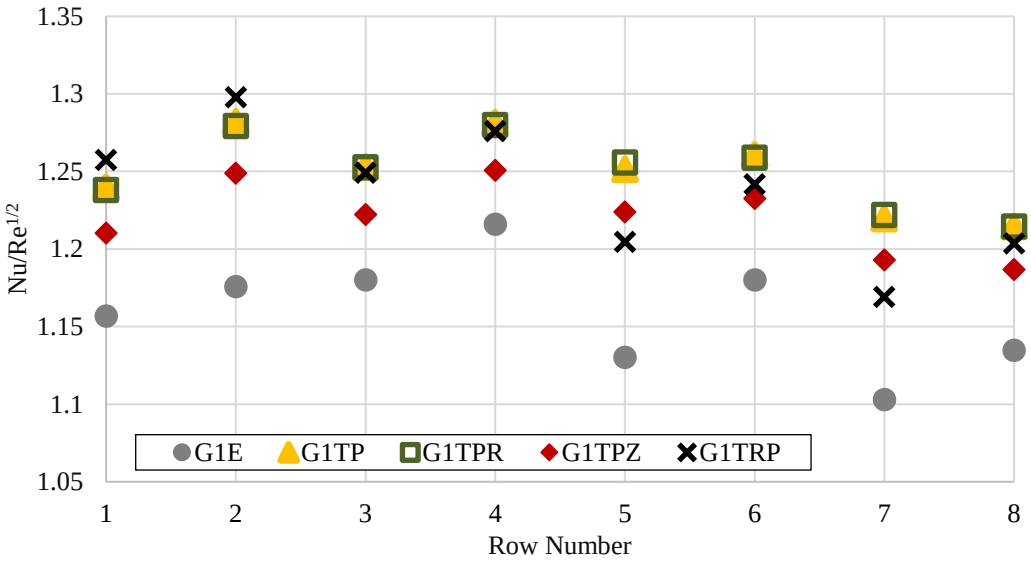

Figure A.5 Group 1: Row average Nusselt number

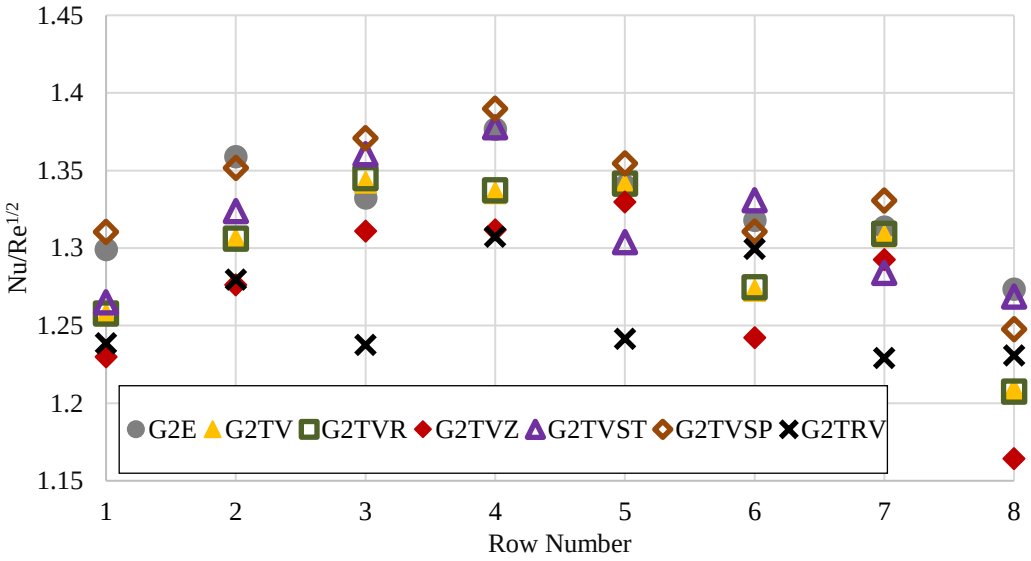

Figure A.6 Group 2 and 3: Row average Nusselt number

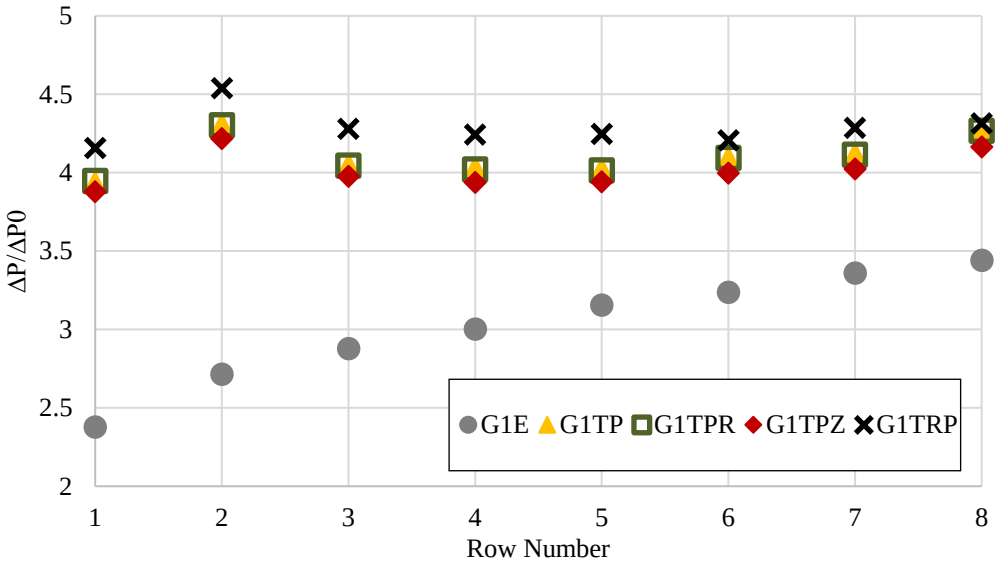

Figure A.7 Group 1: Pressure drop along the channel

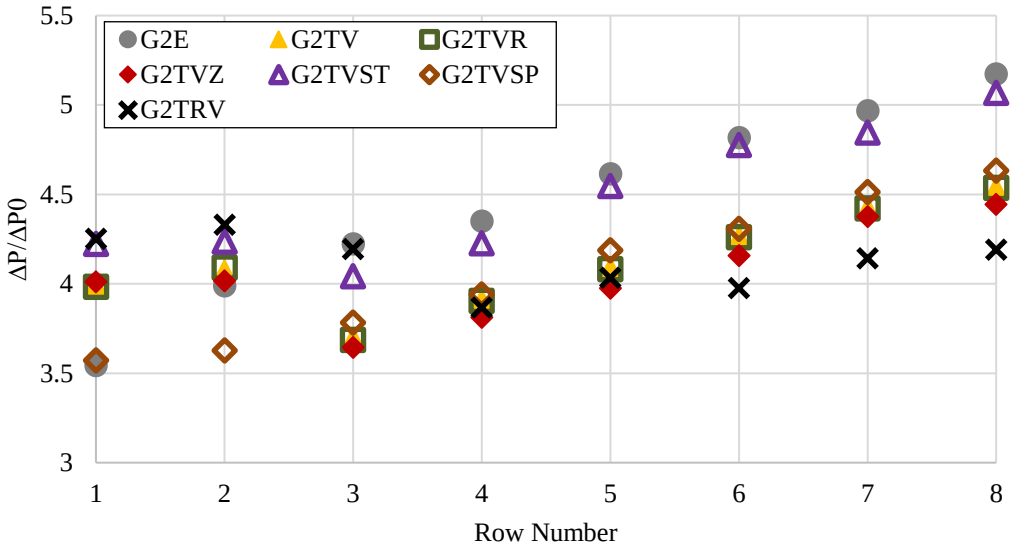

Figure A.8 Group 2 and 3: Pressure drop along the channel

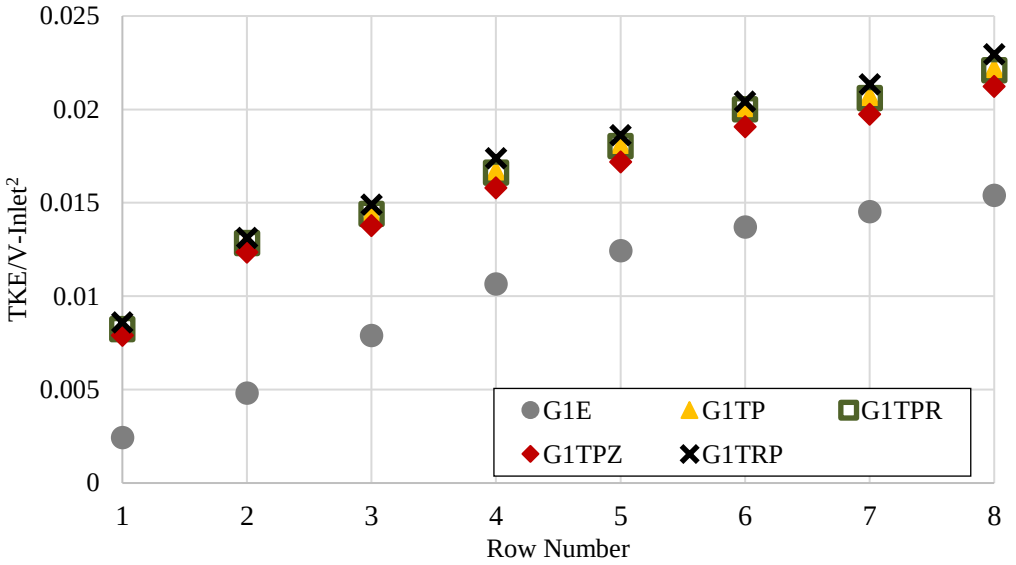

Figure A.9 TKE – Group 1

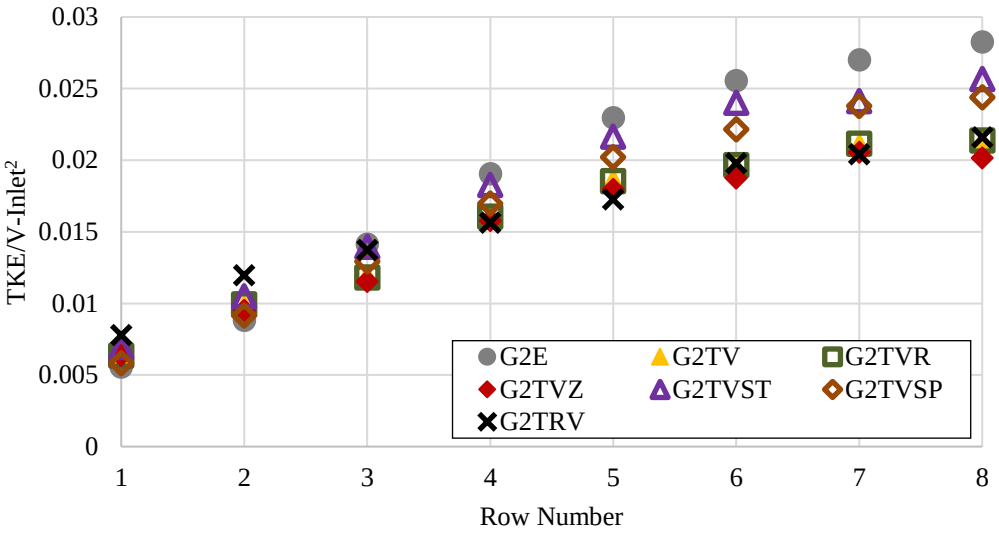

Figure A.10 TKE – Group 2 and 3